



GA - 5798

PLEASE RETURN TO  
ENGINEERING LIBRARY

## INTEGRAL NEUTRON THERMALIZATION

Annual Summary Report

October 1, 1963 through September 30, 1964

By  
J. R. Beyster  
J. R. Brown  
N. Corngold, etc.

ENGR. LIBRARY JUN 28 1967  
APR 6 1967  
UNIV. OF WASH. by ENGINEERING LIBRARY

October 15, 1964

General Atomic Division  
General Dynamics Company  
San Diego, California

metadc304066



## LEGAL NOTICE

This report was prepared as an account of Government sponsored work. Neither the United States, nor the Commission, nor any person acting on behalf of the Commission:

A. Makes any warranty or representation, expressed or implied, with respect to the accuracy, completeness, or usefulness of the information contained in this report, or that the use of any information, apparatus, method, or process disclosed in this report may not infringe privately owned rights; or

B. Assumes any liabilities with respect to the use of, or for damages resulting from the use of any information, apparatus, method, or process disclosed in this report.

As used in the above, "person acting on behalf of the Commission" includes any employee or contractor of the Commission, or employee of such contractor, to the extent that such employee or contractor of the Commission, or employee of such contractor prepares, disseminates, or provides access to, any information pursuant to his employment or contract with the Commission, or his employment with such contractor.

This report has been reproduced directly from the best available copy.

Printed in USA. Price \$6.00. Available from the Clearinghouse for Federal Scientific and Technical Information, National Bureau of Standards, U. S. Department of Commerce, Springfield, Va.

# INTEGRAL NEUTRON THERMALIZATION

October 15, 1964

---

## ANNUAL SUMMARY REPORT OCTOBER 1, 1963 THROUGH SEPTEMBER 30, 1964

Prepared under  
Contract AT(04-3)-167  
Project Agreement No. 2  
for the  
San Francisco Operations Office  
U. S. Atomic Energy Commission

### Work done by:

J. R. Beyster  
W. Brouwer  
J. R. Brown  
N. Corngold  
H. C. Honeck  
D. H. Houston  
D. Huffman  
G. D. Joanou  
J. Kirkbride

J. U. Koppel  
W. Mowry  
Y. D. Naliboff  
J. M. Neill  
D. E. Parks  
J. L. Russell  
J. R. Triplett  
J. A. Young  
J. C. Young

### Report written by:

J. R. Beyster  
J. R. Brown  
N. Corngold  
H. C. Honeck  
D. H. Houston  
G. D. Joanou  
J. Kirkbride  
J. U. Koppel  
W. Mowry  
Y. D. Naliboff  
J. M. Neill  
D. E. Parks  
J. R. Triplett  
J. A. Young  
J. C. Young

**GENERAL ATOMIC**  
DIVISION OF  
**GENERAL DYNAMICS**

JOHN JAY HOPKINS LABORATORY FOR PURE AND APPLIED SCIENCE  
P.O. BOX 608, SAN DIEGO, CALIFORNIA 92112





## TABLE OF CONTENTS

<u>Section No.</u>	<u>Title</u>	<u>Page No.</u>
I.	INTRODUCTION . . . . .	1
II.	NEUTRON THERMALIZATION IN $H_2O$ . . . . .	7
2.1	Introduction and Summary . . . . .	7
2.2	Position and Angular Dependent Neutron Spectra in $H_2O$ . . . . .	8
2.2.1	Position Dependent Spectra in $H_2O$ . . . . .	9
2.2.2	Angular Dependent Spectra in $H_2O$ Near a Poison Interface . . . . .	14
III.	NEUTRON THERMALIZATION IN $D_2O$ . . . . .	19
3.1	Introduction and Summary . . . . .	19
3.2	Self and Intramolecular Interference Scattering by $D_2O$ . . . . .	19
3.2.1	Total Scattering Cross Section and and Intermolecular Effects . . . . .	24
3.2.2	Conclusion . . . . .	34
3.3	Position Dependent Spectra in $D_2O$ . . . . .	34
3.3.1	Poisoning by a $1/v$ Absorber. . . . .	34
3.3.2	Position Dependent Spectra in Cadmium Poisoned $D_2O$ . . . . .	40
IV.	NEUTRON THERMALIZATION IN POLYETHYLENE . . . . .	43
4.1	Introduction and Summary . . . . .	43
4.2	Scattering Kernel for Polyethylene . . . . .	43
4.2.1	Frequency Spectrum . . . . .	43
4.2.2	Neutron Scattering . . . . .	45
4.3	Heterogeneous Studies . . . . .	48
V.	NEUTRON THERMALIZATION IN ZIRCONIUM HYDRIDE . . . . .	57
5.1	Introduction and Summary . . . . .	57
5.2	Zirconium Hydride Scattering Description . . . . .	57
5.2.1	Introduction . . . . .	57
5.2.2	Thermalization Model . . . . .	58
5.2.3	Experimental Considerations . . . . .	59



<u>Section No.</u>	<u>Title</u>	<u>Page No.</u>
VI.	NEUTRON THERMALIZATION IN BERYLLIUM . . . . .	65
6.1	Introduction and Summary. . . . .	65
6.2	Interference Effects in Neutron Scattering . . . . .	65
VII.	NEUTRON THERMALIZATION IN BeO. . . . .	73
7.1	Introduction and Summary. . . . .	73
7.2	Neutron Spectra in BeO . . . . .	73
7.3	Coherent Elastic Scattering in BeO. . . . .	78
VIII.	EXPERIMENTAL STUDIES ON MULTIPLYING ASSEMBLIES . . . . .	80
8.1	Neutron Spectrum Measurements . . . . .	80
8.2	Pulsed Reactivity Measurements . . . . .	86
IX.	FAST NEUTRON STUDIES . . . . .	97
9.1	Fast Neutron Penetration Through H <sub>2</sub> O . . . . .	97
9.2	Fast Neutron Penetration Through Graphite . . . . .	100
X.	DIFFERENTIAL SCATTERING STUDIES. . . . .	109
10.1	Introduction . . . . .	109
10.2	Principle of the Measurement . . . . .	111
10.3	Multiple Scattering Correction . . . . .	119
10.4	Experimental Arrangements . . . . .	122
10.4.1	Beam Tube System . . . . .	123
10.4.2	Electron Beam Target (Fansteel Source) . . . . .	123
10.4.3	Water Thermal Source . . . . .	123
10.4.4	Flight Path and Collimation . . . . .	125
10.4.5	Detector and Scattering Sample Arrangement . . . . .	126
10.4.6	Electronics and Monitoring System . . . . .	126
10.4.7	Sample Design . . . . .	130
10.4.8	Background Studies . . . . .	130
10.4.9	Detector Spatial Response . . . . .	132
10.5	Cross Section Results . . . . .	132



<u>Section No.</u>	<u>Title</u>	<u>Page No.</u>
XI.	EXPERIMENTAL AND CALCULATIONAL TECHNIQUES . .	147
11.1	Sensitivity of Detector Banks . . . . .	147
11.2	Calibration of Zirconium Scatterer . . . . .	150
11.3	Neutron Monitor Studies . . . . .	150
11.4	Data Reduction Methods . . . . .	154
11.5	Description of Gaker Code . . . . .	155
XII.	UNIVERSAL SCATTERING CODE . . . . .	163
12.1	Introduction and Summary . . . . .	163
12.2	Scattering Law . . . . .	163
12.2.1.	GASKET Code . . . . .	163
12.2.2	Translation Mode . . . . .	166
12.2.3	Brownian Motion . . . . .	167
12.2.4	Vibrational Modes . . . . .	167
12.2.5	Problem Input . . . . .	172
12.2.6	Main Program . . . . .	173
12.2.7	Subroutines . . . . .	174
12.2.8	FLANGE Code . . . . .	177
12.3	Status of the Codes . . . . .	179
XIII.	NEUTRON SPECTRUM BOOK . . . . .	181
13.1	Introduction and Summary . . . . .	181
13.2	Normalization of Experiment and Theory . . . . .	181
XIV.	RESEARCH EQUIPMENT AT THE GENERAL ATOMIC LINAC FACILITY . . . . .	191
	REFERENCES . . . . .	195
	APPENDICES:	
A.	Neutron Thermalization and Reactor Applications . . . . .	A-1
B.	Lattice Vibrational Spectra of Beryllium, Magnesium, and Zinc . . . . .	B-1



## LIST OF ILLUSTRATIONS

<u>Fig. No.</u>	<u>Title</u>	<u>Page No.</u>
2.1	Experimental Arrangement for Spectral Measurements in $H_2O$ . . . . .	10
2.2	Spatial Distribution of Indium Resonance Flux in the $H_2O$ Tank . . . . .	11
2.3	Ninety Degree Angular Spectra in Borated $H_2O$ . . . . .	13
2.4	Geometrical Configuration for Water Interface Experiment . . . . .	15
2.5	Calculated Spatial Distribution of Peak Thermal Flux in the Water Interface Experiment . . . . .	16
2.6	Angular Spectra Near a Poison Interface in Water . . . . .	18
3.1	Schematic Representation of the Short Collision Approximation . . . . .	25
3.2	$D_1D_1$ and OD Contributions to the $P_0$ Kernel . . . . .	26
3.3	Scattering Law $S(\alpha, \beta)$ for $D_2O$ at $\beta = -0.5$ . . . . .	27
3.4	Scattering Law $S(\alpha, \beta)$ for $D_2O$ at $\beta = -1.0$ . . . . .	28
3.5	Contribution of the Intermolecular Interference scattering to the Differential Cross Section for $D_2O$ . . . . .	30
3.6	Self and Intramolecular Interference Terms in the $D_2O$ Scattering Cross Section . . . . .	31
3.7	Contributions of the Intermolecular Interference Scattering to the Total Cross Section . . . . .	32
3.8	Calculated Total Cross Section for $D_2O$ Including all Interference Terms. . . . .	33
3.9	Experimental Arrangement for Spectral Measurements in $D_2O$ . . . . .	35
3.10	Spatial Distribution of Indium Resonance Flux in the $D_2O$ Tank . . . . .	37
3.11	Ninety Degree Angular Spectra in Boron Poisoned $D_2O$ at Various Axial Positions . . . . .	38
3.12	Ninety Degree Angular Spectra in Boron Poisoned $D_2O$ at Various Transverse Positions. . . . .	39
3.13	Ninety Degree Angular Spectra in Cadmium Poisoned $D_2O$ . . . . .	41
4.1	Frequency Dependence of the Vibrational Phase Difference Between Neighboring $CH_2$ Groups (Data of Lin and Koenig) . . . . .	44
4.2	Histogram of the Frequency Spectrum of Polyethylene . . . . .	46
4.3	Total Cross Section of Polyethylene . . . . .	49
4.4	Infinite Medium Neutron Spectrum in 1% Borated Polyethylene . . . . .	50



<u>Fig. No.</u>	<u>Title</u>	<u>Page No.</u>
4.5	Experimental Arrangement for Spectral Measurements in a Heterogeneous Assembly . . . . .	51
4.6	Effect of Re-entrant Hole Size on the Neutron Spectra Measured in an Heterogeneous Assembly . . . . .	53
4.7	Ninety-degree Angular Spectra at the Cell Interface of a Polyethylene - Iron Heterogeneous Assembly. . . . .	54
4.8	Ninety-degree Angular Spectra at the Cell Centers of a Polyethylene - Iron Heterogeneous Assembly . . . . .	55
5.1	Predicted Neutron Spectral Changes with Temperature Using the Fermi-Dirac and Einstein Oscillator Models . . . . .	61
5.2	Comparison of Neutron Spectra Calculated with the Doppler Broadened Oscillator Model and the Natural Width Model (SUMMIT) . . . . .	63
7.1	Geometrical Arrangement Used for BeO Spectral Measurements . . . . .	74
7.2	Relative Intensity of the Indium Resonance Neutron Flux Measured in the BeO Assembly . . . . .	75
7.3	Ninety-degree Angular Spectra in BeO . . . . .	77
8.1	Geometrical Arrangement for Spectral Measurements in a $UF_4$ + Paraffin Mixture. . . . .	81
8.2	Decay Characteristic of the $UF_4$ + Paraffin Multiplying Assembly . . . . .	83
8.3	Quasi-infinite medium spectrum in a $UF_4$ + Paraffin Mixture . . . . .	85
8.4	Zero Degree Angular Neutron Spectra in a Water Moderated Multiplying Assembly . . . . .	87
8.5	Scalar Neutron Spectra in a Water Moderated Multiplying Assembly . . . . .	88
8.6	Decay Characteristic of $UF_4$ + Paraffin in Configuration B-2 . . . . .	90
8.7	Decay Characteristic of $UF_4$ + Paraffin in Configuration B-4 . . . . .	91
8.8	Schematic Diagram Showing Locations of Source and Detector (for use with Table 8.2) . . . . .	92
8.9	Variation of $k\beta/l$ with Measurement Configuration . . . . .	94
9.1	Experimental Geometry for Fast-neutron-penetration Studies . . . . .	98
9.2	Calculational Geometry for Fast-neutron-penetration Studies . . . . .	99
9.3	Fast-neutron Flux at $0^\circ$ Emission Angle . . . . .	101
9.4	Experimental Arrangement for Fast Neutron Penetration Studies in Graphite . . . . .	102
9.5	Fast Neutron Spectra Through a Graphite Shield . . . . .	103

<u>Fig. No.</u>	<u>Title</u>	<u>Page No.</u>
9.6	Geometry of the Isotropic Source . . . . .	105
9.7	Neutron Spectra from the Isotropic Source . . . . .	106
9.8	Angular Distribution around the Isotropic Source . . . .	107
10.1	Experimental Arrangement for Measurement of the Differential Scattering Cross Section of Water . . . . .	112
10.2	Geometry of the Scattering Sample and the Detector . . .	113
10.3	Honeck Correction Factor for Scattering by a 21.5 mil H <sub>2</sub> O Sample . . . . .	117
10.4	Honeck Correction Factor for Scattering by a 32 mil H <sub>2</sub> O Sample . . . . .	118
10.5	Ratio of Multiple Scattering Correction Factors . . . . .	120
10.6	Geometrical Arrangement for Angular Distribution Measurements . . . . .	124
10.7	Spatial Variation of Neutron Flux Intensity at the Sample Position in the Original Experimental Arrangement . . . . .	127
10.8	Spatial Variation of Neutron Flux Intensity at the Sample Position in the Present Experimental Arrangement . .	128
10.9	Electronic Block Diagram for Differential Scattering Experiment . . . . .	129
10.10	Original H <sub>2</sub> O Sample Design . . . . .	131
10.11	Final H <sub>2</sub> O Sample Design . . . . .	131
10.12	Spatial Variation of Relative Sensitivity of Li <sup>6</sup> Detector .	133
10.13	Variation of Detector Spatial Response with Position. . .	134
10.14	Elastic and Inelastic Contributions to the Scattering Cross Section of Vanadium . . . . .	136
10.15	Calculated and Experimental Scattering Cross Sections for Vanadium at Three Scattering Angles . . . . .	137
10.16	The Eisenhower-Pelah Frequency Distribution for Vanadium . . . . .	138
10.17	Calculated and Measured Differential Scattering Cross Sections for H <sub>2</sub> O . . . . .	141
10.18	Comparison of Scattering Cross Sections Calculated from the Isotropic and Anisotropic H <sub>2</sub> O Models . . . .	142
10.19	Comparison of the Scattering Cross Sections Calcu- lated from Different Models for H <sub>2</sub> O . . . . .	143
11.1	Measured and Calculated Sensitivity of 16-M BF <sub>3</sub> Detector Bank . . . . .	148
11.2	Scalar Flux Correction Factor for the Zirconium Scattering Plug. . . . .	151
11.3	Corrected and Uncorrected Scalar Flux in Borated Water at 293°K . . . . .	152
13.1	Example of Spectrum Book Format . . . . .	182
13.2	Scattering Cross Section for H <sub>2</sub> O in the Thermal- epithermal Joining Region . . . . .	184



<u>Fig. No.</u>	<u>Title</u>	<u>Page No.</u>
13.3	Neutron Flux in Borated H <sub>2</sub> O in the Thermal-Epithermal Joining Region Based on the Bound Hydrogen Model. . . . .	186
13.4	Neutron Flux in Borated H <sub>2</sub> O in the Thermal-Epithermal Joining Region Based on the Free Gas Model. . . . .	187
13.5	Ratio of Scattering Cross Section for H <sub>2</sub> O using Different GAKER Energy Mesh Intervals. . . . .	189
14.1	Basic Linac Facility, 1963. . . . .	192
14.2	Present and Planned Linac Facility . . . . .	193





## I. INTRODUCTION

This Annual Summary Report covers the Integral Neutron Thermalization activities at General Atomic from October 1, 1963 through September 30, 1964, under Contract AT(04-3)-167, Project Agreement No.2, with the U. S. Atomic Energy Commission. For general reviews of experimental, analytical and theoretical investigation previously performed under this program, the reader is referred to the three previous annual summary reports, <sup>(1)</sup> <sup>(2)</sup> <sup>(3)</sup>

The research program for the present contract year included the following areas of work:

1. D<sub>2</sub>O spectral investigations (Section III)
2. Measurements of scattering angular distributions, (Section X).
3. BeO spectral measurements (Section VII)
4. Studies of space dependent problems (Sections II, III and IV)
5. Theoretical studies (Sections III through VII and XII)
6. Preliminary studies of fast neutron shielding (Section IX).

The work listed above has been supplemented by studies in the following areas:

1. Neutron spectra and reactivity measurements in multiplying assemblies (Section VIII).
2. Improvement in experimental and calculational techniques (Section XI).
3. Compilation of spectral measurements into the Spectrum Book (Section XIII).

In addition, improvements have been made to the research equipment available for experimental neutron thermalization studies and these are discussed in Section XIV. The underlying purpose of the research

program given above is to provide realistic theoretical procedures for describing slow neutron scattering from bound atoms; particularly the common reactor moderators, and to provide and correlate experimental tests of these procedures under conditions appropriate to reactor design.

This year's activities under the Integral Neutron Thermalization Program are summarized briefly below:

Measurements of neutron spectra were performed in  $\text{H}_2\text{O}$ ,  $\text{D}_2\text{O}$  and  $\text{BeO}$  in various geometries with various poisons. The agreement between the measured and theoretical spectra was improved considerably since last year. These improvements were predominantly experimental in nature.

Single differential scattering measurements were performed on  $\text{H}_2\text{O}$  with improved geometries and samples utilizing better multiple scattering correction procedures. The problem of normalization to obtain absolute cross sections is still being investigated.

Studies of multiplying assemblies have been made which produced conclusions on the feasibility of reactivity measurements by pulsed neutron methods. In addition, improved background correction procedures were discovered in spectral measurements in multiplying assemblies. Resonances in  $\text{U}^{238}$  were clearly observed in these spectra pointing to the desirability of increasing the energy range of the measurements.

The analysis of preliminary fast neutron penetration measurements in graphite and water showed particular difficulties, indicating a need for improved neutron shielding computer codes. Experimental problems still remain in the fast neutron time of flight spectral measurements. The solution of these problems has been started and, in addition, studies of the experimental problems in intermediate energy neutron spectra measurements have been initiated.

The major effort of the theoretical group has been directed to the development of a general computer code capable of calculating the scattering kernel for most moderators. This code is becoming operational and should soon provide useful results. It is anticipated that this code will be of great help in reactor design and will aid research into each moderator. Other phenomena which were investigated this year are the intermolecular scattering in  $\text{D}_2\text{O}$ , coherent elastic scattering in  $\text{BeO}$ , the scattering kernel for polyethylene and the lattice vibrational spectra of magnesium and zinc. In addition, the formalism for interference effects in neutron scattering by crystalline moderators has been written and will be applied shortly to beryllium. Experimental measurements in Be are planned soon in this connection.



The other major area of effort this year was the compilation of spectral measurements into a standardized format known as the Spectrum Book. About 30 spectra were compiled into this book, which was sent to various firms and institutions in this and other countries. The Spectrum Book will be of value to the reactor designer in allowing him to make comparative calculations to check the physics, mathematics and numerical procedures used in their analyses. The book was well received and the critical response has been most encouraging.

During the present contract year, several papers originating from this project were presented at various scientific meetings or submitted to technical journals for publication. They were:

#### RECENT PUBLICATIONS

J. C. Young, G. D. Trimble, Y. D. Naliboff, D. H. Houston, and J. R. Beyster, "Neutron Spectrum Measurements in  $H_2O$ ,  $CH_2$  and  $C_6H_6$ ," Nuc. Sci. and Eng., 18, 376, (1964).

J. C. Young, J. A. Young, G. K. Houghton, G. D. Trimble and J. R. Beyster, "Neutron Thermalization in Zirconium Hydride," Nuc. Sci. and Eng. 19, 230 (1964).

J. A. Young and J. U. Koppel, "Lattice Vibrational Spectra of Be, Mg and Zn," Phys. Rev. 134A, 1476, (1964).

J. A. Young and J. U. Koppel, "Scattering Kernel for Beryllium," Nuc. Sci. and Eng., 19, 1367 (1964).

J. U. Koppel and J. A. Young, "Neutron Scattering by Water Taking into Account the Anisotropy of the Molecular Vibrations," Nuc. Sci. and Eng., 19, (1964).

#### Papers Presented at the ANS Meeting November 1963 in New York:

J. R. Brown, J. C. Young, J. R. Beyster, D. H. Houston, and W. R. Mowry, "Measurements of Subcritical Reactivity Using a Pulsed Neutron Source."

J. U. Koppel, "Neutron Scattering by Water, Taking into Account the Anisotropy of the  $H_2O$  Molecular Vibrations."

G. D. Trimble, J. C. Young, J. R. Beyster, and G. K. Houghton, "Temperature - Dependent - Scalar Neutron Spectra in Borated Water."

J. A. Young, "Scattering Kernel for Beryllium."

Papers Presented at the APS Meeting April 1964 in Washington:

J. R. Beyster and W. R. Mowry, "Angular Distribution of Thermal Neutron Scattering from  $H_2O$ ."

J. A. Young and J. U. Koppel, "Lattice Vibrational Spectra of Be, Mg, and Zn."

Papers Presented at the ANS Meeting June 1964 in Philadelphia:

J. L. Russell, J. R. Brown, and J. C. Young, "On the Validity of the Pulsed Neutron Measurement of  $K\beta/\ell$ ."

J. C. Young, J. M. Neill, and J. R. Beyster, "Neutron-Spectrum Measurements in a ( $UF_4$  + Paraffin) Multiplying Assembly."

Paper Presented at International Conference on Peaceful Uses of Atomic Energy at Geneva, August 1964:

J. R. Beyster, N. Corngold, H. C. Honeck, G. D. Joanou, and D. E. Parks, "Neutron Thermalization and Reactor Applications."

Papers to be Presented at the ANS Meeting November 1964 in San Francisco:

J. M. Neill, J. C. Young, and W. Brouwer, "Positron and Angular-Dependent Spectrum Measurements in  $H_2O$ ."

J. C. Young, J. M. Neill, and W. Brouwer, "Neutron Spectrum Measurements in  $D_2O$ ."

Papers to be submitted to Nuclear Science and Engineering for Publication:

J. U. Koppel and J. A. Young, "Neutron Scattering by Polyethylene."

J. C. Young, J. M. Neill, D. H. Houston, and J. R. Beyster, "Neutron Spectrum Measurements in  $H_2O$  and  $D_2O$ ."

REPORTS

Scattering Kernel for Beryllium, General Atomic Report GA-4638.

Measurement of Subcritical Reactivity Using a Pulsed Neutron Source, General Atomic Report GA-4838.

Neutron Scattering by  $H_2O$  Taking into Account the Anisotropy of the  $H_2O$  Molecular Vibrations, General Atomic Report GA-4850.

Lattice Vibrational Spectra of Beryllium, Magnesium and Zinc, General Atomic Report GA-4879.

Integral Neutron Thermalization, Quarterly Report ending December 31, 1963, General Atomic Report GA-4881.

Integral Neutron Thermalization, Quarterly Report ending March 31, 1964, General Atomic Report GA-5176.

Angular Distribution of Thermal Neutron Scattering from  $H_2O$ , General Atomic Report GA-5373.

On the Analysis of Pulsed Multiplying Systems, General Atomic Report GA-5404.

CAP - A Collimator Analysis Program, General Atomic Report GA-5418.

Neutron Scattering by Polyethylene, General Atomic Report GA-5600.

Integral Neutron Thermalization, Quarterly Report ending June 30, 1964, General Atomic Report GA-5486.





## II. NEUTRON THERMALIZATION IN H<sub>2</sub>O

### 2.1 INTRODUCTION AND SUMMARY

This year a number of neutron spectra were measured in water moderated systems. The measurements were conducted in finite geometries. An attempt was made to maximize leakage and transport phenomena yet maintain simple one-dimensional configurations. Under this program there have been numerous difficulties in comparing measured spectra with spectra calculated under similar conditions. We have attempted to refine and improve the measurements, and to remove the remaining experimental uncertainties. The comparisons shown in the following sections are greatly improved over past results. However, much difficult work remains to be done to establish that spectra in water systems, especially heterogeneous configurations, are being calculated correctly. The work of Mostovoi<sup>(4)</sup> which supplements and corroborates the previous lattice spectral work requires study and experimental verification since the suggested interpretation of the experiments is not in agreement with that of Honeck and Takahashi.<sup>(5)</sup>

The theoretical description of neutron scattering in H<sub>2</sub>O has not been changed during the last year. It will be recalled that the Nelkin<sup>(6)</sup> bound hydrogen model has been used in the past for most of our comparisons. Last year Koppel<sup>(7)</sup> modified this model to include anisotropic vibration of the hydrogen atoms. The results did not affect spectral predictions markedly. It should be noted that the rotational degrees of freedom cover a broad frequency range in our model, but we will not be able to make this improvement until the new kernel code GASKET-FLANGE (Section XII) is completed. Hindered translational or diffusive motion of the water molecule can also be treated at that time. Haywood<sup>(8)</sup> has constructed a scattering kernel for water which includes these phenomena and has achieved much success in some comparisons<sup>(9)</sup> with experimental spectra and diffusion parameters. We plan to compare our data with predictions of this model soon. In the future, theoretical predictions of various models will be compared with our single differential scattering experiments, which serve as an excellent test of the transport properties of the kernel. In addition, selected spectral studies in finite media, at high temperatures, with resonance absorbers and in clean heterogeneous configurations will be undertaken.

## 2.2 POSITION AND ANGULAR DEPENDENT NEUTRON SPECTRA IN H<sub>2</sub>O

The understanding of neutron thermalization in H<sub>2</sub>O was considerably improved by the introduction of the bound hydrogen model<sup>(6)</sup> describing neutron scattering by the water molecules. In this model, the two hydrogen atoms are bound harmonically to the heavier oxygen nucleus and the dynamics of the system is represented by several discrete oscillators with appropriate weights. Although the model is fairly simple, it has been immensely useful in calculating neutron spectra in quasi-infinite medium geometries. However, infinite medium neutron spectra do not provide conclusive tests of the scattering model, but they do have the advantage that they can be easily and accurately measured, they serve as a tie point by the fact that if they can not be calculated correctly, the model is very inaccurate, and they are of practical use in reactor design. Strong emphasis has been placed on integral studies because substantiation of the details of the scattering description by differential measurements is difficult. Previous spectral studies in light water<sup>(10, 11)</sup> have been made in predominantly infinite medium geometries (in which leakage effects are insignificant) in order to test gross features of the scattering model and to provide a good basis for preliminary refinements in the model. The agreement between experimental and calculated values for H<sub>2</sub>O has been reasonable in such geometries, and it was felt that more critical tests were necessary. It is possible to devise experimental situations in which the neutron spectra are more sensitive to the details of the scattering model. Situations of this sort can be achieved by the introduction of poison or temperature discontinuities into the experimental assembly, by poisoning the moderator with resonance absorbers, and by appropriate variation of the measurement position. Although such spectra may be of less direct use in reactor design, their calculation provides a good test of the physics, mathematics, and numerical procedures used in reactor analysis.

Refinements have been made to the scattering model for H<sub>2</sub>O and calculational methods and presentation of data have become more standardized. Spectral measurements in H<sub>2</sub>O moderated systems under more critical conditions than were utilized in Refs. 10 and 11 are reported in this section. Comparisons with the theoretical values are made which show the extent of the improvement in the knowledge of integral neutron thermalization in water.

Neutron spectra are calculated at General Atomic utilizing a variety of computer codes. The scattering kernel based on the bound model for H<sub>2</sub>O is generated by means of the GAKER<sup>(12)</sup> code (see also Section 11.5). Group cross sections ( $P_0$  and  $P_1$ ) are then calculated using

these scattering kernels by the GATHER<sup>(13)</sup> code, which solves the  $B_1$  approximation to the position independent Boltzmann equation. A distributed source ( $P_0$  and  $P_1$ ) in a single dimension is calculated by the DSZ<sup>(2)</sup> code using smoothed flux-plot data. The angular neutron spectra are then calculated by the GAPLSN<sup>(14)</sup> code using these group cross sections and the distributed source. GAPLSN is a one dimensional  $S_n$  transport theory code and is generally used in the  $P_1$  approximation with  $n = 16$ .

Reduction of the experimental configuration to a one dimensional geometry in the calculation is achieved by a diffusion theory correction in which  $D(E)B^2$  terms are added to the group absorption cross sections. Here the diffusion constant  $D(E)$  is obtained from the GATHER code output, and  $B^2$  is the net buckling transverse to the direction of the calculation.  $B^2$  obtained from the flux plots may be either positive or negative.

The  $P_1$  source from the DSZ code is also calculated from a diffusion theory approximation. In  $H_2O$ , this component is probably underestimated, but at present no techniques for its measurement have been developed.

### 2.2.1 Position Dependent Spectra in $H_2O$

Position dependent spectral measurements were made in  $H_2O$  poisoned by boric acid to about 5.2 barns/hydrogen atom at 2200 meters/sec. The atom densities are given in Table 2.1. The experimental arrangement, approximating a one dimensional geometry for these measurements, is illustrated in Fig. 2.1. Neutron spectra were measured at  $90^\circ$  to the source-assembly axis across the 4-inch dimension of the tank with  $D$  of Fig. 2.1 equal to 1, 2, 3, and 4 inches (surface). One inch thick boundaries of  $B_4C$  were placed along the 12 inch sides of the tank. These boundaries were designed to prevent room return of thermal and epithermal neutrons, and they proved to be a significant factor in permitting the surface leakage spectrum to be measured accurately even though the spectra measured as near as 1 inch to the surface were not affected by the improvement in the boundaries. The spatial distribution of the flux was measured by activating cadmium-covered indium foils and is shown in Fig. 2.2 for the 12-inch horizontal axial direction both with and without the  $B_4C$  boundaries. It can be seen that although these boundaries reduced thermal neutron return, they also reflected fast neutrons back into the assembly which modified the spatial distribution of the flux at indium resonance. The problem remained calculable, however, since it was the modified flux distribution that was used to calculate the distributed source.



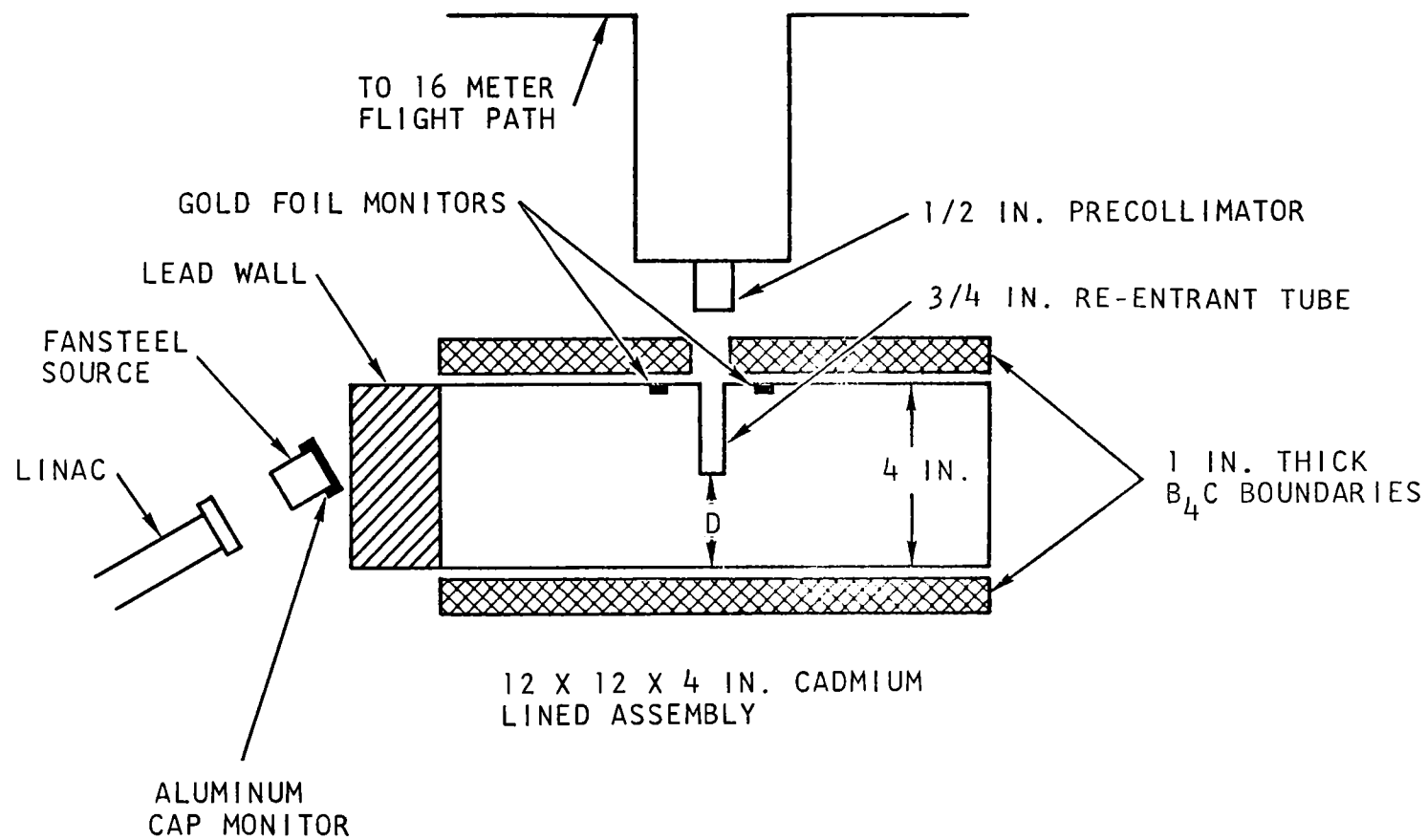


Fig. 2.1 -- Experimental arrangement for spectral measurements in  $H_2O$

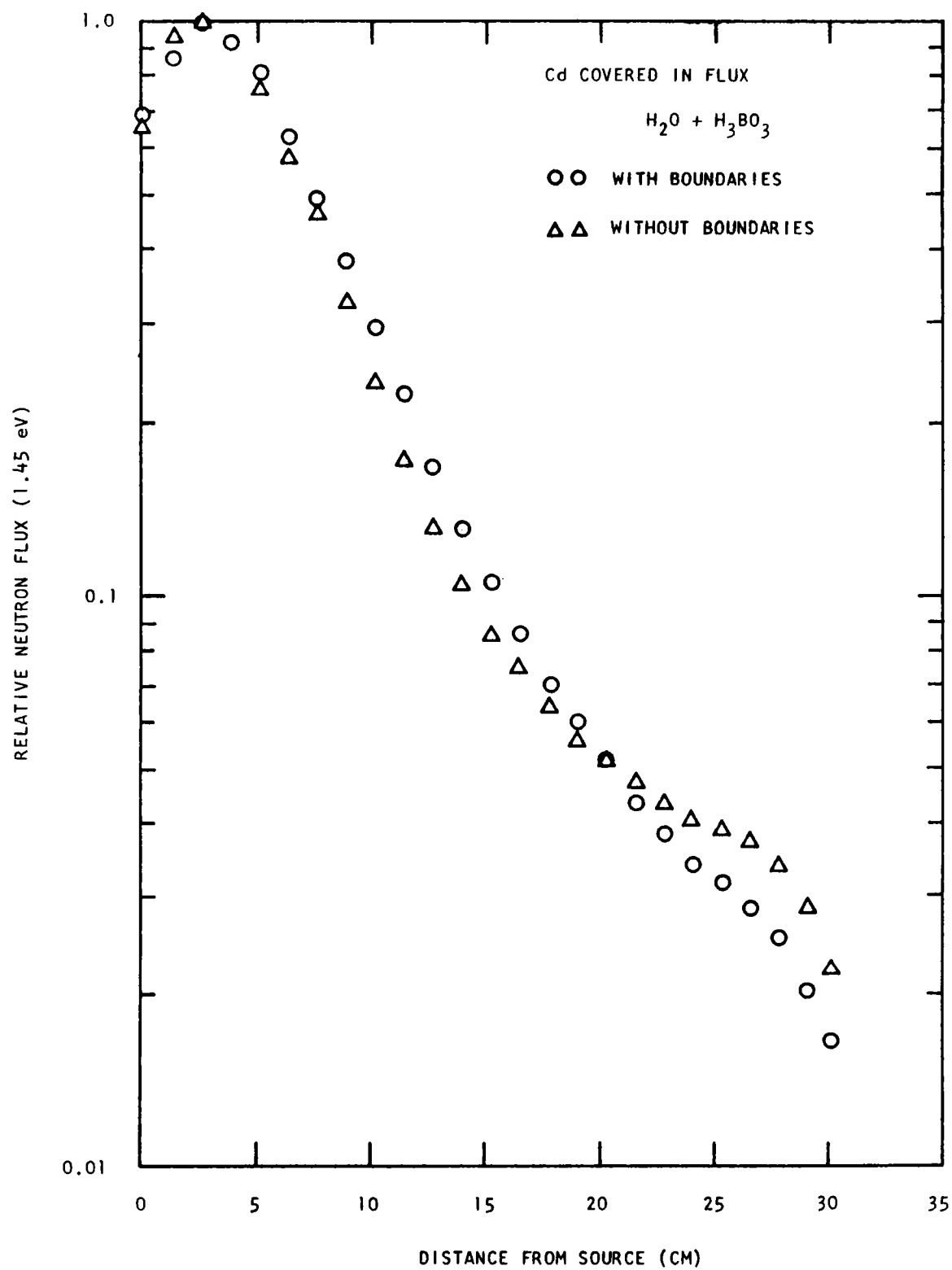


Fig. 2.2 -- Spatial distribution of indium resonance flux in the  $H_2O$  tank

TABLE 2.1

Atom Densities for Neutron Spectral Measurements in H<sub>2</sub>O  
(atoms/barn-cm units)

Borated H<sub>2</sub>O

Boron	0.000424
Hydrogen	0.06605
Oxygen	0.03366

The results of the spectral measurements are shown in Fig. 2.3 together with spectra calculated using the bound model for H<sub>2</sub>O and show fairly good agreement. The spectral shape of the surface leakage spectrum shown in Fig. 2.3 is as good as at the other three positions measured if the theory and experiment are normalized without regard to their relative intensity. The error bars indicated in the figure are statistical. In the calculations, both  $P_0$  and  $P_1$  scattering were considered, and the 4 inch axis was the direction accounted for in the one dimensional calculation. The lack of agreement in relative intensities between the theory and experiment at the surface may indicate that either the  $P_1$  scattering matrix is incorrect, which would manifest itself principally at the surface, or the reflection from the B<sub>4</sub>C boundaries has boosted the source intensity at the surface. Alternatively the restriction of the cross section anisotropy to  $P_1$  only may have caused the observed discrepancy although this is doubtful in view of the numerical studies undertaken previously. (15)

A second calculation was performed in which  $P_1$  scattering was neglected. At the center of the tank ( $D = 2$  inches), the neglect of  $P_1$  scattering made little or no difference, but at the edge of the tank the neutron spectrum calculated with isotropic scattering only is both lower in magnitude and has a changed shape as shown in Fig. 2.3. Since the calculated and measured spectra of Fig. 2.3 were all normalized with respect to their relative intensities, it becomes obvious that consideration of anisotropic scattering is essential if the surface leakage spectrum is to be calculated accurately. It is not possible to discuss quantitatively the adequacy of the  $P_1$  scattering description by the Nelkin model since the experiment was not sensitive enough. While neglect of  $P_1$  scattering leads to obvious errors, it appears that in order to test severely the anisotropic scattering matrices by integral measurements, larger flux gradients must be imposed than those observed in this experiment. Alternatively, as a procedure for determining whether these differences in intensity of spatial flux are associated with the scattering kernel, we have undertaken the scattering angular distribution measurements (Section IX) which are very sensitive to the  $P_1$  kernel. The theoretical curves shown in Fig. 2.3 have been calculated with a scattering kernel which includes the modification

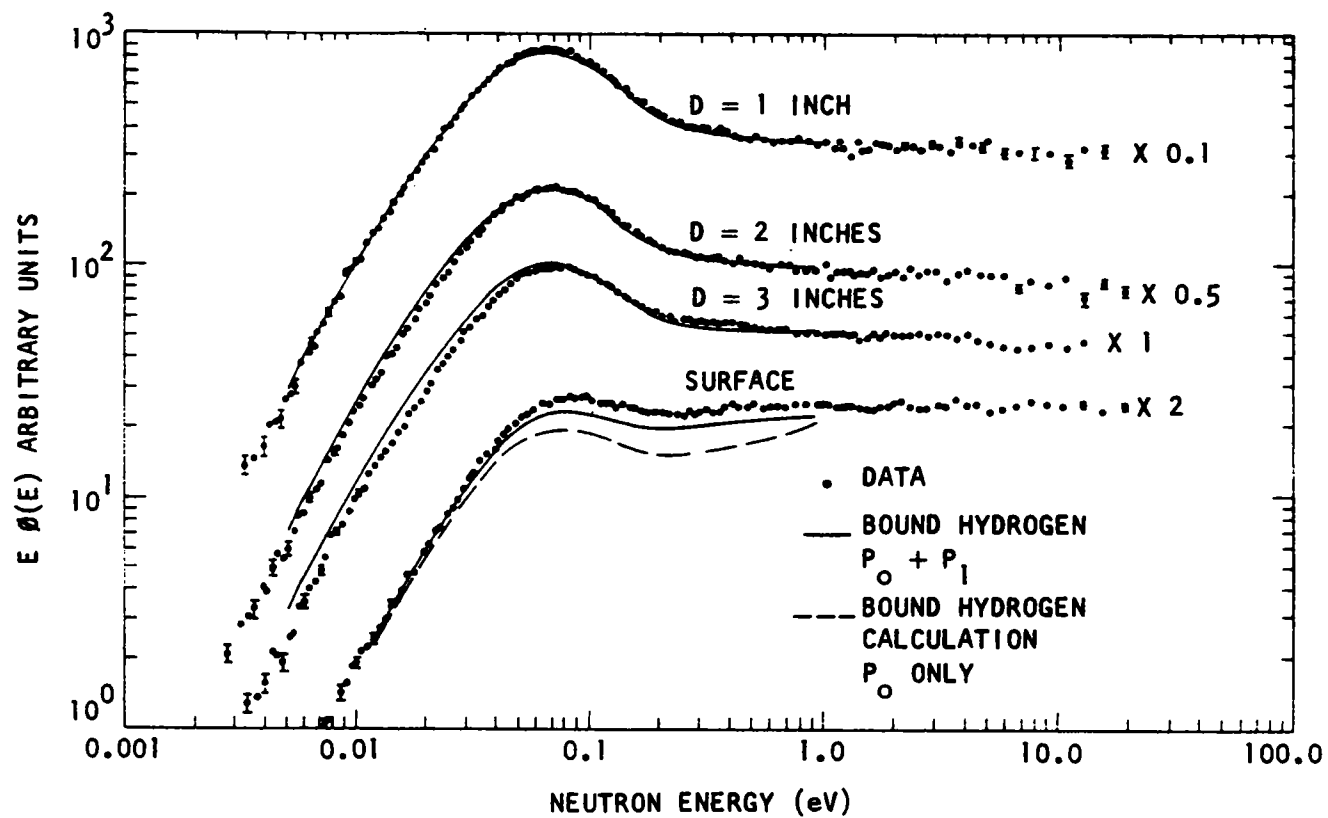


Fig. 2.3 -- Ninety-degree angular spectra in borated  $H_2O$



for anisotropic vibration made by Koppel to the Nelkin model. The agreement between theory and experiment in the measurements reported here is sufficiently good that one can state with confidence that the modified Nelkin model provides an excellent description of  $P_0$  scattering. Since the nonrigorous features of this model (Section 2.1) must then be of more importance in anisotropic scattering, further studies to detail these features quantitatively must come from the differential measurements or integral measurements in the presence of poison or material discontinuities. An experiment of the latter type was performed and is discussed in Section 2.2.2.

### 2.2.2 Angular Dependent Spectra in $H_2O$ Near a Poison Interface

Measurements of neutron spectra in the presence of a strong flux gradient have been made this year in order to investigate the adequacy of the anisotropic scattering description by the modified Nelkin model. Prior to this time, these measurements were of neutron spectra near the boundary of an assembly, but the flux gradient there did not, as a rule, appear to be large enough to provide a measurement highly sensitive to  $P_1$  and higher order scattering.

Therefore, the experimental geometry of Fig. 2.4 was designed in which a strong flux gradient was obtained by placing concentrated cadmium sulphate solution outside a thin tank containing dilute boric acid. The calculated spatial variation of the thermal flux peak in this geometry is shown in Fig. 2.5. The inner tank was mildly poisoned with boric acid to reduce its transverse leakage probability. The diffusion corrections for transverse leakage then became sufficiently small to allow an accurate calculation of the angular spectra in the horizontal flight path direction by the code GAPLSN.<sup>(14)</sup> By rotating the assembly about a horizontal axis at a point 3/8 inch outside the inner tank, preliminary GAPLSN calculations showed that neutron spectra would exhibit a strong angular dependence reflecting the change in the flux gradient from the 4-inch to the 12-inch dimension. In addition, since the measurements were made always in a direction perpendicular to the source flux gradient, effects due to the anisotropy of the source were minimized.

Spectral measurements were made with the horizontal axis of the tank at  $0^\circ$ ,  $30^\circ$ , and  $45^\circ$  to the flight path direction. Some difficulties were encountered during the measurements. The lead used to spread the neutrons was attached directly to the assembly and the heat generated in the lead was transmitted directly to the tanks so that the fluids inside each tank became warm and expanded. The outer tank was able to leak the excess, but since the inner tank containing the boric acid solution was not vented some bowing occurred. This bowing was estimated to be about 0.010 inch at the position of measurement, and was serious because the

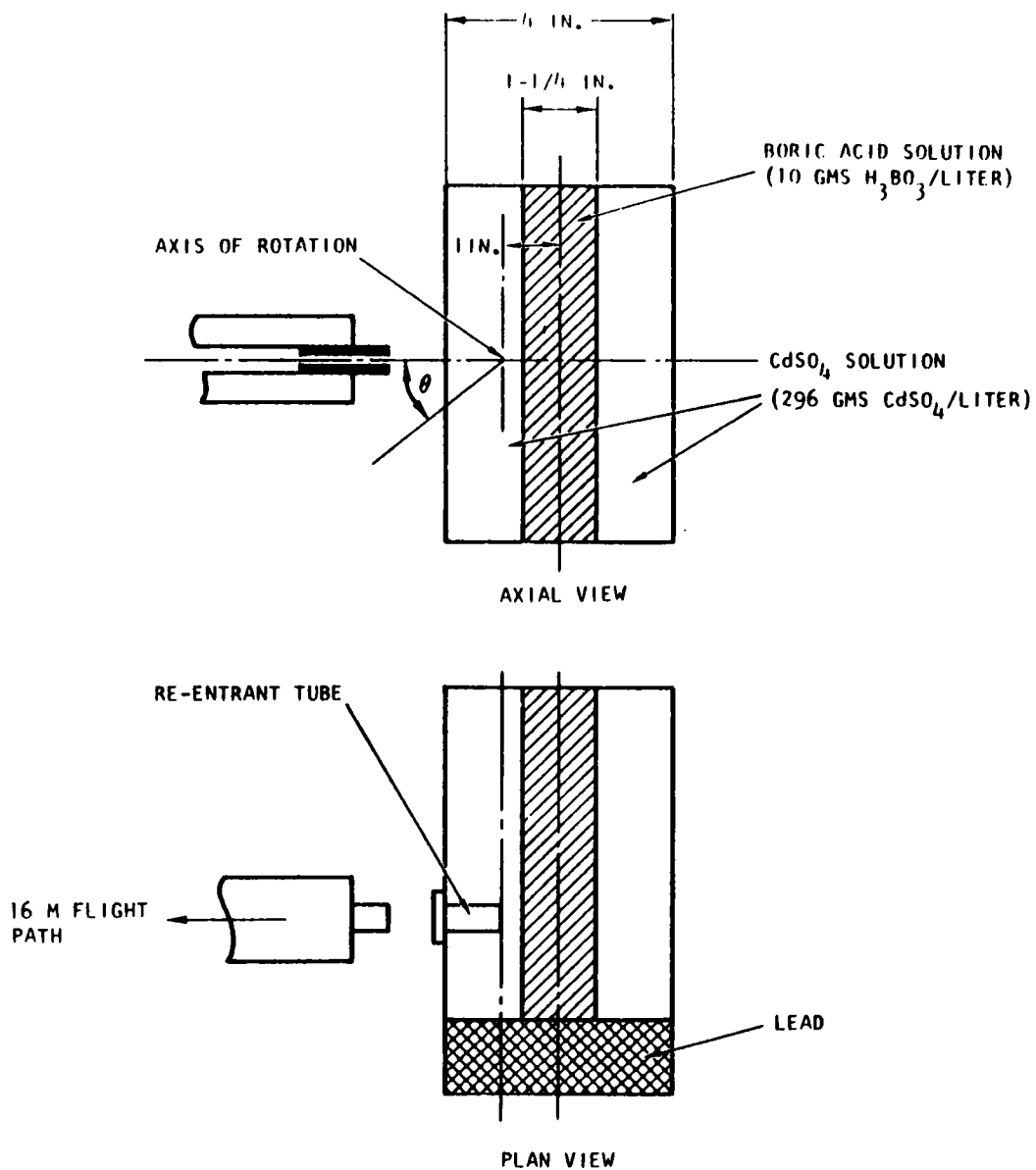


Fig. 2.4 -- Geometrical configuration for water interface experiment

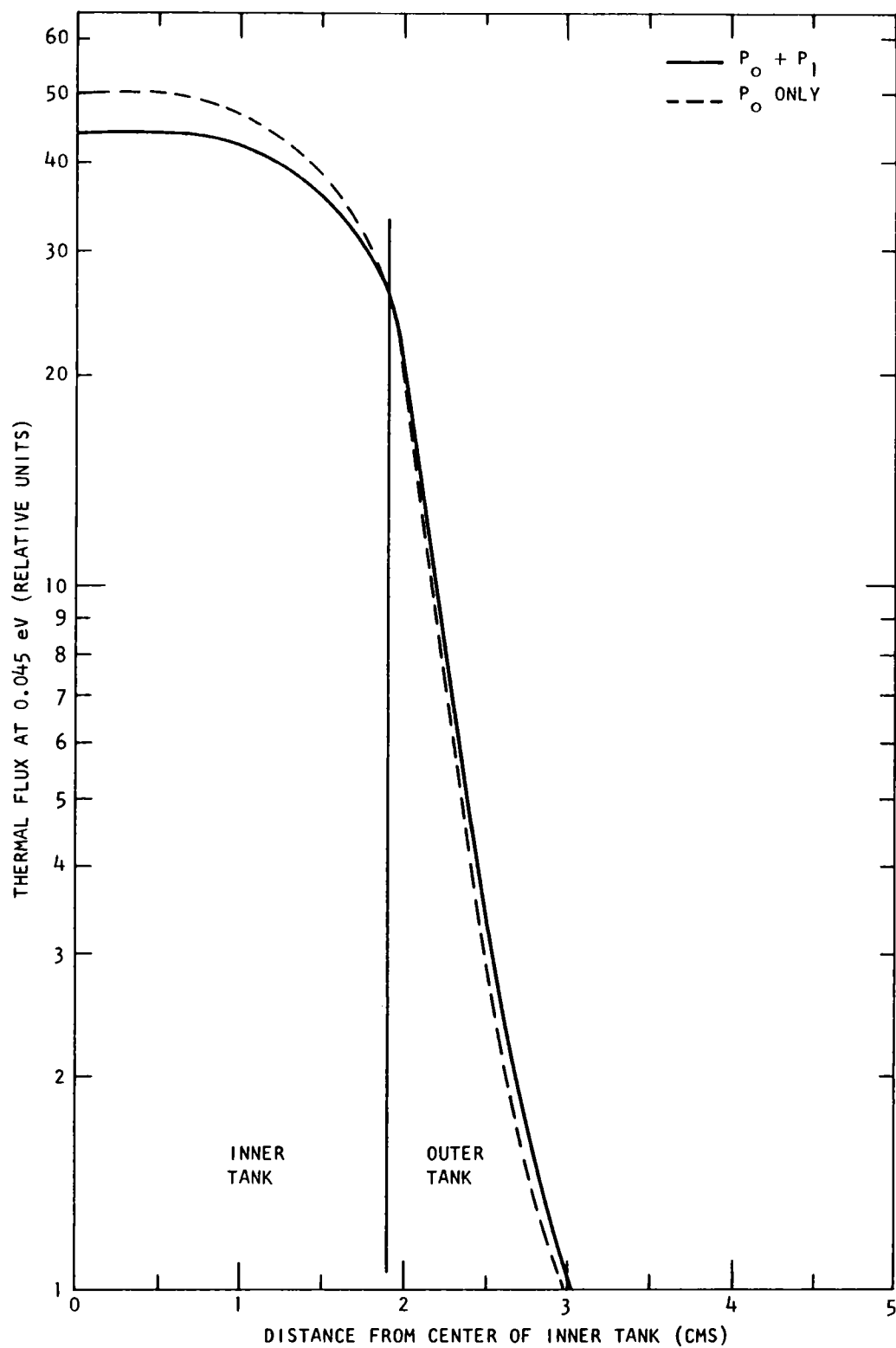


Fig. 2.5 -- Calculated spatial distribution of peak thermal flux in the water interface experiment

neutron spectra were strongly spatially dependent. Monitoring difficulties were encountered during the experiment. Gold foils were utilized for the background subtraction and normalization purposes and did not prove to be entirely satisfactory since the fluxes did not normalize correctly in the  $1/E$  region.

In performing the calculations for this problem, a water kernel at  $39.5^{\circ}\text{C}$  was used instead of the  $54^{\circ}\text{C}$  which was more typical for this assembly. This was done because the difference of  $15^{\circ}\text{C}$  was considered to be too small to affect the spectra significantly, and did not justify the additional cost of generating a new kernel at this temperature.

The experimental results together with the theoretical values are shown in Fig. 2.6, and each pair is normalized independently instead of relatively due to the monitoring difficulties. The anticipated strong angular dependence was realized. The  $0^{\circ}$  measurements fit the calculated values to within 15%, but the fit of experiment to theory at the other two angles is not as good, with errors of up to 25% being indicated. Because the spectra are very sensitive to position and angle, and because there are uncertainties in the measured positions and angles, it is impossible to be sure that the discrepancies arise from an inadequacy of the Nelkin water model. These angular spectra were also calculated with  $P_0$  scattering only; however, this did not change the shape or intensity of the flux spectrum at the position of measurement. It appeared that the particular position of measurement was insensitive to  $P_1$  scattering and that a better choice would have been at 1 inch outside or at the center of the inner tank.

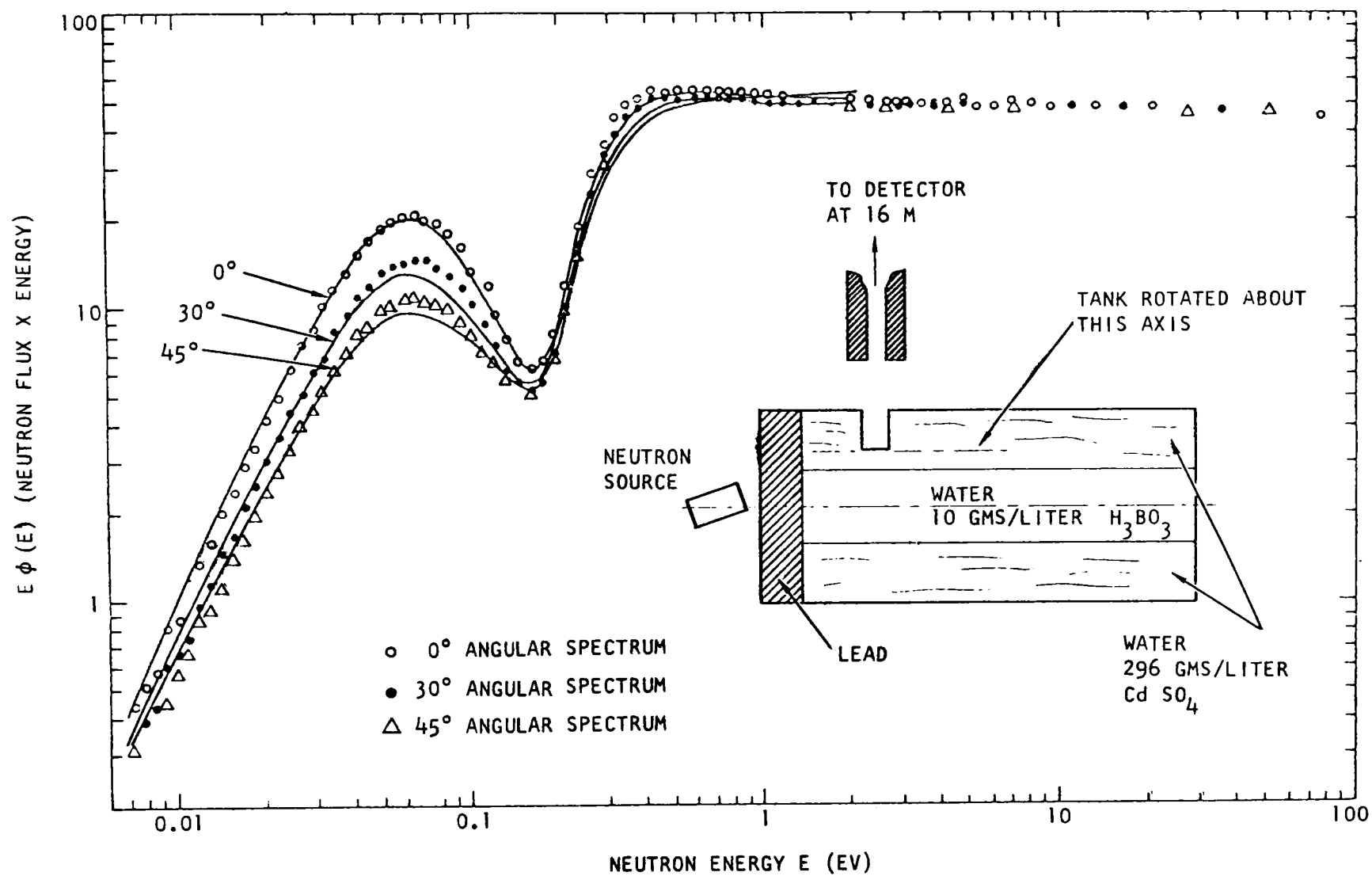


Fig. 2.6--Angular Spectra Near a Poison Interface in Water



### III. NEUTRON THERMALIZATION IN D<sub>2</sub>O

#### 3.1. INTRODUCTION AND SUMMARY

The thermal scattering description for D<sub>2</sub>O used in most of our calculations of spectra is obtained from the extension by Honeck<sup>(16)</sup> of the Nelkin<sup>(6)</sup> model for H<sub>2</sub>O. This extension has not been on good theoretical grounds because it assumes a completely incoherent scatterer whereas deuterium is mostly coherent. During this year, the self and intramolecular interference scattering by D<sub>2</sub>O have been studied. The conclusions are detailed fully in Section 3.2 and it appears that these interference terms tend to cancel each other so that Honeck's incoherent approximation gives quite good results for infinite media and weakly space-dependent spectra. Some small changes were made however in Honeck's oscillator weights and frequencies using the data of Butler.<sup>(17)</sup>

Spectral measurements have been performed in D<sub>2</sub>O this year in space dependent geometries and also with poisoning by a strong resonance absorber. These studies were performed to clear up discrepancies remaining from previous measurements<sup>(2)</sup> and to establish the theoretical conclusion given above. In both these endeavors, we were quite successful as shown in the results given in Section 3.3.

#### 3.2. SELF AND INTRAMOLECULAR INTERFERENCE SCATTERING BY D<sub>2</sub>O

Because of the great similarity between the D<sub>2</sub>O and H<sub>2</sub>O molecules it is straightforward to extend Nelkin's<sup>(6)</sup> selfscattering kernel to D<sub>2</sub>O. This was done by H. Honeck<sup>(16)</sup> some time ago. However, whereas for hydrogen the ratio of incoherent to coherent cross sections is 39:1, it is only 1:2.7 for deuterium. Also the oxygen cross section is no longer small compared to the total molecular scattering cross section as it is for H<sub>2</sub>O. Hence in the case of the D<sub>2</sub>O molecule it is not obvious that the incoherent approximation, as used by Nelkin, is good enough for predicting neutron spectra at thermal energies. In order to find out about the importance of the interference scattering we have adapted the code GAKER,<sup>(12)</sup> originally written for Nelkin's water kernel, to compute and add up the 2 self and the 2 interference terms, as given by Butler,<sup>(17)</sup> according to the formula

$$\sigma_{D_2O} = 2\sigma^{DD} + 2\sigma^{D_1D_2} + 4\sigma^{OD} + \sigma^{OO} \quad (3.2.1)$$

Butler's calculation uses Zemach and Glauber's<sup>(18)</sup> formalism and postulates, as did Nelkin, the following degrees of freedom:

1. Free translation of the D<sub>2</sub>O molecule
2. Harmonic torsional vibrations of small amplitudes about the three principal axes of inertia, all with the same frequency  $\omega_1$ .
3. Two-stretching (symmetric and antisymmetric) vibrational modes with the same frequency  $\omega_3$ .

The exact scattering kernel corresponding to these assumptions is given by the following expressions.

$$\sigma(E_0 \rightarrow E, \Omega) = \sum_{\nu\nu'} \sigma^{\nu\nu'}(E_0 \rightarrow E, \Omega) \quad (3.2.2)$$

$$\sigma^{\nu\nu'}(E_0 \rightarrow E, \Omega) = \frac{A_\nu A_{\nu'} + \delta_{\nu\nu'} C_\nu^2}{T} \frac{\sin b_{\nu\nu'} \kappa}{b_{\nu\nu'} \kappa} \sqrt{\frac{E}{E_0}} e^{-\frac{\beta}{2}} S^{\nu\nu'}(\alpha, \beta)$$

$$S^{\nu\nu'}(\alpha, \beta) = \sqrt{\frac{1}{4\pi\alpha}} \exp \left[ - \left( \lambda_{\nu\nu'} + \frac{1}{4} \right) \alpha \right]$$

$$\sum_{n_1=-\infty}^{\infty} \sum_{n_2=-\infty}^{\infty} \sum_{n_3=-\infty}^{\infty} \exp \left[ \frac{- \left( \beta - \sum_{\mu} n_{\mu} \frac{\omega_{\mu}}{T} \right)^2}{4\alpha} \right] \prod_{\mu} I_{n_{\mu}} \left( \frac{\alpha}{B_{\mu}^{\nu\nu'}} \right) \quad (3.2.3)$$

Here the meaning of the different constants is:

- $A_\nu$  = coherent scattering length of nucleus  $\nu$   
 $C_\nu$  = incoherent scattering length  
 $b_{\nu\nu'}$  = distance between nuclei  $\nu$  and  $\nu'$   
 $M$  = D<sub>2</sub>O molecule mass  
 $m$  = neutron mass

$$\frac{1}{B_{\mu}^{\nu\nu'}} = \frac{MQ_{\mu}^{\nu\nu'} T}{m\omega_{\mu} \sinh \frac{\omega_{\mu}}{2T}} \quad (3.2.4)$$

$$\lambda^{\nu\nu'} = \frac{M}{m} \sum_{\mu=1}^3 P_{\mu}^{\nu\nu'} \frac{\coth \omega_{\mu}/2T}{\omega_{\mu}/T} \quad (3.2.5)$$

$$\alpha = \frac{\kappa^2}{2MT} ; \quad (3.2.6)$$

$$\beta = \frac{\epsilon}{T} = \frac{E - E_0}{T} \quad (3.2.7)$$

The coefficients  $P_{\mu}^{\nu\nu'}$  and  $Q_{\mu}^{\nu\nu'}$  are vibrational and torsional amplitudes which are tabulated in Butler's paper. The diagonal coefficients are equal:  $P_{\mu}^{\nu\nu} = Q_{\mu}^{\nu\nu}$ . The  $\lambda^{\nu\nu'}$  and  $B_{\mu}^{\nu\nu'}$  are also tabulated by Butler but in our calculations they were recomputed by the input routine to GAKER. Actually the coefficient  $\lambda^{\text{OD}}$  listed by Butler is too small by a factor of 10 and this error invalidates his results for the OD term.  $\kappa$  and  $\epsilon$  denotes as usual, the momentum and energy exchange.

The computing time for the exact evaluation of Eq. (3.2.3) in the energy range 0.001 - 1.0 eV is prohibitive, but fortunately it can be considerably reduced by making suitable approximations. The usual procedure for evaluating Nelkin's kernel is to split the energy range in two regions. In the first region one treats the first oscillator rigorously and the second and third oscillators in the low temperature limit (only the ground state is populated). Furthermore, one only retains the elastic (0 phonon) term of the third oscillator.

At an energy such that the third oscillator can also be excited one then switches to another approximation in which the first oscillator is treated in the short collision approximation, the second oscillator is treated exactly (this actually is unnecessary: the low temperature approximation should be good enough for  $\omega_2 = 0.205 \text{ eV}$ ), and the third oscillator is treated in the low temperature approximation. It is clear that this procedure used for the D self scattering can be extended immediately to the oxygen. However, for the interference scattering ( $D_1 D_2$  and OD terms) the situation is different, as shown below.

In order to analyze the different approximations it is best to go back to Zemach and Glauber's intermediate scattering function:

$$\chi^{\nu\nu'} = \int e^{i\epsilon t} e^{-\frac{\beta}{2}} S^{\nu\nu'}(\alpha, \beta) \quad (3.2.8)$$

For a harmonic system  $\chi^{\nu\nu'}$  is a product of the  $\chi$  functions corresponding to each mode.

$$\chi^{\nu\nu'} = \tilde{a}_{\nu\nu'} \prod_{\mu} \chi_{\mu}^{\nu\nu'} \quad (3.2.9)$$

with

$$\tilde{a}_{\nu\nu'} = (A_{\nu} A_{\nu'} + C_{\nu}^2 \delta_{\nu\nu'}) \frac{\sin b_{\nu\nu',\kappa}}{b_{\nu\nu',\kappa}} \quad (3.2.10)$$

The expression for the factors  $\chi_{\mu}^{\nu\nu'}$  leading to the result (3.2.3) is

$$\chi_{\mu}^{\nu\nu'} = \exp \left[ -\alpha T P_{\mu} \frac{M \coth \frac{\omega_{\mu}}{2T}}{m \omega_{\mu}} \right] \cdot \exp \left\{ \frac{M \alpha T Q_{\mu}^{\nu\nu'}}{2 \omega_{\mu} m \sinh \frac{\omega_{\mu}}{2T}} \left[ \exp \left( \frac{\omega_{\mu}}{2T} - i \omega_{\mu} t \right) + \exp \left( -\frac{\omega_{\mu}}{2T} + i \omega_{\mu} t \right) \right] \right\} \quad (3.2.11)$$

The exact phonon expansion (3.2.3) is obtained using the formula

$$\exp \left[ \frac{x}{2} \left( y + \frac{1}{y} \right) \right] = \sum_{n=-\infty}^{\infty} y^n I_n(x) \quad (3.2.12)$$

which gives:

$$\chi_{\mu}^{\nu\nu'} = \exp \left[ -\frac{M \alpha T}{m \omega_{\mu}} P_{\mu}^{\nu\nu'} \coth \frac{\omega_{\mu}}{2T} \right] \cdot \sum_{n=-\infty}^{\infty} I_n \left( \frac{\alpha}{B_{\mu}^{\nu\nu'}} \right) e^{-n \frac{\omega_{\mu}}{2T} + i n \omega_{\mu} t} \quad (3.2.13)$$

The low temperature limit is obtained by writing:

$$\frac{1}{B_{\mu}^{\nu\nu'}} = \frac{M Q_{\mu}^{\nu\nu'} T}{m \omega_{\mu} \sinh \frac{\omega_{\mu}}{2T}} \rightarrow 2 \frac{M Q_{\mu}^{\nu\nu'} T}{m \omega_{\mu}} e^{-\frac{\omega_{\mu}}{2T}} \quad (3.2.14)$$

and

$$I_n \left( \frac{\alpha}{B_{\mu}^{\nu\nu'}} \right) \rightarrow \left( \frac{Q_{\mu}^{\nu\nu'} M T \alpha}{m \omega_{\mu}} \right)^{|n|} \frac{e^{-\frac{n \omega_{\mu}}{2T}}}{|n|!} \quad (3.2.15)$$

The terms with  $n > 0$  can then be neglected and we get

$$\chi_{\mu}^{\nu\nu'} \text{ LT} = \exp\left[-\frac{M\alpha T}{m\omega_{\mu}} P_{\mu}^{\nu\nu'} \coth \frac{\omega_{\mu}}{2T}\right] \sum_{n=0}^{\infty} \left(\frac{Q_{\mu}^{\nu\nu'} MT\alpha}{m\omega_{\mu}}\right)^n \frac{e^{-in\omega_{\mu} t}}{n!} \quad (3.2.16)$$

This approximate result applies both to self and interference terms. A different situation arises in the case of the short collision approximation which is obtained from (3.2.11) by expanding the exponent in powers of  $t$  and retaining only terms up to 2nd order.

$$\exp\left(\frac{\omega}{2T} - i\omega t\right) + \exp\left(-\frac{\omega}{2T} + i\omega t\right) = 2 \cosh \frac{\omega}{2T} - 2 i\omega t \sinh \frac{\omega}{2T} - \omega^2 t^2 \cosh \frac{\omega}{2T} + 0(t^3) \quad (3.2.17)$$

Within this approximation

$$\chi_{\mu}^{\nu\nu'} \text{ sc} = \exp\left\{-\frac{\alpha MT}{m} \left[\frac{P_{\mu}^{\nu\nu'} - Q_{\mu}^{\nu\nu'}}{\omega_{\mu}^2} 2 \bar{E}_{\mu} + Q_{\mu}^{\nu\nu'} \left(it + \bar{E}_{\mu} t^2\right)\right]\right\} \quad (3.2.18)$$

where

$$\bar{E}_{\mu} = \frac{\omega_{\mu}}{2} \coth \frac{\omega_{\mu}}{2T} \quad (3.2.19)$$

is the average energy corresponding to the oscillator of frequency  $\omega_{\mu}$ . Now it is clearly seen that a Fourier transform of  $\chi_{\mu}^{\nu\nu'} \text{ sc}$  exists only if the coefficient  $Q_{\mu}^{\nu\nu'}$  is positive. This is always the case for the self terms  $\nu = \nu'$ , for which also  $P_{\mu}^{\nu\nu} = Q_{\mu}^{\nu\nu}$  thus yielding the familiar result

$$\chi_{\mu}^{\nu\nu} \text{ sc} = \exp\left[-\frac{M}{m} \alpha T P_{\mu}^{\nu\nu} \left(it + \bar{E}_{\mu} t^2\right)\right] \quad (3.2.20)$$

For the interference terms, however, it turns out that  $Q_1^{\nu\nu'}$  is negative. In fact

$$Q_1^{\text{OD}} = -0.051968$$

$$Q_1^{\text{D}_1\text{D}_2} = -0.022003$$

Thus, in this case the coefficient of  $t^2$  is positive and expression (3.2.18) becomes meaningless unless it is multiplied by another  $\chi$ -factor with a larger negative coefficient of the  $t^2$  term in its exponent. This would be the case if

$$-Q_1^{\nu\nu'} \bar{E}_1 < \frac{m}{M} T$$

since then the negative coefficient in  $\chi_{Tr}$ , the  $\chi$ -factor corresponding to the free translation of the  $D_2O$  molecules, would predominate.

For the self terms, where  $Q_1^{\nu\nu'} > 0$ , the effect of the short collision approximation for the lowest frequency is to increase the translational Doppler broadening of the resonances corresponding to the remaining frequencies. Schematically the exact and approximate  $P_0$  kernel compare as shown in Fig. 3.1 so that the result of the approximation is like taking an average over the fine structure due to the lowest frequency. When  $Q_1^{\nu\nu'} < 0$ , consecutive peaks of the kernel have opposite sign and the average tends to 0 as the number of peaks between  $E=0$  and  $E=E_0$  increases. Hence it seems reasonable to drop the interference terms completely in the energy region in which the self terms are calculated in the short collision approximation. With this criteria and a switching energy  $E_s = 0.25$  eV we have computed the  $P_0$  and  $P_1$  kernels to be used in neutron spectrum calculations.

A typical result of these calculations is shown in Fig. 3.2 where we compare the  $D_\nu D_\nu$  and  $OD_\nu$  contributions to the  $P_0$  kernel.

The scattering law  $S(\alpha, \beta)$  defined here by

$$S(\alpha, \beta) = \frac{1}{A_D^2 + C_D^2} \sum_{\nu\nu'} (A_\nu A_{\nu'} + \delta_{\nu\nu'} C_\nu^2) \frac{\sin b_{\nu\nu'\kappa}}{b_{\nu\nu'\kappa}} S^{\nu\nu'}(\alpha, \beta) \quad (3.2.21)$$

has also been calculated for several sets of  $\alpha$  and  $\beta$ . Two examples are given in Figs. 3.3 and 3.4 again showing the relative contributions of all terms.

### 3.2.1. Total Scattering Cross Section and Intermolecular Effects

In a liquid the correlation function between atoms of different molecules cannot be set equal to zero as it is done in the case of a dilute gas. This nonvanishing correlation leads to intermolecular interference scattering ("outer effect") which must be added to the intramolecular effect considered previously. In fact, it turns out that the contributions to the total cross section from inter and intramolecular interference roughly cancel each other, thus showing that consideration of the intramolecular interference without taking into account the outer effect might actually give worse results than simply neglecting all interference scattering as is done in the incoherent approximation. The predominantly elastic intermolecular interference scattering can be roughly estimated (3.2.20) using Debye's static approximation



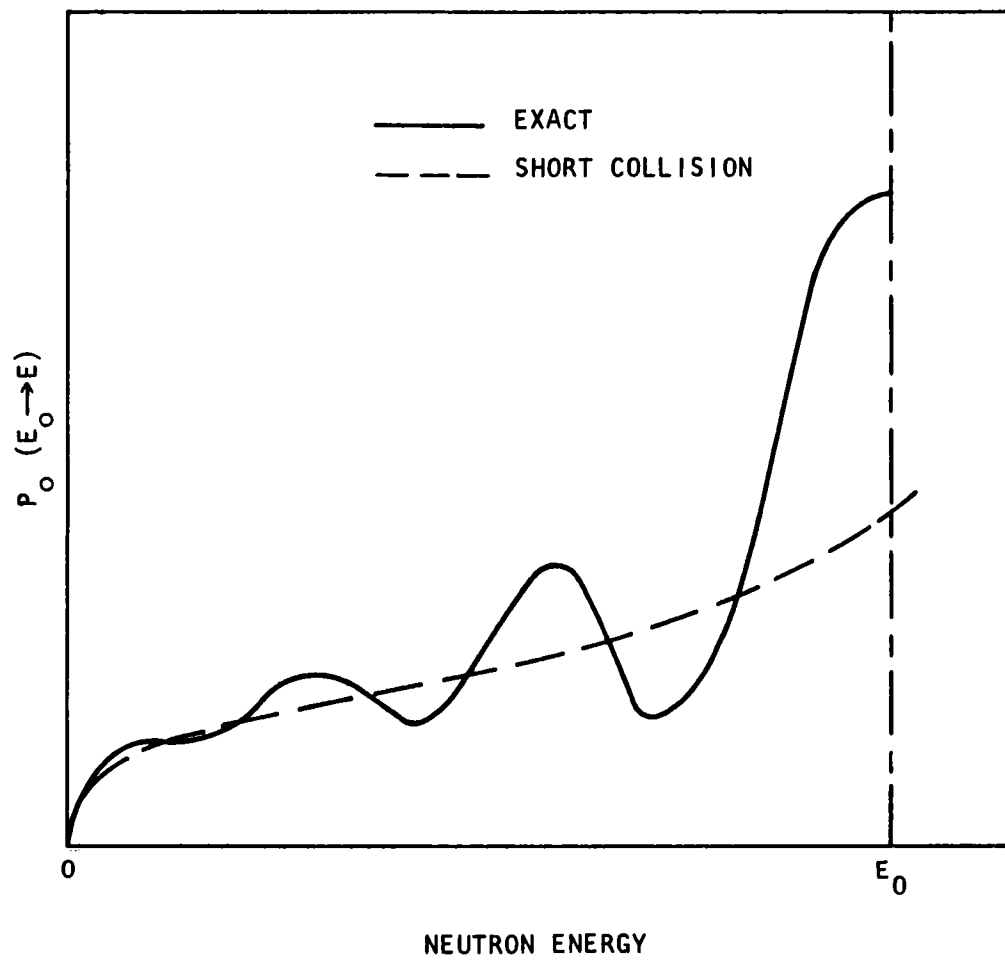


Fig. 3.1 -- Schematic representation of the short collision approximation

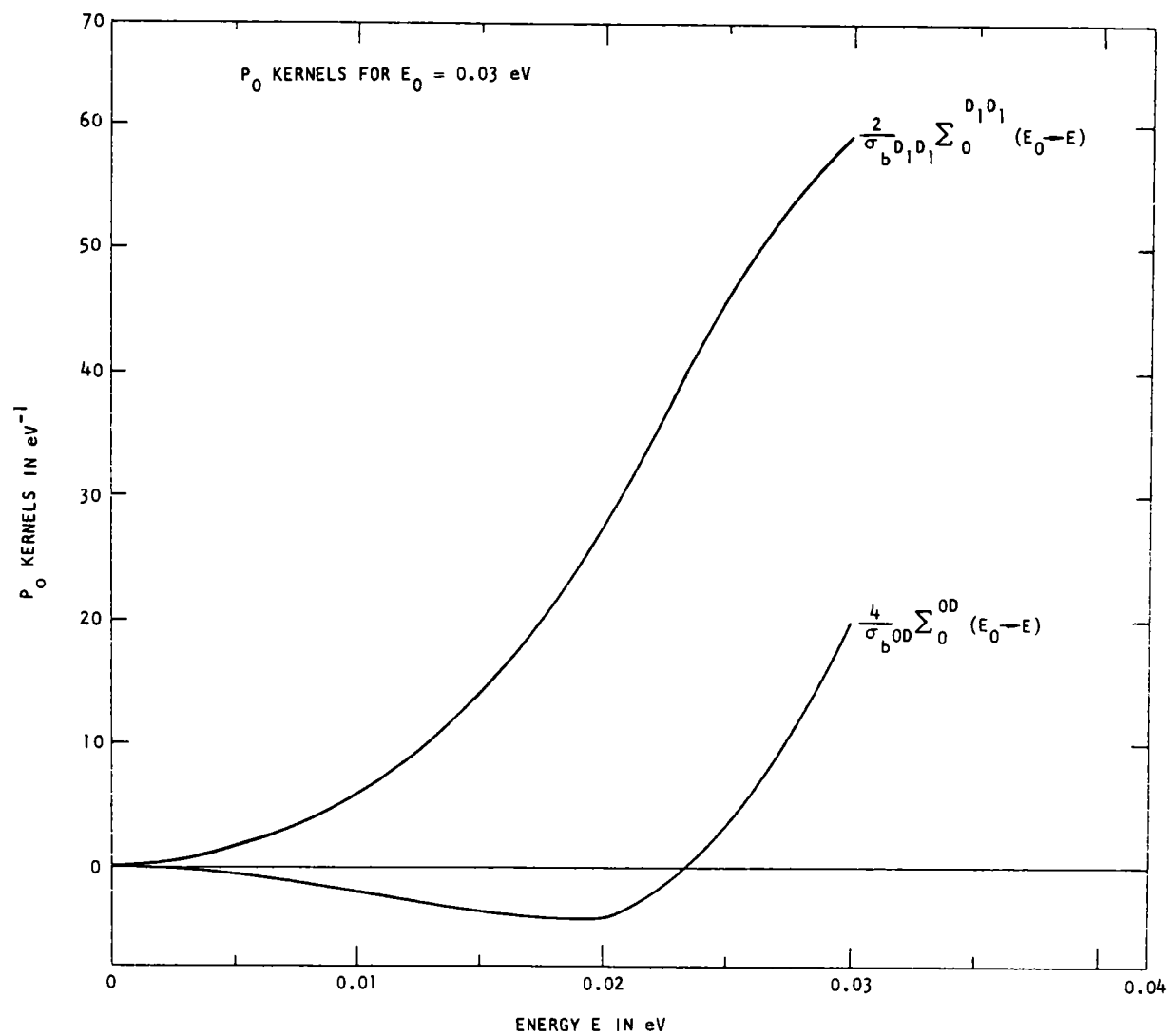


Fig. 3.2 --  $D_1 D_1$  and OD contributions to the  $P_0$  kernel

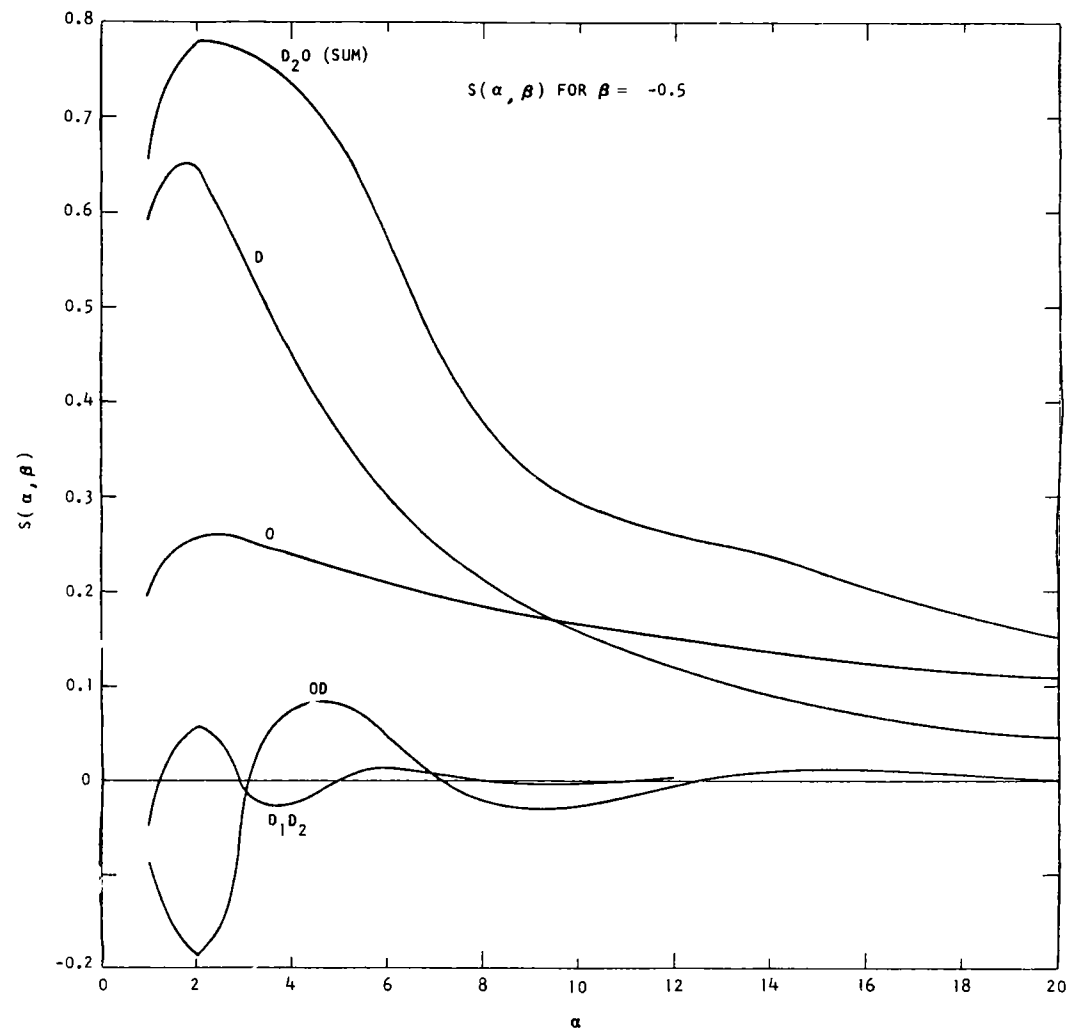


Fig. 3.3 -- Scattering law  $S(\alpha, \beta)$  for  $D_2O$  at  $\beta = -0.5$

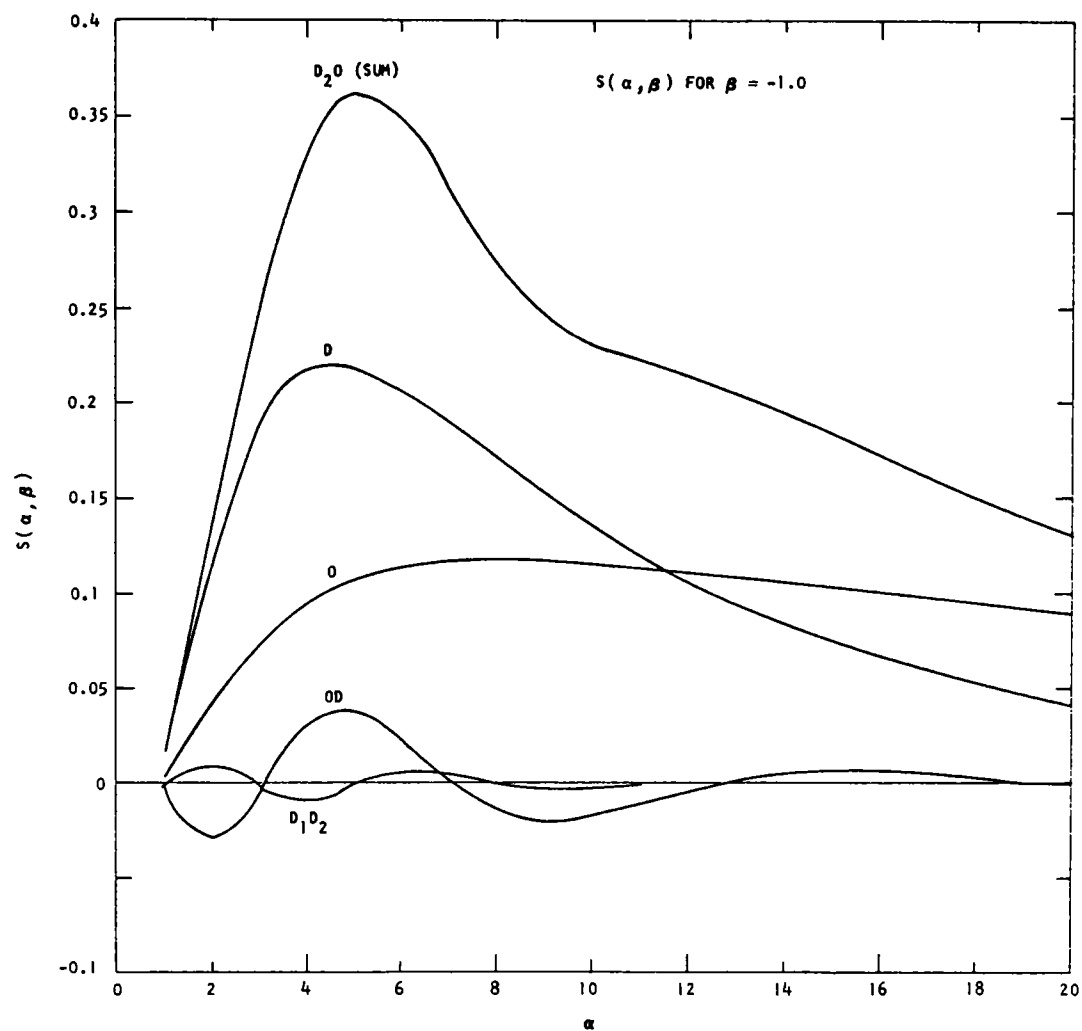


Fig. 3.4 -- Scattering law  $S(\alpha, \beta)$  for  $D_2O$  at  $\beta = -1.0$

Calling  $\sigma^I(\theta)$  the outer contribution to the differential cross section, the results of this approximate calculation are as follows:

$$\sigma^I(\theta) = \sigma_{OO'}^I(\theta) + \sigma_{DD'}^I(\theta) + \sigma_{OD'}^I(\theta) \quad (3.2.22)$$

$$\sigma_{\nu\nu'}^I(\theta) = -N_\nu n_{\nu'} A_\nu A_{\nu'} \frac{4\pi s_{\nu\nu'}^2}{\kappa} j_1(s_{\nu\nu'}, \kappa) \quad (3.2.23)$$

$j_1(\chi)$  = spherical Bessel function of 1st order

$N_\nu$  = no of atoms  $\nu$  per unit volume

$n_\nu$  = no of atoms  $\nu$  per molecule

$s_{\nu\nu'}$  = average minimum distance between centers of atoms  $\nu$  and  $\nu'$

$\kappa = 2k \sin \theta/2$  = momentum exchange

From x-ray diffraction, it is known that  $s_{OO'} = 2.9 \text{ \AA}$ , and since the length of the O-D bond is  $1.0 \text{ \AA}$ , we can set  $s_{OD'} = 1.9 \text{ \AA}$ . The average minimum distance between deuterium atoms of neighboring molecules is not as easily estimated but following Butler, (17) we shall take it as  $s_{DD'} \cong s_{OD'} = 1.9 \text{ \AA}$ . Some typical results of this calculation are shown in Fig. 3.5.

The expression (3.2.23) for the differential cross section can be easily integrated over angle to give the outer interference contribution to the total cross section. The result of the integration is

$$\sigma^I = \sigma_{OO'}^I + \sigma_{DD'}^I + \sigma_{OD'}^I \quad (3.2.24)$$

$$\sigma_{\nu\nu'}^I = N_\nu n_{\nu'} A_\nu A_{\nu'} \frac{8\pi^2 s_{\nu\nu'}^2}{k^2} [j_0(2ks_{\nu\nu'}) - 1] \quad (3.2.25)$$

where  $k = 21.958 \text{ \AA}^{-1} \sqrt{E(\text{eV})}$  and  $j_0(X)$  = spherical Bessel function of 0th order.

The different contributions to the total cross section are shown in Figs. 3.6 and 3.7. Also shown in Fig. 3.6 is the sum of all self terms (that is the total cross section in the incoherent approximation) as compared to the BNL-325 experimental curve. Finally Fig. 3.8 shows the sum of all terms (self and interference) also compared to the BNL-325 curve.

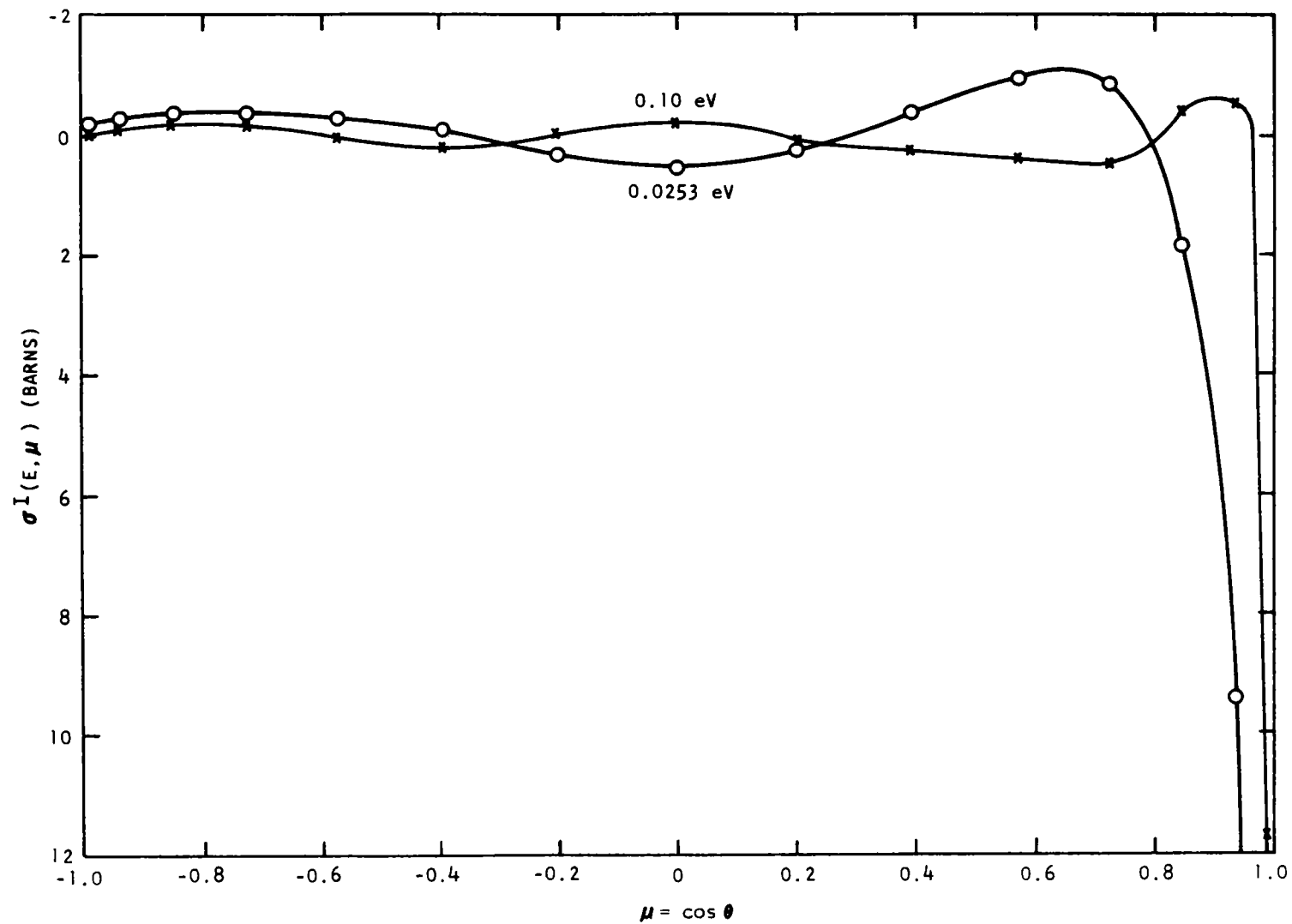


Fig. 3.5 -- Contribution of the intermolecular interference scattering to the differential cross section for  $D_2O$

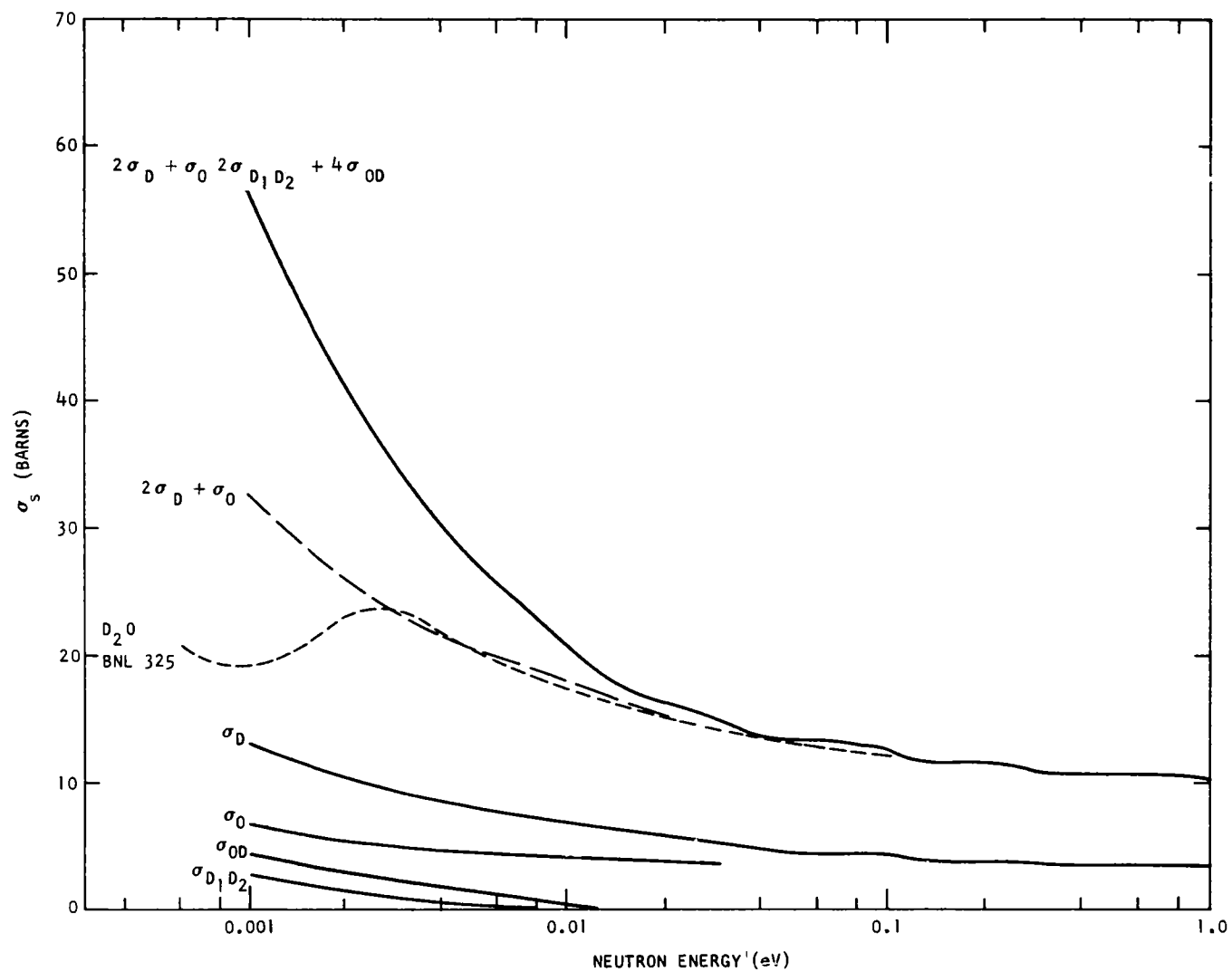


Fig. 3.6 -- Self and intramolecular interference terms  
in the  $D_2O$  scattering cross section



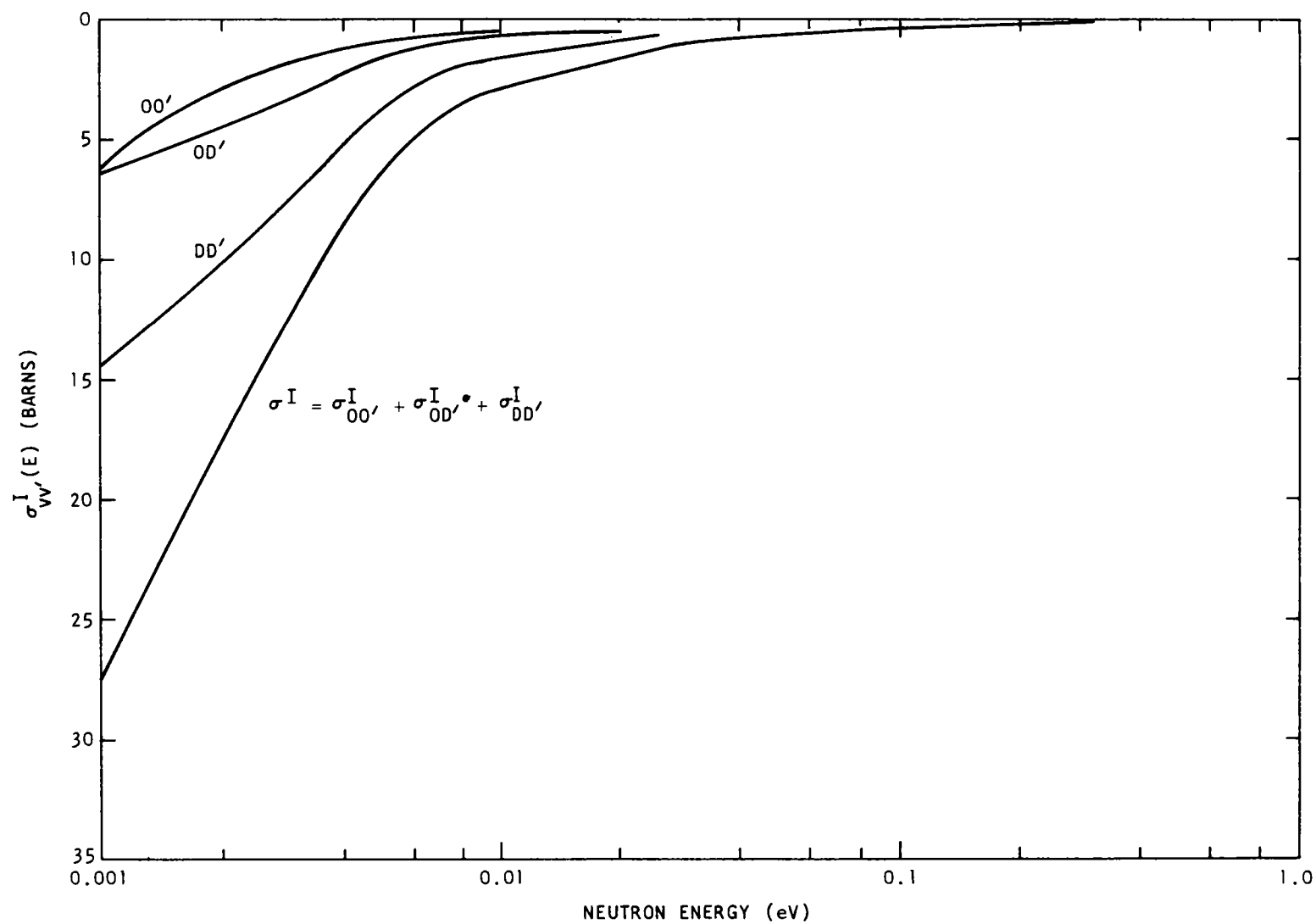


Fig. 3.7 -- Contributions of the intermolecular interference scattering to the total cross section

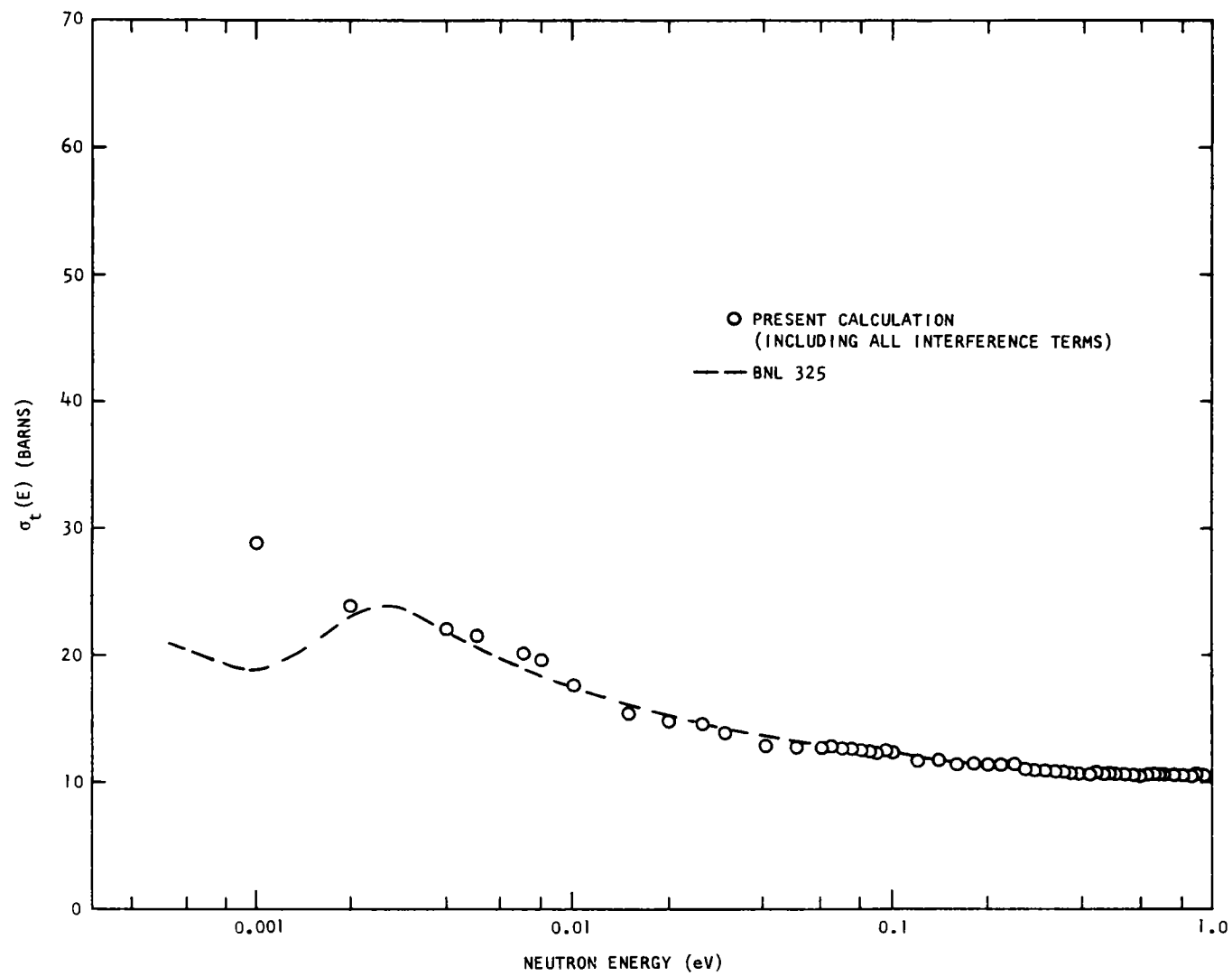


Fig. 3.8 -- Calculated total cross section for  $D_2O$  including all interference terms

### 3.2.2. Conclusion

From the preceding calculations one can draw the following conclusions:

1. Interference scattering occurs predominantly for small energy and momentum exchange.
2. The contribution of interference scattering to the  $P_0$  and  $P_1$  scattering kernel decreases rather quickly with increasing initial neutron energy. For instance, at 0.03 eV the quasi-elastic peaks of the OD and  $D_1 D_1 P_0$  kernels are in the ratio 1:3 whereas at 0.06 eV this ratio has decreased to 1:7.
3. The intra and intermolecular interference tend to cancel each other. This cancellation is quite complete for the total cross section, at least above 0.002 eV.

As a consequence of these facts, it turns out that Honeck's incoherent approximation<sup>(16)</sup> in which only the self terms are retained gives very accurate results in the case of infinite media or weakly space-dependent problems. However, for angular dependent and strongly space dependent problems as well as for leakage spectra, it is possible that the interference scattering will have to be considered.

Although the difference between Butler's and Honeck's oscillator weights and frequencies is small, in the future we shall prefer the former set of parameters, since they are physically better founded. Finally, it should be mentioned that Butler's oxygen self scattering term gives, as expected, practically the same results as the free oxygen gas kernel used in Honeck's calculation.

### 3.3. POSITION DEPENDENT SPECTRA IN D<sub>2</sub>O

#### 3.3.1. Poisoning by a 1/v Absorber

Measurements of thermal neutron flux spectra in D<sub>2</sub>O were performed because experimental techniques had been improved since earlier measurements<sup>(2)</sup> were made. In addition, it was desirable to check the conclusions of the theoretical studies on D<sub>2</sub>O made this year and discussed in Section 3.2.

Two sets of spectral measurements were made in D<sub>2</sub>O with the experimental configuration of Fig. 3.9. The D<sub>2</sub>O was poisoned with boron-aluminum plates to about 1.94 barns/D atom. The light water contamination in the D<sub>2</sub>O was less than 0.5 percent in each case, the atom densities being given in Table 3.1.

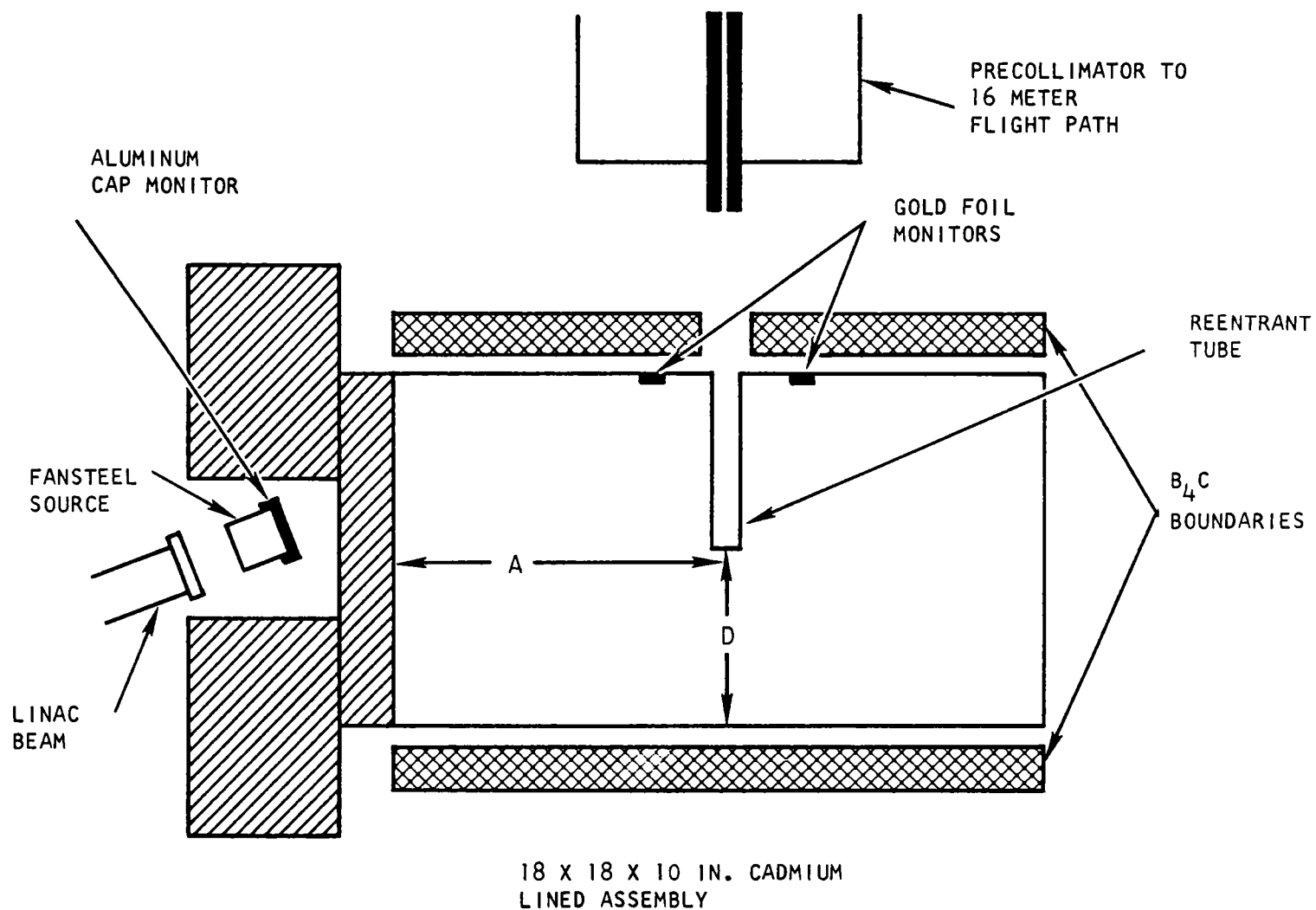


Fig. 3.9 -- Experimental arrangement for spectral measurements in  $D_2O$

Table 3. 1  
CONCENTRATIONS IN BORON POISONED D<sub>2</sub>O  
(atom/barn-cm units)

Boron . . . . .	0.000143
Aluminum . . . . .	0.00915
Oxygen . . . . .	0.02849
Deuterium . . . . .	0.05672
Hydrogen . . . . .	0.0002608

The spatial distribution of the neutron flux was measured in all three directions using cadmium covered indium foils. These distributions were used to determine leakage corrections and to calculate the source used in the calculations performed with the computer code GAPLSN.<sup>(14)</sup> Figure 3.10 shows the activity of the cadmium covered indium foils along the source-assembly axis.

In the first experiment, neutron spectra were measured at 90° to the source-assembly axis at three positions in the 18 inch long tank. Here D of Fig. 3.9 was equal to 5 inches while A was 6, 9, and 12 inches. The measured spectra are compared to the calculated values in Fig. 3.11 and are in good agreement. The relative intensities between the three positions have been preserved by normalizing theory and experiment at only one location. The source input to GAPLSN had to be modified so that the scalar flux from the code in an energy group around the indium resonance (1.4 eV) matched the measured spatial indium activity in order to obtain the proper relative intensities between spectra at the different positions.

In the second experiment, neutron spectra were measured in the same direction but at different positions across the 10 inch axis. Here A of Fig. 3.9 was equal to 6 inches and D was 5, 7, 8, 9, and 10 inches (surface). These measurements are shown in Fig. 3.12 together with the calculated values. Good agreement between theory and experiment is indicated; even the comparison at the surface is reasonable. In the calculations, both P<sub>0</sub> and P<sub>1</sub> scattering were considered. Neglecting the P<sub>1</sub> scattering makes little difference at the center of the tank but gives rise to both a shape and magnitude change in the surface leakage spectrum. Since the measurements at the center of the tank are well described by P<sub>0</sub> scattering alone, the Honeck<sup>(16)</sup> description of D<sub>2</sub>O must then be adequate for isotropic scattering. At the surface, however, where an obvious P<sub>1</sub> dependence is indicated, the agreement is surprising in view of the incoherent treatment of deuterium. In effect the theory disagrees with the experiment in the same direction though to a lesser amount as that observed for light water. One can only suppose that the neutron balance equations in

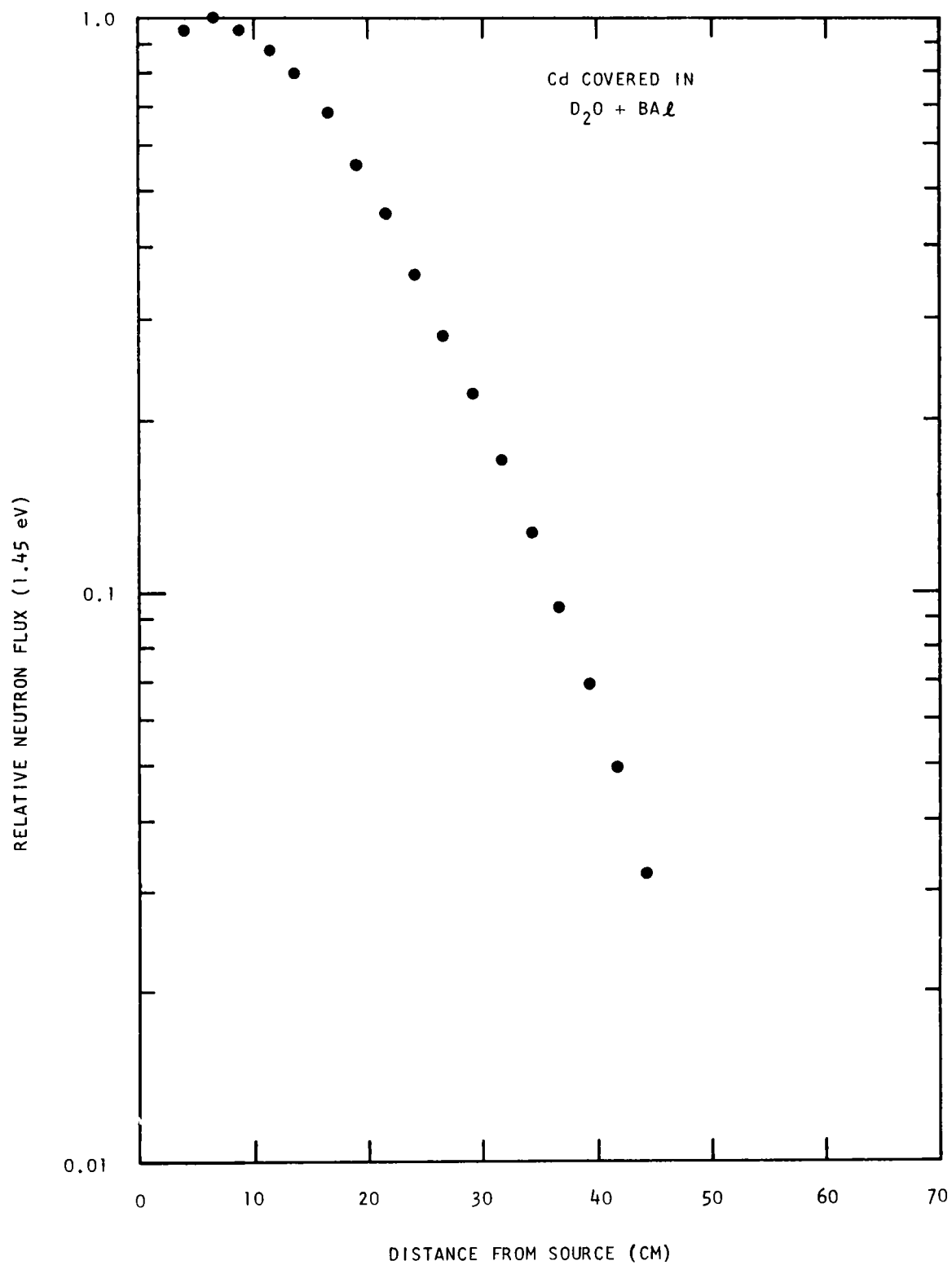


Fig. 3.10 -- Spatial distribution of indium resonance flux in the  $D_2O$  tank

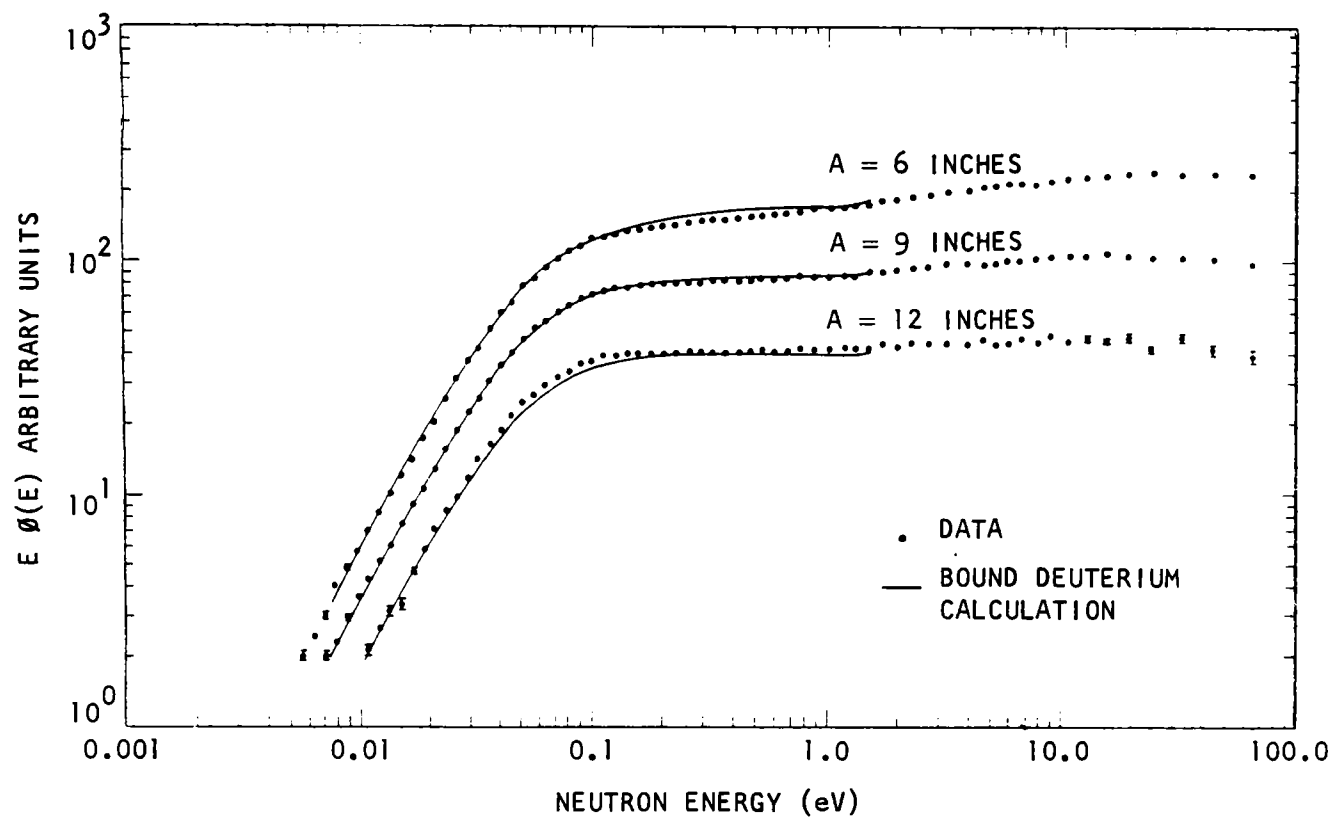


Fig. 3.11 -- Ninety-degree angular spectra in boron poisoned  $D_2O$  at various axial positions

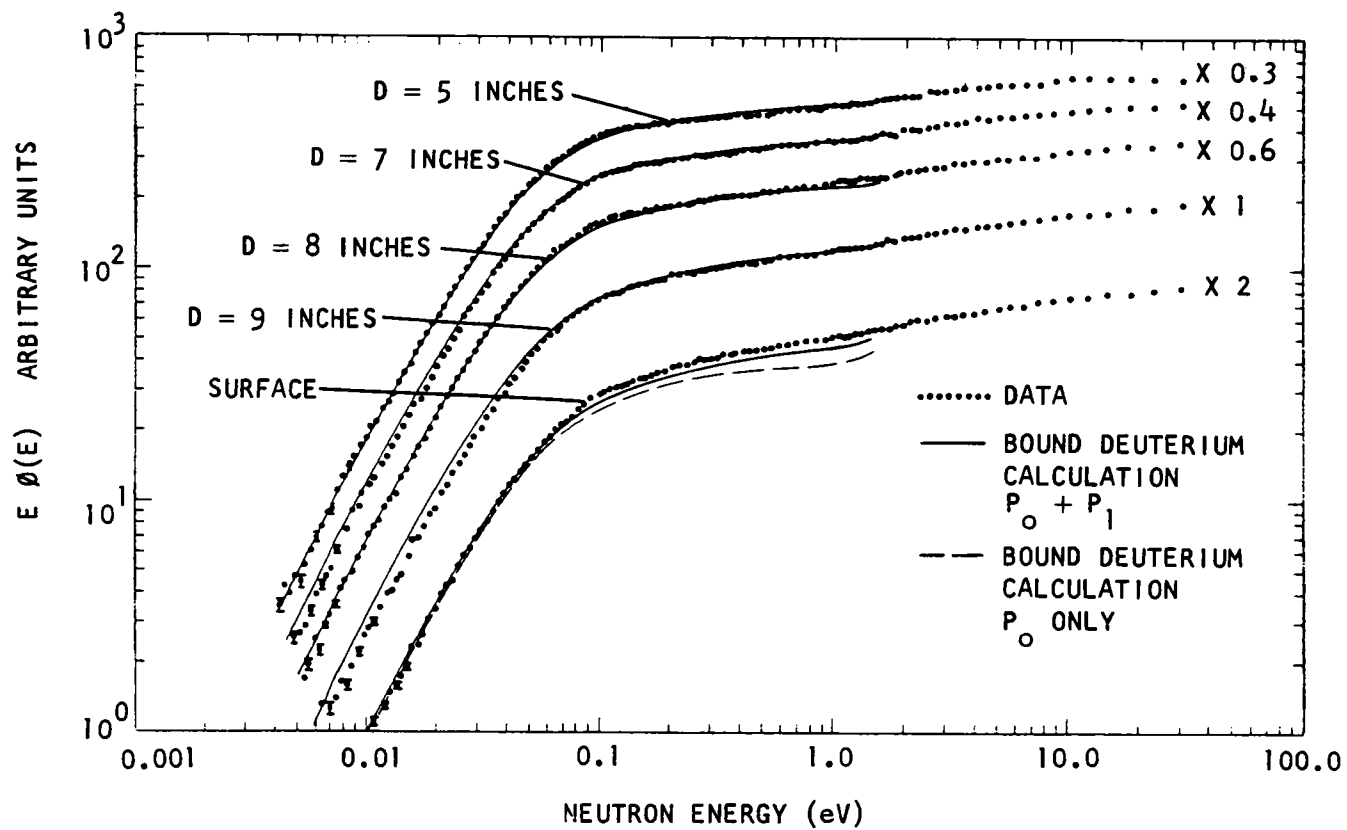


Fig. 3.12 -- Ninety-degree angular spectra in boron poisoned  $D_2O$  at various transverse positions



the energy flux groups below 0.01 eV are dominated by the down scattering and absorption terms or that the test point is insufficiently sensitive to details of the anisotropic scattering.

### 3.3.2. Position Dependent Spectra in Cadmium Poisoned D<sub>2</sub>O

A third spectral experiment was performed utilizing D<sub>2</sub>O to attempt to test the scattering kernel more severely. For this experiment, the borated-aluminum plates were replaced with Cd(NO<sub>3</sub>)<sub>2</sub> salt. The Cd(NO<sub>3</sub>)<sub>2</sub> poison concentration was 2.44 barns/D atom at 0.025 eV. The atom densities are given in Table 3.2.

Table 3.2  
CONCENTRATIONS IN CADMIUM POISONED D<sub>2</sub>O  
(atom/barn-cm units)

Material	Atom Density
Cadmium . . . . .	0.00006569
Nitrogen . . . . .	0.0001314
Oxygen . . . . .	0.03347
Deuterium . . . . .	0.065996
Hydrogen . . . . .	0.0001584

Prior to loading the cadmium salt, a drying procedure was performed to drive off any light water which was attached. Chemical analysis of the D<sub>2</sub>O solution before and after the salt was added indicated no increase in the light water contamination. The geometrical arrangement used for these spectrum measurements was identical to that shown in Fig. 3.9.

In this experiment, neutron spectra were measured at 90° to the source assembly axis where D of Fig. 3.9 was held constant at 5 inches and A was 6, 9, and 12 inches. The purpose of these measurements was to prepare an integral test of the P<sub>0</sub> scattering matrix in the vicinity of the cadmium resonance, 0.175 eV. The measurements are compared with the theoretical values in Fig. 3.13 and show good agreement. Here also the input source to GAPLSN was modified to give the correct 1.4 eV resonance flux distribution. The good agreement between theory and experiment again supports the view that the P<sub>0</sub> scattering by D<sub>2</sub>O is adequately described in Honeck's kernel and that the method is very suitable at least for large assemblies in which leakage is small and no discontinuities are present.

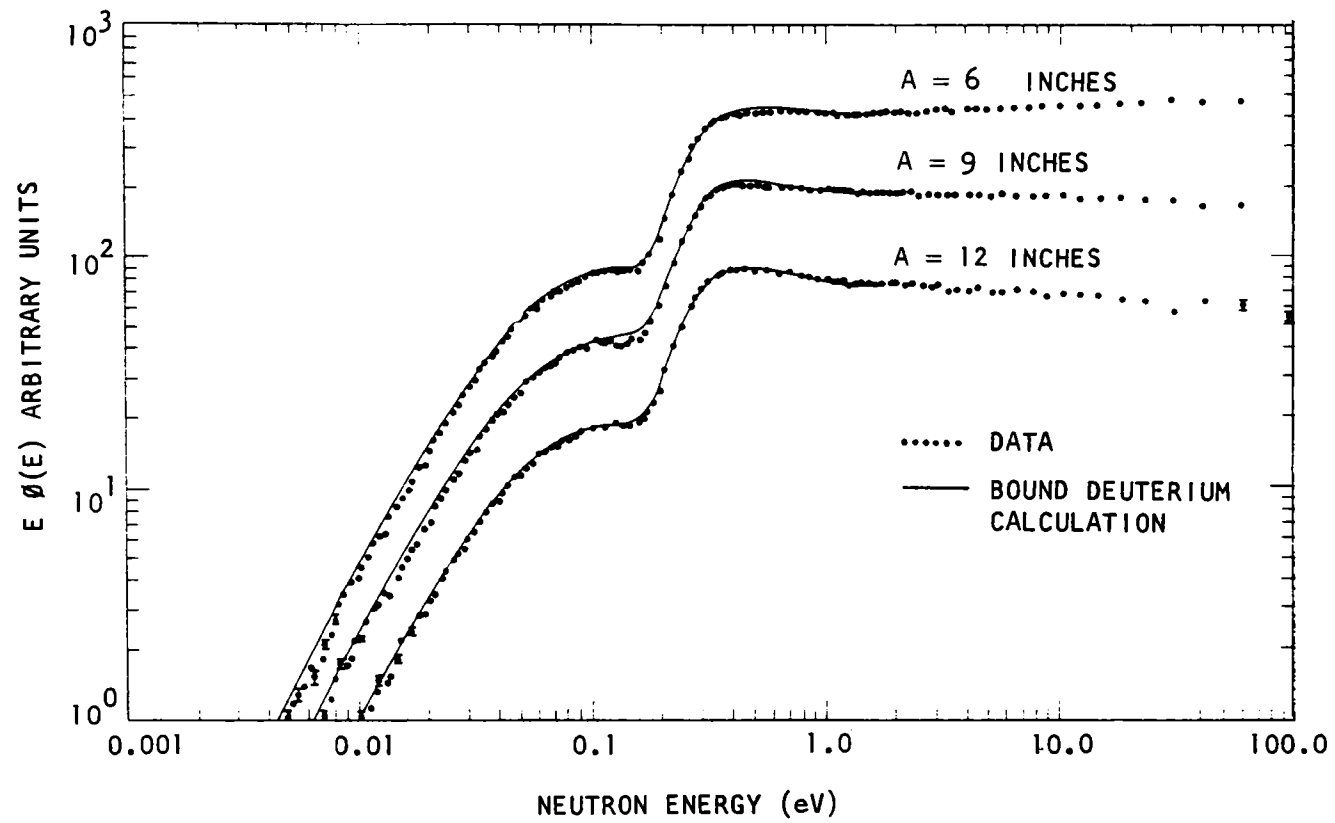


Fig. 3.13 -- Ninety-degree angular spectra in cadmium poisoned  $D_2O$



## IV. NEUTRON THERMALIZATION IN POLYETHYLENE

### 4.1 INTRODUCTION AND SUMMARY

During the past year, a neutron scattering kernel for polyethylene has been calculated by lumping a distributed frequency spectrum derived from a theory by Lin and Koenig<sup>(19)</sup> into four discrete Doppler broadened oscillators. The total scattering cross section and quasi-infinite medium neutron spectrum with different poisons predicted by this model are in good agreement with experiment. This scattering kernel may be used in place of the one used by Goldman<sup>(20)</sup> who followed a similar procedure but arrived at different weights and frequencies.

This new model appears to provide an adequate  $P_0$  scattering kernel, but has not been tested regarding anisotropic scattering. This situation may be improved when  $\sigma(E, \mu)$  is obtained from the current differential scattering experiment. Studies were made this year in a lattice assembly of polyethylene and iron slabs, but the measured spectral changes between the two materials were not sufficient to provide a check on the  $P_1$  scattering for the new polyethylene model. The results of these studies are therefore presented here as a preliminary investigation of the problems encountered in direct spectral measurements in heterogeneous assemblies.

### 4.2 SCATTERING KERNEL FOR POLYETHYLENE

#### 4.2.1 Frequency Spectrum

Crystalline polyethylene is known to be formed of very long, kinked and only weakly interacting chains of  $\text{CH}_2$  radicals.<sup>(19)(21)</sup> Therefore, its frequency spectrum is radically different from the one corresponding to a three-dimensional crystal. In fact, analyzing its normal modes of vibration in terms of plane waves  $e^{i\vec{k}\cdot\vec{r}}$ , the corresponding frequencies can only depend on the projection of the wave vector,  $\vec{k}$  on a direction parallel to the chains (at least to the extent that the interaction between neighboring chains can be neglected). In other words, for any direction of  $\vec{k}$ , the frequency  $\omega$  only depends on the phase difference  $\theta$  between the vibration of corresponding elements of two neighboring radicals in the same chain. This dependence, as calculated by Lin and Koenig<sup>(19)</sup>, is shown in Fig. 4.1 where the nine different branches (corresponding to the three atoms per radical) can be assigned to the following vibrational modes:

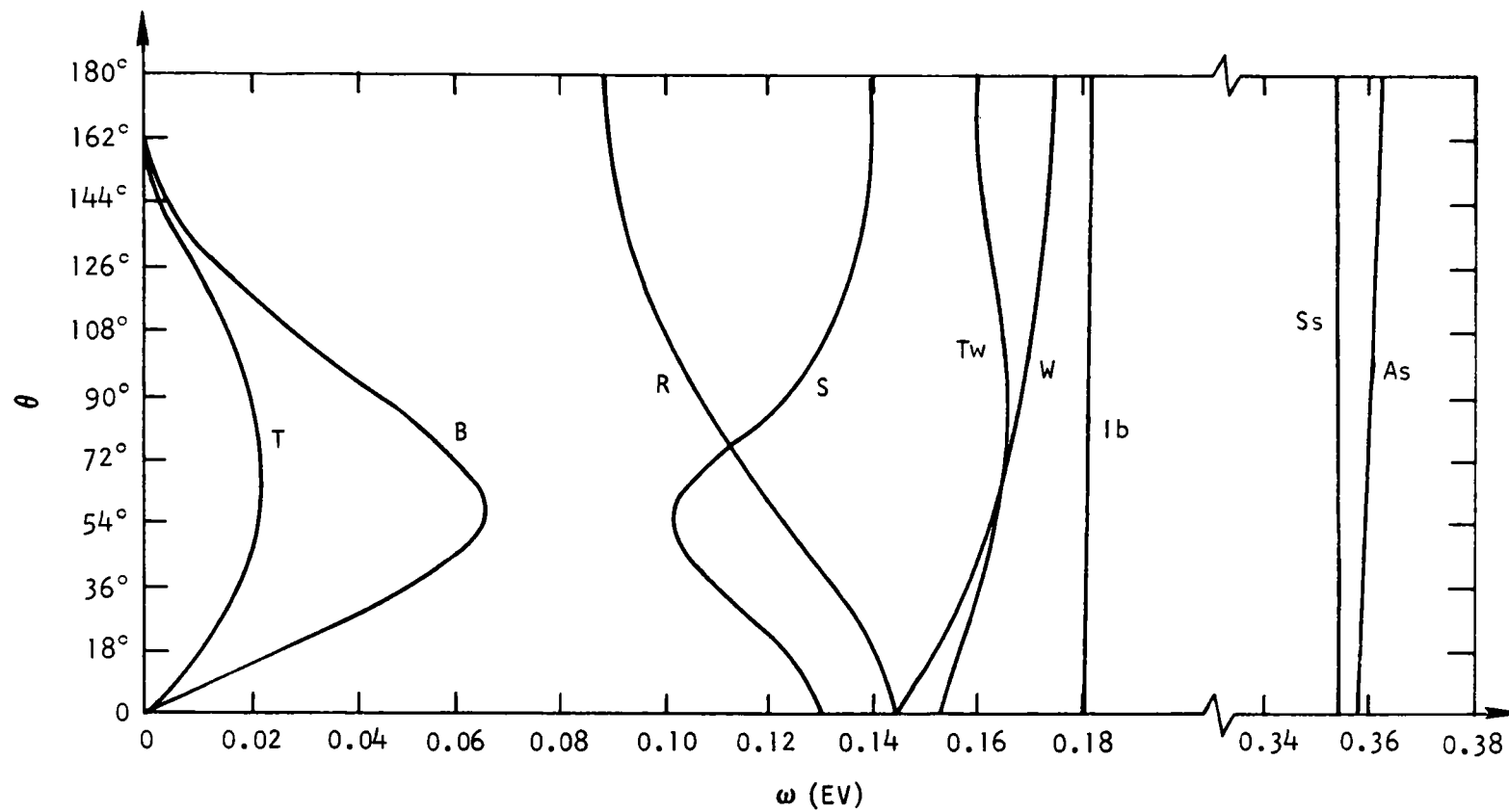


Fig. 4.1 -- Frequency dependence of the vibrational phase difference between neighboring  $\text{CH}_2$  groups (data of Lin and Koenig)

T	C-C-C-C torsion
B	C-C-C bending
S	C-C stretching
R	CH <sub>2</sub> rocking
Tw	CH <sub>2</sub> twisting
W	CH <sub>2</sub> wagging
Ib	H-C-H bending
Ss	H-C-H symmetric stretching
As	H-C-H antisymmetric stretching.

Only two of these branches go to  $\omega = 0$  for  $\theta = 0$  and can thus be considered as acoustical modes. The remaining ones are optical branches. This again shows very clearly the difference with a three-dimensional crystal for which the number of acoustical branches always is three.

We shall consider only the optical part of Lin and Koenig's frequency distribution since the acoustical part is perturbed, at least near  $\omega = 0$ , by the weak coupling between neighboring chains. Due to this, one must recover the typical  $\omega^2$  behavior of a Debye crystal at very low frequencies. Since a frequency spectrum is defined as the fraction of modes per unit frequency interval, in our case we have

$$f(\omega) = c \sum_i \frac{d\theta_i(\omega)}{d\omega}$$

where  $c$  is a normalization constant and the sum is over all branches crossing the frequency  $\omega$ . Hence  $f(\omega)$  becomes singular at all those points where  $d\omega/d\theta = 0$ . A histogram of the spectrum obtained in this manner but leaving out the C-C stretching branch as well as the acoustical branches, is shown in Fig. 4.2. The reason for leaving out the S branch from the optical spectrum will become clear later.

#### 4.2.2 Neutron Scattering

From the frequency distribution described in the previous section, it is possible, making reasonable assumptions, to derive a scattering kernel suitable to calculate thermal neutron spectra in polyethylene. Two different approaches to this problem have been attempted: one using distributed frequencies and the other using discrete frequencies. The more accurate method used a distributed frequency spectrum of the kind shown in Fig. 4.2 complemented by the adequately weighted C-C stretching contributions, and a semiempirical acoustical spectrum given by Wunderlich.<sup>(22)</sup> The need for relative weighting of the different contributions to the effective frequency spectrum is due to the fact that in the acoustical and S-modes the CH<sub>2</sub> radicals move essentially as a whole

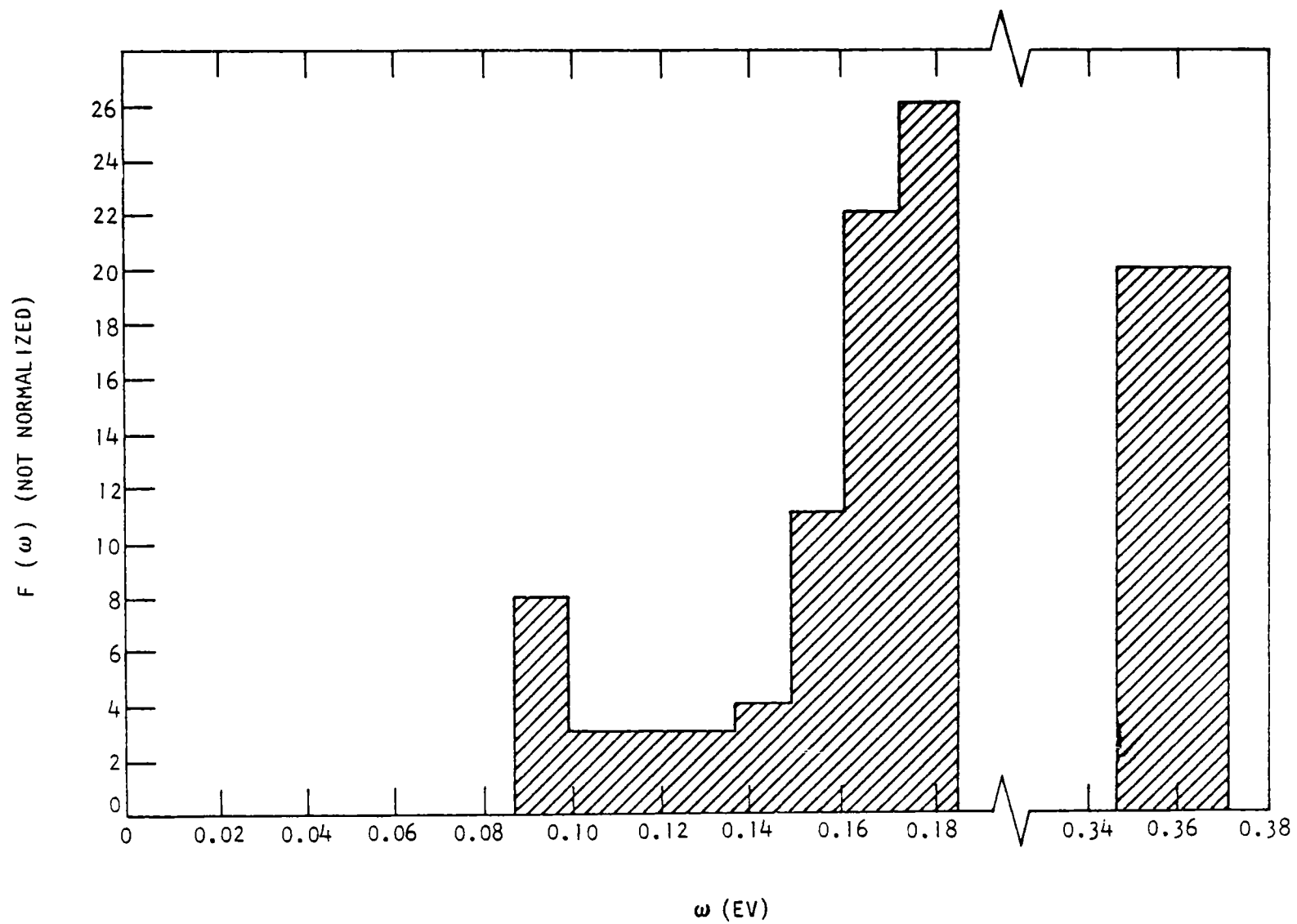


Fig. 4.2 -- Histogram of the frequency spectrum of polyethylene

unit of mass 14 whereas in the remaining optical modes the C-atoms are nearly at rest. The weighting factors are derived from the assumption that the  $\text{CH}_2$  radicals remain rigid in the acoustical and S-modes and have a value of  $2/15$  for these modes. For the other modes, the weighting factor is  $13/15$ . The scattering kernel (SUMMIT) obtained from this effective frequency spectrum gave neutron spectra in reasonable agreement with experiment <sup>(10)(23)</sup> (see also Section VIII). However, it was not possible to get a good fit to the experimental total scattering cross section due perhaps to numerical difficulties.

While the calculation with the distributed frequency spectrum will still be pursued with improved methods, another approach was tried out and found fairly successful. The idea is to lump the frequency spectrum of Fig. 4.2 into a small number of discrete oscillators with weights proportional to the equivalent partial areas of the distributed spectrum. This situation can then be easily handled by the code GAKER, <sup>(12)</sup> originally written for Nelkin's  $\text{H}_2\text{O}$  model, if one makes the additional assumption that the modes not included in the spectrum of Fig. 4.2 can all be treated in the short collision approximation, with  $T_{\text{eff}}$  equal to room temperature, and a total weight of  $1/14$  (corresponding to free translation of  $\text{CH}_2$  radicals of mass 14).

This procedure is in principle the same as used by Goldman <sup>(20)</sup> but the frequencies and weights obtained for the oscillators are quite different. In particular, Goldman's highest frequency of 0.533 eV is in conflict with Lin and Koenig's theory since their highest optical branch does not exceed 0.36 eV.

The number of discrete oscillators used in the present calculations was 4 and the weights and frequencies are given on Table 4.1. Goldman's values are given in the same table for comparison.

TABLE 4.1

	Frequencies	Weights (1/M)	M
Present Calculations	0.089	0.07746	12.91
	0.14	0.2320	4.31
	0.174	0.3096	3.23
	0.360	0.3096	3.23
Goldman's Values	0	0.0714	14.0
	0.089	0.2322	4.308
	0.187	0.2322	4.308
	0.354	0.2322	4.308
	0.533	0.2322	4.308



The numerical results obtained with these parameters seem to be in quite good agreement with experiment. In Fig. 4.3 we compare our calculated total scattering cross section with Bach's<sup>(24)</sup> experimental data. Also shown on the figure is Goldman's calculation and it is seen that the fit of the present model is quite satisfactory.

Furthermore, the agreement obtained between calculated and measured neutron spectra is also quite good. This is seen in Figs. 4.4 and 8.3 which present two infinite medium spectra previously measured at General Atomic, one in 1% borated polyethylene (5.74 barns/H-atom) and the other one in paraffin containing enriched  $\text{UF}_4$ , with atom ratios  $\text{H/U} = 189$  and  $\text{U}^{235}/\text{U}^{238} = 0.02$ . Goldman's results for the borated polyethylene are also shown for comparison.

### 4.3 HETEROGENEOUS STUDIES

The problem of determining neutron spectra in a lattice cell is of special practical interest for reactor design. Large spatial changes can be expected and strong flux gradients are very likely present. Until recently most reaction rate changes throughout a cell were determined by foil activation and were not of high precision. During this contract year, studies have been made of the neutron flux variation in mockup cells of different thicknesses using different size re-entrant tubes in order to determine the feasibility of measuring the flux spectra directly. The problem in essence has been to obtain re-entrant tube and precollimator sizes that are small enough not to perturb the equilibrium cell flux and yet large enough to allow good counting statistics to be obtained in a reasonably short time.

The experimental geometry of Fig. 4.5 was selected; it comprises a 15 in. x 15 in. x 6 in. assembly of iron and polyethylene slabs. The choice of polyethylene and iron as cell materials was dictated by the need to use a solid moderator whose scattering kernel was well known (Section 4.2) and an absorbing material with relatively high scattering and reasonable absorption. The requirement of the solid moderator is desired for convenience in accurately locating the position of the re-entrant hole and the small absorption requirement is necessary if counting rates with reasonable statistics are to be obtained. The slab thicknesses and re-entrant hole sizes studies are given in Table 4.2.

In the first experiment, employing half inch slab thicknesses, three re-entrant holes and precollimator sizes were studied, and spectral measurements were made by the usual time-of-flight means. Neutron spectra were measured at  $90^\circ$  to the source assembly axis at the middle of the central iron and polyethylene slabs. Comparative calculations were made by means of the code GAPLSN in the  $P_1$  approximation, using

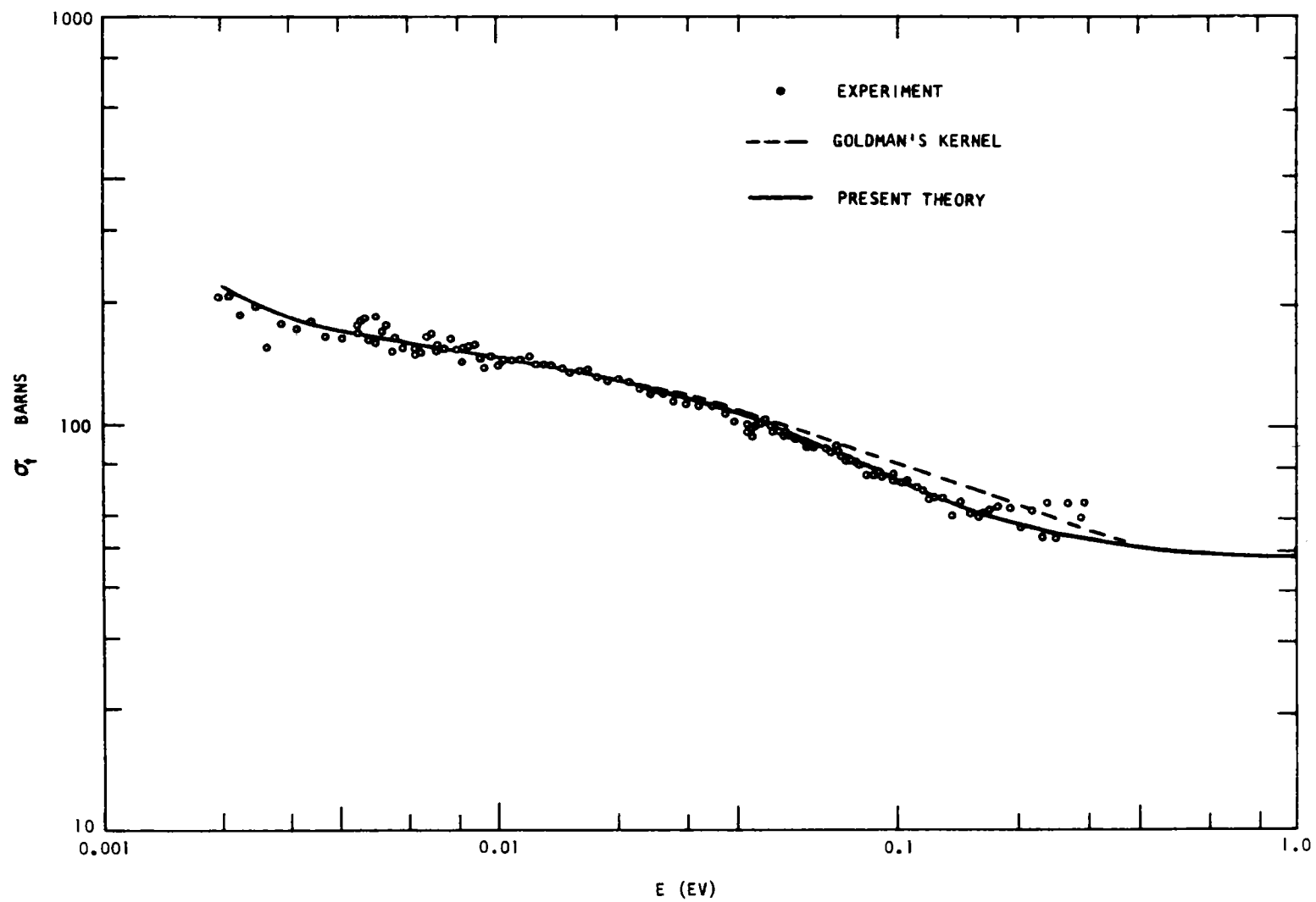


Fig. 4.3 -- Total cross section of polyethylene

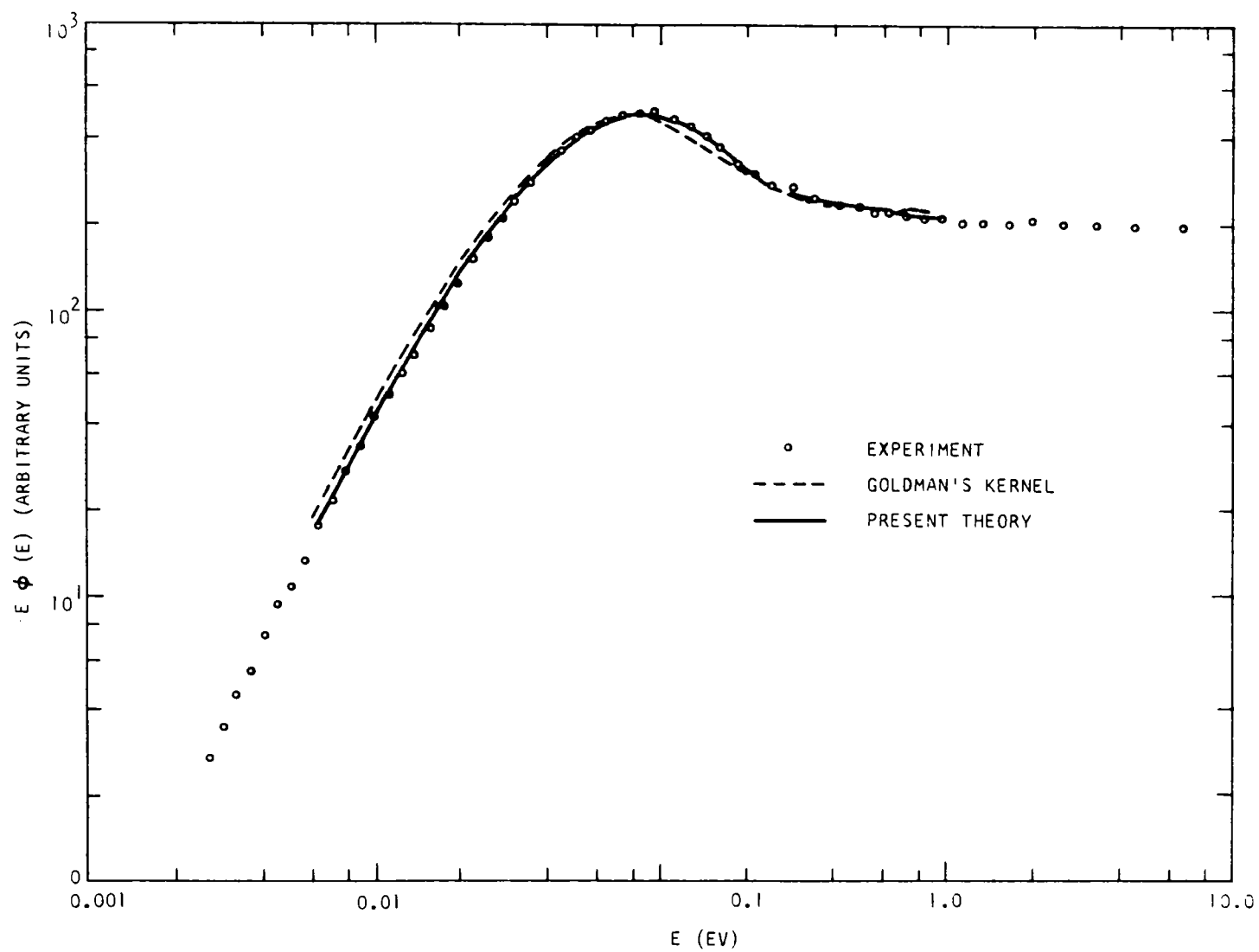


Fig. 4.4 -- Infinite medium neutron spectrum in 1% borated polyethylene

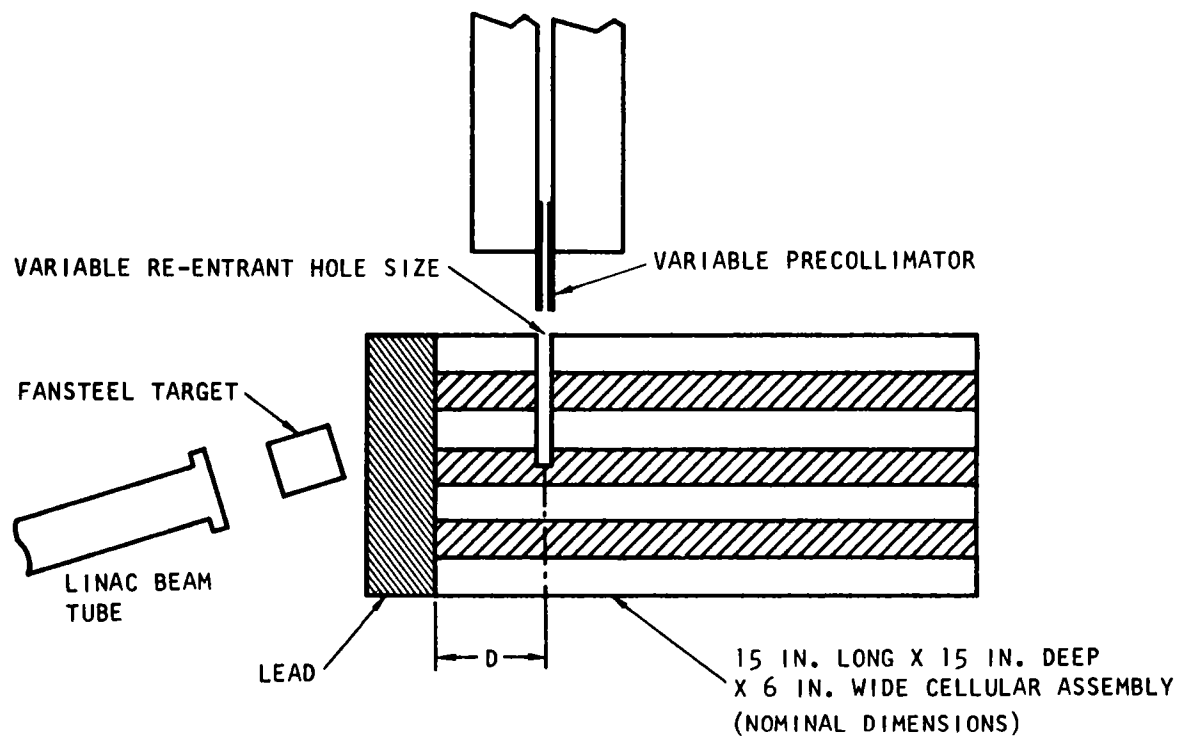


Fig. 4.5 -- Experimental arrangement for spectral measurements in a heterogeneous assembly

Table 4.2

## CELL THICKNESSES AND RE-ENTRANT HOLE SIZES

Thickness of Each Slab of Polyethylene or Iron	Re-entrant Hole Diameter - Inches	Precollimator Diameter - Inches
0.5	0.805	0.562
	0.375	0.20
	0.25	0.15
1.0	0.281	0.15

the scattering kernel for polyethylene discussed in the previous section. The geometry of the calculation was a simple cell with perfect reflection at its boundaries. The leakage arising from the finite geometry of the measurements was accounted for by the usual diffusion theory correction  $D(E)B^2$  in which the total local buckling  $B^2$  was used. Here  $B^2$  was calculated from the flux distributions along the three perpendicular axes which had been measured by activation of cadmium covered indium foils. The correction was small however.

The results are shown in Fig. 4.6. Positive conclusions are difficult to draw from these spectra, but some useful information can be deduced. The fluxes are inconsistent in the  $1/E$  region and this indicates errors in the monitoring system. For the two smaller size re-entrant holes, the effects of Bragg scattering can be seen at 0.005 eV in the flux at the center of the iron. That this effect is not seen in the largest re-entrant hole implies that the hole is too large a perturbation and some cell averaging has occurred. Finally, we are not able to say that the agreement between theory and experiment is better at any one re-entrant hole size than any other. It is worth noting that we could get reasonable statistics and agreement when using only a 150 mil precollimator. This comparison would probably have been more explicit had the iron been replaced by a material with a greater absorption cross section so that the spectral differences would have been accentuated.

It was therefore decided to repeat the measurements in a cell comprising 1 inch of polyethylene and 1 inch of iron using a 0.281 inch diameter re-entrant hole. The results are shown in Fig. 4.7 and 4.8 with the relative intensity of each spectra preserved. Normalization is made in the  $1/E$  region of the angular flux directed towards the iron at the polyethylene iron interface. In general, the agreement between theory and experiment is reasonable although discrepancies of 20% can be seen. This kind of result could have been anticipated since the 1/4 inch re-entrant hole is a

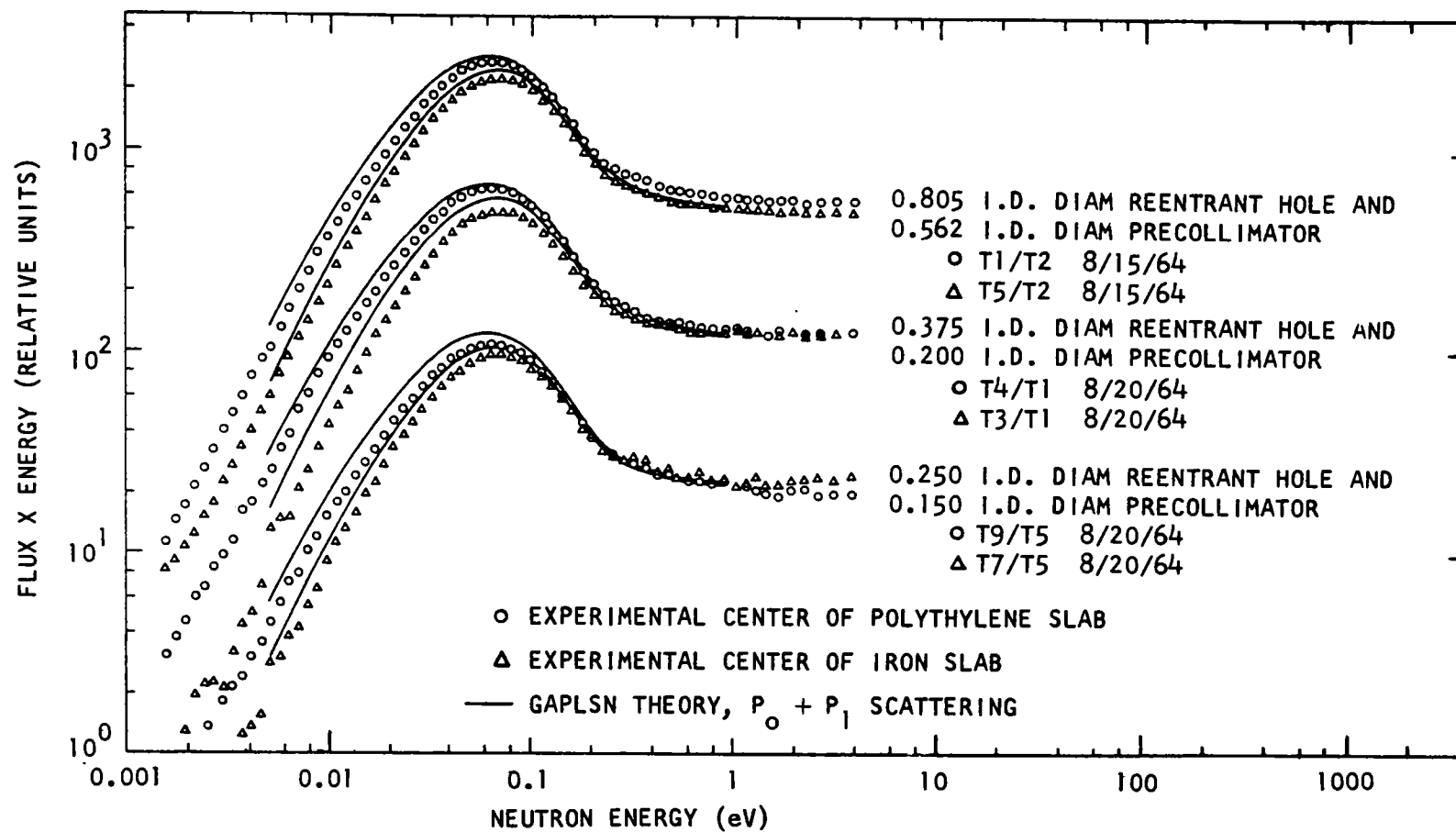


Fig. 4.6 -- Effect of re-entrant hole size on the neutron spectra  
measured in an heterogeneous assembly

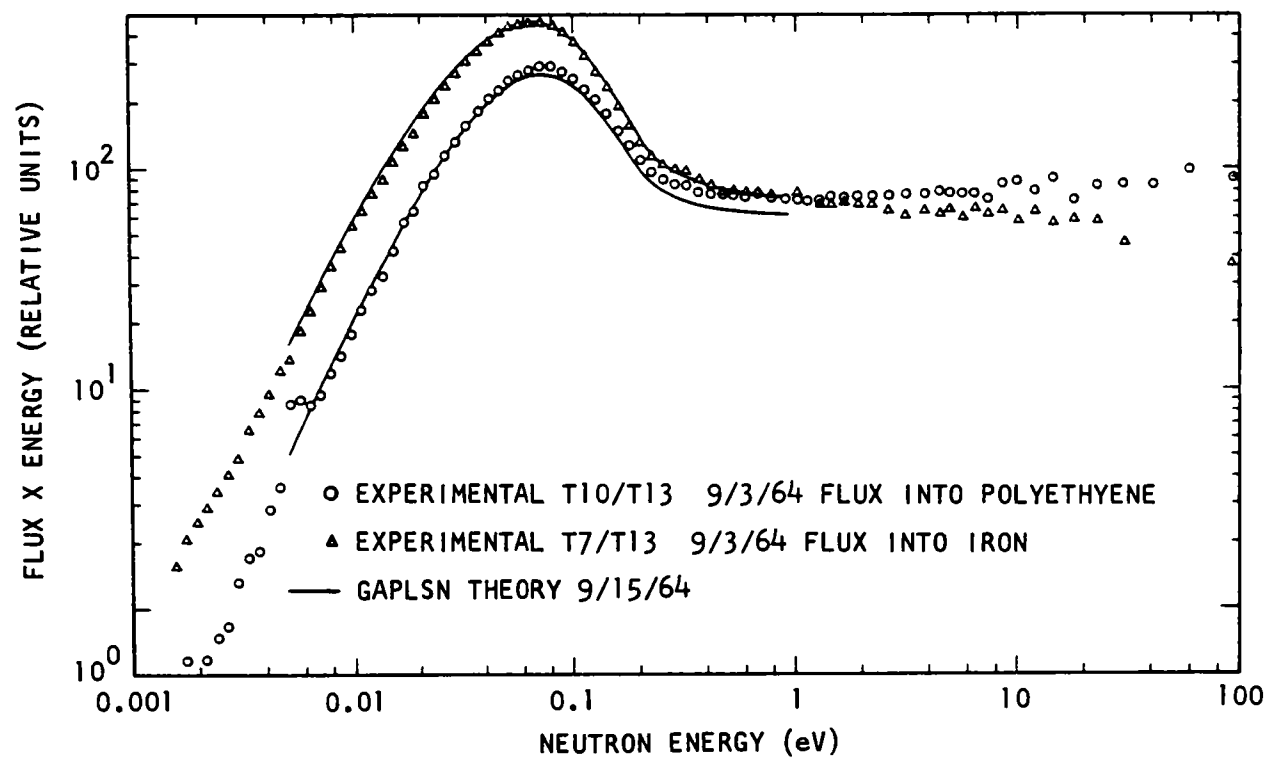


Fig. 4.7 -- Ninety-degree angular spectra at the cell interface of a polyethylene - iron heterogeneous assembly

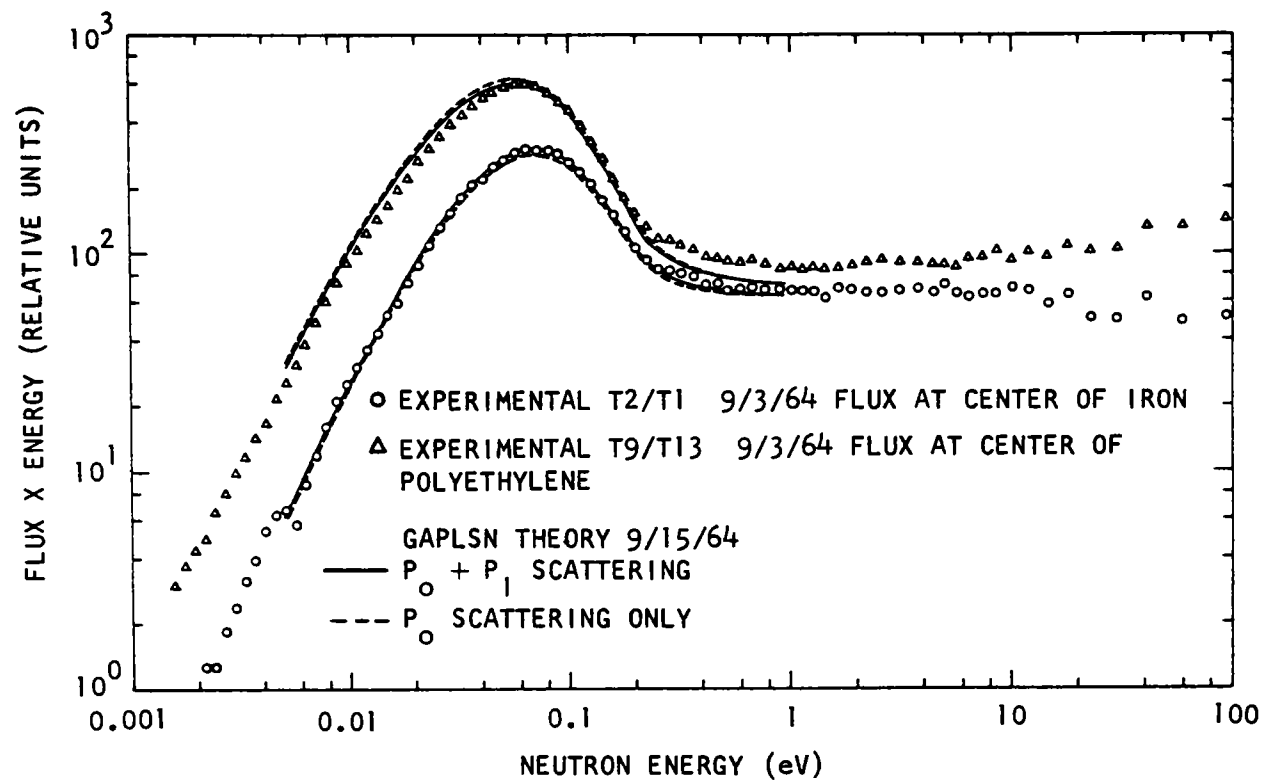


Fig. 4.8 -- Ninety-degree angular spectra at the cell centers of a polyethylene - iron heterogeneous assembly



much smaller perturbation in the 1 inch cell than it was in the 1/2 inch cell. The agreement is also good enough that it is obvious that the theoretical spectra determined by using both the  $P_0$  and  $P_1$  scattering matrices are superior to those using  $P_0$  scattering only. The calculation is performed only out to 1 eV since this is the upper numerical limit obtained for the new polyethylene scattering kernel. The problem of how to calculate the epithermal part of the spectrum above 1 eV is a very real one and will receive attention in the future.

It is not possible to be conclusive about the feasibility of inter-cell spectral measurements based on the results here. The cells studied here are far removed from fuel cells, but the studies here are good enough to justify further experiments which approach a more realistic configuration and material composition.

## V. NEUTRON THERMALIZATION IN ZIRCONIUM HYDRIDE

### 5.1 INTRODUCTION AND SUMMARY

During this past contract year, the status of the zirconium hydride scattering model has not changed since there did not seem to be any new neutron scattering or spectral data in conflict with the model. The model is still based on the assumption of the presence of an Einstein oscillator<sup>(25)</sup>. The scattering kernel is derived using SUMMIT<sup>(26)</sup> from a distributed frequency spectrum which takes into account the natural width of the oscillator level, and a Debye acoustical spectrum having a cut-off energy of 0.02 eV to provide some Doppler broadening of the levels. This model has recently been strongly criticized by Roberts and Miller<sup>(27)</sup> and Section 5.2 has been written as a rebuttal.

### 5.2 ZIRCONIUM HYDRIDE SCATTERING DESCRIPTION

#### 5.2.1 Introduction

The description of neutron thermalization in zirconium hydride has been the subject of much conjecture during the last few years. New experimental data and a theoretical interpretation of these data were published under this program in the June 1964 issue of Nuclear Science and Engineering.<sup>(25)</sup> A letter<sup>(27)</sup> to the editor of NSE (Neutron Thermalization in Zirconium Hydride, by W. J. Roberts and J. Miller) takes exception to many of the statements made in our June publication. In this section these objections are discussed. In Ref. 25 we presented seven new measurements of thermal neutron spectra taken under varying conditions of poison and temperature which illustrate a significant spectral shift with temperature for the moderator  $\text{ZrH}_{1.75}$ . The calculated spectra based essentially on an Einstein oscillator model for the proton motion were also shown. Acceptable agreement was obtained between theory and experiment. To date corresponding comparisons have not been published for other alternative

thermalization models for  $\text{ZrH}_{1.75}$ . In the following will be found our comments on the letter to the editor of NSE in the form of a discussion of the thermalization model, and a discussion of experimental results.

### 5.2.2. Thermalization Model

We restate briefly here how the Einstein oscillator model describes neutron scattering in zirconium hydride. For the model reported in Ref. (25) the computer code SUMMIT<sup>(26)</sup> was used with a distributed frequency spectrum to take account of the natural width of the oscillator level, and a Debye spectrum having a cutoff energy of 0.02 eV to include some Doppler broadening of the levels. The Doppler broadening is relatively quite small due to the large mass of the zirconium atoms neighboring each hydrogen atom. An earlier Einstein oscillator model<sup>(28)</sup> for the proton motion differed with the one currently in use in that all the level broadening was accounted for as Doppler broadening. This model did not explain very well the energy dependence of measured neutron scattering data. While at one time some experiments<sup>(29)</sup> showed that anharmonic effects were important in zirconium hydride, this same series of experiments now<sup>(30)</sup> appear to be in good agreement with the broadened harmonic oscillator model. Nevertheless the differential experiments should not be considered conclusive one way or the other until put on an absolute basis and until corrected for resolution and multiple scattering. The present thermalization model is also supported by the good agreement between calculated and measured neutron spectra under a wide variety of experimental conditions. The statement by Roberts and Miller<sup>(27)</sup> that we have rejected all non-neutron experiments is not correct. What we do reject is the interpretation that Roberts and Miller put on them, and their importance toward obtaining a reasonably accurate neutron scattering description. No doubt future scattering models will include further refinements based on non-neutron experiments, but these will reduce with some degree of approximation to the natural width oscillator model given in Ref. (25).

It has also been stated by RM<sup>(27)</sup> that a better model for neutron scattering from zirconium hydride should include the possibility that the protons exist in a band structure and communicate. This statement is supported by the fact that the protons are known to diffuse. Even though neutron experiments to date show no strong evidence for the quantitative model proposed by the authors; we feel that it should be tested. Our main contention is that the authors have made incorrect use of Eq. (29) of Ref. (31) to express their model in mathematical terms. Their Eq. (29) refers to one phonon scattering from a cubic harmonic crystal. The statistics in that equation come from the displacements from equilibrium of the particles and not from the scattering particles themselves. Our opinion is that the mere changing of the statistics in Eq. (29) and stating that the statistics now refer to the protons is neither correct mathematically (for this procedure has no regard for the origins of that equation), nor

does it reflect the physical model they wish to express in mathematical language. Of course RM might have made the situation clearer by proving mathematically that their Eq. (29) with the statistics reversed is a reasonable approximation for their model. The above objections are aside from those they themselves present in their letter.

A major point of disagreement between our analysis and that of RM lies in the choice of a physical model, or theory, to describe the motions of the protons in  $\text{ZrH}_{1.75}$ . The key to the RM analysis is their assertion that the exclusion principle, applied to the protons, plays a major role in the proton dynamics. We shall show that this cannot be.

Before discussing the protons, we should reflect upon the difference between a "fit" and a theory. A "fit" is little more than an empirical formula or phrase that describes, or correlates, a body of data. It, in itself, offers no scientific explanation. A theory, on the other hand, seeks to explain (i. e. predict) the data through proper reasoning based upon scientific principles that are consistent and acceptable.

The exclusion principle affects the dynamics of a many-proton system to the extent that there is overlap in the wave functions of the individual protons. If the protons are localized in a lattice structure, the overlap will be negligible. If they are free to move through the lattice, experiencing only the mean lattice potential, the overlap will be great. Now, the most direct way of "seeing" the protons in  $\text{ZrH}_{1.75}$  is by means of a neutron diffraction experiment. These experiments<sup>(32)</sup> show conclusively that the protons form a lattice structure, and that the period for "jumping"<sup>(33)</sup> is very long compared to a vibrational period. In other words, the wave function overlap is negligibly small. For the model of RM the diffraction experiments in addition to the double differential neutron experiments would tend to exhibit a smear (due to the protons being so mobile) in contrast to the observed structure.

To appreciate the total irrelevancy of Fermi statistics to this problem, let us compute an "upper bound" by considering a gas of free protons where overlap will be large. The fermi energy of such a gas, with density appropriate to protons in  $\text{ZrH}_{1.75}$ , lies in the millivolt range. Thus, at room temperature only Boltzmann statistics will be found. The exclusion principle has nothing whatever to do with the  $\text{ZrH}_{1.75}$  problem; a proper theory will begin with the picture of protons localized in a lattice structure. The formula of RM, so mysteriously arrived at, must be considered to be a "fit" rather than a theory, no matter how fine its agreement with the data.

### 5.2.3. Experimental Considerations

It is certainly agreed with Roberts and Miller<sup>(27)</sup> that an analysis of reactor prompt temperature coefficients is not the way to establish the

validity of a thermalization model. This lack of sensitivity is of course why the experimental investigation of Ref. (25) was conducted. On the other hand it is not correct as indicated by Roberts and Miller that TRIGA temperature coefficients are "relatively evenly split between  $U^{238}$  Doppler effects; fuel rod expansion and associated water expulsion; and spectra effects". Our previous Ref. (34) states that the spectral effects for TRIGA (i. e. thermal utilization change and enhanced reflector leakage) total  $-9 \times 10^{-5} \Delta k / ^\circ C$  while Doppler and rod expansion give an additional  $-2 \times 10^{-5} \Delta k / ^\circ C$ .

Indeed the matter of the spectral temperature coefficients for SNAP reactors has not been greatly clarified by the Roberts and Miller letter. It appears that our experimental spectral data can be used to estimate the spectral part of the SNAP coefficients and gives good agreement with experimental observations.<sup>(27)</sup> This seems to indicate to Roberts and Miller that the latest version of the Einstein oscillator model will predict SNAP prompt temperature coefficients correctly while the older version<sup>(28)</sup> did not. It has been our observation that the two Einstein models give somewhat different results on predictions of neutron spectra but not a huge difference of temperature coefficients for TRIGA or homogeneous  $ZrH_x$  systems. Fig. 5.1 shows some comparisons of calculated spectra in poisoned zirconium hydride for the two Einstein models. The high temperature results are identical while the ambient results are different, we believe, largely due to the low effective mass of twenty which had to be assigned to the translational modes in the Doppler model to ensure convergence in the calculation. Spectral temperature coefficients of reactivity have been calculated using both thermalization models for two very different TRIGA configurations and for a homogeneous core. For the standard 1 megawatt TRIGA (2-3 barns/hydrogen atom absorption) the calculated negative temperature coefficient decreases by twenty percent using the new SUMMIT model. For a TRIGA configuration in which the poison level is increased a factor of 5 the negative temperature coefficient is only 10 percent different for the two models. For the solid homogeneous configuration discussed before<sup>(25)</sup> with an absorption level of twelve barns/hydrogen, the model change gave rise to a twenty-five percent change in the temperature coefficient. It would appear that poison levels in the SER are in the range of 10 barns/hydrogen atom<sup>(31)</sup> in which case leakage should not constitute an important consideration. Although we have not as yet undertaken a complete analysis of SNAP reactor systems, it is surprising to us that the calculated spectral portion of the temperature coefficient of that reactor is so drastically influenced in magnitude by the particular choice of a thermalization model. It will be recalled that predicted differences of a factor of 3 have been reported<sup>(35)</sup> between Doppler broadened Einstein oscillator calculations on the one hand and Roberts-Miller calculations and natural width Einstein oscillator calculations<sup>(27)</sup> on the other hand.

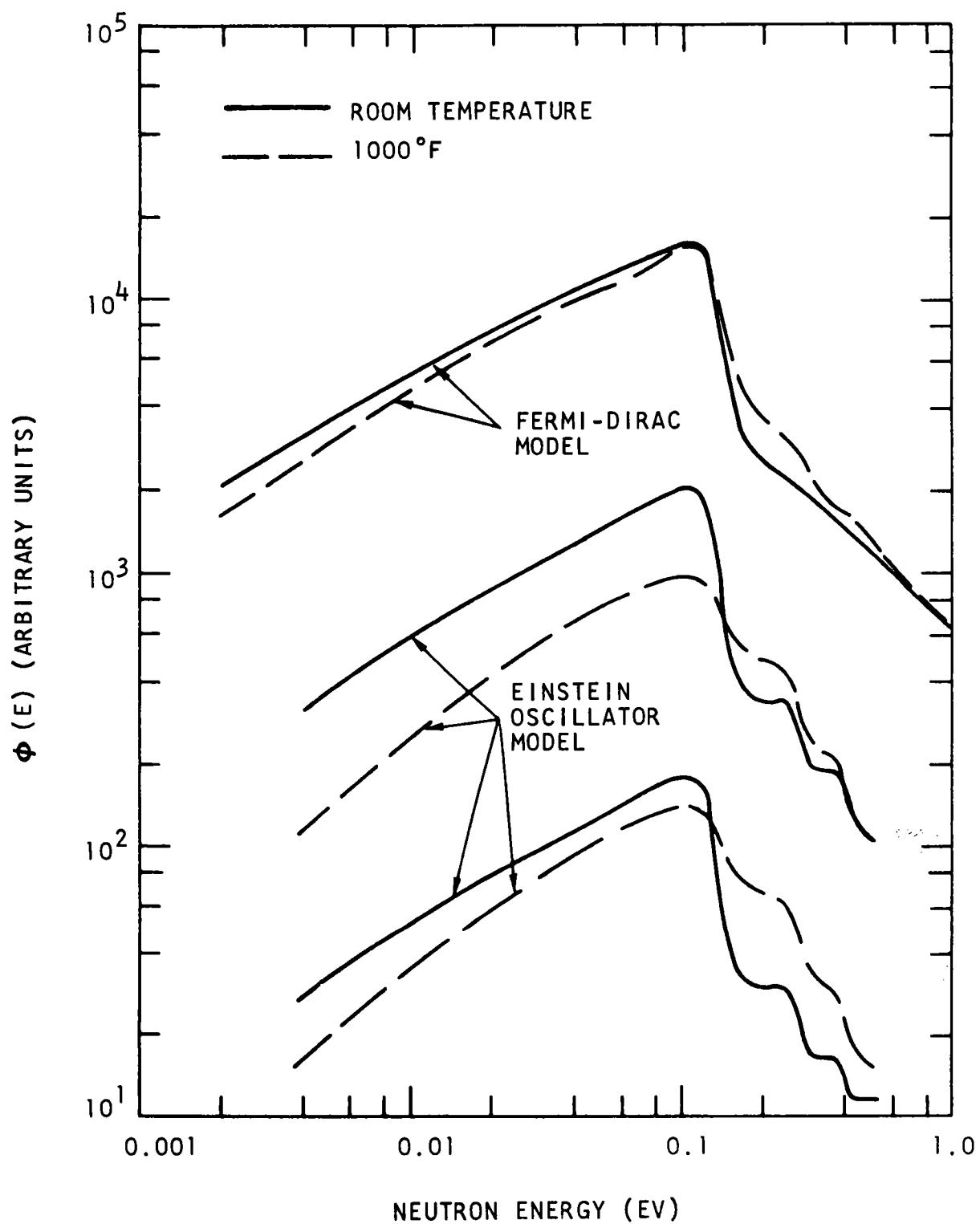


Fig. 5.1 -- Predicted neutron spectral changes with temperature using the Fermi-Dirac and Einstein oscillator models

Regarding Figs. (4) and (5) in our June publication<sup>(25)</sup> which show the temperature dependence of the upscattering cross sections, it is agreed the three statistical occupancies give nearly the same temperature dependence. However only the interpretation of the results in terms of Bose statistics is compatible and consistent with the existence of the vibration level at 0.137 eV for zirconium hydride.

Another point requiring clarification is Fig. (1) in the previous publication.<sup>(25)</sup> The figure was inserted in an attempt to indicate qualitatively the spectral changes with temperature predicted by the two thermalization models. Our only justification for reproducing the SER Fermi-Dirac data from NA-SR-7140 and assuming it was typical is the statement quoted from page 45 of that publication namely: "the calculated spectra for these reactors are indicated in Fig. (22). They are typical of Beyster's measurement for poisoned zirconium hydride media". Our calculational results, shown in the figure, using the Einstein oscillator model were both prepared for 7.08 barns/hydrogen atom absorption at 2200 meters/sec. As stated in our text they are arbitrarily normalized in the slowing down region of the spectrum. The comparison is repeated in Fig. 5.1 of this report and shows a more realistic normalization together with the previous normalization. The spectra are now assumed to have exactly the same slowing down source for the new normalization. Unfortunately for the argument of Roberts and Miller the spectra still differ by the same factor of 2. (The curves would coalesce at higher neutron energies but the calculation was not carried out above 0.5 eV neutron energy.) In fact all measured spectral data show about the same large spectral change with temperature. In explaining the lack of a spectral shift for the Fermi-Dirac data, Roberts and Miller<sup>(27)</sup> indicated that leakage in their SNAP system tends to depress the high energy end of the spectrum and reduce the temperature shift in comparison to an infinite medium calculation. We disagree with this argument since our experience has shown consistently that leakage for hydrogen systems tends to harden the neutron spectrum not soften it, due to a  $DB^2$  leakage correction at thermal energies which is added to  $\Sigma_a$ . As stated previously, however, this effect is usually small for such heavily poisoned systems.

We also disagree with the summary conclusions stated by Roberts and Miller.<sup>(27)</sup> Although the original Nelkin-Rosenbluth Einstein oscillator model,<sup>(28)</sup> with the fictitious Doppler broadening has a number of drawbacks in detail, the over-all spectral change predicted by the model was not unlike that predicted by the new natural width model as Fig. 5.2 illustrates.

In conclusion it is hoped that eventually attempts will be made to incorporate all physically known facts about zirconium hydride into a detailed consistent thermalization model. Our contention at present, however, is that all presently known neutron data is reasonably consistent with the basic Einstein oscillator model incorporating a natural level width

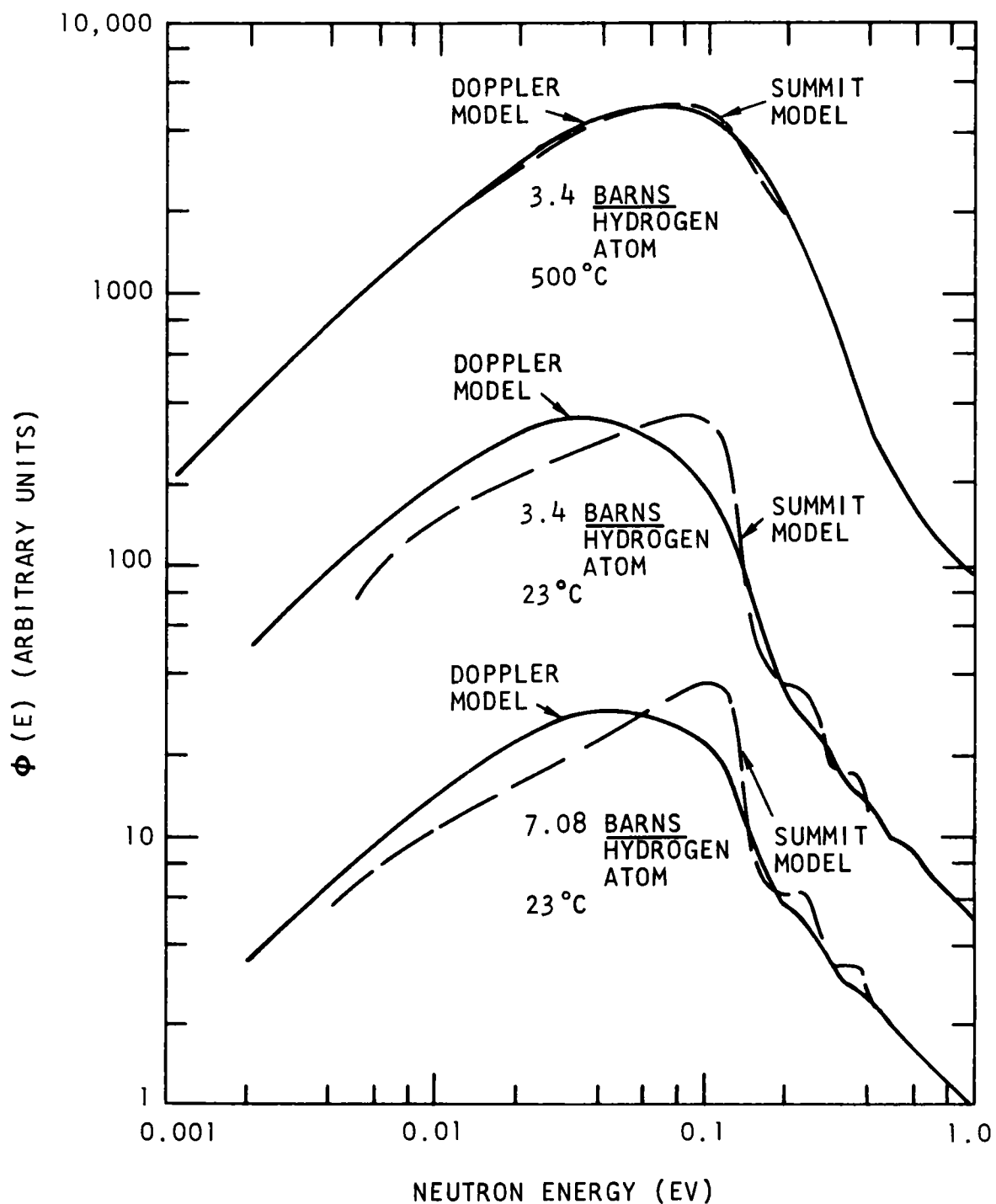


Fig. 5.2 -- Comparison of neutron spectra calculated with the Doppler broadened oscillator model and the natural width model (SUMMIT)



adjusted to fit neutron scattering experiments. Further tests, especially of space dependent neutron spectra, would seem to be warranted in order to establish the range of applicability of this physically simple approach.

## VI. NEUTRON THERMALIZATION IN BERYLLIUM

### 6.1. INTRODUCTION AND SUMMARY

From the work done in the preceding contract year (1962-1963), a scattering kernel has been obtained for beryllium which should predict neutron spectra accurately, since it agrees well with the  $S(\alpha, \beta)$  measurements of Sinclair.<sup>(38)</sup> This situation will be clarified in the coming year when spectral measurements will be made on this moderator. However, an important link remains, in finding a realistic means of taking into account interference effects. This has been studied during this contract year and the formalism describing the phenomenon has been written. (Section 6.2). Quantitative values for these interference effects will be obtained after the description has been programmed for the computer.

### 6.2. INTERFERENCE EFFECTS IN NEUTRON SCATTERING

The inelastic scattering cross sections for the various solid moderators have been calculated in the incoherent approximation which means that interference between neutron waves scattered from different nuclei is neglected. While this approximation has been successful for large energy and momentum transfers, it has been remarkably demonstrated by  $S(\alpha, \beta)$  measurements<sup>(38, 39)</sup> that interference effects are important for low energy and momentum transfers, where theory and experiment differ considerably. Below the Bragg cut-off, calculations of the inelastic scattering in the incoherent approximation using the computer code SUMMIT<sup>(26)</sup> differ from measured values by a factor of two or more for beryllium and graphite. It is suggested that interference effects are responsible for this discrepancy.

The calculation of interference (coherent) scattering is difficult for computational reasons. For the regions of momentum and energy transfer where coherent scattering is important, the assumption that only one phonon is involved is likely to be a good approximation. The Debye<sup>(40)</sup> approximation for calculating the one phonon coherent cross section has been demonstrated to be quantitatively incorrect by Placzek and van Hove<sup>(41)</sup> and to date only calculations involving this approximation have been made. The theoretical work on beryllium reported in the last annual report<sup>(3)</sup> for this project has been done using the actual dynamics of the lattice, and should make it possible to calculate rather accurately the one phonon coherent scattering, since the polarization vectors of the lattice waves are known. Due to other recent work the same situation holds for magnesium, zinc<sup>(42)</sup>

and graphite<sup>(43)</sup> as well as beryllium. Presented below is the derivation of the one phonon coherent scattering cross-section for a general lattice of more than one particle per unit cell. This derivation is given here because it is not possible to find it in the literature in a readily usable form, and for future work the derivation will help considerably in understanding any approximations made.

The cross section for the scattering of neutrons from any molecular system is given by

$$\frac{d^2\sigma}{d\Omega d\epsilon} = a^2 \frac{k}{k_o} \sum_f |\langle f | \sum_m e^{i\vec{\kappa} \cdot \vec{x}_m} | i \rangle|^2 \delta(\epsilon - E_i - E_f) \quad (6.2.1)$$

where the symbols used are completely standard.<sup>(18)</sup> First we consider phonon emission by the neutron, which gives the following wave functions:

$$|i\rangle = |k_o; n_1, n_2, \dots n_j, \dots\rangle \quad (6.2.2)$$

$$|f\rangle = |k; n_1, n_2, \dots n_j+1, \dots\rangle \quad (6.2.3)$$

where  $n_j$  is the number of phonons with wave vector  $\vec{q}$  and polarization  $j$ . For a harmonic crystal we write for the position coordinate  $\vec{x}_m$

$$\vec{x}_m = \vec{R}^\ell + \vec{r}^k + \vec{u}_k^\ell \quad (6.2.4)$$

where  $\ell$  is the lattice index and  $k$  the cell index, so that

$$\sum_m e^{i\vec{\kappa} \cdot \vec{x}_m} = \sum_{k, \ell} e^{i\vec{\kappa} \cdot (\vec{R}^\ell + \vec{r}^k)} e^{i\vec{\kappa} \cdot \vec{u}_k^\ell} \quad (6.2.5)$$

where

$$\vec{u}_k^\ell = \sum_{\vec{q}, j} \left( \frac{\hbar}{2NM\omega_j(\vec{q})} \right)^{1/2} \left[ \vec{C}(k|\vec{q}_j) a_{\vec{q}j} e^{2\pi i \vec{q} \cdot \vec{R}^\ell} + \vec{C}^*(k|\vec{q}_j) a_{\vec{q}j}^\dagger e^{-2\pi i \vec{q} \cdot \vec{R}^\ell} \right] \quad (6.2.6)$$

Here  $N$  is the number of atoms in the crystal,  $M$  the mass of an atom,  $\hbar\omega_j(\vec{q})$  the energy of a phonon with wave vector  $\vec{q}$  and polarization index  $j$ , and  $\vec{C}(k|\vec{q}_j)$  is the polarization vector of the phonon  $\vec{q}, j$  for the  $k$ th atom in the unit cell.  $a_{\vec{q}j}$  is a boson annihilation operator.

First we consider scattering where a phonon  $\omega_j(\vec{q}) = \omega_1(\vec{q})$  is emitted by the neutron.

$$\langle f | e^{i\vec{\kappa} \cdot \vec{u}_\ell^k} | i \rangle$$

$$= \langle \dots, n_{j\vec{q}}, \dots, n+1 | \exp \left[ i \sum_{j\vec{q}} \left( \frac{\hbar}{2NM\omega_j(\vec{q})} \right)^{1/2} \left[ \vec{\kappa} \cdot \vec{C}(\vec{k} | \vec{q}_j) e^{2\pi i \vec{q} \cdot \vec{R}^\ell} a_{j\vec{q}} + \vec{\kappa} \cdot \vec{C}^*(\vec{k} | \vec{q}_j) e^{-2\pi i \vec{q} \cdot \vec{R}^\ell} a_{j\vec{q}}^\dagger \right] \right] | n_1, \dots, n_{j\vec{q}}, \dots \rangle \quad (6.2.7)$$

$$= \langle n_1+1 | \exp \left[ i \left( \frac{\hbar}{2NM\omega_1} \right)^{1/2} \left[ \vec{\kappa} \cdot \vec{C}(\vec{k} | 1) a_1 e^{2\pi i \vec{q} \cdot \vec{R}^\ell} + \vec{\kappa} \cdot \vec{C}^*(\vec{k} | 1) a_1^\dagger e^{-2\pi i \vec{q} \cdot \vec{R}^\ell} \right] \right] | n_1 \rangle$$

$$\cdot \prod_{j\vec{q}=2}^N \langle n_{j\vec{q}} | \exp \left[ i \left( \frac{\hbar}{2NM\omega_j(\vec{q})} \right)^{1/2} \left[ \vec{\kappa} \cdot \vec{C}(\vec{k} | \vec{q}_j) a_{j\vec{q}} e^{2\pi i \vec{q} \cdot \vec{R}^\ell} + \vec{\kappa} \cdot \vec{C}^*(\vec{k} | \vec{q}_j) a_{j\vec{q}}^\dagger e^{-2\pi i \vec{q} \cdot \vec{R}^\ell} \right] \right] | n_{j\vec{q}} \rangle .$$

Let

$$\left( \frac{\hbar}{2NM\omega_j(\vec{q})} \right)^{1/2} \vec{\kappa} \cdot \vec{C}(\vec{k} | \vec{q}_j) e^{2\pi i \vec{q} \cdot \vec{R}^\ell} = Q_{j\vec{q}}^{\vec{k}, \ell} \quad (6.2.8)$$

Then we have

$$| \langle f | \sum_{\vec{k}, \ell} e^{i\vec{\kappa} \cdot (\vec{R}^\ell + \vec{r}^{\vec{k}})} e^{i\vec{\kappa} \cdot \vec{u}_\ell^k} | i \rangle |^2_T$$

$$= \left| \sum_{\mathbf{k}, \ell} \langle n_1 + 1 | e^{i(Q_1^{\mathbf{k}\ell} a + Q_1^{*\mathbf{k}\ell} a^\dagger)} | n_1 \rangle \prod_{jq=2}^N \langle n_{jq} | e^{i(Q_{jq}^{\mathbf{k}\ell} a + Q_{jq}^{*\mathbf{k}\ell} a^\dagger)} | n_{jq} \rangle \right|_T^2 \quad (6.2.9)$$

$$= \sum_{\mathbf{k}\mathbf{k}', \ell\ell'} \left[ \langle n_1 + 1 | e^{i(Q_1^{\mathbf{k}\ell} a + Q_1^{*\mathbf{k}\ell} a^\dagger)} | n_1 \rangle \langle n_1 | e^{-i(Q_1^{\mathbf{k}'\ell'} a + Q_1^{*\mathbf{k}'\ell'} a^\dagger)} | n_1 + 1 \rangle \right]_T \cdot$$

$$\prod_{jq=2}^N \left[ \langle n_{jq} | e^{i(Q_{jq}^{\mathbf{k}\ell} a + Q_{jq}^{*\mathbf{k}\ell} a^\dagger)} | n_{jq} \rangle \langle n_{jq} | e^{-i(Q_{jq}^{\mathbf{k}'\ell'} a + Q_{jq}^{*\mathbf{k}'\ell'} a^\dagger)} | n_{jq} \rangle \right]_T \cdot$$

$$\exp [i\vec{\kappa} \cdot (\vec{R}^\ell - \vec{R}^{\ell'} + \vec{r}^{\mathbf{k}} - \vec{r}^{\mathbf{k}'})] \quad .$$

Now it is necessary to evaluate the matrix elements. First consider:

$$\left[ \langle n | e^{i(Qa + Q^* a^\dagger)} | n \rangle \langle n | e^{-i(Q'a + Q'^* a^\dagger)} | n \rangle \right]_T$$

$$= \left[ \langle n | e^{iQ^* a^\dagger} e^{iQa} | n \rangle \langle n | e^{-iQ'a} e^{-iQ'^* a^\dagger} | n \rangle \right]_T e^{-\frac{1}{2}|Q|^2 + \frac{1}{2}|Q'|^2} \quad (6.2.10)$$

$$= e^{-\frac{1}{2}(|Q|^2 - |Q'|^2)} \left[ \langle n | \sum_p \frac{(-|Q|^2)^p}{(p!)^2} (a^\dagger)^p a^p | n \rangle \langle n | \sum_{p'} \frac{(-|Q'|^2)^{p'}}{(p'!)^2} a^{p'} (a^\dagger)^{p'} | n \rangle \right]_T$$

$$= \left[ \sum_{p, p'} \frac{(-|Q|^2)^{p'}}{(p'!)^2} \frac{n!}{(n-p')!} \frac{(-|Q'|^2)^p}{(p!)^2} \frac{(n+p)!}{n!} \right]_T e^{-\frac{1}{2}(|Q|^2 - |Q'|^2)}$$

$$= (1-z) \sum_{n, p, p'} z^n \frac{(-|Q'|^2)^p (-|Q|^2)^{p'}}{(p! p'!)^2} \frac{n!}{(n-p')} \frac{(n+p)!}{n!} e^{-\frac{1}{2}(|Q|^2 - |Q'|^2)}, \quad z = e^{-\hbar\omega/kT}$$

$$\begin{aligned}
&= (1-z) \sum_{n, p, p'} \frac{(-|Q'|^2)^p (-|Q|^2)^{p'}}{(p! p'!)^2} z^{p'} \left(\frac{d}{dz}\right)^{p'} \left(\frac{d}{dz}\right)^p z^{n+p} e^{-\frac{1}{2}(|Q|^2 - |Q'|^2)} \\
&= (1-z) \sum_{p' p} \frac{(-|Q'|^2)^p (-|Q|^2)^{p'}}{(p! p'!)^2} z^{p'} \left(\frac{d}{dz}\right)^{p'} \left(\frac{d}{dz}\right)^p \left(\frac{1}{1-z}\right) e^{-\frac{1}{2}(|Q|^2 - |Q'|^2)} \\
&= (1-z) \sum_{p'} \frac{(-|Q|^2)^{p'}}{(p'!)^2} z^{p'} \frac{d^{p'}}{dz^{p'}} \left[ \frac{1}{1-z} e^{-|Q'|^2/(1-z)} \right] e^{-\frac{1}{2}(|Q|^2 - |Q'|^2)} \\
&= \sum_{p'} \frac{(-|Q|^2)^{p'}}{p'!} \frac{z^{p'}}{(1-z)^{p'}} e^{-\frac{|Q'|^2}{1-z}} e^{-\frac{1}{2}(|Q'|^2 - |Q|^2)}, \quad \text{since } |Q'|^2 \cong 1/N, \\
&\quad \text{and } N \longrightarrow \infty. \\
&= e^{-\frac{1}{2}(|Q|^2 + |Q'|^2)} \coth \left( \frac{\hbar\omega}{2kT} \right)
\end{aligned}$$

Now we evaluate

$$\begin{aligned}
&\left[ \langle n+1 | e^{i(Qa + Q'^* a^\dagger)} | n \rangle \langle n | e^{-i(Q'a + Q'^* a^\dagger)} | n+1 \rangle \right]_T \\
&= \left[ \frac{1}{n+1} \langle n | a e^{i(Qa + Q'^* a^\dagger)} | n \rangle \langle n | e^{-i(Q'a + Q'^* a^\dagger)} a^\dagger | n \rangle \right]_T \quad (6.2.11) \\
&= \left[ \frac{1}{n+1} \langle n | \sum_{p, p'} \frac{(iQ)^p (iQ'^*)^{p'}}{p! p'!} a^{p+1} (a^\dagger)^{p'} | n \rangle \right]_T \\
&= \left[ \langle n | \sum_{p, p'} \frac{(-iQ')^p (-iQ')^{p'}}{p! p'!} (a^\dagger)^p a^{p'} a^\dagger | n \rangle \right]_T e^{-1/2(|Q'|^2 - |Q|^2)} \\
&= \left[ \frac{1}{n+1} \sum_{p, p'} \frac{(-|Q|^2)^p (-|Q'|^2)^{p'} Q^* Q'}{(p!)^2 (p'!)^2 (p+1)(p'+1)} \frac{(n+p+1)!}{n!} \frac{(n+1)!}{(n-p)!} \right]_T e^{-1/2(|Q'|^2 - |Q|^2)}
\end{aligned}$$

$$\begin{aligned}
&= (1-z) Q' Q^* e^{-1/2(|Q'|^2 - |Q|^2)} \sum_{p'} \frac{(-|Q'|^2)^{p'}}{(p'!)^2 (p'+1)} z^{p'} \left( \frac{d}{dz} \right)^{p'} \left[ \frac{1}{(1-z)^2} e^{-\frac{|Q|^2}{1-z}} \right] \\
&= \frac{Q' Q^*}{1-z} e^{-\frac{(|Q|^2 + |Q'|^2)}{2}} \coth \left( \frac{\hbar \omega}{2kT} \right).
\end{aligned}$$

All that needs to be done now is to sum over all final states with one additional phonon, so that

$$\begin{aligned}
&\sum_f \left| \sum_{\mathbf{k}, \ell} \langle f | e^{i\vec{\kappa} \cdot (\vec{R}^\ell + \vec{r} + \vec{u}_\ell)} | i \rangle \right|_T^2 \\
&= \sum_{\mathbf{k} \mathbf{k}' \ell \ell'} \exp \left[ -1/2 \sum_{\mathbf{j} \mathbf{q}} \left[ |Q_{\mathbf{j} \mathbf{q}}^{\mathbf{k} \ell}|^2 + |Q_{\mathbf{j} \mathbf{q}}^{\mathbf{k}' \ell'}|^2 \right] \coth \left( \frac{\hbar \omega_j(\vec{q})}{2kT} \right) \right] e^{i\vec{\kappa} \cdot (\vec{R}^\ell - \vec{R}^{\ell'})} \\
&\quad \cdot e^{i\vec{\kappa} \cdot (\vec{r}^{\mathbf{k}} - \vec{r}^{\mathbf{k}'})} \sum_{\mathbf{j} \vec{q}} \frac{1}{1 - e^{-\hbar \omega_j(\vec{q})/kT}} Q_{\mathbf{j} \vec{q}}^{\mathbf{k}' \ell'} Q_{\mathbf{j} \vec{q}}^{*\mathbf{k} \ell}. \quad (6.2.12)
\end{aligned}$$

Since

$$\sum_{\ell} \left| e^{i\vec{a} \cdot \vec{R}^\ell} \right|^2 = \frac{(2\pi)^3}{V_c} \sum_{\vec{\tau}} \delta(\vec{a} - 2\pi \vec{\tau}) \quad (6.2.13)$$

where  $V_c$  is the volume of the unit cell, and  $\vec{\tau}$  is a reciprocal lattice vector, the cross section can be written as

$$\left( \frac{d^2 \sigma}{d\epsilon d\Omega} \right) = \frac{(2\pi)^3}{2} \frac{a^2 \hbar}{MNV_c} \frac{k}{k_0} \sum_{\mathbf{j} \vec{q}} \left| \sum_{\mathbf{k}} e^{-W^{\mathbf{k}}} e^{i\vec{\kappa} \cdot \vec{r}^{\mathbf{k}}} \frac{\vec{\kappa} \cdot \vec{C}(\mathbf{k} | \vec{q})}{k} \right|^2. \quad (6.2.14)$$

$$\frac{1}{\omega_j(\vec{q})} \frac{1}{1 - e^{-\hbar \omega_j(\vec{q})/kT}} \delta(\epsilon - \hbar \omega_j(\vec{q})) \delta(\kappa - 2\pi \vec{q} - 2\pi \vec{\tau})$$

where

$$W^k = -\frac{1}{4} \frac{\hbar}{NM} \sum_{j\vec{q}} \frac{|\vec{\kappa} \cdot \vec{C}(k|\vec{q})|^2}{\omega_j(\vec{q})} \coth \left( \frac{\hbar\omega_j(\vec{q})}{2kT} \right) \quad (6.2.15)$$

The cross-section for phonon absorption is obtained in the same way and is

$$\left( \frac{d^2\sigma}{d\Omega d\epsilon} \right)_{\text{abs}} = \frac{(2\pi)^3}{2} \frac{a^2 \hbar}{NMV_c} \frac{k}{k_o} \sum_{j\vec{q}} \left| \sum_k e^{-W^k} e^{i\vec{\kappa} \cdot \vec{r}^k} \vec{\kappa} \cdot \vec{C}(k|\vec{q}) \right|^2 \frac{1}{\omega_j(\vec{q})} \cdot$$

$$\cdot \frac{1}{e^{\hbar\omega_j(\vec{q})/kT} - 1} \delta(\epsilon + \hbar\omega_j(\vec{q})) \delta(\vec{\kappa} + 2\pi\vec{q} - 2\pi\vec{\tau}) \quad (6.2.16)$$

By changing the sum over  $\vec{q}$  into an integral in the standard way, we can write for the cross section for one phonon absorption or emission:

$$\frac{d^2\sigma}{d\Omega d\epsilon} = \frac{(2\pi)^3 \hbar a^2}{2NMV_c} NV_c \sqrt{\frac{E}{E_o}} \sum_{j, \eta=\pm 1} \int d^3q \left| \sum_k e^{-W^k} e^{i\vec{\kappa} \cdot \vec{r}^k} \vec{\kappa} \cdot \vec{C}(k|\vec{q}) \right|^2$$

$$\cdot \frac{1}{1 - e^{-\eta\hbar\omega_j(\vec{q})/kT}} \frac{1}{\eta\omega_j(\vec{q})} \delta(\epsilon - \eta\omega_j(\vec{q})) \delta(\vec{\kappa} - 2\pi\vec{q}) , \quad (6.2.17)$$

or

$$\frac{d^2\sigma}{d\epsilon d\Omega} = \frac{\hbar a^2}{2M} \sqrt{\frac{E}{E_o}} \sum_{j, \eta=\pm 1} \left| \sum_k e^{-W^k} e^{i\vec{\kappa} \cdot \vec{r}^k} \vec{\kappa} \cdot \vec{C}(k|\vec{\kappa}/2\pi) \right|^2 \frac{1}{1 - e^{-\eta\hbar\omega_j(\vec{\kappa}/2\pi)/kT}}$$

$$\cdot \frac{1}{\eta\omega_j(\vec{\kappa}/2\pi)} \delta(\epsilon - \eta\hbar\omega_j(\vec{\kappa}/2\pi)) \quad (6.2.18)$$

For a powder we must integrate over all possible orientations of the crystal. This can be achieved by integrating over the directions of  $\vec{\kappa}$  and dividing by  $4\pi$ . This procedure yields the result:



$$\begin{aligned}
\left. \frac{d^2 \sigma}{d\epsilon d\Omega} \right|_{av} &= \frac{a_c^2}{2M} \sqrt{\frac{E}{E_o}} \frac{1}{4\pi} \sum_{j, \eta=\pm 1} \int_{-1}^1 d\mu_{\kappa} \frac{1}{\left| \frac{\partial \omega_j(\vec{\kappa}/2\pi)}{\partial \phi} \right|} \frac{1}{1 - e^{-\eta \hbar \omega_j(\vec{\kappa}/2\pi)/kT}} \frac{1}{\eta \omega_j(\vec{\kappa}) 2\pi} . \\
&\cdot \left| \sum_{\vec{k}} e^{-W^{\vec{k}}} e^{i\vec{\kappa} \cdot \vec{r}} \frac{\vec{k}}{\kappa \cdot \vec{C}(\kappa)} \frac{\vec{\kappa}}{2\pi} \right|^2 \quad (6.2.19)
\end{aligned}$$

During the next contract year, this cross section will be evaluated using the actual polarization vectors  $\vec{C}$  of the lattice for beryllium in order to try to match experimental results for small  $\vec{\kappa}$  and  $\epsilon$ .

## VII. NEUTRON THERMALIZATION IN BeO

### 7.1 INTRODUCTION AND SUMMARY

During the past contract year, spectral measurements in BeO were performed because experimental techniques had been improved since earlier studies<sup>(1)</sup> were made. The comparative calculations for these measurements employed a scattering kernel based on a Debye frequency spectrum with a cut-off frequency adjusted to satisfy the specific heat data for BeO. Reasonably good results were obtained in these finite medium studies which are discussed in Section 7.2. Bragg trapping of neutrons was observed in the measurements and this has justified the study of coherent elastic scattering in beryllium oxide discussed in Section 7.3. The study has been completed and elastic scattering should be added to the BeO scattering kernel that will be generalized shortly. This proposed kernel will be calculated with the frequency spectrum measured by Sinclair<sup>(38)</sup> using the Egelstaff<sup>(44)</sup> extrapolation technique. Due to the inherent limitations of this extrapolation technique (as shown in previous examples for beryllium<sup>(3)</sup> and graphite<sup>(2)</sup>), a calculation performed with a deeper theoretical background would be most desirable.

### 7.2 NEUTRON SPECTRA IN BeO

Measurements of neutron spectra in BeO were made this year as part of the program to improve the understanding of thermal neutron scattering in this moderator.

Figure 7.1 illustrates the geometry in which angular flux measurements were made at  $90^\circ$  to the source assembly axis. The beryllium oxide was poisoned by placing two 0.005 in. thick sheets of 1% by weight boron loading stainless steel between 0.42 in. thick layers of BeO. This poisoning represented about 1.2 barns/Be atom. The homogeneous atom concentrations are given in Table 7.1. An axial flux plot was taken with cadmium covered indium foils to provide a basis for the source distribution, and is shown in Fig. 7.2. This figure shows that the local buckling is less negative at

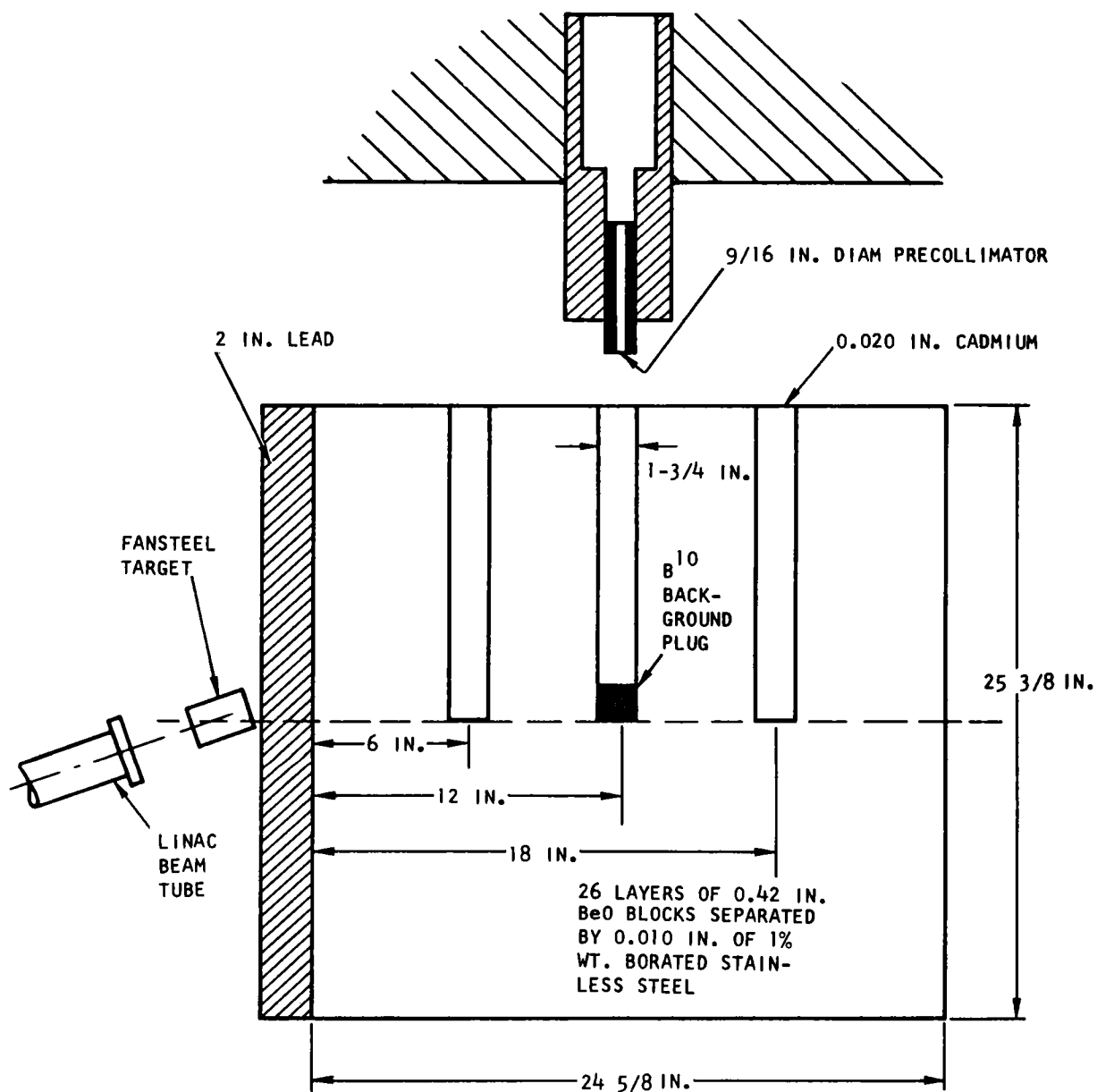


Fig. 7.1 -- Geometrical arrangement used for BeO spectral measurements

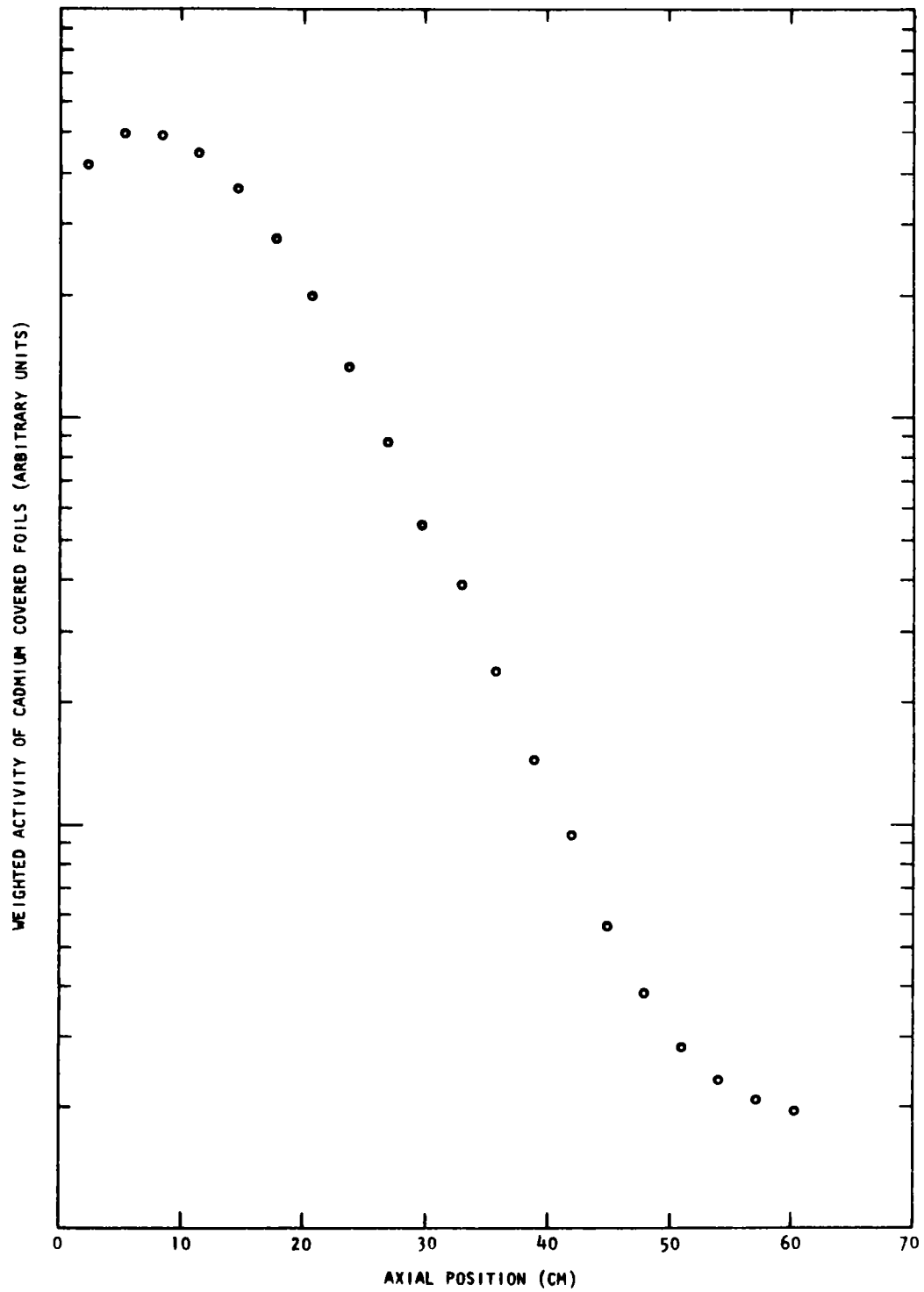


Fig. 7.2 -- Relative intensity of the indium resonance neutron flux measured in the BeO assembly

Table 7.1  
 ATOM CONCENTRATIONS IN POISONED BeO STUDIES  
 (atom/barn-cm units)

Atom	Concentration
BeO . . . . .	0.06708
B. . . . .	$8.508 \times 10^{-5}$
Cr . . . . .	$3.589 \times 10^{-4}$
Fe . . . . .	$1.2196 \times 10^{-3}$
Ni . . . . .	$2.339 \times 10^{-4}$

the 6 inch measurement position so that the neutron spectrum there should be harder than those at the 12 inch and 18 inch positions. This deduction was borne out by the measurements shown in Fig. 7.3. The calculated curves show good agreement with the measured fluxes at the 6 inch and 12 inch positions, though obvious discrepancies are to be seen at the 18 inch position. It is believed that these discrepancies are experimental in origin, since there is no obvious reason for expecting significant spectral differences between the 12 inch and 18 inch position, and the other two measurements agree with theory so well. The neutron spectra are presented as flux,  $\phi(E)$ , to illustrate clearly the effects of the Bragg scattering at the low energy giving rise to observable peaks. The Bragg trapping is a spatial effect and can be understood qualitatively as follows. The flux in an infinite homogeneous medium is given by

$$\phi(E) = \frac{S(E)}{\Sigma_a(E)} + \frac{1}{\Sigma_a(E)} \int_0^\infty dE' \Sigma_s(E' \rightarrow E) \phi(E') - \frac{\Sigma_s(E)}{\Sigma_a(E)} \phi(E). \quad (7.2.1)$$

On the right hand side of the equation the scattering kernel  $\Sigma_s(E' \rightarrow E)$  can be divided into an inelastic component and an elastic component, and on integration that elastic component becomes  $\Sigma_s(E) \phi(E) / \Sigma_a(E)$ , which cancels with the last term on the right hand side of the equation. However, the BeO assembly was characterized by a large negative total buckling  $B^2$ , so that in the diffusion theory approximation  $\Sigma_a(E)$  in the equation above is replaced by  $[\Sigma_a(E) + D(E)B^2]$ . Since

$$D(E) \propto \frac{1}{\Sigma_s(E)} \quad (7.2.2)$$

it can be seen that when the neutron wavelength becomes larger than the Bragg cut-off,  $D(E)B^2$  becomes a larger negative term, which means that  $[\Sigma_a(E) + D(E)B^2]$  becomes smaller. This gives rise to a change of neutron intensity at the Bragg cut-off causing the peak observed in the measured

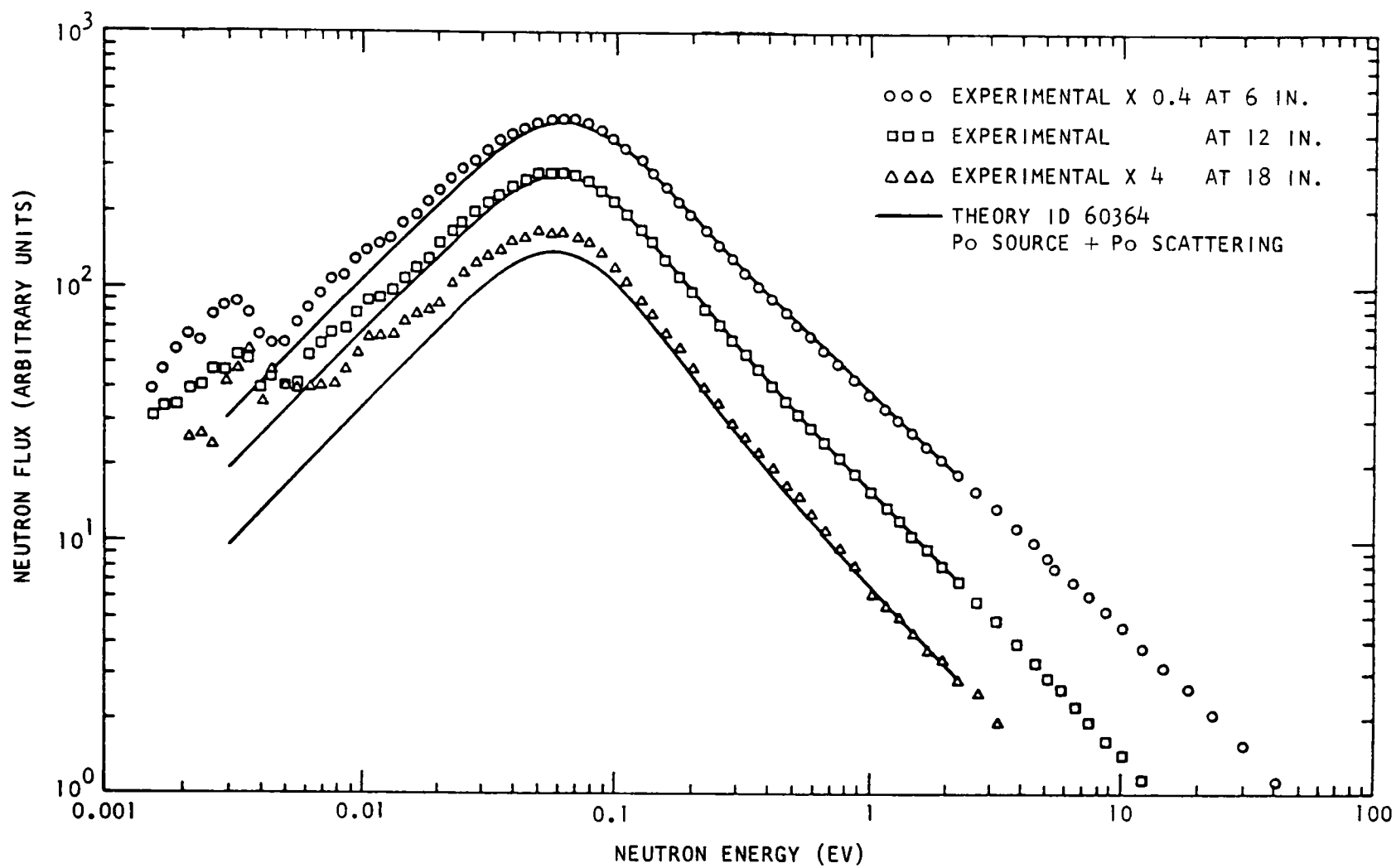


Fig. 7.3 -- Ninety-degree angular spectra in BeO

spectra. The calculated fluxes do not show these low energy peaks because elastic coherent scattering has not been included in the BeO description. This is probably not important as far as reactor calculations are concerned since that portion of the flux spectrum would contribute little to gross reaction rates. Elastic coherent scattering for BeO is, however, discussed in Section 7.3.

The present position on BeO can be summarized by saying that the present scattering kernel, based on a Debye frequency spectrum, will be adequate for calculating neutron flux spectra in the absence of strong flux gradients.

The theoretical fluxes were calculated in the  $P_0$  approximation only due to numerical difficulties encountered in determining anisotropic scattering cross sections. The cause of these difficulties has not yet been discovered though it is believed to rise from some local coarseness of the energy mesh used in the calculation of the kernel, or in the selection of the same arbitrary constants used in the phonon expansion in SUMMIT, (26) (kernel generating code).

### 7.3. COHERENT ELASTIC SCATTERING IN BeO

In the last annual report<sup>(3)</sup> the elastic coherent scattering cross section of beryllium was presented along with a derivation of the results. In addition, a machine program was written to compute this cross section. In the case of BeO, recent experiments undertaken in this program have shown that the elastic coherent cross section would be useful to have since at low energy one sees the effect of coherence in the neutron spectrum. Beryllium oxide has basically the same structure as beryllium (close packed hexagonal), and in the same notation the lattice positions are:

$$\text{Be} \rightarrow (0, 0, 0), \left(\frac{1}{3}, \frac{2}{3}, \frac{1}{2}\right); \quad \text{O} \rightarrow \left(0, 0, \frac{3}{8}\right), \left(\frac{1}{3}, \frac{2}{3}, \frac{7}{8}\right)$$

In this way, one can immediately write down the result for BeO from that for Be:

$$\sigma_{\text{coh}} = \frac{\pi}{2Bk_1^2} \sum_{\tau \leq k_1/\pi} F_{\tau}^2 \frac{M_{\tau}}{\tau} \quad (7.3.1)$$

where  $B$  is the volume of a unit cell ( $3a_c^2/4$ ),  $k_1 = 2\pi/\lambda$ ,  $\tau$  a reciprocal lattice vector and

$$F_{\tau} = \frac{1}{2} (1 + \cos \phi) \left\{ \sigma_{\text{Be}} + \sigma_{\text{O}} + 2\sqrt{\sigma_{\text{Be}}\sigma_{\text{O}}} \cos(3\pi l/4) \right\} e^{-2W} \quad (7.3.2)$$

For  $\phi$  we have

$$\phi = 2\pi \left[ \frac{1}{3} (h + 2k) + \frac{1}{2} \ell \right] \quad (7.3.3.)$$

as in beryllium.  $\sigma_{\text{Be}}$  and  $\sigma_{\text{O}}$  are the bound coherent scattering cross-sections for beryllium and oxygen respectively. The lattice constants are  $a = 2.695 \text{ \AA}$ ,  $c = 4.39 \text{ \AA}$ . The Debye-Waller factor is calculated using an average mass of 12.5 a. m. u. and the frequency spectrum experimentally obtained by Sinclair,<sup>(38)</sup>

It is clear that Eq. (7.3.1) can be calculated by a simple modification of the machine code for beryllium coherent elastic scattering.



## VIII. EXPERIMENTAL STUDIES ON MULTIPLYING ASSEMBLIES

### 8.1 NEUTRON SPECTRUM MEASUREMENTS

In the studies of multiplying assemblies, measurements were performed on a  $\text{UF}_4$  + paraffin assembly and a re-analysis was made of neutron spectra measured in a U-Al water-moderated assembly.<sup>(3)</sup>

The  $\text{UF}_4$  + paraffin was obtained on loan from the Oak Ridge National Laboratory where the mixture had been studied extensively in criticality experiments by Mihalcz and Neely.<sup>(45)</sup> Two types of experiments were performed on this material. First, it was utilized in a clean geometrical configuration under actual multiplying conditions to measure the quasi-infinite-medium neutron spectrum. Second it provided a multiplying assembly in which the decay constant and subcritical reactivity could be studied by pulsing techniques. This Section covers the neutron spectrum measurements while Section 8.2 describes the results of the reactivity measurements. The atom concentrations for this material are given in table 8.1 for reference.

The neutron spectrum measurements were made using standard neutron time-of-flight techniques at the General Atomic Linac. The machine operating parameters were 28 Mev, 500 ma, 4.5  $\mu$ secs pulse width and 15 pps. The plan view of the geometrical arrangement is illustrated in Fig. 8.1 and shows the assembly surrounded by a biological shield comprising 4 inches of lead. In the geometrical configuration shown here, the assembly had a multiplication factor of about 2. The neutrons travelling towards the  $\text{B}^{10}\text{F}_3$  detectors located at the end of a 50-meter flight path were extracted from the center of the assembly by means of a 1 inch square re-entrant hole. A  $\text{B}^{10}_4\text{C}$  plug was used to subtract the time dependent background.

The  $\text{UF}_4$  + paraffin mixture had a poison concentration of 4.6 barns/hydrogen atom at 0.025 eV neutron energy. The neutron spectrum was calculated using a bound hydrogen scattering kernel for polyethylene. The scattering kernel for polyethylene was expected to be almost identical to that for paraffin due to the similarity in chemical composition of the two materials. The kernel was calculated by Koppel<sup>(2)</sup> to include the more realistic frequency distribution that was based on the data of Wunderlich.<sup>(3)</sup> This was the first of the two approaches discussed in Section 4.2.2. The agreement between the calculated and measured neutron spectra seem to indicate that the SUMMIT scattering kernel for polyethylene is adequate

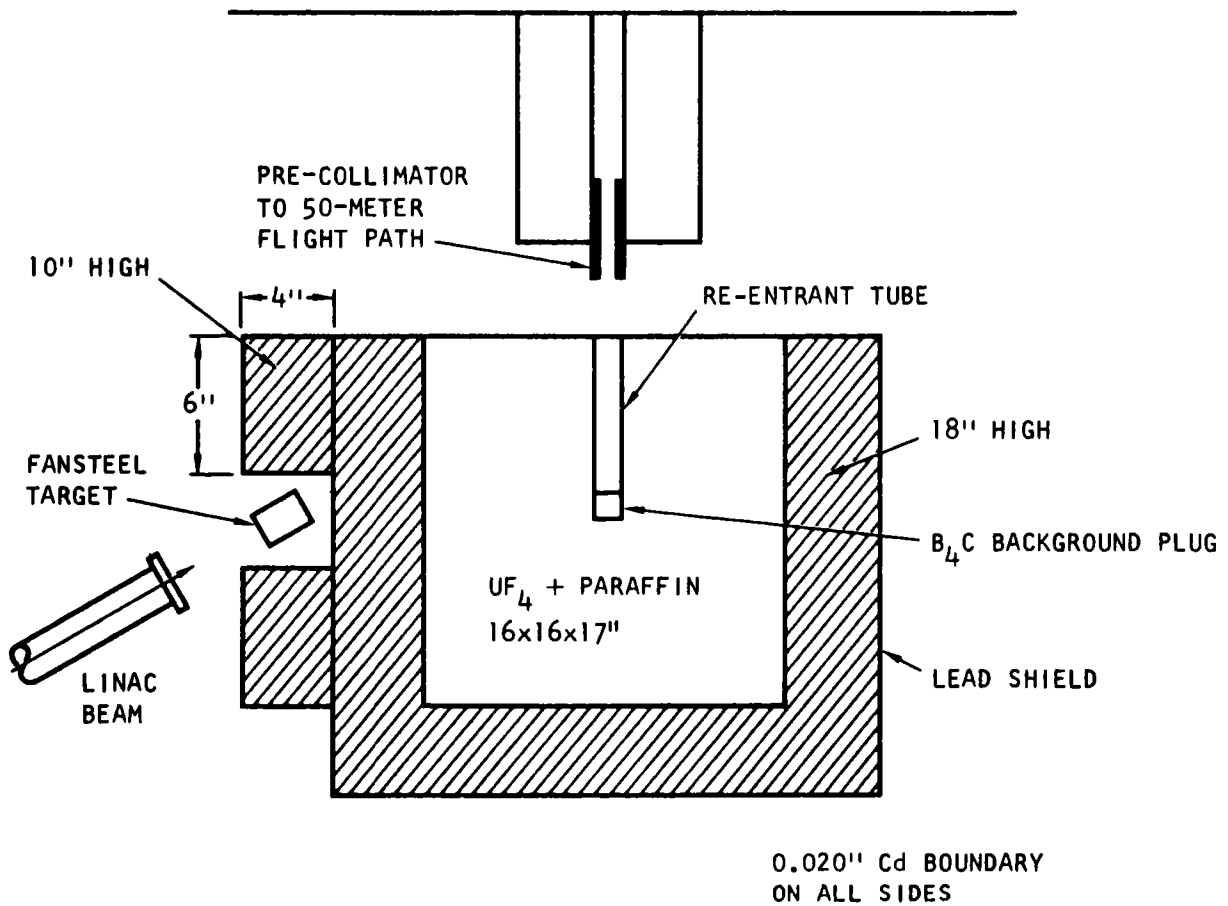


Fig. 8.1 -- Geometrical arrangement for spectral measurements in a UF<sub>4</sub> + paraffin mixture

Table 8. 1  
 ATOM CONCENTRATIONS IN  $\text{UF}_4$  +  
 PARAFFIN MIXTURE (atoms/barn-cm units)

Material	Concentration
U <sup>238</sup>	$7.789 \times 10^{-3}$
U <sup>235</sup>	$1.611 \times 10^{-4}$
H	0.0315
C	0.01519
F	0.03179

for reproducing the characteristics of the neutron spectrum in the  $\text{UF}_4$  + paraffin mixture.

It was noted in this measurement that the neutron spectrum deviated drastically from the calculated behavior for energies less than 0.025 eV. It was determined that a background of delayed neutrons, present at the 50-meter detector station, was not properly subtracted. To subtract this background, a small fission counter was placed at the base of the re-entrant tube and the complete time behavior of the neutron density was measured. The result of this measurement is shown in Fig. 8.2. The area under the curve between 0 and 1.5 milliseconds represents the number of prompt plus delayed neutrons, for each accelerator pulse in the assembly, while the flat portion of the curve represents the corresponding number of delayed neutrons.

Let

$$C(t) = \psi'(t) + N_d,$$

where  $C(t)$  is the observed time spectrum at 50 meters and  $\psi(t)$  is the desired prompt portion of the neutron spectrum.  $N_d$  is the delayed neutron background, which is assumed constant and is in equilibrium over the short time interval observed. Then

$$\int_0^{1/R} C(t) dt = P + D$$

is the total number of prompt (P) plus delayed (D) neutrons at the 50-meter detector emitted from the base of the re-entrant tube. R is the pulse rate.

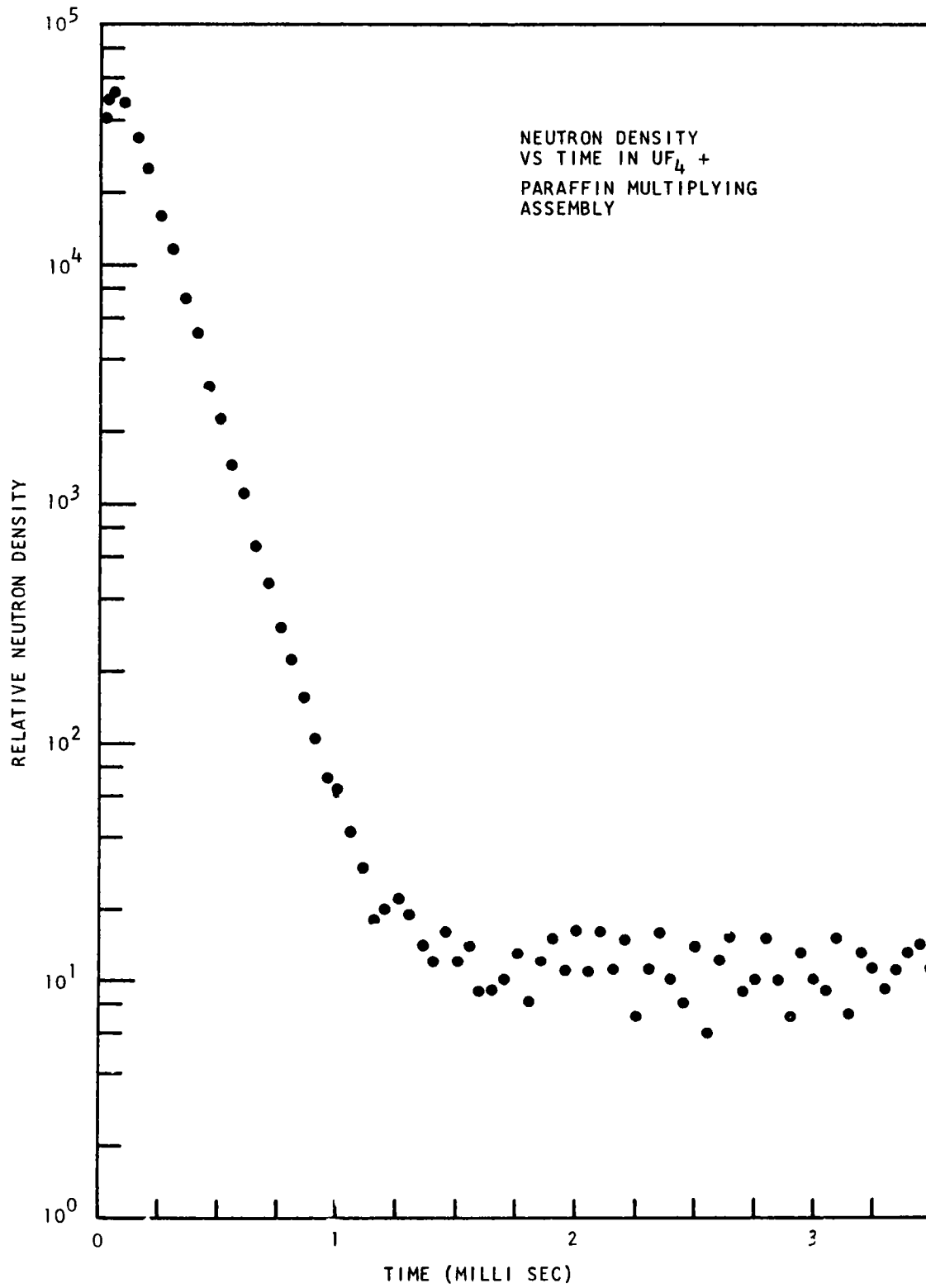


Fig. 8.2 -- Decay characteristic of the  $\text{UF}_4$  + paraffin multiplying assembly

Therefore

$$D = \frac{A}{1+A} \int_0^{1/R} C(t) dt,$$

where  $A = D/P$ , since the delayed-neutron background,  $N_d$ , is a constant over the time interval  $1/R$  and is given by

$$N_d = \frac{RA}{1+A} \int_0^{1/R} C(t) dt.$$

The complete time behavior of the neutron density measured at the base of the re-entrant tube may be used to determine the value of  $A$ . At the base of the re-entrant tube  $A = D'/P'$ , where the number of prompt neutrons

$$P' = \int_0^{1/R} N_p(t) dt;$$

$N_p(t)$  is the observed count per unit time minus the average delayed neutron height, and  $D'$  is just the average delayed neutron height times  $1/R$ .

This method for correcting the spectrum was based on the assumption that the delayed neutrons have the same spectrum as the prompt neutrons. This, of course, is true the nearer the assembly is to critical. From the success of the correction made to this spectrum, it would seem that the assumption is quite good also, for assemblies fairly subcritical. Figure 8.3 shows the results of the measured spectrum before and after the delayed neutron background was subtracted in comparison with calculated spectra using the bound hydrogen and the free gas model.

From the success of the delayed neutron background correction made to this spectrum, it would seem that the method is adequate for removing the delayed neutron background present in spectra measured in multiplying assemblies where time-of-flight techniques are utilized. This same correction was applied to other spectra measured previously<sup>(3)</sup> at General Atomic in multiplying assemblies with equally satisfactory results. These measurements were made in 1962 on a subcritical multiplying assembly composed of uranium-aluminum plates in water. A complete description of this assembly is given in references 3 and 46. The improved analysis of the data was made by using a more accurate mean-emission-time correction and by removing the background arising from delayed neutrons. The agreement between theory and experiment has been im-

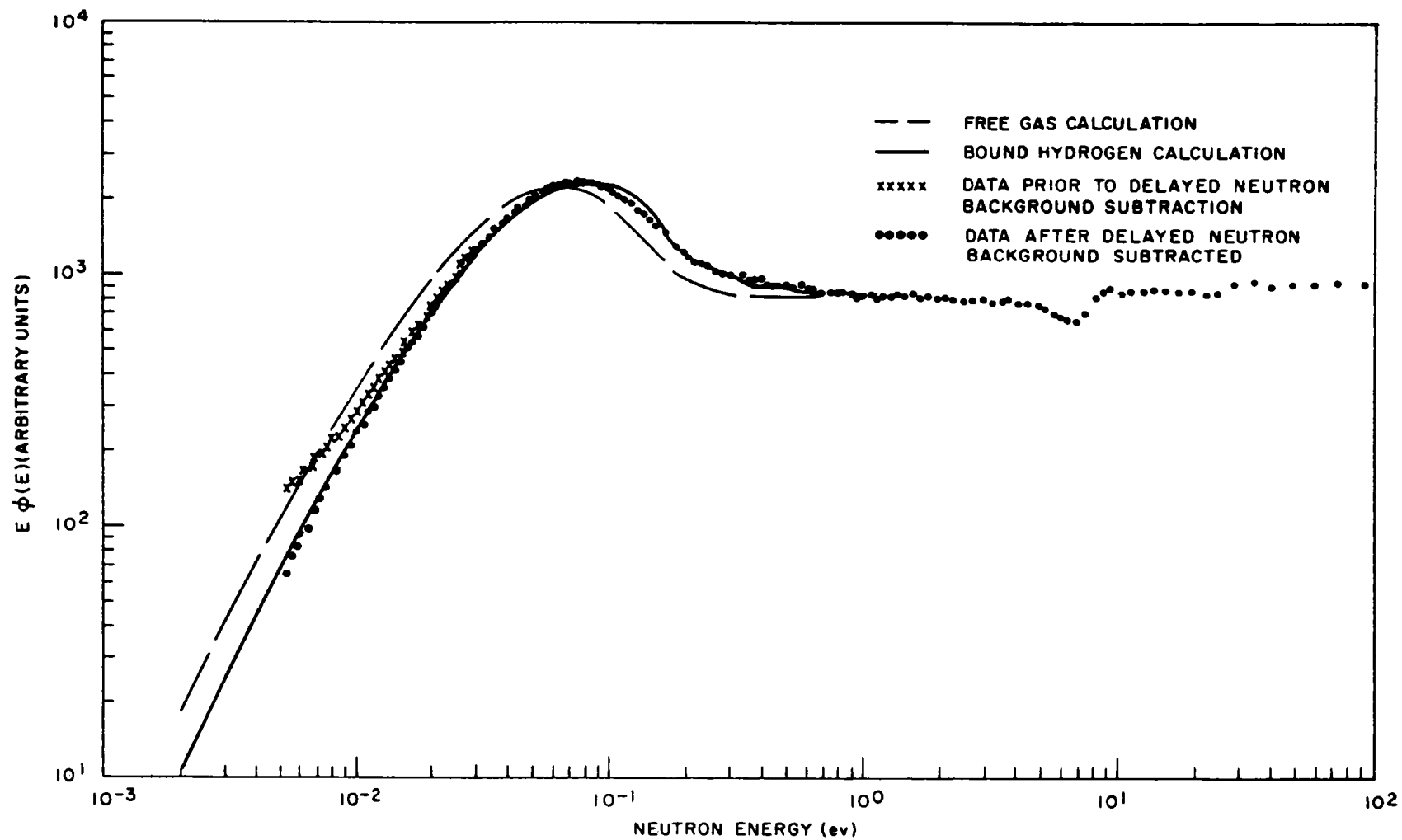


Fig. 8.3 -- Quasi-infinite medium spectrum in a  $\text{UF}_4$  + paraffin mixture

proved for both the angular flux measurements illustrated in Fig. 8.4 and the scalar flux measurements illustrated in Fig. 8.5. The surface leakage measurement, which disagreed considerably with the calculations, is not shown, since the inaccuracy of the measurement is believed to arise from a positional error.

## 8.2 PULSED REACTIVITY MEASUREMENTS

In reference (47) it was shown that for a one-group, homogeneous reactor, the delayed "background" in a pulsed neutron source measurement is related to the prompt component of the flux by:

$$\bar{\phi}_d = \int_0^{1/R} \phi_p \left[ \exp \left( \frac{\kappa\beta}{\ell} t \right) - 1 \right] dt \quad (8.2.1)$$

where

$\bar{\phi}_d$  = average value of the delayed neutron flux

$\phi_p$  = time dependent prompt neutron flux

$R$  = pulse repetition rate

$t$  = time

$\kappa\beta/\ell$  = constant of the system

It appeared that the relationship might apply to actual reactors and hence provide an experimental method for determining  $\kappa\beta/\ell$ . The potential advantage of the method is that it would not be sensitive to the existence of higher, source excited, neutron time modes (3, 48, 49) in contrast with a similar method of Sjöstrand.<sup>(50)</sup>

The measurements reported in references 3 and 49 were obtained in a simple, bare (unreflected) water moderated reactor. It was then desirable to extend the measurements to a relatively simple reflected system. To this end, an assembly of blocks of a homogeneous mixture of  $\text{UF}_4$  and paraffin which had been used for spectrum measurements (Section 8.1) was utilized in a short study of the effect of a reflector on the pulsed neutron determination of reactivity by the  $\kappa\beta/\ell$  technique.

The data obtained demonstrate that equation (8.2.1) is not valid for a reflected reactor that is very subcritical. This conclusion is the

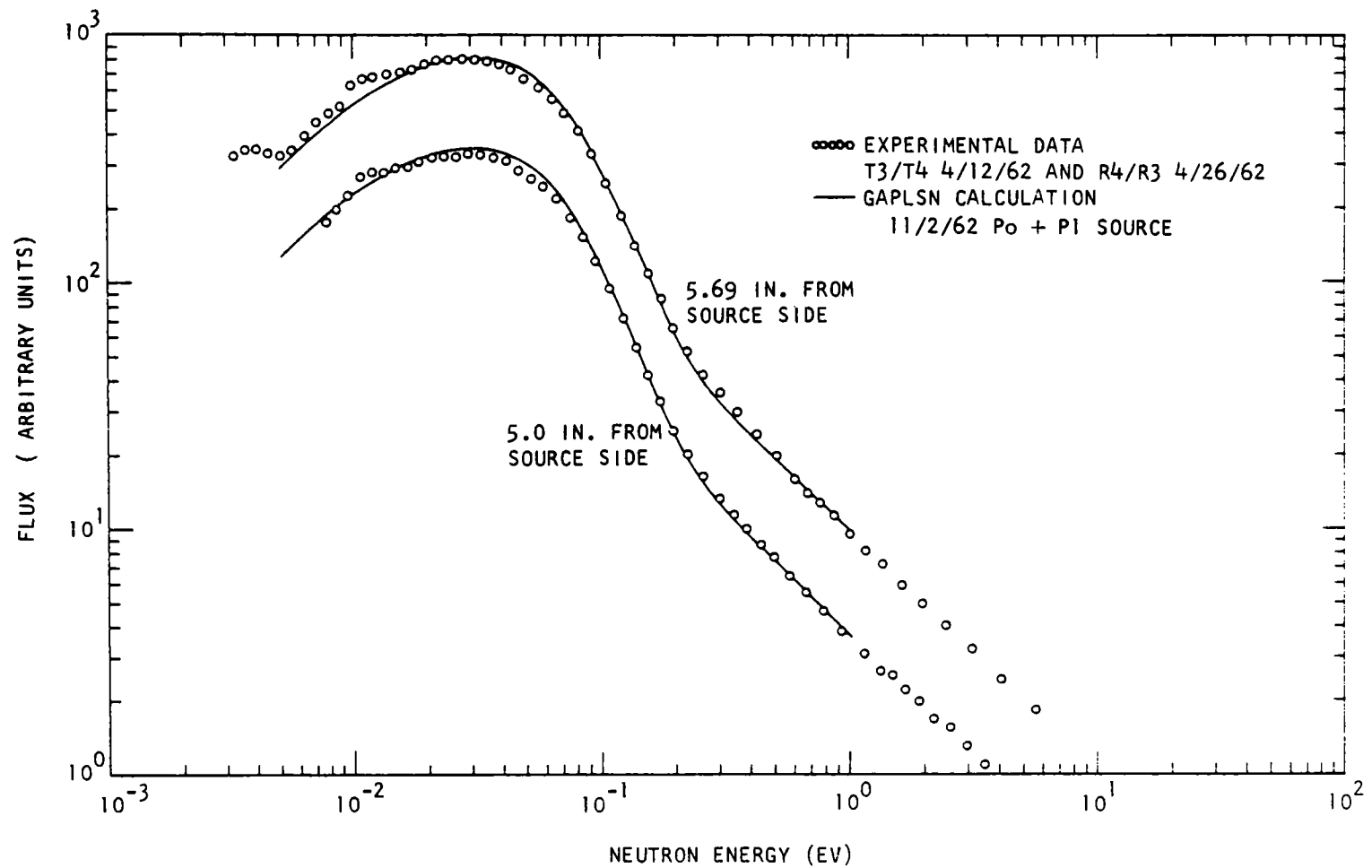


Fig. 8.4 -- Zero degree angular neutron spectra in a water moderated multiplying assembly



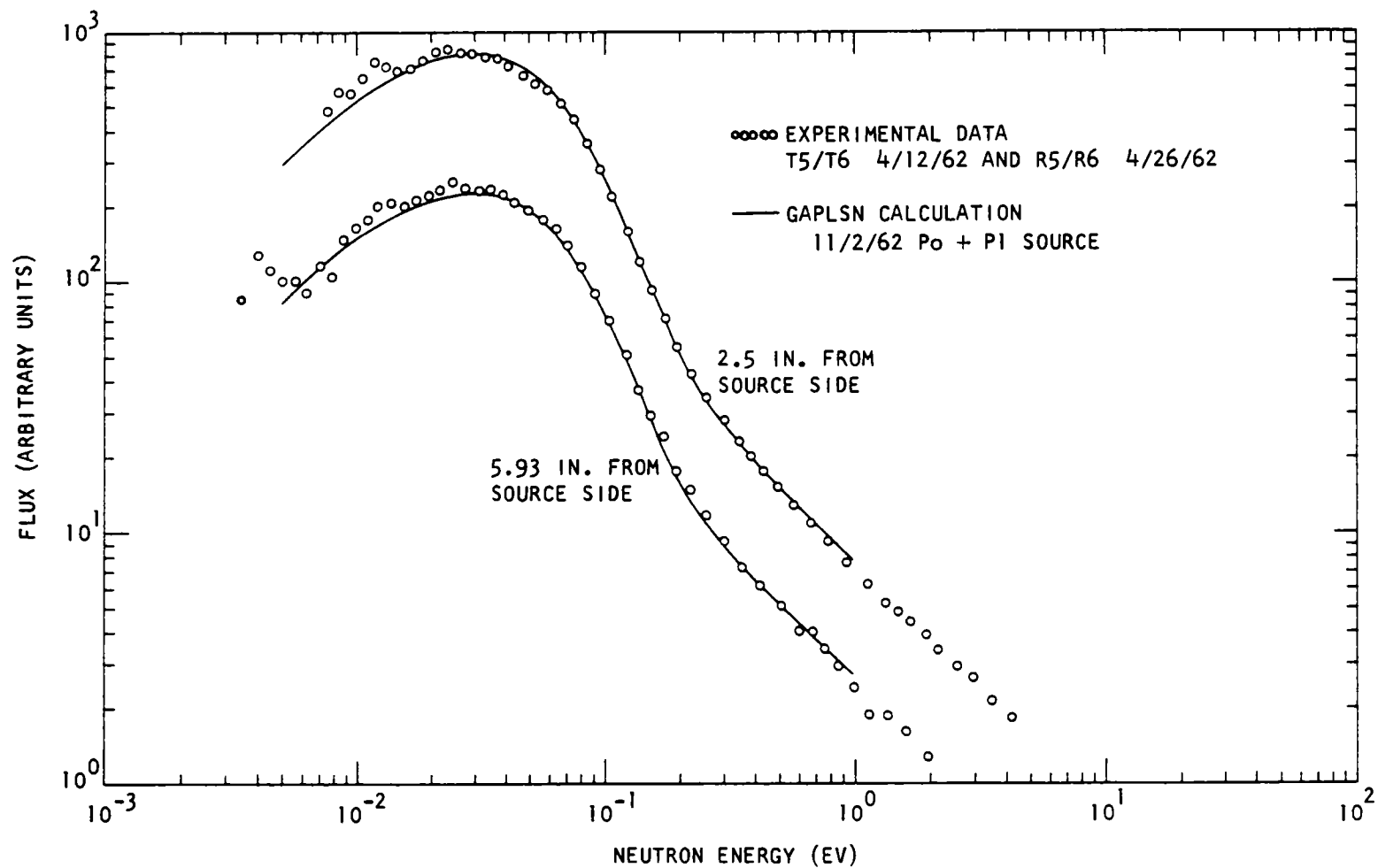


Fig. 8.5 -- Scalar neutron spectra in a water moderated multiplying assembly

result of the fact that the  $\kappa\beta/\ell$  determined from equation (8.2.1) and data taken with the detector in the core differ drastically from that determined by data taken in the reflector. The method is probably still useful for reflected systems not so subcritical as this extreme case, and also appears valid for bare systems. A theoretical analysis of pulsed - multiplying systems has been made in connection with these experiments and is reported in reference (51). It indicates that even in this extreme case, a reasonable reactivity can be defined in principle.

The amount of  $\text{UF}_4$  and paraffin mixture available for these experiments permitted the building of a bare assembly 16 in. by 16 in. by 17 in. high. In the bare condition, the reactivity is approximately  $\$39$  subcritical.(52) To investigate the effect of a reflector on this method of analyzing the experimental data, experiments were carried out on the  $\text{UF}_4$ -paraffin assembly with a reflector on one side. The reflector was either a 4 in. thick paraffin slab or a 4 in. thick water solution of 10.8 g/liter of  $\text{H}_3\text{BO}_3$ . The entire assembly was cadmium covered. Placing the reflector on one side only was expected to provide an extreme case for checking the method of Garelis and Russell.(47)

A small 0.25 in. diameter  $\text{U}^{235}$  fission counter was placed in various positions in the core and reflector to measure the time distribution of neutrons following repetitive pulsing of the assembly by the electron linear accelerator (LINAC). The source location was also changed for several measurements. In one measurement, a cadmium-covered  $\text{U}^{238}$  fission counter was used for comparison with the  $\text{U}^{235}$  counter and was found to give the same result.

In the first measurements in the core and in the reflector it was observed that at a pulse repetition rate of 60 pps, the fundamental mode decay had not been attained by the time the delayed neutron "background" had been reached. As a result it appeared that the  $\alpha$  was different in the core from that in the reflector. Once the fundamental-mode decay is established, all parts of the assembly will have the same  $\alpha$ .

To demonstrate that a fundamental-mode decay did exist, the assembly was pulsed at very low repetition rates of 0.84 and 0.43 pps. The full source intensity of the Linac, approximately  $10^{12}$  neutrons per pulse, was used, with a long delay ( $\sim 800 \mu\text{sec}$ ) prior to the start of the multichannel time analyzer. Because of the large source strength it was possible to get reasonable counting rates at these long times after the pulse. Figures 8.6 and 8.7 show the combined results of the measurements at 60 pps, 0.84 pps, and 0.43 pps with the delayed neutron background subtracted. The positions of measurements and source location are shown in Fig. 8.8. The measurement positions are along a line through the core center and reflector center.

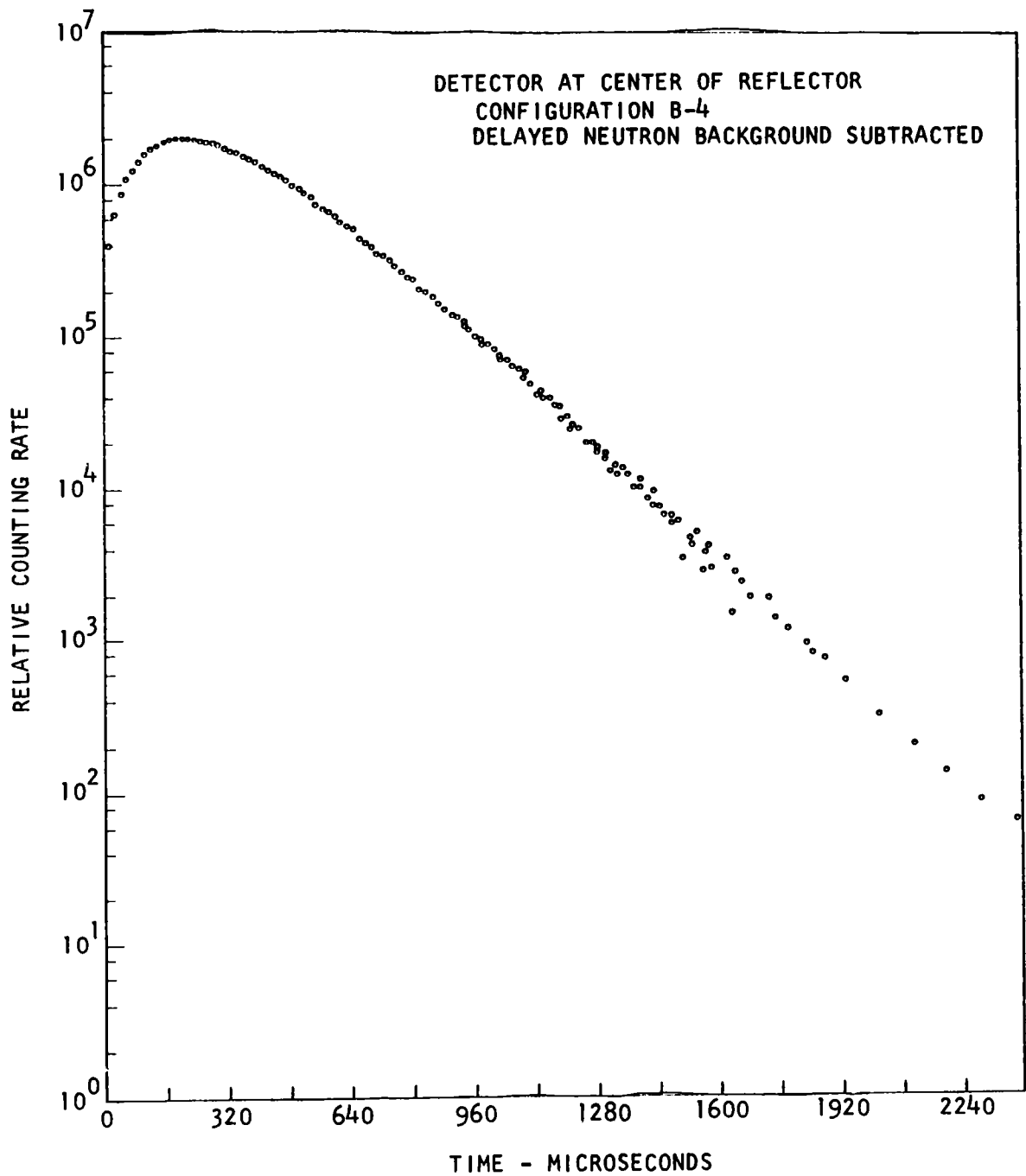


Fig. 8.6 -- Decay characteristic of  $\text{UF}_4$  + paraffin in configuration B-4

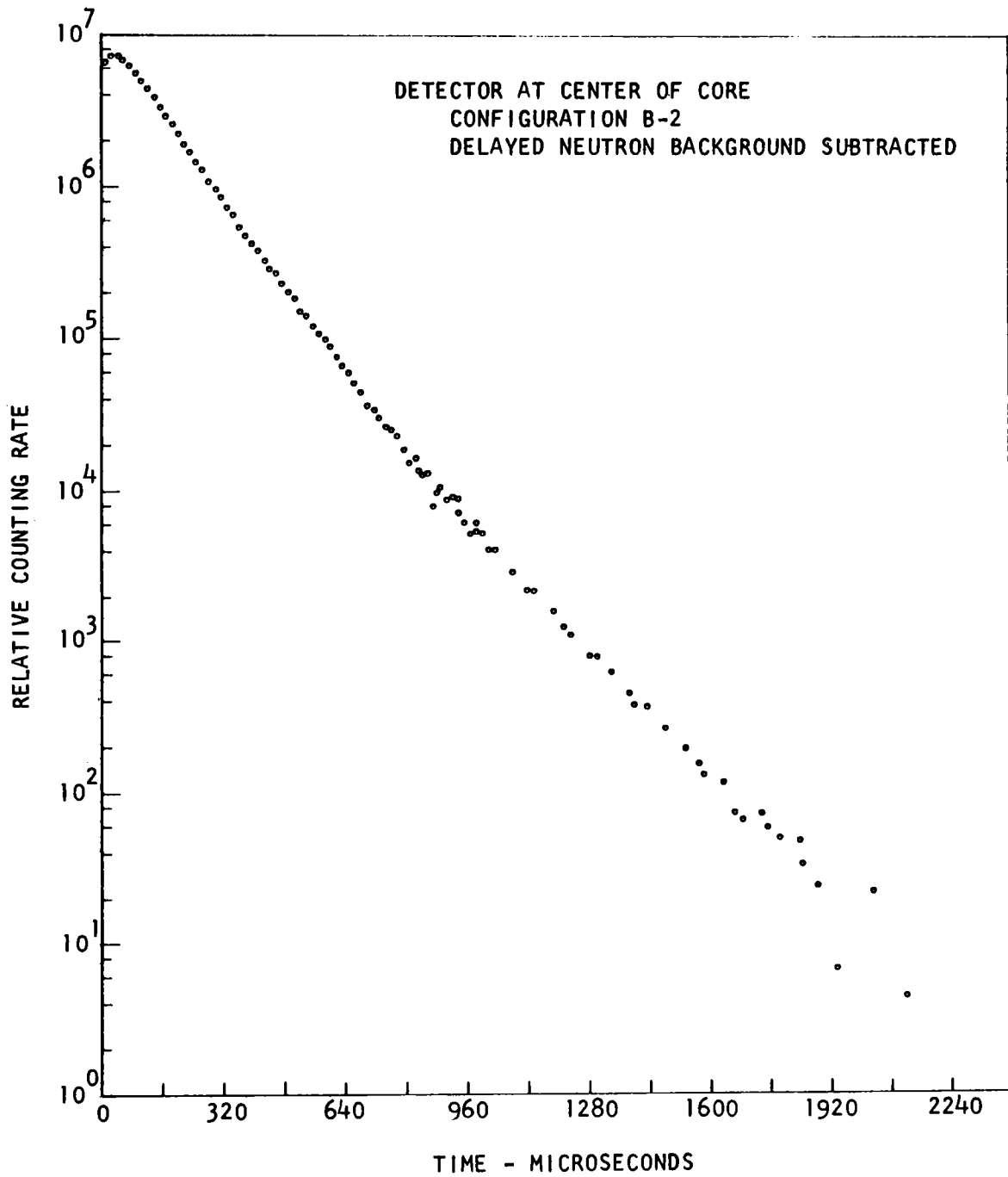


Fig. 8.7 -- Decay characteristic of  $\text{UF}_4$  + paraffin in configuration B-2

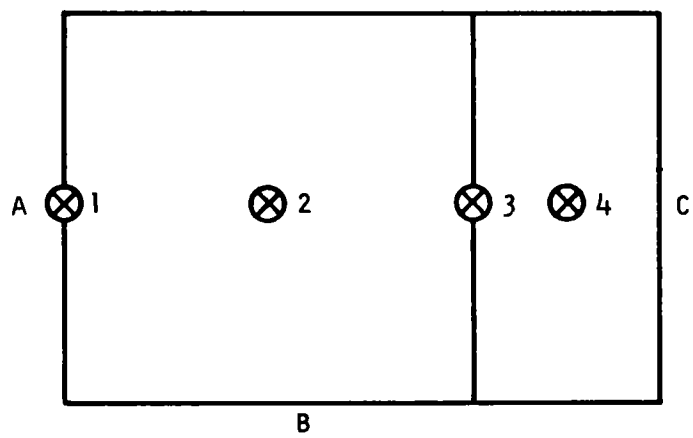


Fig. 8.8 -- Schematic diagram showing locations of source and detector  
(for use with Table 8.2)

It can be seen in Figs. 8.6 and 8.7 that for this extreme case, time modes close in magnitude to the fundamental exist and that the fundamental is just beginning to be observed at very long times after the pulse. One effect which is observed from these measurements at long times after the pulse is that this can be carried only so far in time, since room return begins to be observed. From Figs. 8.6 and 8.7 the  $\alpha$  determined from times beyond 1300  $\mu$ sec is 163  $\text{sec}^{-1}$  in the core and 183  $\text{sec}^{-1}$  in the reflector, indicating that they have probably not yet quite reached the fundamental mode. Within the uncertainties in these measurements, a value of  $170 \pm 10 \text{ sec}^{-1}$  probably represents the fundamental-mode  $\alpha$ , since both core and reflector seem to be approaching this value from opposite directions.

Table 8.2 gives the results obtained for each of the positions measured. The  $k\beta/\ell$  is obtained from the integration of the data according to the Garelis - Russell expression as given in Eq. (8.2.1). All these measurements were made with a pulse repetition rate of 60 pps except for those of the  $\text{U}^{238}$  counter, which was run at 30 pps. The results of Table 8.2 are shown schematically in Fig. 8.9.

It can be seen that the  $k\beta/\ell$  determined for this core depends upon position thus is not a constant for the system and as such is meaningless for this extreme case. This is a result of the interplay between several time modes, one associated with the core, one with the reflector, one with the combination of the two, and perhaps others. These different time modes do not differ greatly in the present situation, so the effect of each is observed at relatively long times.

More analysis along the lines of trying to separate these time modes and associate a  $k\beta/\ell$  with each is indicated. Some preliminary hand unfolding of some of these data for the paraffin reflector case indicates that a large part of the observed neutron flux versus time behavior may be made up of various magnitudes (positive and negative) of the following approximate time decay modes: 170, 130, 110 and 20  $\mu$ sec. If it were possible to fit the experimental data with a sum of exponentials (by a machine code), it would in principle be possible (using the Garelis - Russell integral) to assign a  $k\beta/\ell$  to each of the time modes and, if there were as many positions of measurements as there were individual time modes, to obtain the  $k\beta/\ell$  for each mode in the following way:

$$(\bar{N}_D)_x = R \sum_{i=1}^m \frac{Q_i}{\alpha_i} C_i \quad (8.2.2)$$

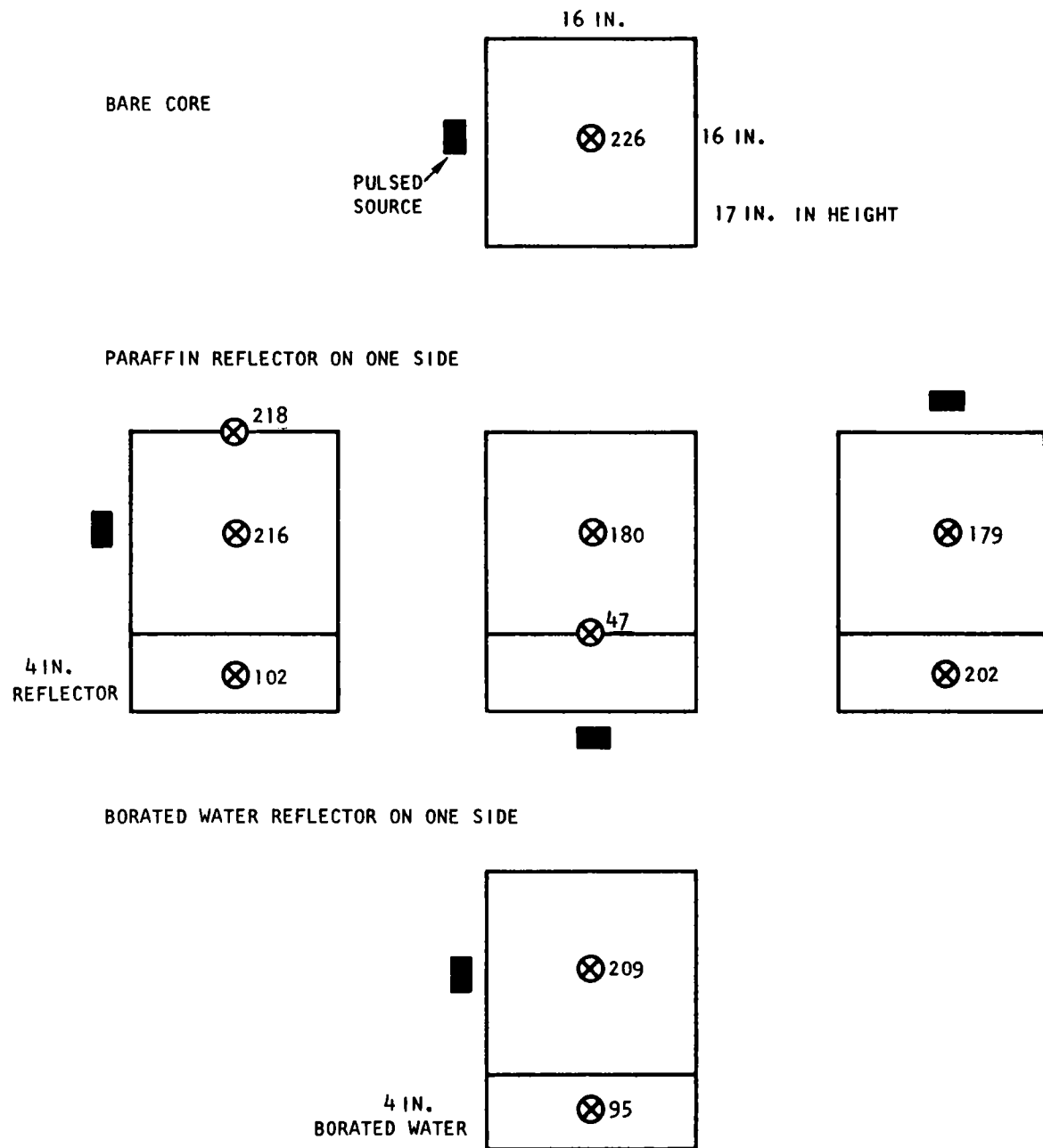


Fig. 8.9 -- Variation of  $k\beta/l$  with measurement configuration

where

$x$  = position of measurement

$i$  = time mode

$m$  = number of modes

$Q_i$  = magnitude of mode  $i$  at  $t = 0$

$\alpha_i$  = reciprocal of dieaway time of mode  $i$  ( $\text{sec}^{-1}$ )

$C_i$  = unknown value of  $k\beta/\ell$  for mode  $i$

$R$  = repetition rate

$\bar{N}_D$  = average delayed neutron flux.

This latter analysis has been attempted by hand without much success owing to the fact that when two decays are not greatly separated in time, the hand method of unfolding is not sufficiently accurate.

Table 8.2

VARIATION OF  $k\beta/\ell$  WITH MEASUREMENT CONFIGURATION

Core Condition	Configuration	$k\beta/\ell$	$\alpha^{-1}$ ( $\mu\text{sec}$ )
Bare Core	A-2	226	110
Paraffin Reflector	A-2	179	---
	A-4	202	---
	B-1	218	---
	B-2	216 (208 <sup>a</sup> )	163
	B-4	102	183
	C-2	180	---
	C-3	47	---
Borated Reflector	B-2	209	117
	B-4	95	---

a\_ Using cadmium-covered  $\text{U}^{238}$  fission counter.



In summary, the result is that the Garelis - Russell method does not work in this extreme case but is probably still useful for reflected reactors not so subcritical and for bare systems.

## IX. FAST NEUTRON STUDIES

### 9.1 FAST NEUTRON PENETRATION THROUGH H<sub>2</sub>O

The fast-neutron penetration of water shields was measured at the General Atomic Linac as a joint project with ORNL. In an earlier report,<sup>(3)</sup> the General Atomic time-of-flight data were reduced and presented as neutron flux,  $\phi(E)$ , versus neutron energy,  $E$ . Subsequently, a GAPLSN transport theory calculation was performed on the water shields; the comparison of the GAPLSN results with experimental data is reported here. The experimental geometry, illustrated in Fig. 9.1, was essentially a large pseudo-spherical source (8 by 8 by 8 in.) at the center of a spherical shell water shield. This geometry was selected by ORNL to approximate the code geometry of NIOBE<sup>(53)</sup> (Numerical Integration of the Boltzmann Equation). A series of experiments was performed in which the thickness of the water shield was varied while the emergent flux was studied at  $0^\circ$  and  $30^\circ$ .

The General Atomic computer code GAPLSN<sup>(14)</sup> is a one-dimensional  $S_n$  transport-theory code which can calculate problems with the following geometries:

1. Spherical shield, central point source
2. Cylindrical shield, axial line source
3. Slab shield, slab source.

In spherical geometry, the forward peaking of the flux is maximized so that it would have been impossible to calculate the problem without weighting the forward direction to obtain more detail. GAPLSN allows no such weighting in spherical geometry (1), but permits it in plane geometry (3). Since the experimental source in Fig. 9.1 was extensive (8 by 8 by 8 in.) compared with the precollimator (2 in. diameter) and the separation of the source and shield was large (40 cms) giving low flux curvature, it was considered that a slab geometry, Fig. 9.2, would approximate the experiment at least for the case of  $0^\circ$  emergent angle. In both geometries, the uncollided flux is dominant, but the peaking is less in the plane geometry allowing the use of regular angular weighting there. The GAPLSN calculation was performed with 64 angular components in equal increments of  $\cos \theta$ , 20 space points and 27 energy groups from 0.13 to 10 MeV using differential cross sections for hydrogen and oxygen. The source spectrum was made identical to the measured target spectrum and was inserted in the first angular increment only ( $\pm 10^\circ$  approximately).

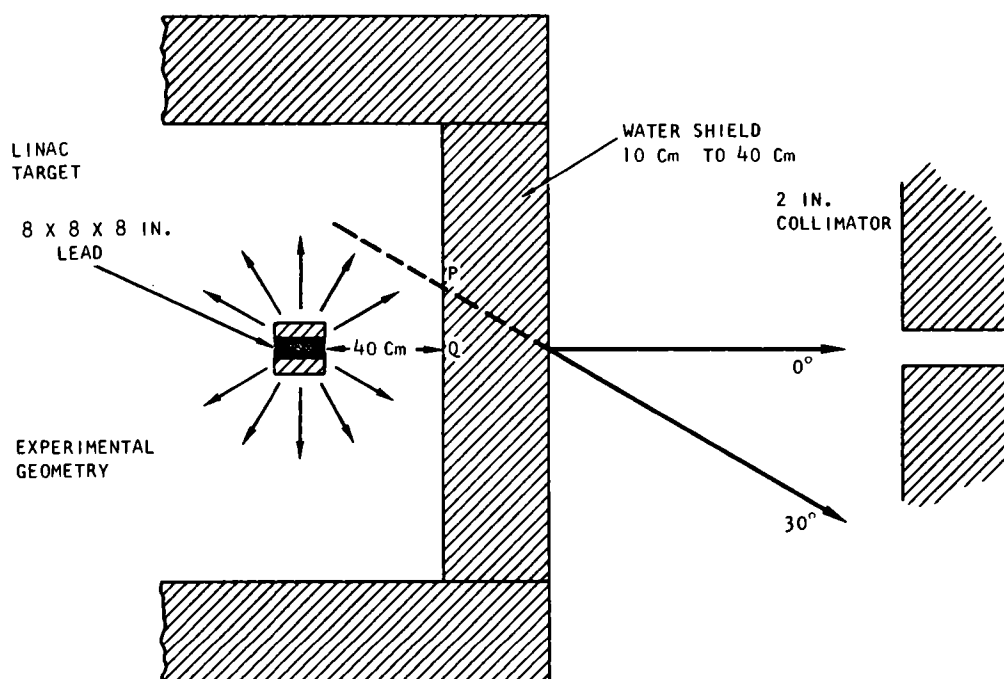


Fig. 9.1 -- Experimental geometry for fast-neutron-penetration studies

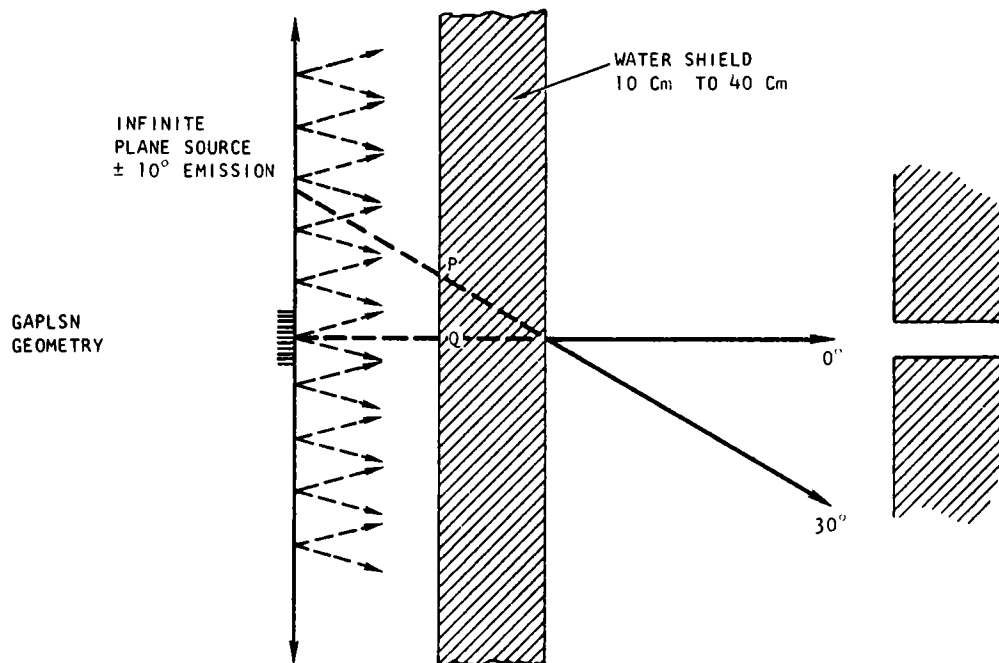


Fig. 9.2 -- Calculational geometry for fast-neutron-penetration studies

The results for the  $0^\circ$  direction are shown in Fig. 9.3 for which there is reasonable similarity between the experimental and the theoretical geometries. Both the absolute magnitudes and the spectral shapes are in better agreement than could have been expected, especially above 2 MeV. Below 2 MeV there are discrepancies which could possibly be attributed to moderation of neutrons from regions outside the "visible" source. Since GAPLSN has an infinite source, it is to be expected that the theoretical values are higher at lower energies.

The calculations also show structure at the large oxygen resonance (3 to 4 MeV) which is not found in the experiment, although the experiment is capable of detecting such structure.

No comparisons are presented at  $30^\circ$  emission angle since the theoretical geometry is incorrect and the calculations do not apply.

## 9.2 FAST NEUTRON PENETRATION THROUGH GRAPHITE

A similar experiment was performed in which the fast neutron penetration through a graphite shield was studied. The pulsed neutron source was placed in front of a 24-inch thick slab of graphite backed up by a 12-inch slab of graphite. Fast neutron spectra through the 24-inch slab was measured at  $0^\circ$  and  $14^\circ$  to the source slab axis as illustrated in Fig. 9.4. The results are shown in Fig. 9.5 together with theoretical values calculated with GAPLSN.

The calculations were again made in slab geometry due to the numerical difficulties in spherical geometry. The angular representation of the flux was made by using 16 increments of  $\cos \theta$  heavily weighted in the forward direction. Eighty-seven space points were used and twenty-one energy groups from the range 0.2 to 14 MeV. The source was inserted as a uniformly distributed isotropic source in the central 0.002 cms of a 123 cm wide slab. Only the  $0^\circ$  flux is meaningful due to the incorrect representation of the geometry. The calculated flux does have the correct order of magnitude though there is little agreement in shape. The scattering resonance at 4 MeV in carbon is seen in the theoretical curve and is hinted at in the data. An attempt was made to determine the  $14^\circ$  flux as follows: The  $0^\circ$  flux was calculated through a slab whose thickness was  $(24/\cos 14^\circ)$  inches. This flux was subtracted from the  $14^\circ$  flux from the 24-inch slab to give the estimate shown in the figure. This estimate does not agree in shape with the measurement, but is reasonable as regards magnitude in the high energy region where scattered neutrons provide less contribution.

The experimental data was poor in that statistics were bad and monitoring by sulfur foils was not completely satisfactory. Unfortunately,

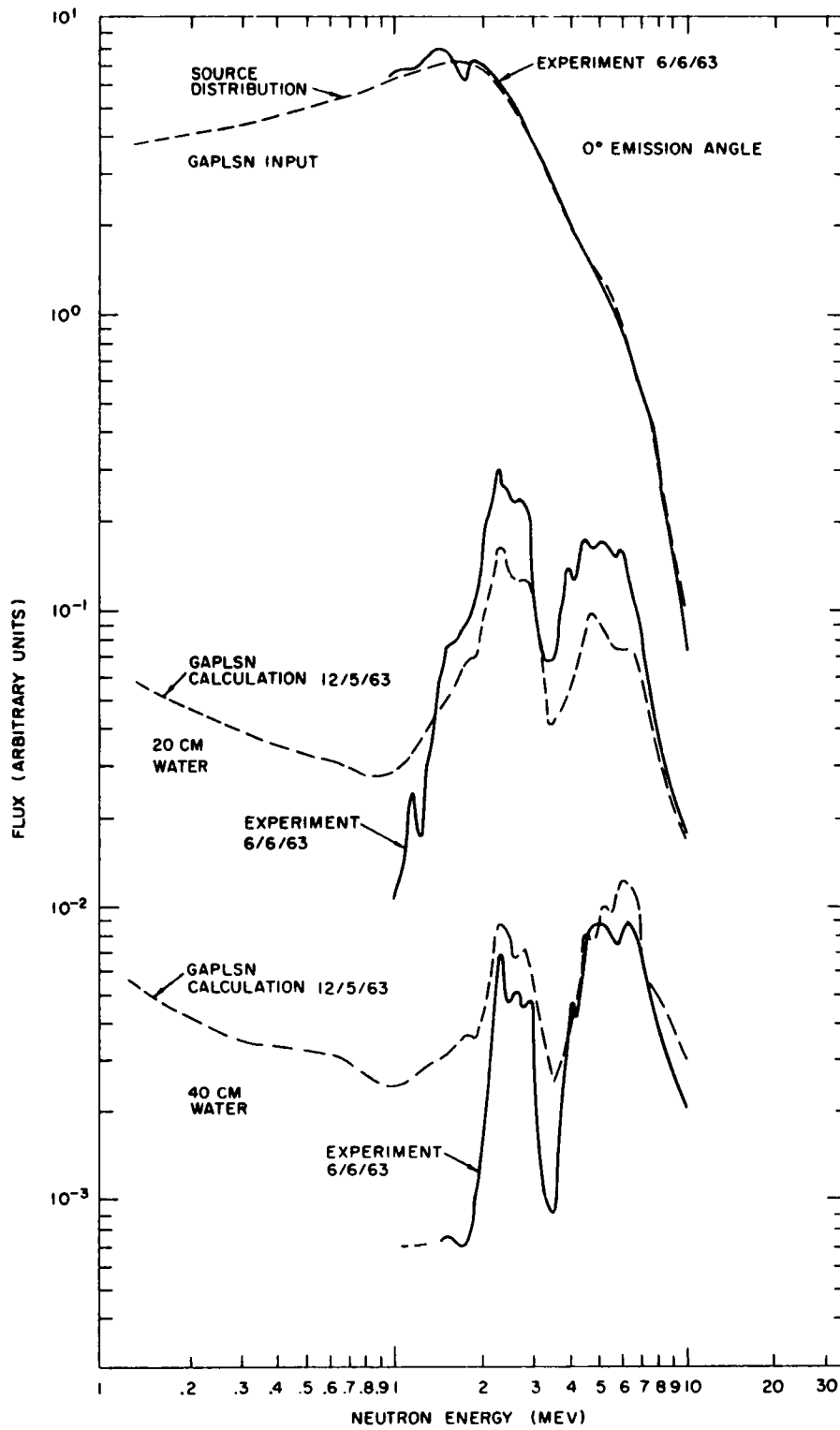


Fig. 9.3 -- Fast-neutron flux at 0° emission angle

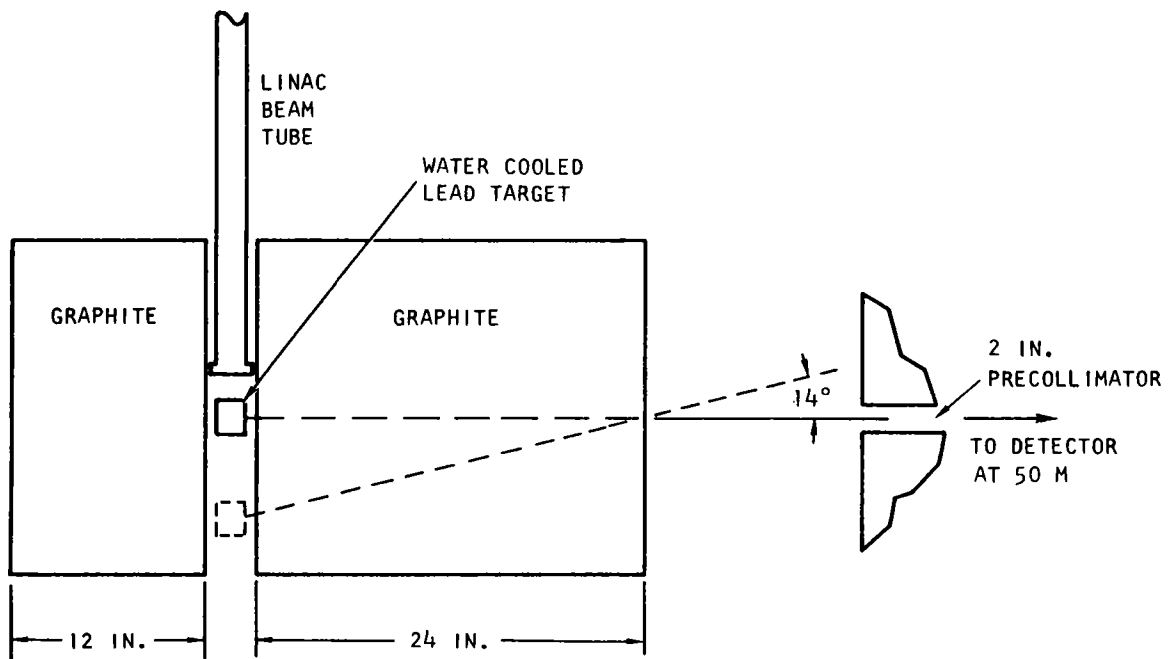


Fig. 9.4 -- Experimental arrangement for fast neutron penetration studies in graphite

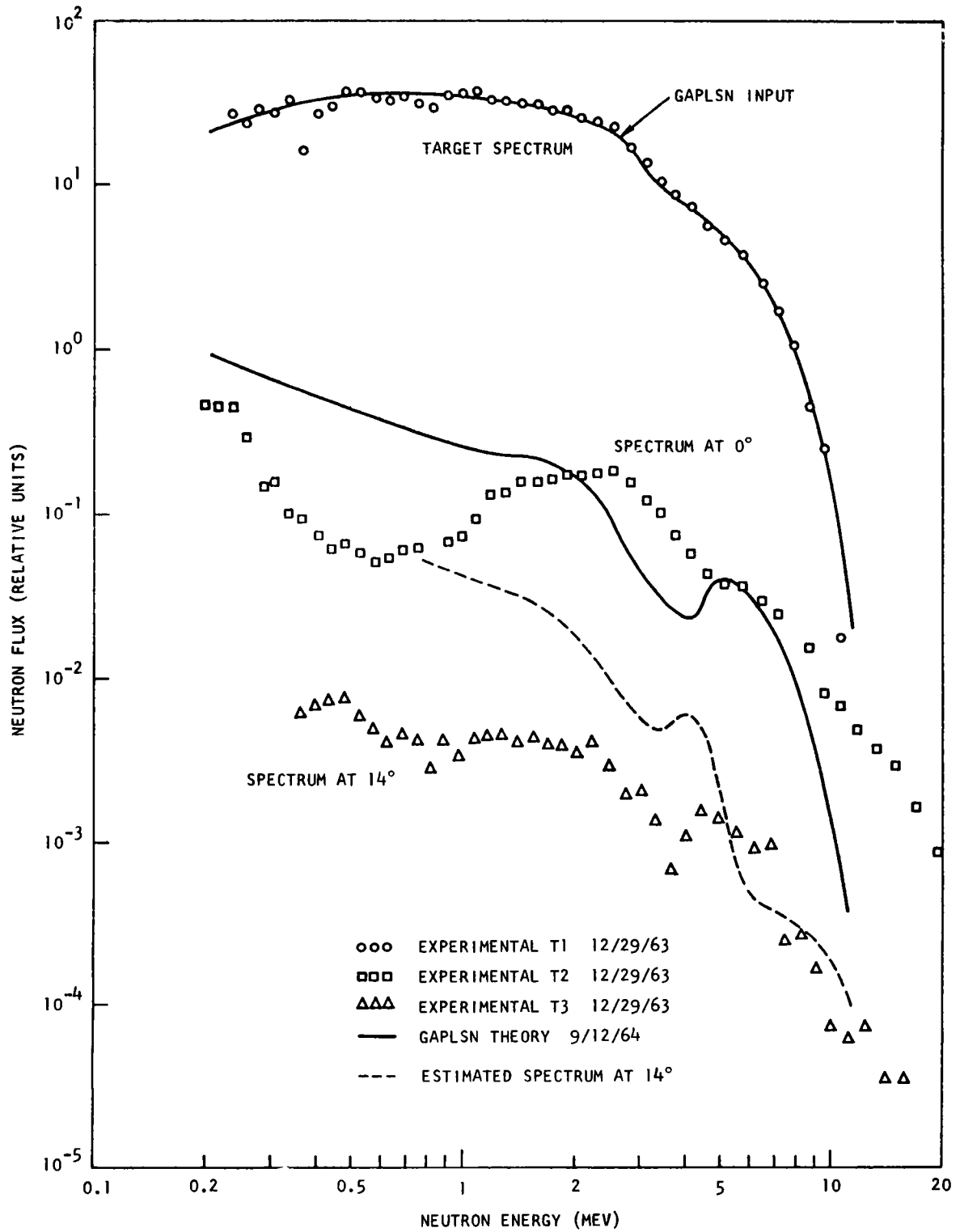


Fig. 9.5 -- Fast neutron spectra through a graphite shield



the calculational methods are not in much better shape. When the flux falls off by a factor of 10 in only  $14^\circ$ , it is obvious that equal increments of  $\cos \theta$  cannot provide an adequate representation. For example, in an  $S_{64}$  calculation, the 63rd angular ray would already be at greater than  $14^\circ$ . The use of Monte Carlo codes in the analysis has been excluded since the experimental data are not good enough to justify such an expensive comparison. This experiment serves to point up the need for improved experimental methods and calculational techniques in the measurement and analysis of fast neutron spectra.

Subsequent to this experiment, an improved pulsed source was constructed of natural uranium designed for use in fast neutron spectra studies. This 3-inch diameter source provides not only an isotropic neutron distribution but also spectra which are independent of emission angle. Its use can be expected to improve substantially the quality of fast spectrum measurements and the correspondence between the experimental and calculation geometries. The source is shown in Fig. 9.6. Its spectrum and angular distribution measured with sulfur and aluminum threshold detectors are given in Figs. 9.7 and 9.8 respectively.

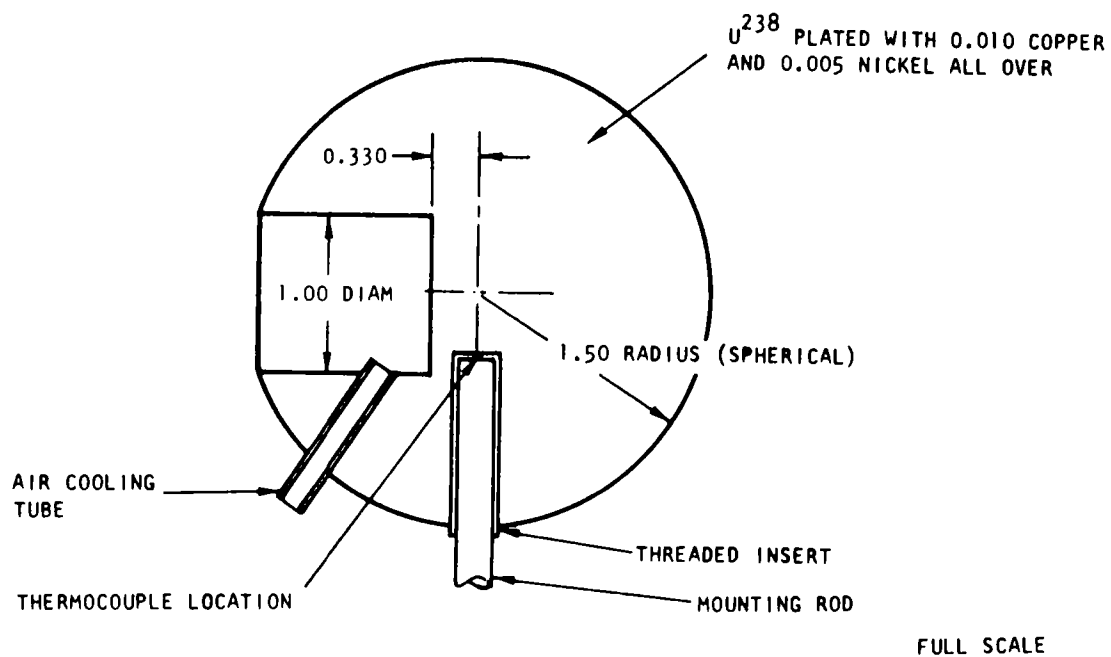


Fig. 9.6 -- Detail of 3 inch diameter uranium sphere, source No. 7

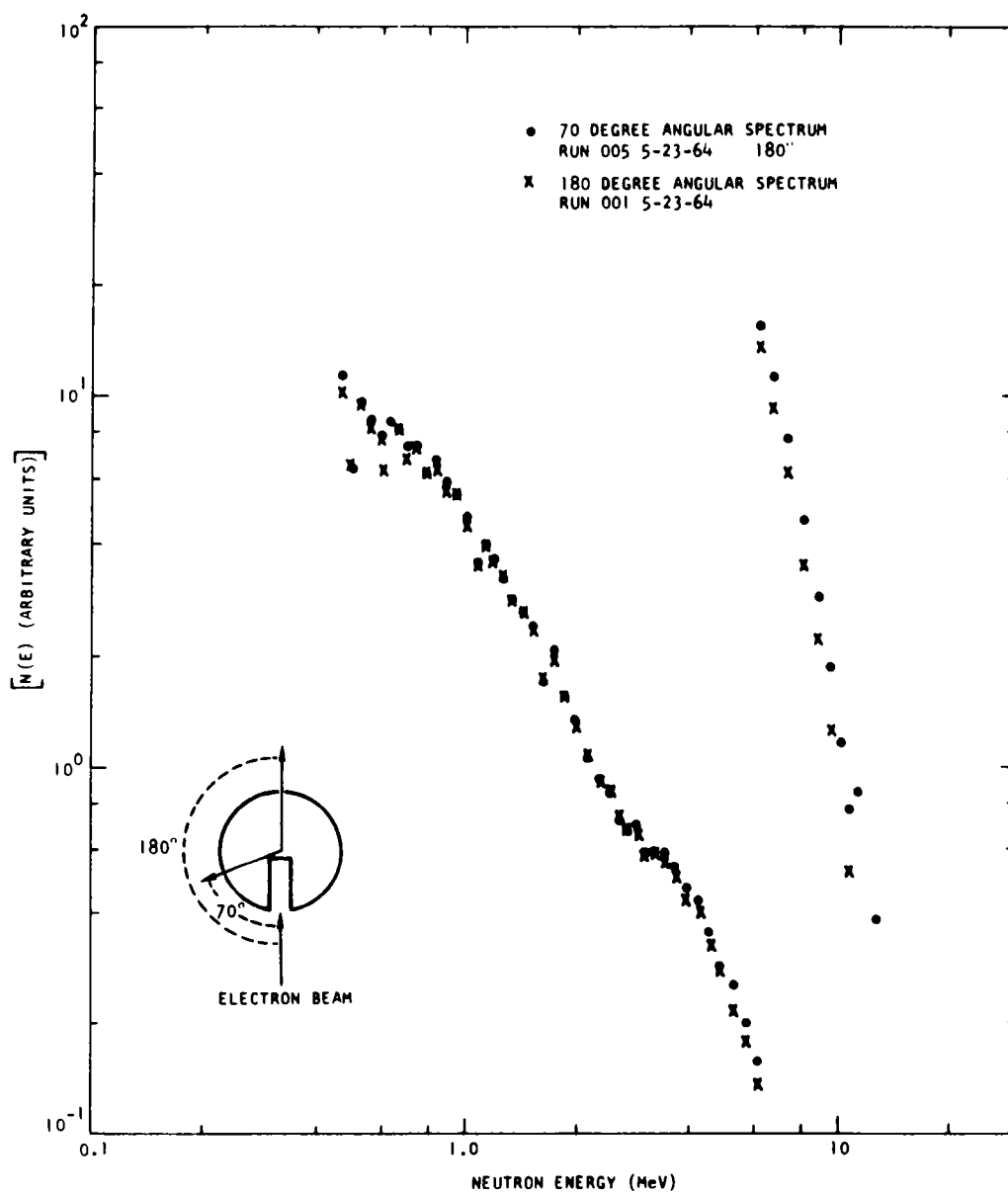


Fig. 9.7 -- Neutron time of flight spectra for source No. 7

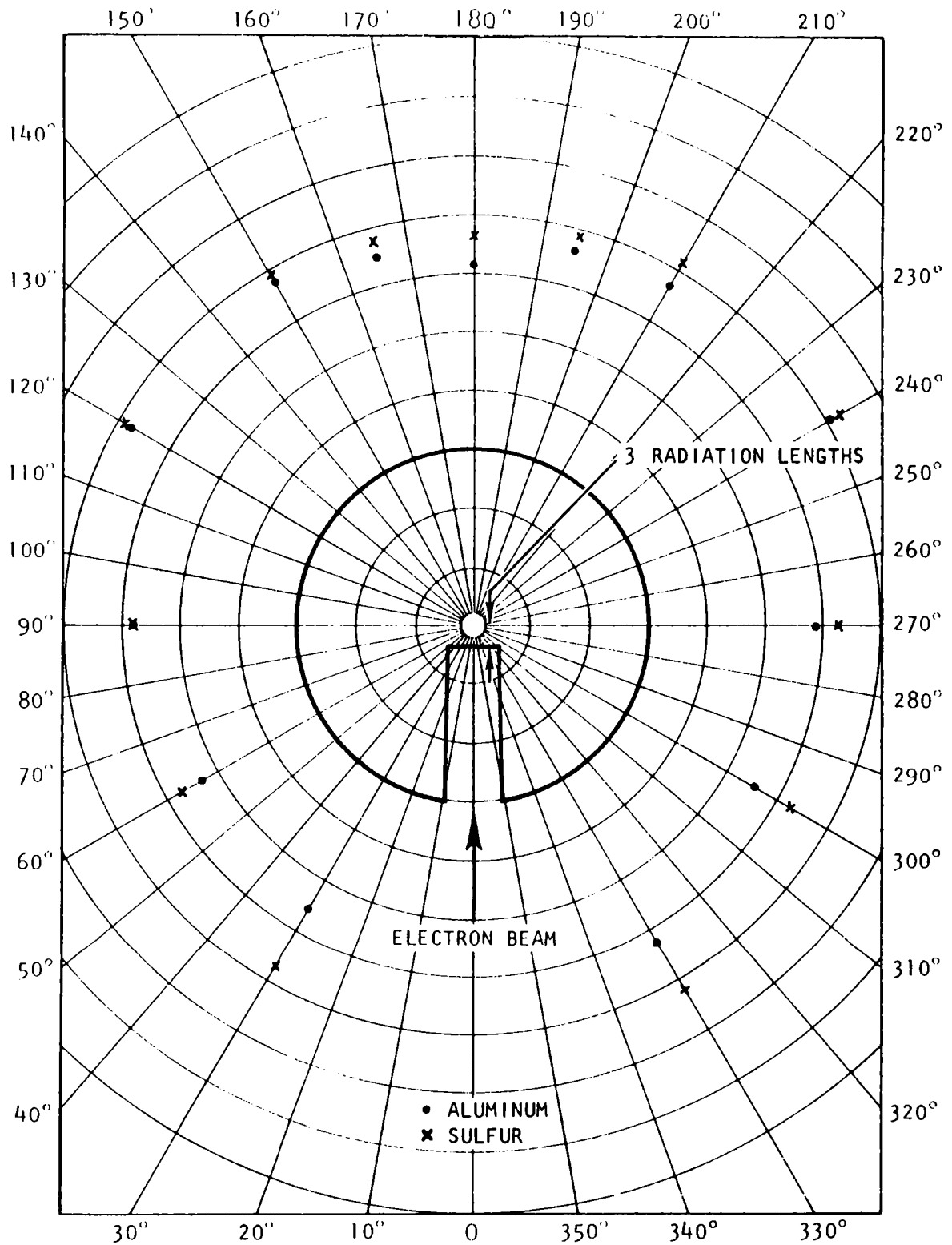


Fig. 9.8 -- Sulfur and aluminum activation data for source No. 7



## X. DIFFERENTIAL SCATTERING STUDIES

### 10.1 INTRODUCTION

During the spring of 1963 we began an investigation to determine the feasibility of measuring differential scattering cross sections for the common moderators. The single differential scattering cross section can be defined in terms of the well known scattering law<sup>(54)</sup>  $S(\vec{\kappa}, \omega)$  as follows:

$$\frac{d\sigma(E)}{d\Omega} = \sigma_0 \int_0^\infty \sqrt{\frac{E'}{E}} S(\vec{\kappa}, \omega) dE' \quad (10.1.1)$$

$4\pi$

where  $\sigma_0$  is the bound atom cross section,  $E'$  and  $E$  are the final and initial neutron energies,  $\omega = (E' - E)/\hbar$  and  $\kappa = p' - p$  are the energy and momentum transfers on a collision. From the definition of the scattering cross section it is clear that the experimental apparatus is expected to provide the cross section integrated over final neutron energies. It is also clear, therefore, that this single differential cross section is less sensitive to the physical details of a scattering model than the double differential cross section, but far more sensitive to these details than the total cross section, transport cross section, diffusion constant, thermalization time or diffusion cooling constant. It had become obvious at the time of initiation of this program that some steps had to be taken to try to resolve the remaining discrepancies between theory and experiment apparent in space-dependent spectral studies. Initially, one had hoped that the double differential scattering cross section data would serve as a guide. However, a number of uncertainties arose regarding the quality of double differential data which precluded its complete utilization. These are briefly reviewed here.

Double differential scattering cross section measurements have been conducted on the common moderators for over ten years at many laboratories using simple choppers, triple and double axis crystal spectrometers and multiple chopper setups. Much data are available from many research groups, and we can only generalize on the problems one encounters in trying to correlate these data. To begin with, the scattering data are of two forms (1) dispersion measurements using single crystals of the moderator and (2) scattering law measurements on polycrystalline materials or liquids. Only limited data of the first form are available over a rather

small neutron energy range. Of the second form one finds that much scattering law data are available but that wide experimental discrepancies exist between measurements at various laboratories. These difficulties are enhanced especially when an attempt is made to deduce the characteristic lattice or molecular frequency spectra from the scattering law data. Not only do various experimental determinations of the general shape of frequency spectra differ by large factors but the over-all statistical weight of measured portions usually do not conform to expectation and are sometimes inconsistent with conclusions from other experiments, (for example infinite medium spectral measurements or molecular structure studies). Thus for water, various independent measurements of the hindered rotational part of the frequency spectrum are quite different.<sup>(55)</sup> In addition spectra deduced from scattering law data have in general been quite different in shape from those calculated from neutron dispersion relation measurements or from other well known non-neutron data.<sup>(56)</sup> The general quality of the data is perhaps best illustrated by the fact that it is impossible to find a systematic error analysis associated with any of the available experimental data. Further, in attempting to repeat procedures used by one group<sup>(38)</sup> in scattering law data analysis totally different answers have often been obtained by another group.<sup>(57)</sup> In addition double differential data have often been somewhat inconsistent on rather fundamental grounds with other observations. Examples are the drastic temperature dependent effects<sup>(44)</sup> ( $\text{H}_2\text{O}$ ) and anharmonic effects<sup>(58)</sup> ( $\text{ZrH}_n$ ) presumably observed on the double differential scattering for common moderators which do not manifest themselves at all in the more integral experiments<sup>(3,25)</sup> (spectra, total cross section, and single differential scattering). We have tried to understand why there is often such a large difference between the measurements and analyses in the double differential scattering experiments from a given laboratory, and why the results from different laboratories are so much at variance. We discovered that the experimental data are seldom if ever corrected for multiple scattering in the target (which is expected to be a large effect and in addition the double differential scattering intensity is integrated over angle and final energy and normalized to the total cross section. Absolute cross sections are not measured, thus spurious background effects which would show up clearly in absolute cross section determinations can not be as easily or directly detected. The list of criticism goes on and on including the fact that it has not been possible to measure double differential cross sections by existing techniques in the 0.1 - 10 eV neutron energy region to see the transition to the free gas limit and to observe completely the influence of the high energy vibrational degrees of freedom. There is of course good reason for hope that the above situation will change since many meticulous workers are now engaged in repeating and refining double differential measurements throughout the world.

Meanwhile other courses of action are open to those requiring more immediate results. Our program of single differential measurements was instigated largely to complement the excellent results being obtained at Munich by Reinch and Springer<sup>(59)</sup> under Maier-Leibnitz. These results for water have been discussed before in our progress reports.<sup>(3, 52, 60)</sup> Further detailed results<sup>(61)</sup> are also available from these workers on  $H_2O$ , phenyls,  $ZrH_{1.96}$ , and  $D_2O$  at room and elevated temperatures for a few neutron energies. The lack of a pronounced temperature dependence of the angular distributions and the well resolved coherent scattering peaks are but two of the more obvious observations one can make from these data. On the other hand our own program has concentrated on developing the measurement apparatus and technique beyond that used in our first attempts reported last year. All experimental scattering work has concentrated on determining the single differential cross section for water over the energy range 0.005 to 10 eV. A considerable effort has been made to develop procedures for measuring the absolute cross section and for correcting results for the serious effects of multiple scattering in the samples.

## 10.2 PRINCIPLE OF THE MEASUREMENT

Although the principle of the scattering measurement has been discussed by others<sup>(59)</sup> it is reviewed here. Figure 10.1 illustrates the general arrangement. Pulses of electrons from the linear accelerator strike a tungsten target in which large numbers of fast neutrons are produced by photo-reactions. The  $\gamma$  flash from the target is suppressed (in the flight path direction) by a lead cone while the fast neutrons moderate in a water bath behind the target. Moderated neutrons stream down the flight path ( $\ell_1$ ), strike the thin scattering sample at times corresponding to their energies and are detected in a "black"  $Li^6$  glass detector. The source moderator is carefully shielded from the room with borated plastic. The flight path collimator has been designed so that the beam spot on the scattering sample is uniformly irradiated and has sharp edges. This has necessitated the addition of a special post collimator. The flight path  $\ell_1$  is much longer than the flight path  $\ell_2$  after scattering, which allows the desired experimental time or energy resolution to be obtained. Neutrons of course may change energy in collision and the flight time from the sample to the detector must be small or this energy change will transfer the count from a channel corresponding to the initial energy before collision to a channel corresponding to a lower initial energy. This effect is small for our new 12 meter flight path and in addition a small first order correction can be made for it. The correction assumes (as do most target corrections) that one has some idea of the scattering model for the moderator since one must compute the average energy  $\bar{E}_f(E_i, \theta)$  after a collision.



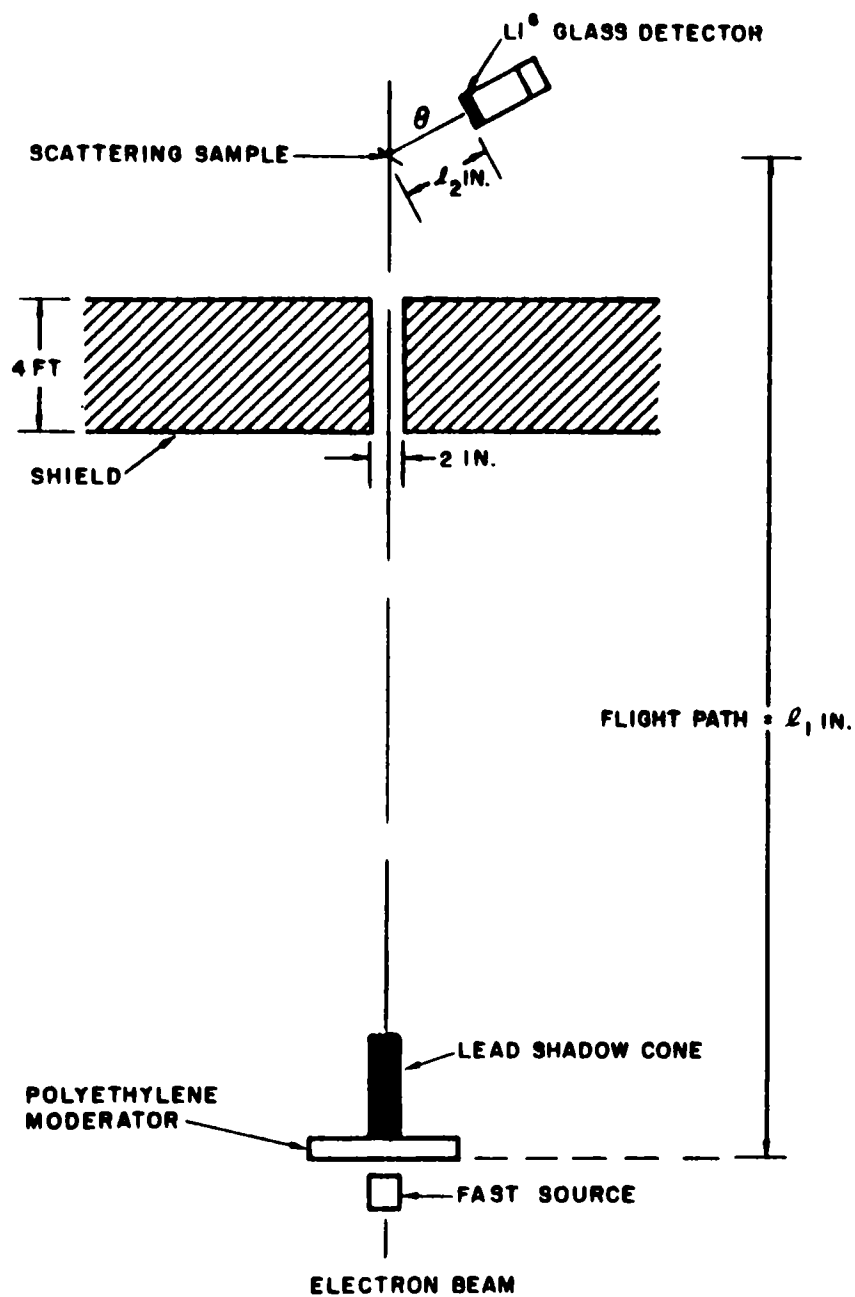


Fig. 10.1 -- Experimental Arrangement for Measurement of the Differential Scattering Cross Section of Water

One has the problem therefore of determining what incident energy  $E_i$  caused the events recorded in the time of flight channel which would normally have been associated with energy  $E_A$  (assuming no energy change on collision). This may be determined from the expression

$$E_i = \frac{E_A \ell_1^2}{(\ell_1 + \ell_2)^2 \left( 1 - \frac{\ell_2}{\ell_1 + \ell_2} \sqrt{\frac{E_A}{E_f}} \right)^2} \quad (10.2.1)$$

Corrections at back angles for hydrogenous moderators could be as large as 10% but in the cases studied so far ( $H_2O$ ), even this is not significant.

The procedure for determining the absolute scattering cross section from the measurement may be seen in the following discussion of the pertinent details with reference to Fig. 10.2.

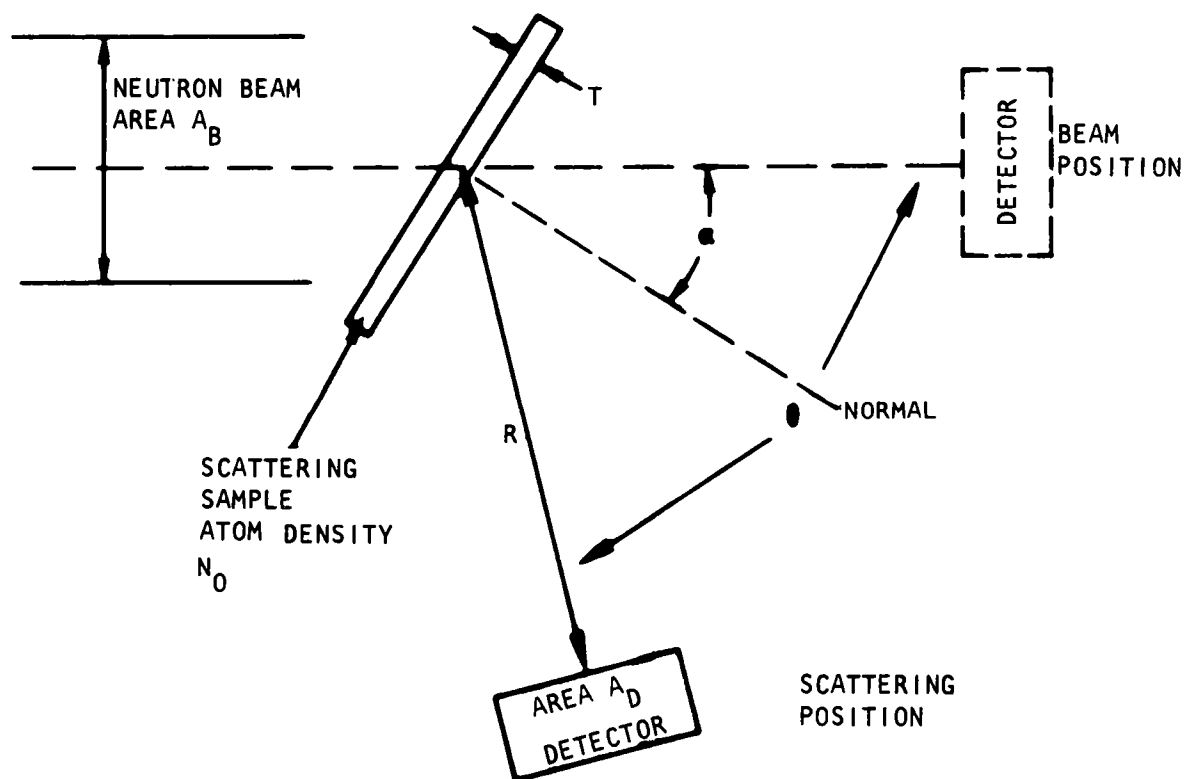


Fig. 10.2 -- Geometry of the scattering sample and the detector

Assuming a black detector the ideal counting rate in the beam with scatterer removed is

$$C(0^\circ) = \epsilon \phi(E) A_D \quad (10.2.2)$$

where  $\phi(E)$  is the incident neutron flux and  $\epsilon$  the detector absolute efficiency. With an infinitely thin scattering sample the detector response at angle  $\theta$  is given by

$$C(\theta) = \phi(E) A_B \frac{N_o T}{\cos \alpha} \frac{d\sigma(E)}{d\Omega} \frac{A_D \epsilon}{R^2} \quad (10.2.3)$$

Dividing equation 10.2.3 by equation 10.2.2 and defining  $R(\theta) = C(\theta)/C(0^\circ)$  one obtains for the differential cross section

$$\frac{d\sigma}{d\Omega} = \frac{R(\theta) R^2 \cos \alpha}{A_B N_o T} \quad (10.2.4)$$

In practice several assumptions implicit in the above analysis must be handled more exactly. For example, the neutron beam striking the scattering sample does not have infinitely sharp edges and the detector response is not absolutely uniform even though the detector is essentially black to neutrons below 1 eV everywhere. Also the detector is not placed at the sample position for the zero degree measurement so that the spatial distribution of flux at the sample  $\phi_s(E, r)$  may be slightly different than that at the detector  $\phi_D(E, r)$  behind it. If, however, one has been careful to choose a detector radius  $R_d$  which is smaller than the flat portion of the incident neutron flux pattern one may include these effects simply to obtain

$$\frac{d\sigma}{d\Omega} = \frac{R(\theta) R^2 \cos \alpha}{A_B N_o T} \left[ \frac{\phi_D(E, < R_d) A_B}{\int_0^a 2\pi r \phi_s(E, r) dr} \right] \quad (10.2.5)$$

where  $a$  is a radius which envelopes the entire neutron beam. The correction factor in brackets will be referred to subsequently as  $C_f$ . This correction assumes that the detector sensitivity does not depend on position on the  $\text{Li}^6$  glass.  $C_f$  may be made to approach 1.0 by choosing the effective radius of the detector at the half sensitivity point. A possibly important correction to equation (10.2.4) is caused by the fact that the source is not a point source and the detector size is also not a negligible fraction of the source to detector distance ( $R$ ). An angularly dependent correction factor ( $C_R$ ) can

be formulated for this effect by Taylor series expansion of the exact solid angle expressions. This is given to a first approximation by

$$C_R = 1 + \frac{R_d^2}{2R^2} + \frac{a^2}{4R^2} (2 - 4 \sin^2 \theta + \tan^2 \alpha (1 - 4 \cos^2 \theta) + 8 \tan \alpha \sin \theta \cos \theta), \quad (10.2.6)$$

where  $a$  is the radius of the beam striking the sample. For our conditions,  $a \approx R_d \approx 1$  inch and  $R = 12$  inch, it can be seen that this correction is small.

The most important correction to the naive expression given in equation (10.2.5) is that for multiple elastic and inelastic scattering in the material of the sample and its holder. There are several approximations that can be used in making this correction. The simplest procedure formulated years ago by Vinyard<sup>(62)</sup> assumes isotropic scattering on all collisions and no energy change in collision. Another procedure is to use the measured angular distributions to formulate the multiple scattering correction for the first and second scattering, to assume isotropy after that, but to retain the elastic scattering approximation. This is the method used by Lemmel and Springer.<sup>(63)</sup> A third procedure is to calculate the correction for multiple scattering by using the theoretical scattering model for the moderator and one dimensional transport theory. This is the procedure introduced by H. C. Honeck in MUSE I, discussed in Section 10.3, and used in our data analysis. A fourth procedure would be to calculate the first collision using a measured scattering kernel and the subsequent collisions by transport theory. This procedure is allowed in MUSE II but as yet we have not used it. Obviously the most exact procedure is the Monte Carlo method but we have not employed this technique since it is not clear that it is necessary.

A formulation used to include the multiple scattering effect by the first procedure outlined above is

$$\frac{d\sigma(E)}{d\Omega} = \left[ \frac{R_T(\theta) R_e^2 N_o \sigma T / \cos \alpha}{A_B N_o T} - \frac{\sigma_s}{4\pi} \frac{\zeta}{1-\zeta} \right] C_f C_R \quad (10.2.7)$$

where  $\zeta$  is defined by Vinyard.<sup>(62)</sup> One can rewrite formula (10.2.7) in terms of a multiple scattering correction factor  $C_V$  as follows

$$\frac{d\sigma(E)}{d\Omega} = \frac{R(\theta) R^2 \cos \alpha}{A_B N_o T} C_f C_R C_V \quad (10.2.8)$$

where  $C_V$  is given by

$$C_V = \frac{e^{N_o \sigma_t T / \cos \alpha}}{1 + \frac{\sigma_s}{4\pi d\Omega} \left( \frac{\zeta}{1-\zeta} \right)} \quad (10.2.9)$$

$d\sigma/d\Omega$  in equation (10.2.9) could either be obtained from theory or experiment. It is assumed here that it is the true value, therefore the theoretical estimate may be preferable. The Lemmel-Springer<sup>(63)</sup> procedure assumes the scattered intensity is given by

$$Z(\theta) = P \left( \frac{1}{\sigma_s} \frac{d\sigma}{d\Omega} K_d + K_m(\theta) \right) \quad (10.2.10)$$

where  $P$  is a normalization constant, adjusted to give the correct total cross section, and  $K_m$  is the multiple scattering correction.

$$K_d = \left( e^{-N_o \sigma_t T / \cos \alpha} \right) \frac{N_o \sigma_s T}{\cos \alpha} \text{ for transmission geometry} \quad (10.2.11)$$

and

$$K_d = \frac{1}{2} \left( 1 - e^{-2N_o \sigma_t T / \cos \alpha} \right) \text{ for reflection geometry} \quad (10.2.12)$$

$\zeta$  is defined as  $\zeta = K_m(\theta)/K_d$  and has been tabulated. The third procedure, that employed so far in our work is to calculate the absolute cross section from

$$\frac{d\sigma}{d\Omega} = \frac{R(\theta) R^2 \cos \alpha}{A_B N_o T} C_f C_R C_H \quad (10.2.13)$$

where  $C_H$  is the Honeck correction factor (Section 10.3). This correction factor for our experimental angular mesh is shown in Figures 10.3 and 10.4 for 21.5 mil and 32 mil thick water samples. In these calculations the sample is oriented so that its normal bisects the scattering angle. Obviously the correction is large, especially beyond  $90^\circ$  for energies greater than 0.1 ev even for reasonably thin samples oriented to minimize the correction. In figure 10.4 the  $120^\circ$  correction factor is also given for 3 sample thicknesses.  $C_H$  does not decrease linearly with thickness so that rather thin samples are not really free from the correction. It is important to make this correction accurately at back angles because the back angle cross section data contains the most information

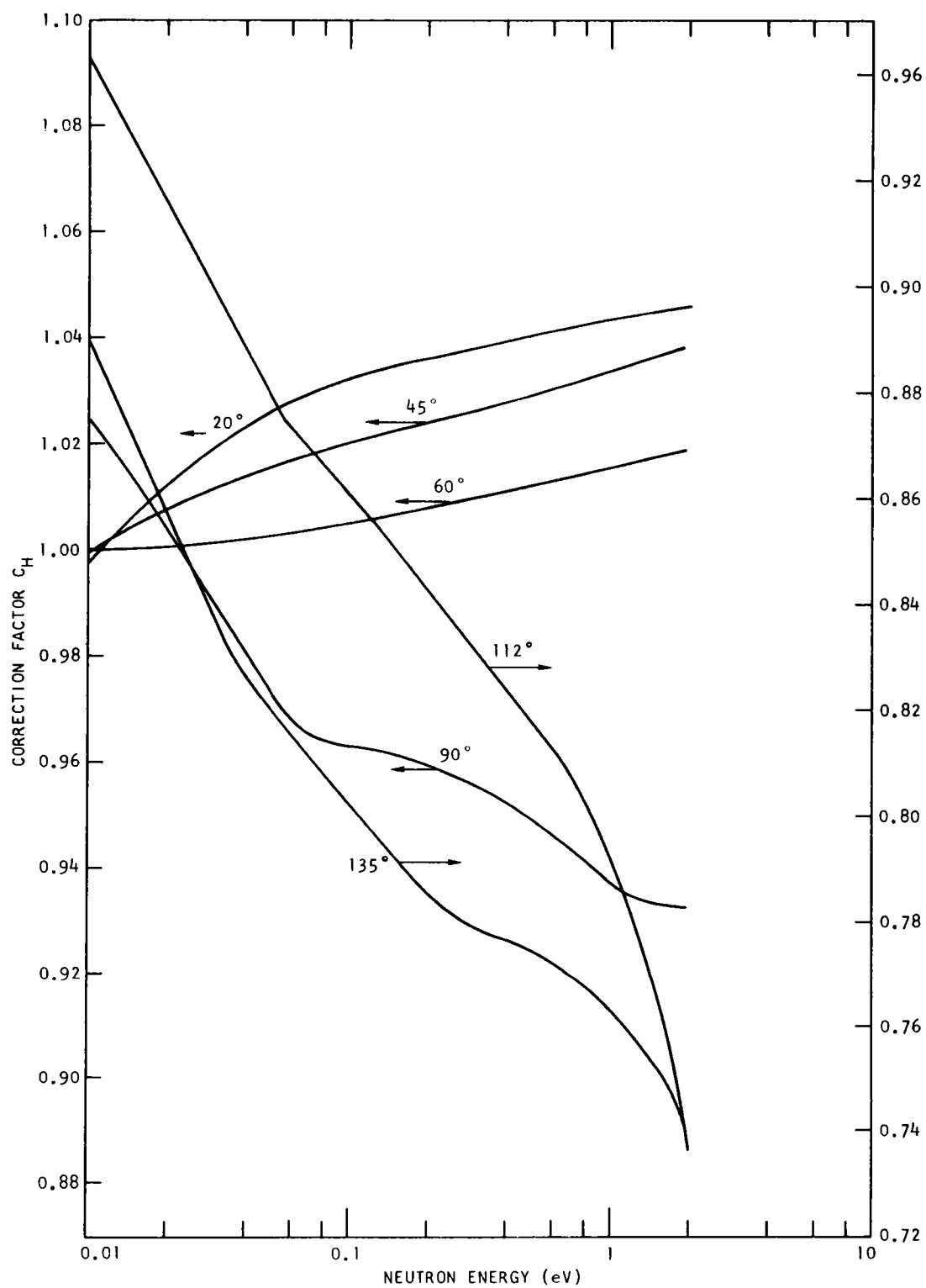


Fig. 10.3 -- Honeck correction factor for scattering by a 21.5 mil  $H_2O$  sample

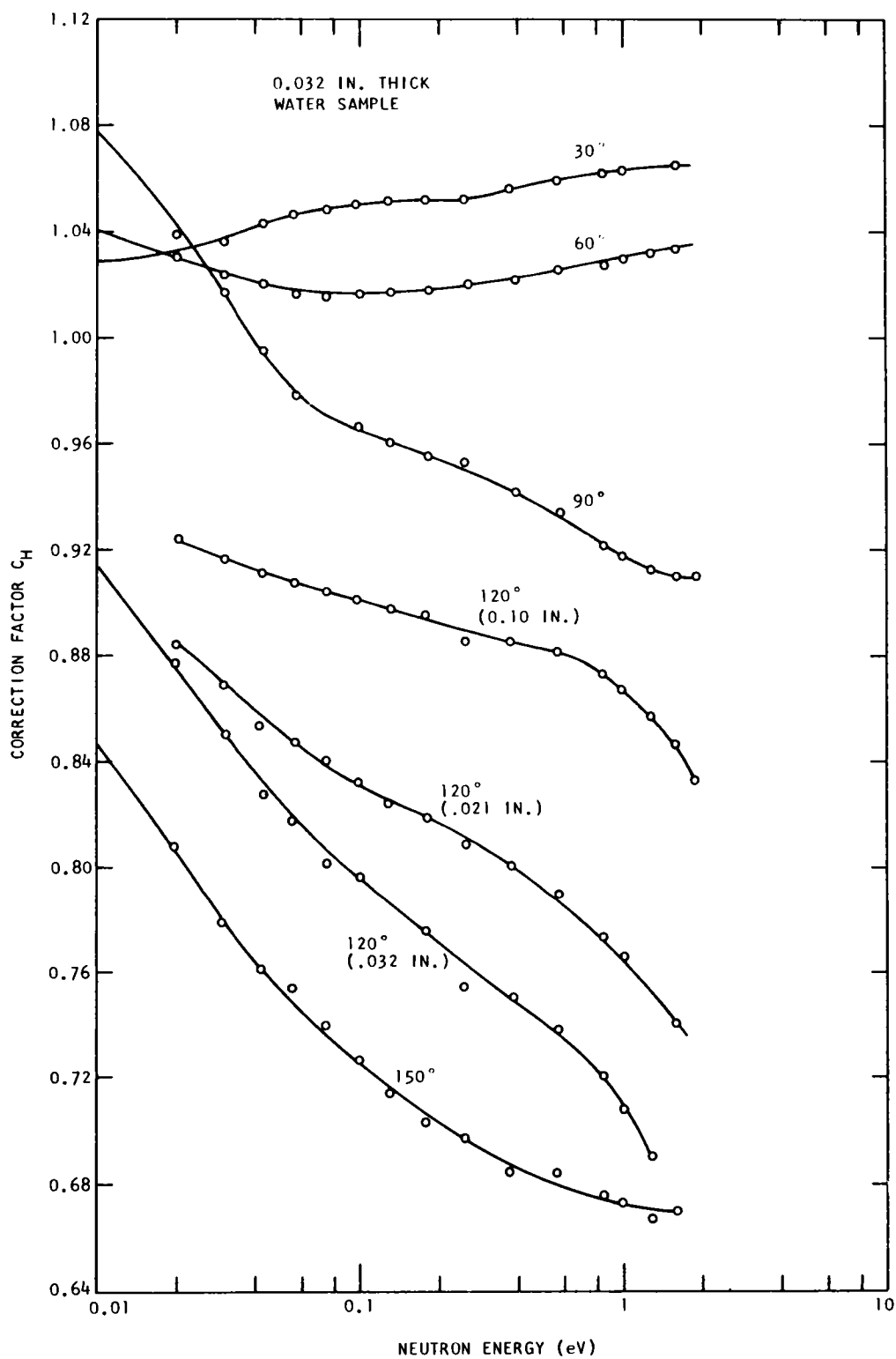


Fig. 10.4 -- Honeck correction factor for scattering by a 32 mil  $H_2O$  sample

on the inelastic scattering and also makes the largest contribution to the transport cross section.

Another interesting comparison of multiple scattering correction procedures has been made between the Vineyard correction  $C_V$  (equation 10.2.9) and the Honeck correction  $C_H$  (section 10.3). The ratio of these two corrections for a 20 mil water sample is given in Fig. 10.5. The difference is certainly enough to justify the use of the more exact procedure. However, several questions arise in considering the curves. It might, for example, appear that the Honeck correction factor  $C_H$  is sometimes larger than the Vineyard. Since both correction factors are less than 1 (no correction) at angles greater than  $90^\circ$ , Fig. 10.5 shows that  $C_H$  is closer to 1 than  $C_V$  and thus is a smaller correction. Further, why are the two corrections so nearly the same? If one were to compare  $\xi$  or the correction for collisions subsequent to the first collision one would find much larger disagreements between the various procedures for calculating multiple scattering. However, the various procedures treat the escape of the first collided neutrons differently and some compensation results. An equivalent way of explaining the relative success of the simple procedure in the cases studied so far is that in this procedure the isotropic scattering assumption produces an over-estimate of the multiple scattering contribution at a given (back) angle while the neglect of inelastic scattering produces a partially compensating effect. Further detailed comparison is needed in the multiple scattering correction procedures. For example, it may be worse to try to include anisotropic scattering and at the same time neglect the inelastic scattering as in the Lemmel<sup>(63)</sup> procedure. Also the degree of success of the simple Vineyard<sup>(62)</sup> procedure may be limited only to a certain class of special cases which we have fortuitously chosen. This general problem will receive much attention as we proceed to the study of more complex angular scattering, such as where coherent effects are present.

### 10.3. MULTIPLE SCATTERING CORRECTION

The flux leaving or in the scattering sample is a solution of the transport equation

$$\phi(Z, E, \underline{\Omega}) = \frac{1}{|\underline{\mu}|} \int dZ' H(Z', E, \underline{\Omega}) \exp \left[ -\Sigma(E) \left( \frac{Z-Z'}{\mu} \right) \right] \quad (10.3.1)$$

$$H(Z', E, \underline{\Omega}) = \int d\underline{\Omega}' \int dE' \Sigma_s(E' \rightarrow E, \mu_o) \phi(Z', E', \underline{\Omega}') \quad (10.3.2)$$

where the symbols have their usual meaning. The coordinate system is chosen so that  $Z$  is normal to the sample,  $\mu = \cos \theta$  and  $\theta$  is measured from



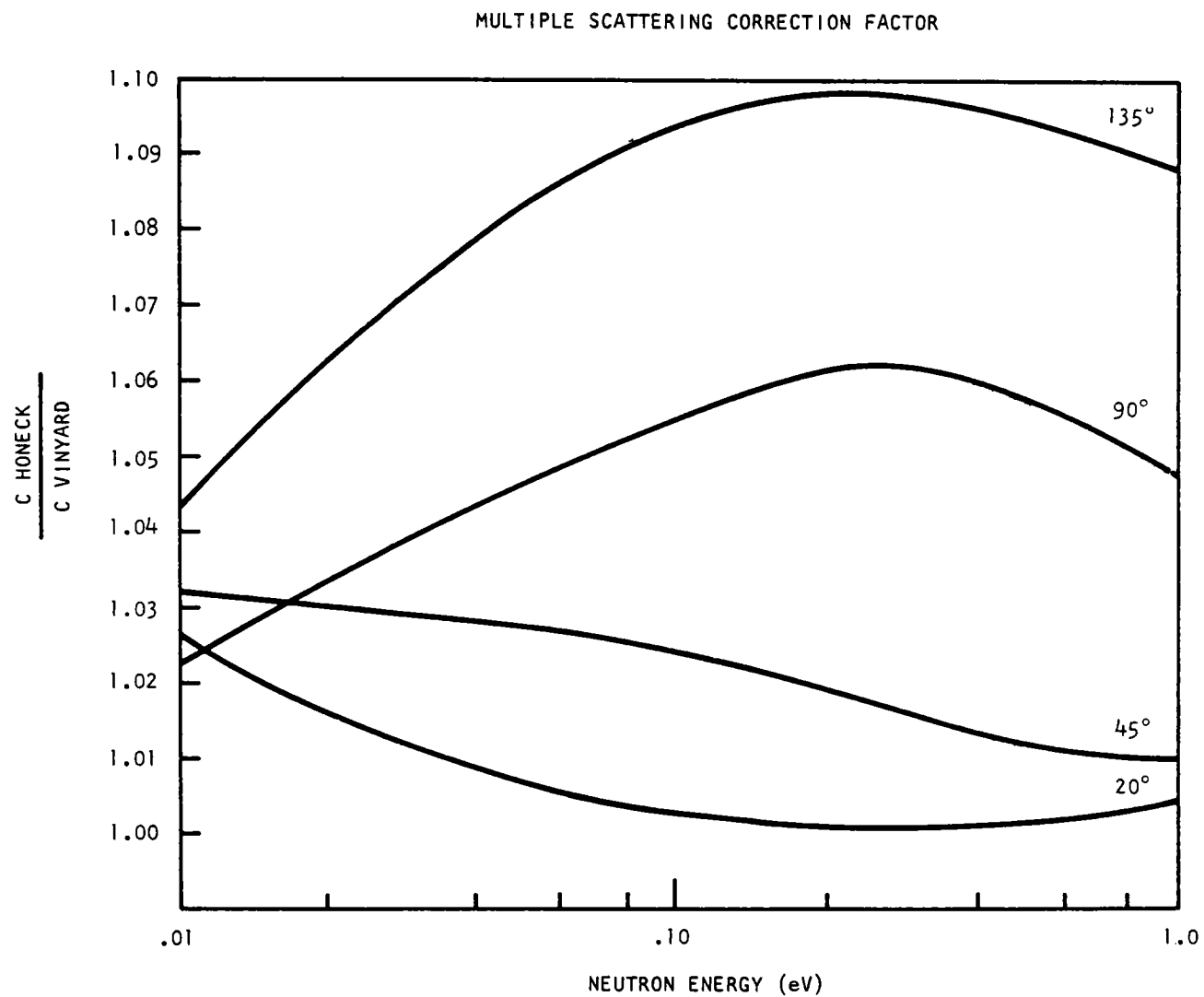


Fig. 10.5 -- Ratio of multiple scattering correction factors

Z to the neutron direction, and  $\psi$  is the azimuthal angle measured from the plane formed by Z and the incident beam. Subscript 1 denotes the incident beam and 2 the outgoing beam. The sample thickness is given by T.

The incident flux is monoenergetic and in the direction  $\underline{\Omega}$ , so that the uncollided flux in the sample is

$$\phi(Z, E, \underline{\Omega}) = e^{-\Sigma(E)Z/\mu} \delta(E - E_1) \delta(\underline{\Omega} - \underline{\Omega}_1) \quad (10.3.3)$$

If this is inserted in (10.3.2) and (10.3.2) into (10.3.1) and the appropriate integrations performed, there results the first collision flux  $\phi'$  leaving the sample in direction  $\underline{\Omega}_2$ .

$$\begin{aligned} \phi'(E_2, \underline{\Omega}_2) &= \frac{T}{\mu_2} \left[ \frac{e^{-\chi_1} - e^{-\chi_2}}{\chi_2 - \chi_1} \right] \Sigma_s(E_1 \rightarrow E_2, \mu_o), \mu > 0 \\ &= \frac{T}{|\mu_2|} \left[ \frac{1 - e^{-\chi_1 - \chi_2}}{\chi_1 + \chi_2} \right] \Sigma_s(E_1 \rightarrow E_2, \mu_o), \mu < 0 \end{aligned} \quad (10.3.4)$$

where  $\mu_o = \underline{\Omega}_1 \cdot \underline{\Omega}_2$ ,  $\chi_1 = T\Sigma(E_1)/\mu_1$ ,  $\chi_2 = T\Sigma(E_2)/|\mu_2|$ . In the limit  $T \rightarrow 0$  the bracketed terms approach unity and  $T/|\mu_2|$  is the "effective sample thickness". We then define the response of a black detector as

$$R'(\underline{\Omega}_2) = \frac{|\mu_2|}{T} \int_0^\infty dE_2 \phi'(E_2, \underline{\Omega}_2) \quad (10.3.5)$$

so that in the limit  $T \rightarrow 0$ ,  $R'(\underline{\Omega}_2) \rightarrow \Sigma_s(E_1, \mu_o)$ , the angular scattering cross section.

Equation (10.3.4) is the flux leaving the sample. A similar equation can be obtained for the flux in the sample  $\phi'(Z, E, \underline{\Omega})$ , which, when inserted in (10.3.2), and (10.3.2) inserted in (10.3.1), gives the second collision flux  $\phi''(Z, E, \underline{\Omega})$ . Thus, each "iteration" of equations (10.3.1) and (10.3.2) corresponds to one collision. The response of the detector corresponding to each collision,  $R^n(\underline{\Omega}_2)$  can then be summed to give the total response.

$$R(\underline{\Omega}_2) = \sum_{n=1} R^n(\underline{\Omega}_2) \quad (10.3.6)$$

and a correction factor defined as

$$C_H(\underline{\Omega}_2) = \Sigma_s(E_1, \mu_0) / R(\underline{\Omega}_2) \quad (10.3.7)$$

The above procedure with some modification has been incorporated into a computer code called MUSE. The approximations used are:

1. The kernel  $\Sigma_s(E' \rightarrow E, \mu_0)$  used in (10.3.4) is in a matrix form with 30-40 intervals in energy and 20-30 intervals in  $\mu_0$ . Intermediate values are obtained by linear interpolation and the integration in (10.3.5) is done using the trapezoidal rule.
2. For the second and higher order collisions, equations (10.3.1) and (10.3.2) and the scattering kernel are expanded in spherical harmonics to terms in  $P_3$ . The sample is divided into subregions (up to 5) in which the spatial flux is assumed to be uniform. The multigroup method with 30-40 groups is used for the energy variable.
3. Four scattering collisions are allowed.

Two versions of MUSE exist. The first, MUSE 1, contains the theory described above. The second, MUSE 2, provides corrections for the double differential experiment and is the same as MUSE 1 except the energy integration in (10.3.5) omitted.

The above procedure is quite straightforward and the numerical approximations should introduce little error. The major difficulty is that a scattering kernel must be used as an input quantity. In the double differential experiment the kernel is measured and could be used as input. The correction factors that are computed can be applied to the measured kernel and the process iterated until a fully corrected kernel is obtained. In the single differential experiment the quantity  $\Sigma_s(E', \mu_0)$  is measured but  $\Sigma_s(E' \rightarrow E, \mu_0)$  is needed as input to MUSE 1. It is thus necessary to use a theoretical kernel or, if one is available and sufficiently complete, a measured kernel. Provision has been made in MUSE 1 to add an arbitrary amount of elastic scattering, so that it is possible to adjust the kernel so that the input and measured angular cross sections  $\Sigma_s(E', \mu_0)$  are the same. This procedure should be sufficient to give correction factors whose accuracy is consistent with that of the experiment.

#### 10.4. EXPERIMENTAL ARRANGEMENTS

The experimental program of differential scattering measurements has been performed this year on two different flight paths at the General Atomic Linac Facility. To test the practicality of making absolute cross section determinations, to investigate sample multiple scattering problems,

and to determine intensities, a temporary setup was constructed at a 25 meter flight station located behind the large liquid scintillator used for our capture cross section program. The thermal neutron target normally used for these capture experiments was used also for the scattering work. During this year, however, we have been able to construct a new flight path specifically for these studies. Only the new facility is described here.

#### 10.4.1. Beam Tube System

The electron beam is piped to the Fansteel neutron source through a 2-1/4 in. stainless steel tube 173 inches long beyond the new shield wall (see Fig. 10.6). The output window, 2 inches in diameter, 10 mil thick, is constructed of titanium and is air cooled. Our quadrapole lenses are spaced along the beam tube to focus the beam to a 1/8 - 1/4 in. diameter spot on the target. The first quadrapole is placed 18 in. beyond the magnet used for bending the electron beam from the Linac axis. The center of the beam tube window is located 85 in. off the original beam axis of the machine, the fast neutron target is located 80 feet from the end of the Linac proper. The ability to pipe the electron beam from the Linac with no loss of current depends mostly on the energy spread on the beam. It has been shown that greater than 90% of the beam will pass through the titanium window within the 1/4 in. spot. The energy spread in the electron beam is about two percent at half maximum. The electron beam must travel a short distance through air to impinge upon the fansteel target in which the fast neutrons are produced by ( $\gamma$ , n) reactions.

#### 10.4.2. Electron Beam Target (Fansteel Source)

The fansteel source is cooled by a flow of 1.5 gallons of water per minute. The present source is 1-3/8 in. in diameter by 1-1/2 inches long with a 1/4 in. pipe tap hole drilled through the fansteel normal to the incident electron beam.  $\gamma$ -rays from the source are shielded from the flight path direction with a lead shadow cone. The Fansteel source is electrically insulated from its stand. It is grounded through a 50  $\Omega$  resistor whose voltage drop provides the machine operator with an electron beam current monitor.

#### 10.4.3. Water Thermal Source

The water thermal source adjacent to the fansteel fast neutron source was designed to have nearly uniform thermal flux intensity over its surface. This is necessary to produce a uniformly illuminated beam spot at the scatterer position. The water thermal source is a thin cylinder 10 inches in diameter with an average thickness of 3 inches. One side is a flat plate but the other side is a curved dish with a 10-inch radius to further surround the fansteel source and to adjust the leakage flux distribution of the thermal neutrons. Water is circulated through the source at about 0.2 gpm and 7 psi.

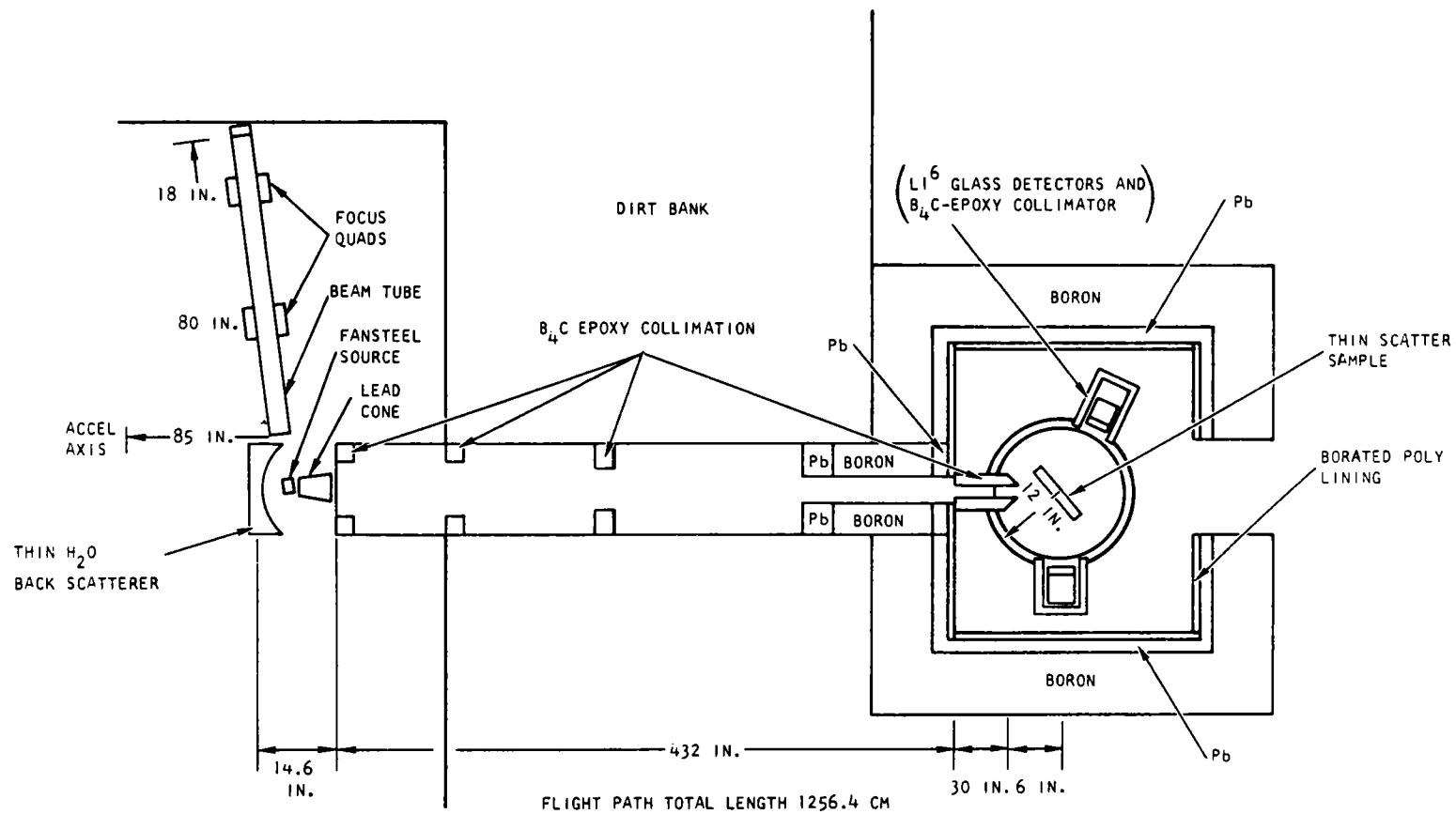


Fig. 10.6 -- Geometrical arrangement for angular distribution measurements

The dieaway of the thermal source was measured using a miniature fission counter placed at the side of the moderator. A comparison was made with a bare source and with the source covered by 1/8 inch borated polyethylene (28 wt% boron). The data indicated no change in the dieaway. However, the long term room return background at the source was reduced by a factor of 2. Thus source shielding is therefore provided on our final target source design.

The water target equivalent buckling ( $B^2$ ) for this irregular configuration was determined from the complete dieaway curves ( $\lambda$  vs  $B^2$ ) for water measured by Lopez.<sup>(64)</sup> The equivalent  $B^2$  obtained was 0.289, and this was used in the GATHER<sup>(13)</sup> code to calculate the mean emission time  $T$ .  $T$  was calculated as a function of neutron energy in the standard manner

$$T = \frac{\int_0^{\infty} \phi(E, t) dt}{\int_0^{\infty} \phi(E, t) dt} \quad (10.4.1)$$

and all measured flight times were corrected to first order for the time spent in the water moderator.

#### 10.4.4. Flight Path and Collimation

The new flight path consists of an evacuated (100  $\mu$  pressure) 12.5 inch diameter steel pipe assembled in two sections (See Fig. 10.6). The primary section is 30.0 feet long with a 6.0 feet section extending into the accelerator experimental room. The 30 foot section extends through a transite pipe of 22 inch inside diameter which permits access through the dirt embankment.

The 12.5 inch drift tube terminates immediately inside of a metal shed which houses the experimental scattering cave. The cave consists of a 6 foot square room 4-1/2 feet high surrounded by 4 inches of lead brick, with 12 inches of boric acid neutron shielding on the outside. To reduce the back scattering from the inside walls of lead, the walls are lined with heavily borated polyethylene (28 wt% boron).

The collimation of the flight path includes both gamma ray and neutron shielding to define the neutron beam shape on the scattering sample. The gamma flash in the general direction of the experiment is attenuated in two places. The attenuation is obtained first with a lead shadow cone 2 in. in diameter and 8-1/2 in. long located at the target shown in Fig. 10.6. Further attenuation comes from 8 inches of lead in the form of an annular ring, positioned in front of the collimator at the far end of the 12.5 in. diameter flight tube.

The collimation of the neutron beam is paramount to the success of the experiment. Keeping this in mind, the following improvements have been made:

- a. None of the intermediate collimators are limiting ones.
- b. The evacuated flight path has been extended as near as possible to the scattering position. Thin windows are used on each end of the flight tube; the inlet window is .032 in. aluminum and the exit window is .004 in. aluminum.
- c. The collimator defining the final spot is located immediately after the exit window in order to reduce the effects of neutrons which are scattered from the window itself.

The flux across the normal position of the scattering sample was determined by shielding the  $\text{Li}^6$  glass detector with boron carbide except for a 1/8 inch dia. hole. This small opening was then positioned throughout the area of the beam spot to check the flux uniformity. Also the incident spectrum was measured by time of flight means at representative locations on this spot - for example the edges where one might intuitively expect differences. In Fig. 10.7 we show the distribution of neutron intensity across the sample position in our original experimental setup. Obviously the spot is irregular and non-uniform. Fig. 10.8 shows our present beam spot shape after collimator and source design were optimized. This is an acceptable shape to use for the calculation of  $C_f$  (formula 10.2.5). Further the measured neutron spectrum is the same at various locations and even at the edges.

#### 10.4.5. Detector and Scattering Sample Arrangement

The setup inside the experimental cave is arranged in such a manner that scattering samples may be changed easily and rotated to intersect the neutron beam at any angle. The  $\text{Li}^6$  detectors are also permitted to be moved independently to any desired angle  $\pm 150$  degrees with respect to  $0^\circ$  (the beam axis position). The  $\text{Li}^6$  glass detectors and their phototubes and sockets are housed in a 1/2 in. thick  $\text{B}_4\text{C}$ -epoxy collar to reduce the background from scattered neutrons from elsewhere in the cave (air mostly) except the sample direction. Fig. 10.6 illustrates the layout of the apparatus.

#### 10.4.6. Electronics and Monitoring System

The instrumentation utilized in the angular distribution measurements has been improved and expanded over that used in the previous measurements.<sup>(3)</sup> A block diagram of this instrumentation is shown in Fig. 10.9. Three completely independent monitoring systems are used. Two systems

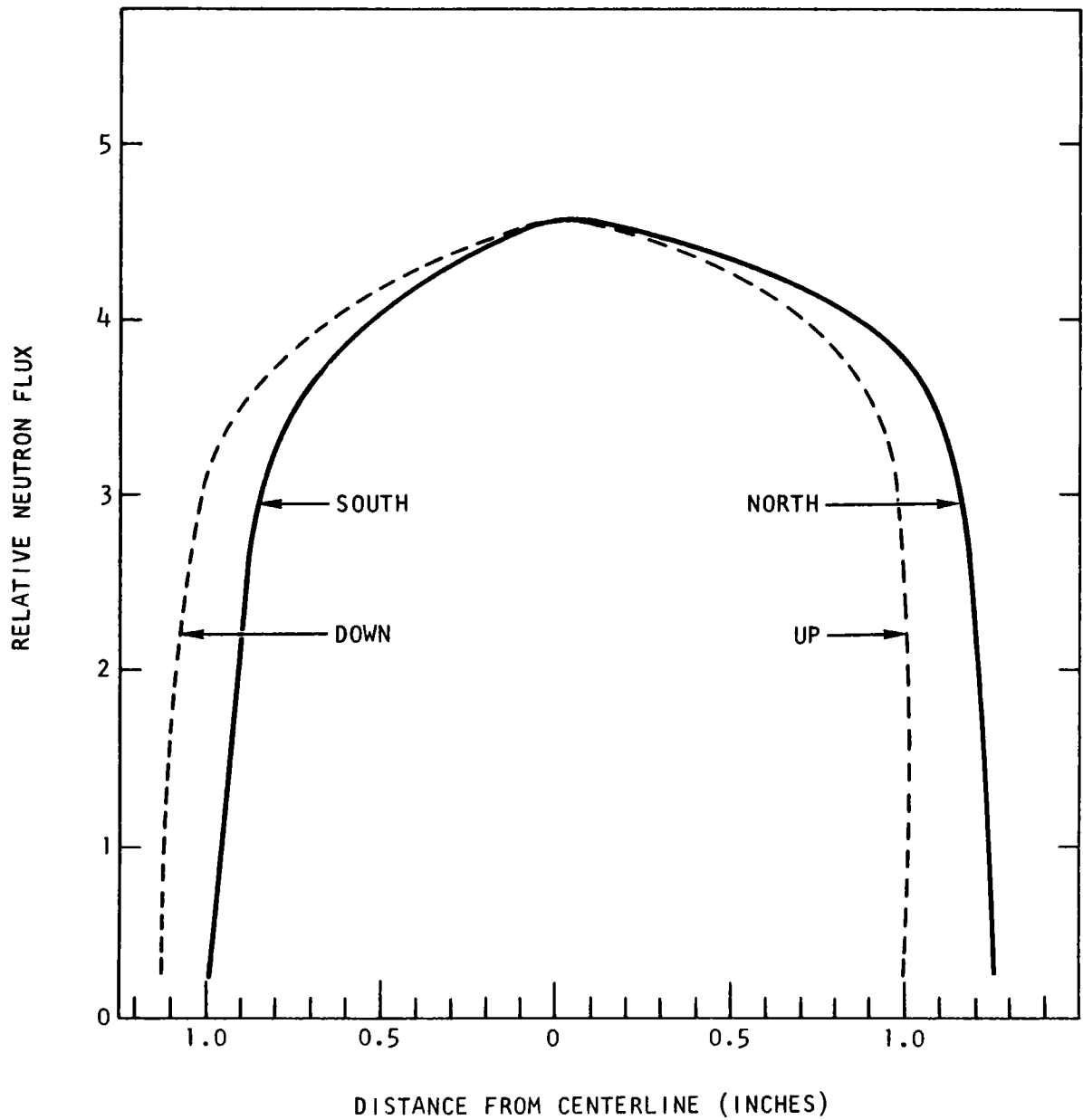


Fig. 10.7 -- Spatial variation of neutron flux intensity at the sample position in the original experimental arrangement



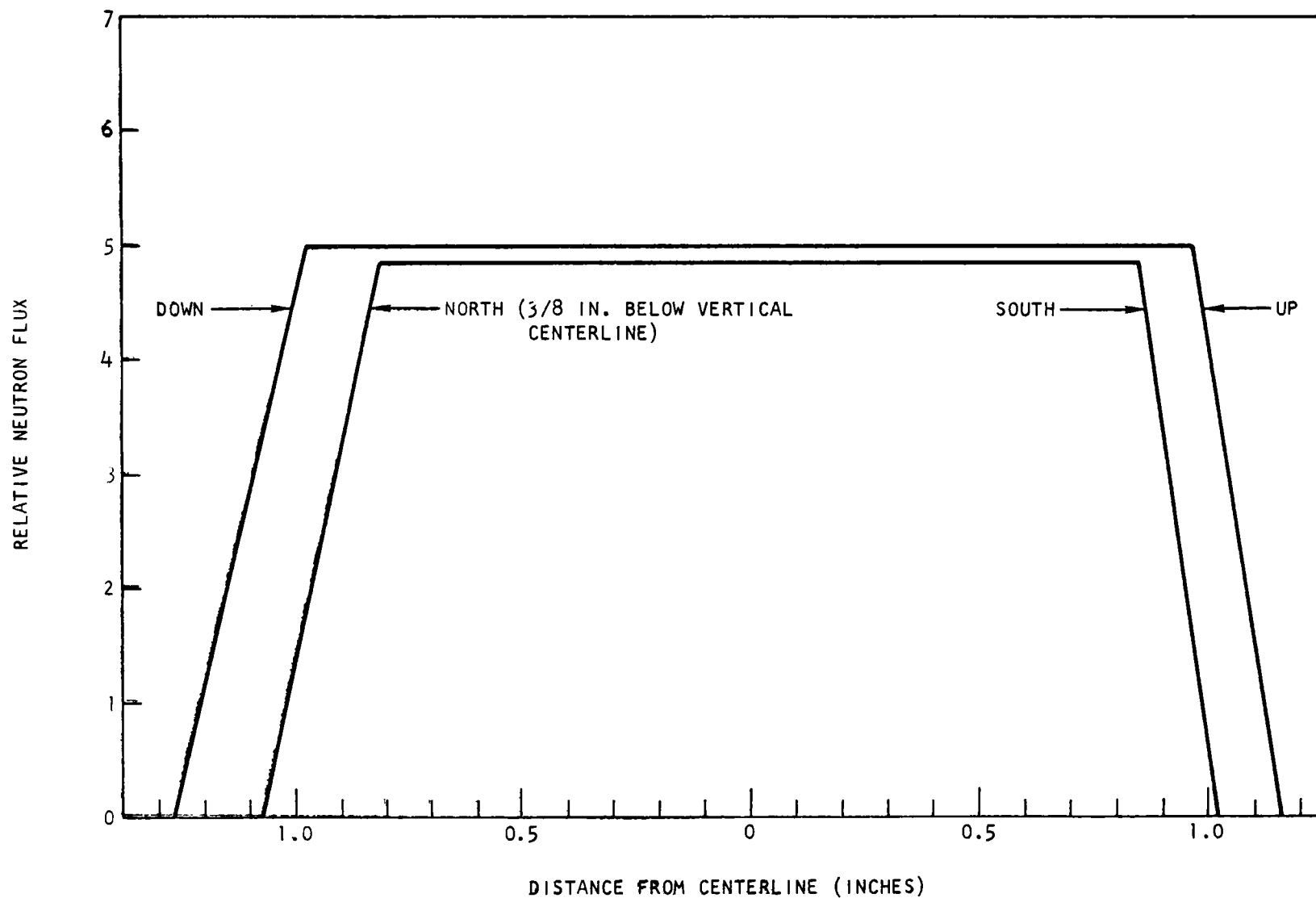


Fig. 10.8 -- Spatial variation of neutron flux intensity at the sample position in the present experimental arrangement

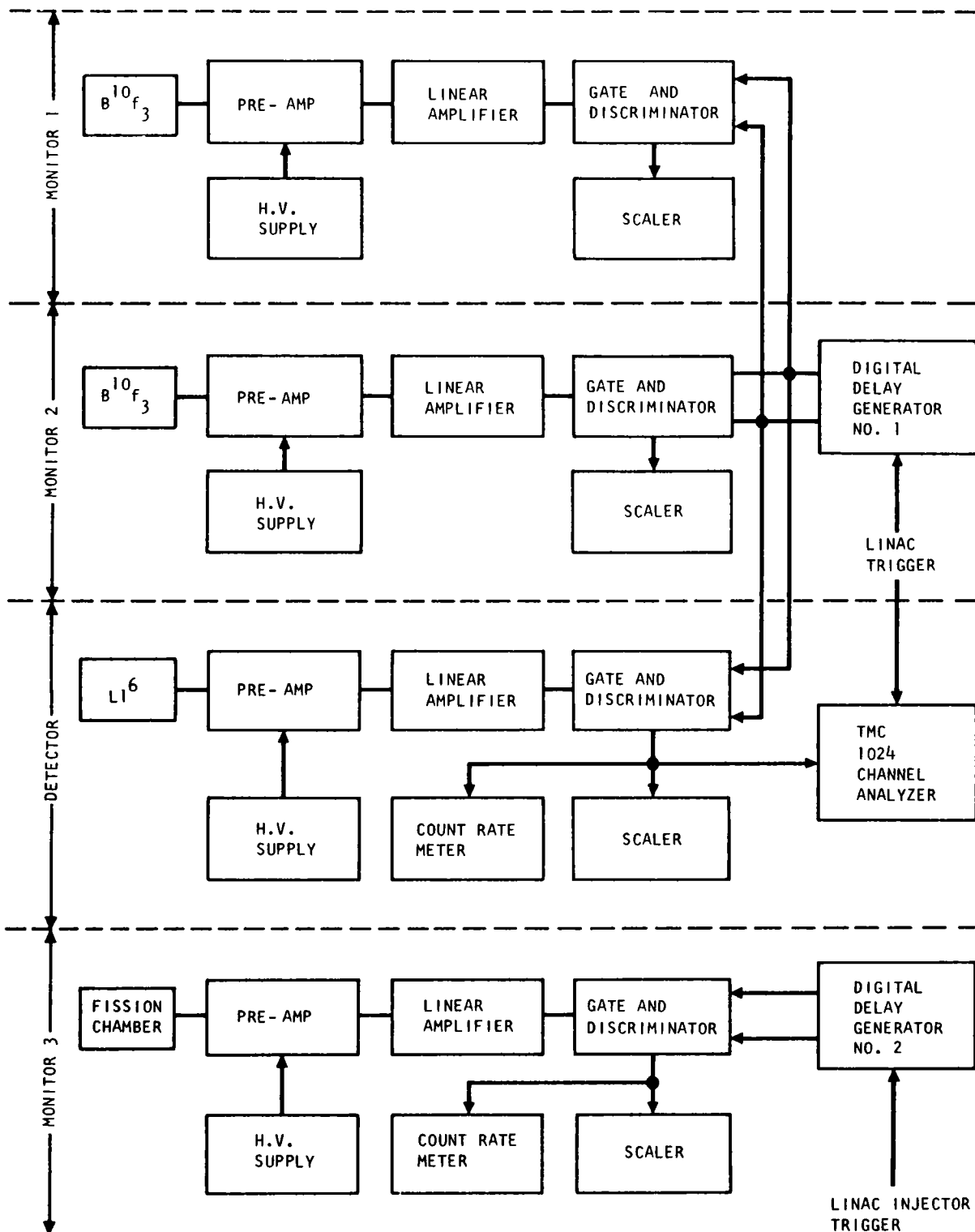


Fig. 10.9 -- Electronic block diagram for differential scattering experiment

comprise  $B^{10}F_3$  detectors located adjacent to the flight path near the scattering sample position. These monitors are proportional to the neutron flux striking the scattering sample. The third monitor (fission chamber) is located in the experimental room and detects the room return neutrons which are proportional to the pulsed source intensity. These three monitors have been used in preliminary checks of the new flight path arrangement and have "tracked" each other to within about 3 percent over large changes in linac intensity. The time gate units shown in Fig. 10.9 are used to adjust the time the monitors count between each linac pulse. Normally, these monitors and the  $Li^6$  detectors start counting about 300  $\mu$ sec after the linac pulse. The  $Li^6$  detector is used to count the scattered neutrons from the sample at various angles. The system is being expanded to provide more than one  $Li^6$  detector so as to obtain data at several angles simultaneously.

#### 10.4.7. Sample Design

Since it is desired in these experiments to try to obtain absolute cross sections, great care must be taken with the scattering sample design. Bulging and non-uniformity are not permissible. Further, thick walled targets are unacceptable because one cannot treat separately the scattering effect due to target holder and that of the sample. One cannot for example treat the serious multiple scattering on a thin water sample and at the same time ignore the perturbation to this of a thick aluminum cell wall. The first design employed in our experiments is shown in Fig. 10.10. The walls are 4 mil aluminum. The present design using stretched aluminum foil 2 mil thick is shown in Fig. 10.11 and should be more satisfactory.

#### 10.4.8. Background Studies

Although the routine elimination of background plagues most neutron experiments, some particularly interesting effects were discovered with the  $Li^6$  glass detector system. First it is essential to choose carefully the shielding material used everywhere in the flight path so that the neutron absorption takes place in  $B^{10}$ . Otherwise high energy capture gamma rays are produced which, due to the gamma sensitivity of the detector, may give pulses that fall in the window set to detect the  $Li^6 (n, \alpha)H^3$  reaction, and are thus counted. Even cadmium placed near the neutron source, to prevent room return, introduced unwanted counts into the neutron detector. Natural and cosmic background was relatively high in the  $Li^6$  detector until the shield cave was constructed for the angular distribution setup and even then great care had to be taken to monitor all construction materials used in the cave to avoid possible induced activity. The cave walls were placed as far as practical (3 feet) from the sample to eliminate scattered room return and these walls were heavily borated.

Due to the sensitivity of the detector to gamma rays it was necessary to test that the capture gamma rays from the water sample were not counting

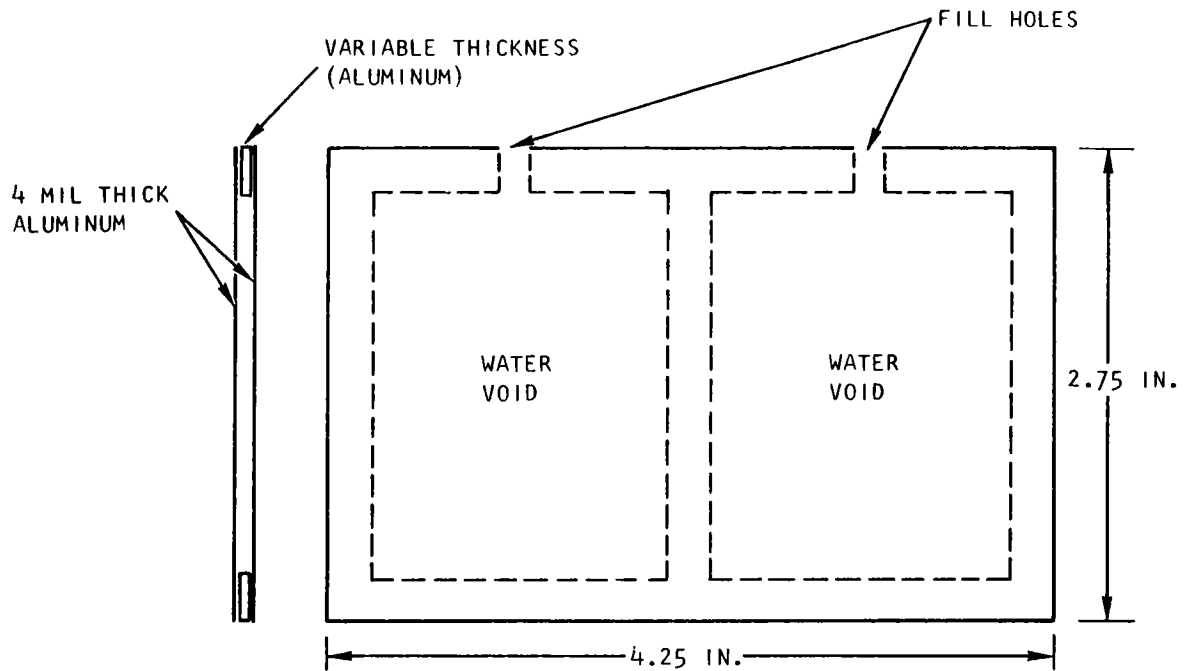


Fig. 10.10 -- Original H<sub>2</sub>O sample design

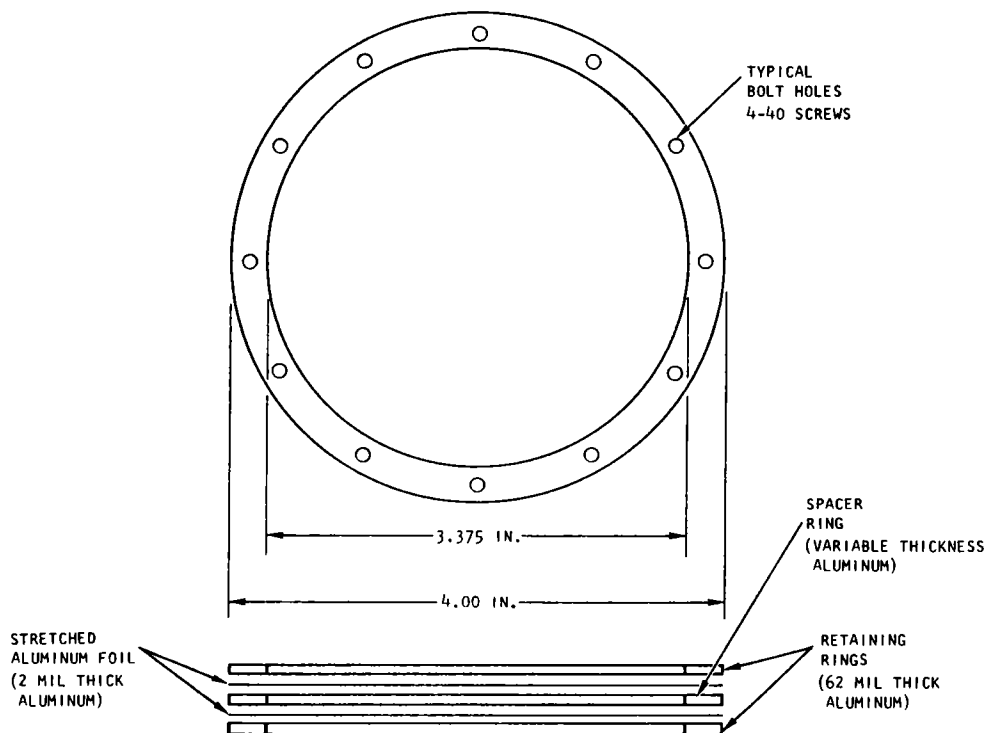


Fig. 10.11 -- Final H<sub>2</sub>O sample design

significantly. To perform this test the counting rate in the  $\text{Li}^6$  detector was measured with a water sample and the detector oriented at  $90^\circ$ . The water sample was left in place and a thin  $\text{B}^{10}$  slab was used to close off the opening to the detector. The counting rate observed was one percent of that with the thin  $\text{B}^{10}$  slab removed, essentially the ambient background. The sources of background present at the scattering angles appear to be from neutrons scattered from the air and room structure and from the water sample container itself. This latter background source is perhaps 20 percent of the former corrections. The total background is 10 to 20 percent of the signal count at the back scattering angles where the direct intensity is relatively low. Further improvements are possible by eliminating air scattering and also by improving the energy resolution of the  $\text{Li}^6$  detector system.

#### 10.4.9. Detector Spatial Response

It would be highly undesirable if the  $\text{Li}^6$  glass neutron detectors had a large spatially non-uniform response to thermal neutrons ( $< 5$  eV). Two types of effects could be present: (1) A non-uniformity of the  $\text{Li}^6$  distribution in which case the detector would not be black everywhere, (2) a black response but a variation of pulse height with position on the glass. To study these effects a 1/8 in. diameter collimated beam of thermal neutrons was positioned at various locations on the 2 in. diameter  $\text{Li}^6$  glass crystals. The pulse height distribution and absolute count rate (monitored) were recorded. It was found that the pulse height distribution did indeed depend on where the beam impinged on the crystal, but that the energy of pulse height window normally used was wide enough to include the entire variation. The total neutron response of the crystal under these typical circumstances is shown in Fig. 10.12. It is believed that these data demonstrate that the  $\text{Li}^6$  content is uniform in the glass and that no large regions of low sensitivity occur. The pulse height variations experienced with this crystal at various positions are shown in Fig. 10.13. The present system with the wide pulse height window is acceptable for our experiments now but we plan to improve the uniformity of the pulse height distribution by using short light pipes to separate the  $\text{Li}^6$  glass from the phototube. Thus phototube cathode non-uniformity will not produce as significant an effect on the local pulse height distributions. It is expected that this change will further increase the signal to background ratio at the large scattering angles. A further change which will be made in the detector is to restrict the size of the neutron beam striking the  $\text{Li}^6$  glass to avoid the edge effects.

#### 10.5. CROSS SECTION RESULTS

Differential scattering cross section ( $d\sigma/d\Omega$ ) measurements have been confined to two materials during the last year. An attempt was made to

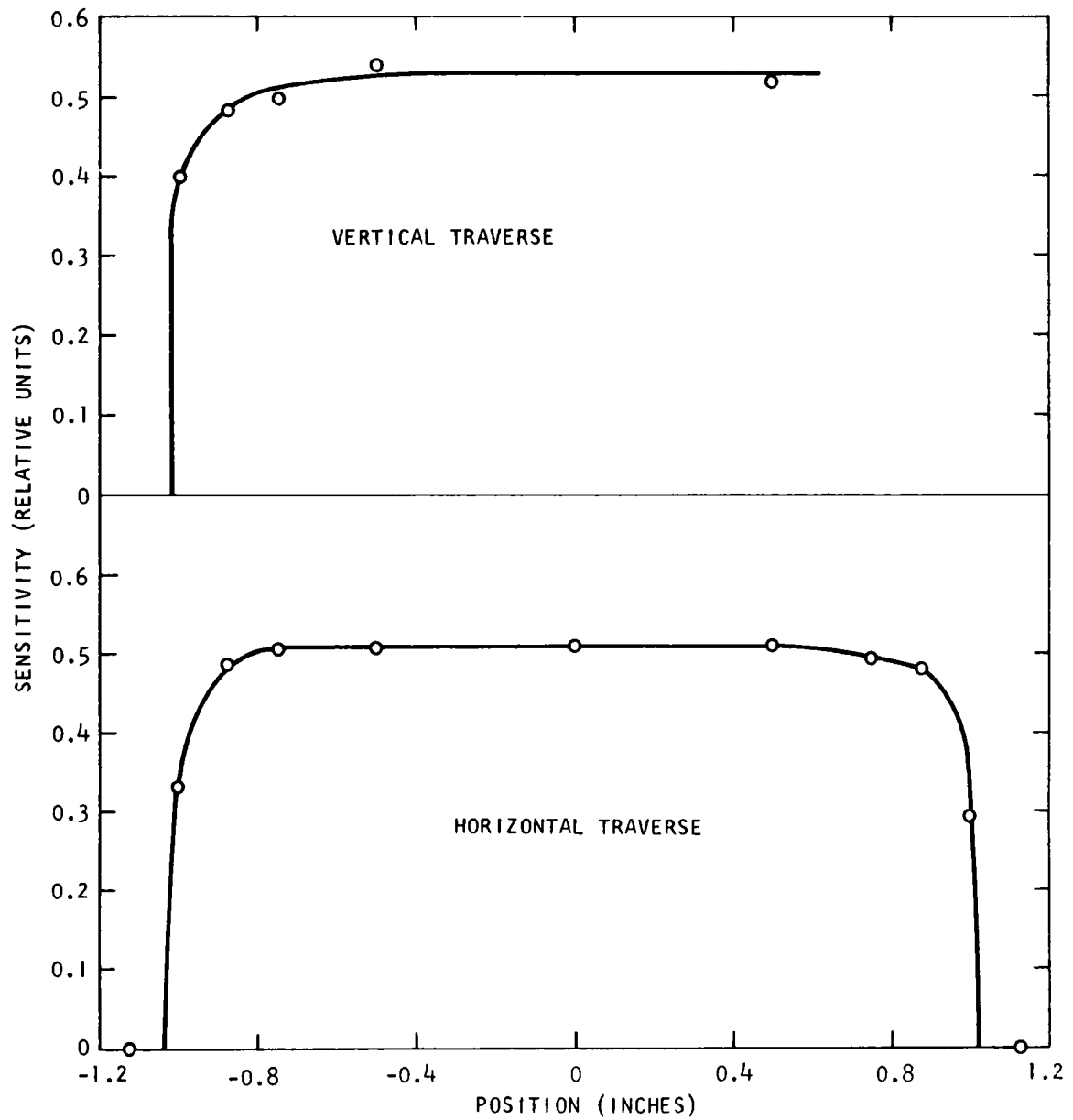


Fig. 10.12 -- Spatial variation of relative sensitivity of  $\text{Li}^6$  detector

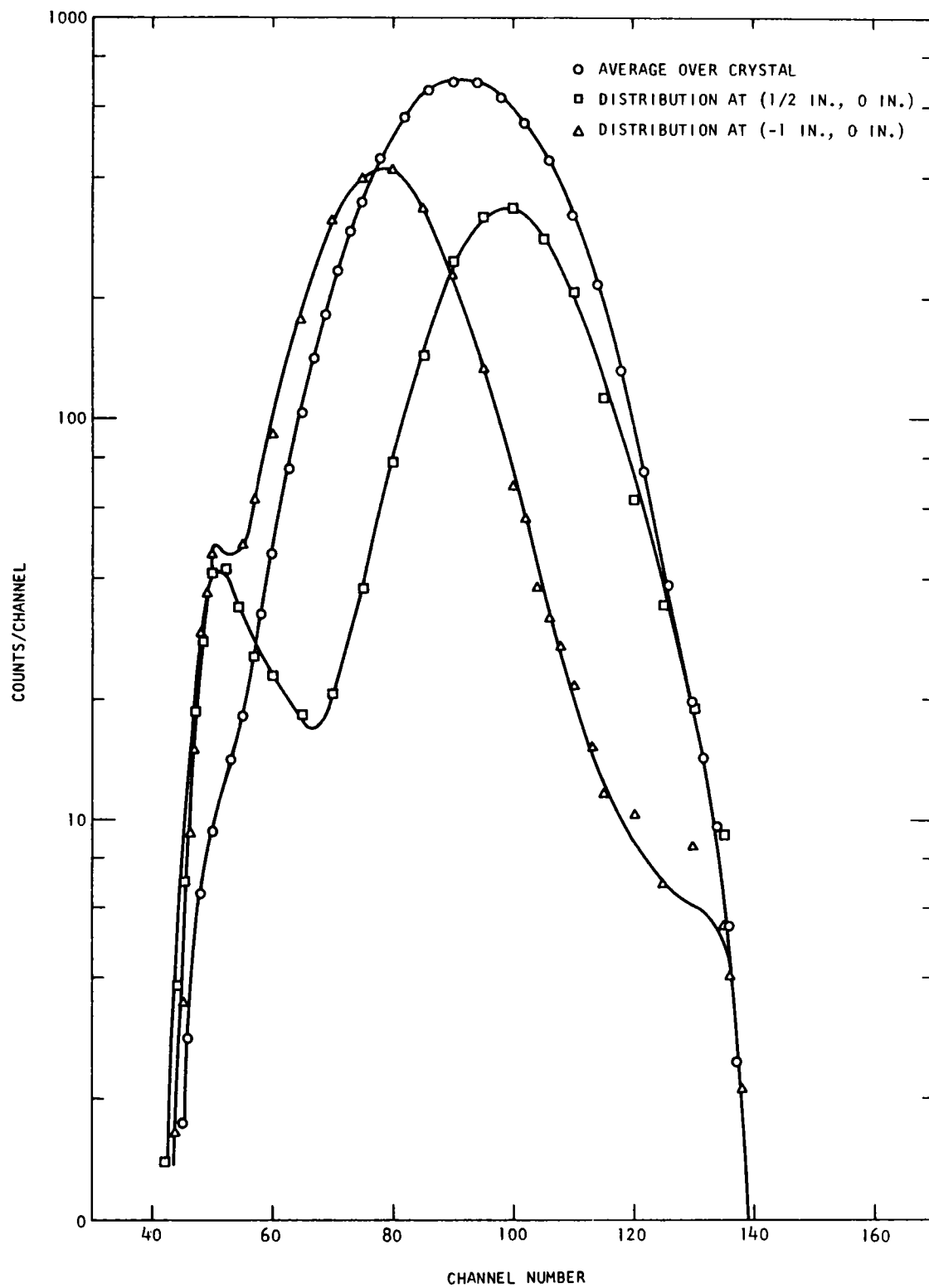


Fig. 10.13 -- Variation of detector spatial response with position

test the experimental apparatus using vanadium, and repeated runs have been made to measure the light water scattering cross section with precision. The status of these measurements is reviewed here.

Vanadium has been used by most workers performing scattering measurements for apparatus check and calibration. The lattice structure of this metal is of a simple cubic form and the neutron scattering is entirely incoherent due to the spin (7/2) of the ground state. The incoherent inelastic scattering cross section is given simply by

$$\frac{d^2\sigma}{d\Omega dE} = \frac{\sigma_b}{4\pi} \frac{k'}{k} \frac{\alpha e^{-\alpha\lambda}}{\left( \frac{\hbar\omega}{e^{\beta\hbar\omega} - 1} \right)} f(\omega) + \text{higher order terms} \quad (10.5.1)$$

where  $k$  and  $k'$  are the wave numbers of the incident and scattered neutrons,  $\hbar\omega$  is the energy transferred,  $\alpha = \hbar^2 \xi^2 / 2mk_B T$  where  $\xi = |k - k'|$  and  $\lambda$  is the Debye-Waller factor. The elastic incoherent scattering cross section is given by

$$\frac{d\sigma}{d\Omega} = \frac{\sigma_b}{4\pi} e^{-\alpha\lambda} \quad (10.5.2)$$

The Debye Waller factor depends on the lattice frequency spectrum as follows:

$$\lambda = \int_0^\omega \max \frac{f(\omega)}{\omega} \coth \frac{\omega}{2T} d\omega \quad (10.5.3)$$

Thus knowing  $f(\omega)$  and  $\sigma_b$  we can calculate total cross sections, and elastic and inelastic scattering angular distributions. In practice, equation (10.5.1) can only be used over an extremely small energy range since the higher order phonon excitation becomes important. Thus the inelastic scattering part of the cross section is calculated by introducing the characteristic frequency spectra  $f(\omega)$  into the computer code SUMMIT,<sup>(26)</sup> which considers higher order phonon terms. The general magnitude of the elastic and inelastic components of the scattering cross section can be seen in Fig. 10.14. The wiggles in the inelastic cross sections are not real but represent energy mesh difficulties in SUMMIT. The energy mesh used in the calculation was not sufficiently fine due to the computational expense. Calculated angular distributions are given in Fig. 10.15. The reliability of the data used in this calculation is certainly subject to discussion. The Eisenhauer-Pelah<sup>(65)</sup> frequency distribution (Fig. 10.16) was employed to make the calculations of both elastic and inelastic scattering. This "experimentally" determined spectrum may be quite uncertain<sup>(66)</sup> in view of the disagreements with theoretical predictions



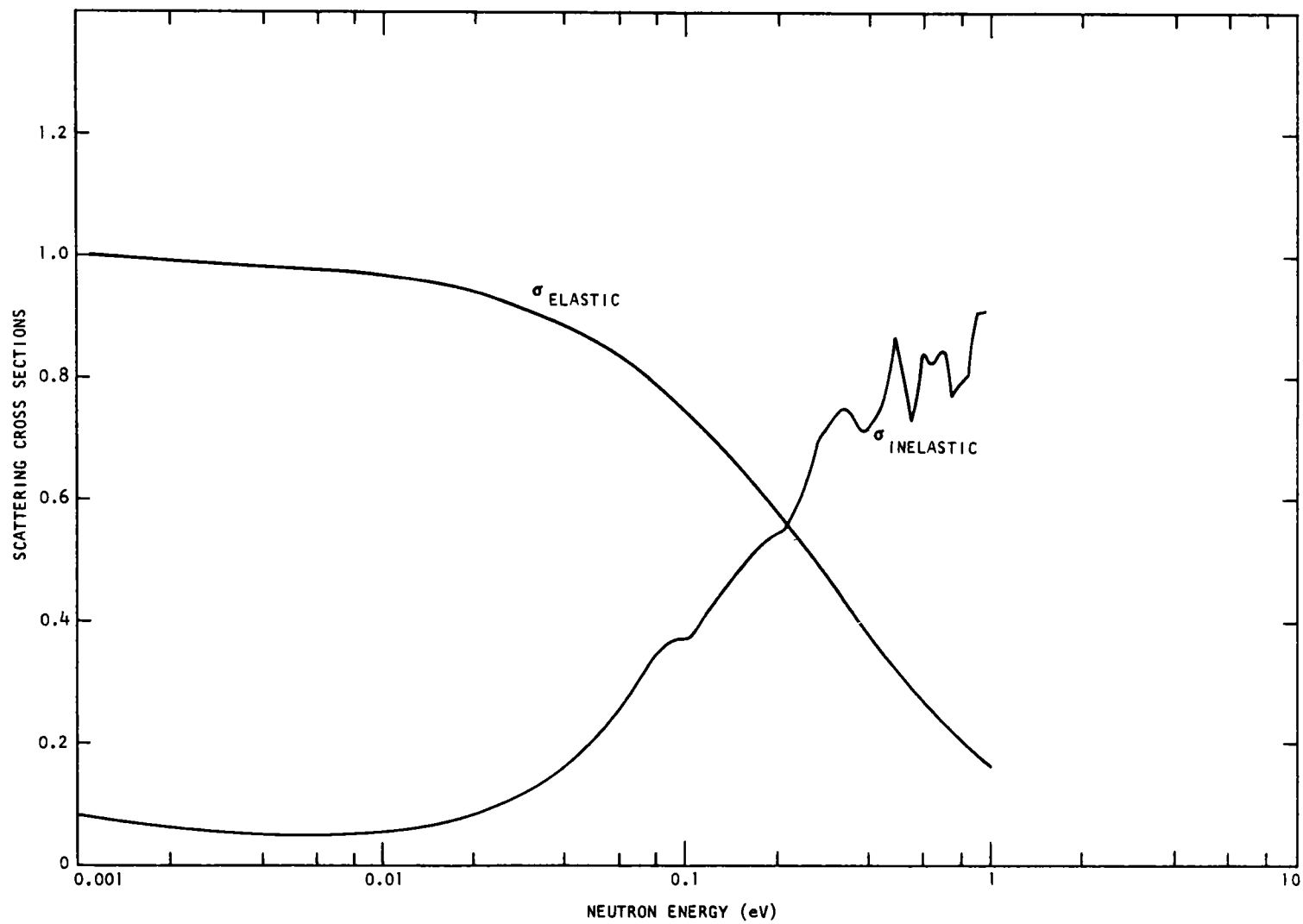


Fig. 10.14 -- Elastic and inelastic contributions to the scattering cross section of vanadium

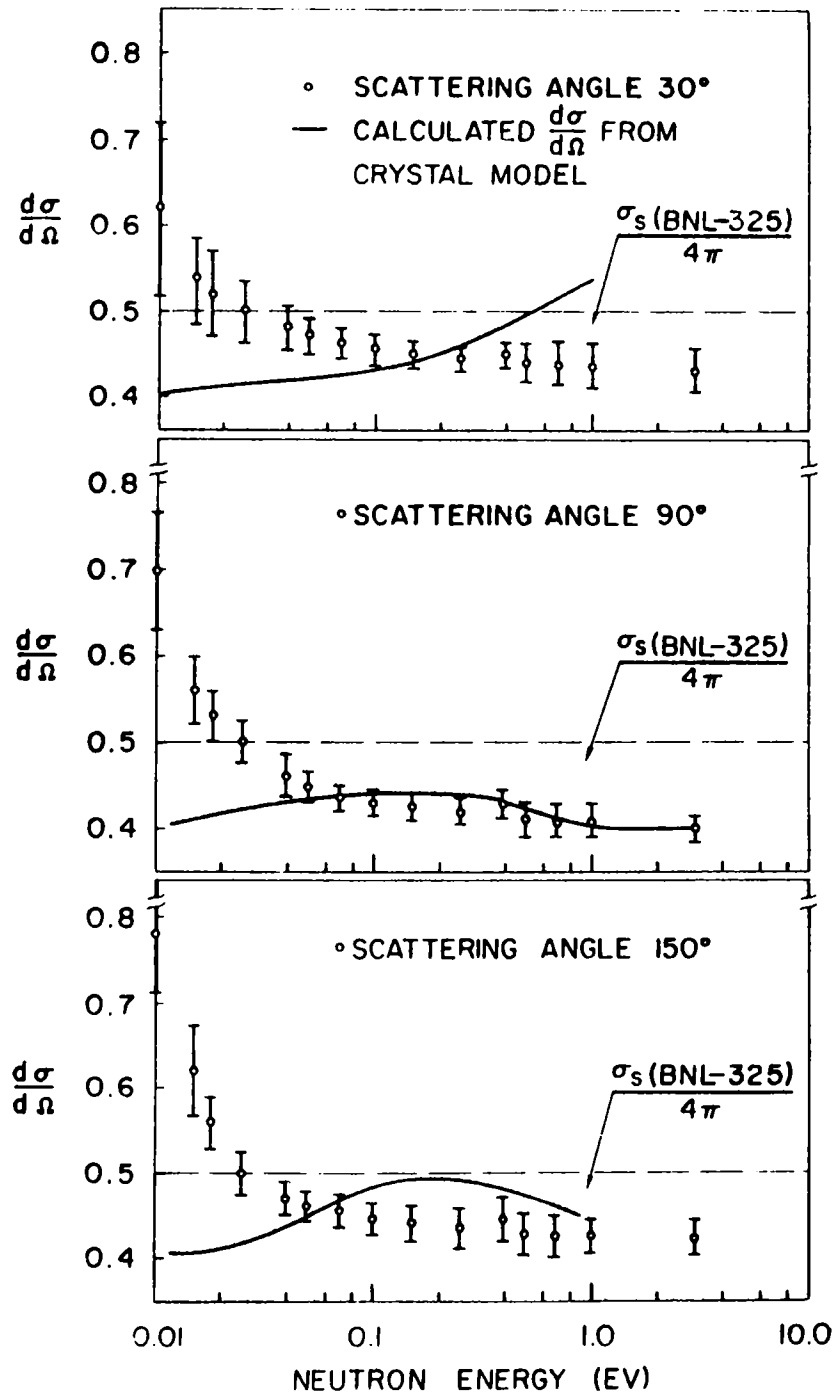


Fig. 10.15 -- Calculated and experimental scattering cross sections for vanadium at three scattering angles

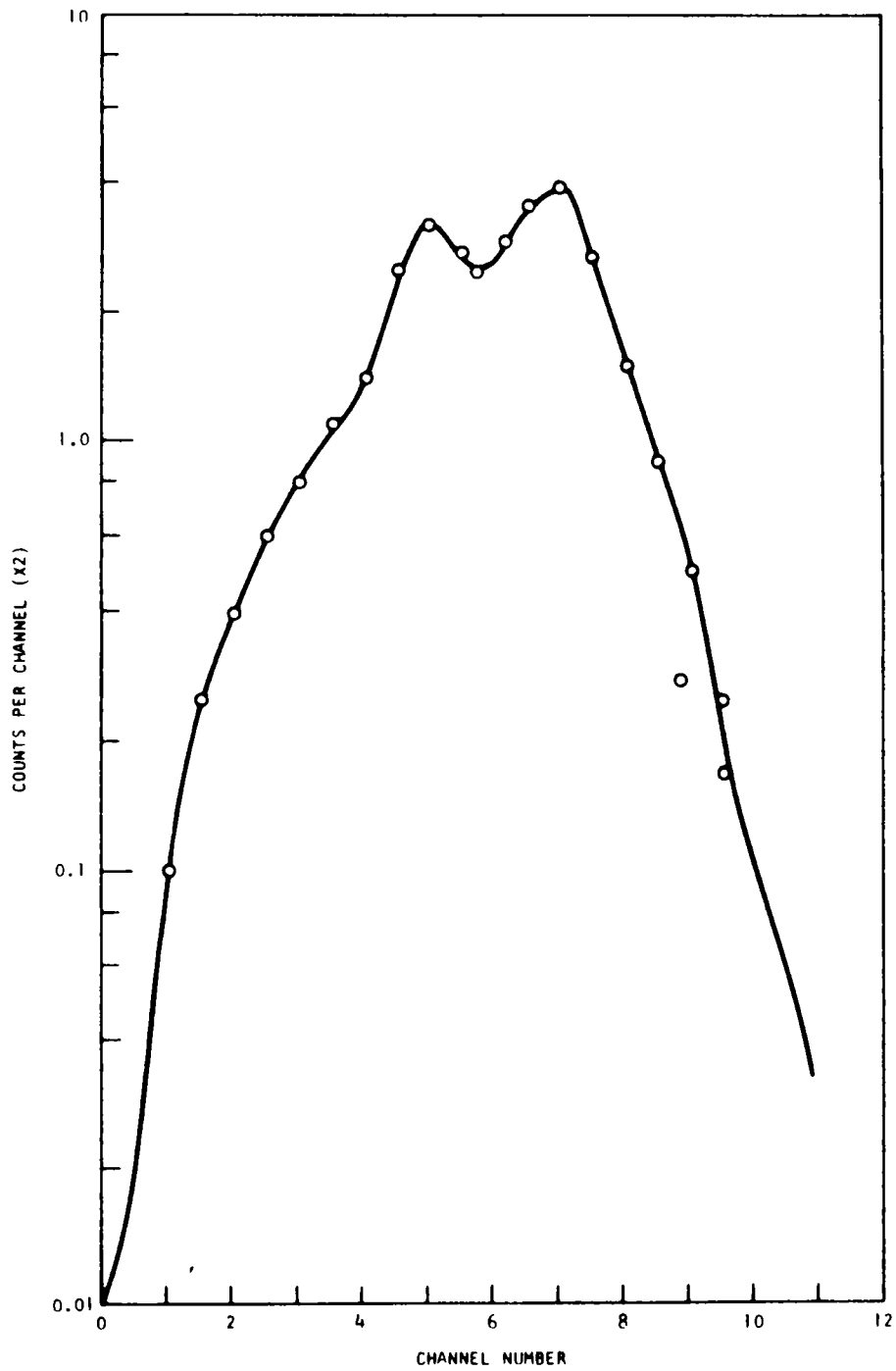


Fig. 10.16 -- The Eisenhauer-Pelah frequency distribution for vanadium

(a factor of 2). However, even this much variation in the frequency spectrum can usually be tolerated because various integrals over the spectrum are performed in obtaining the scattering cross sections. However, the bound atom cross section for vanadium is a different story. Cross section values given in BNL 325 would lead one to believe this cross section to be uncertain by  $\pm 10\%$ . Therefore in Fig. 10.15 only a rather coarse range of acceptable values for  $d\sigma/d\Omega$  can be established on theoretical grounds. Only this range of values established by the scattering cross section divided by  $4\pi$  is shown in Fig. 10.15. The theoretical calculation of the non isotropic angular distribution (shown by the solid line) is of course equally uncertain by a multiplicative factor due to questions on the precision of the bound atom scattering cross section. As a result we simply do not know at this stage the cross sections of vanadium well enough to provide a really sensitive check of the experimental apparatus.

The experimental measurements of vanadium cross sections are given as a function of energy and angle in Fig. 10.15; experimental error is also given. The cross section was calculated from the experimental data using equation 10.2.13 although  $C_f$  and  $C_R$  were set equal to 1. Due to uncertainties in the calculated values, one cannot say that the experimental results differ from the theoretical predictions although the general shape of the predicted cross section curve is different than the experimental.

The differential scattering cross section for water ( $H_2O$ ) has been measured at room temperature over the energy range 0.01 eV to 2 eV. The experimental data are given in Fig. 10.17. Also shown is the calculated cross section for water using the original Nelkin model<sup>(6)</sup> in the computer code GAKER.<sup>(12)</sup> The experimental cross section data are still normalized in this case to the theory at one energy, although the methods of analysis under development in this program should make this step unnecessary in the future. There are a number of disagreements apparent between the theory and experiment. First the pronounced variation in the calculated cross section curve, at about 0.06 eV, is not apparent in the experimental data largely because the Nelkin procedure assumes all rotational motion can be represented by a properly weighted torsional oscillator at 0.06 eV. This is known not to be the case; rather a continuous band of frequencies is present. At high energies and large angles, clear-cut disagreement between theory and experiment is apparent. It is believed that under these conditions the angular distribution is especially sensitive to the gross properties of the inelastic scattering description, so the present discrepancy here is important.

The Nelkin model is not able to reproduce in detail the differential scattering data reported here or that from Springer.<sup>(67)</sup> The German work<sup>(67)</sup> especially indicates that  $\bar{\mu}$  (Nelkin)<sup>(6)</sup> is too large but that  $\bar{\mu}$  calculated for the molecular frequency spectrum of Haywood<sup>(8)</sup> is in better

agreement with the experimental values. In fact detailed comparisons of angular distribution data<sup>(67)</sup> and neutron spectral data<sup>(68)</sup> for water appear to show better agreement with the predictions of the Haywood kernel. A lower value for the diffusion constant  $\langle D \rangle$  is also calculated by the Haywood kernel than the Nelkin kernel which seems to be called for on the basis of results from pulsed neutron experiments.<sup>(69)</sup>

An attempt has been made to see if one can account for the disagreements reported in Fig. 10.17 on the basis of the isotropic vibration assumption made in the GAKER<sup>(12)</sup> code. A scattering kernel which includes the anisotropic vibration of the hydrogen atoms in the molecule has been reported in the last annual report. It has been shown to predict large changes in the double differential cross section. This kernel was used to calculate the differential scattering cross section  $d\sigma/d\Omega$  and the result is compared to the simple Nelkin model result in Fig. 10.18. Disagreements are present but the general shape of the cross section is not greatly different from the previous result and it is believed that the effect of anisotropy cannot explain the disagreements with experiment. However, neglecting the continuous nature of the rotational frequency band may be the cause of the difficulties.

One further series of calculations performed this year indicates the sensitivity of this differential cross section to the physical model used to describe the hydrogen binding. Results from the Nelkin model are given as well as the free gas model in Fig. 10.19. The results based on the Radkowski<sup>(70)</sup> prescription are also shown. It will be recalled that the Radkowski prescription consists of  $P_0$  and diagonal  $P_1$  scattering matrices devised in such a way that one can predict the total cross section of  $H_2O$  correctly. The procedure also gives the correct transport cross section. However, it is clear from Fig. 10.19 that one obtains large differences between the free gas, Radkowski prescription, and bound hydrogen models in the calculations of the angular scattering cross section, in contrast to the experience in infinite medium or space dependent spectral investigations where disagreements are usually not in excess of twenty percent.

During this year some effort has also been made to determine whether it would be possible to construct  $S(\alpha, \beta)$  from the  $d\sigma/d\Omega$  measurements. Equivalent attempts at synthesis are underway in Germany.<sup>(67)</sup> The procedure is briefly as follows:

We can define the scattering law for a material by the relation

$$\frac{d^2\sigma}{dE d\Omega} = \frac{kT}{4\pi} \sigma_f \left( \frac{A+1}{A} \right)^2 e^{-\beta/2} \left( \frac{E}{E_0} \right)^{1/2} S(\alpha, \beta) . \quad (10.5.4)$$

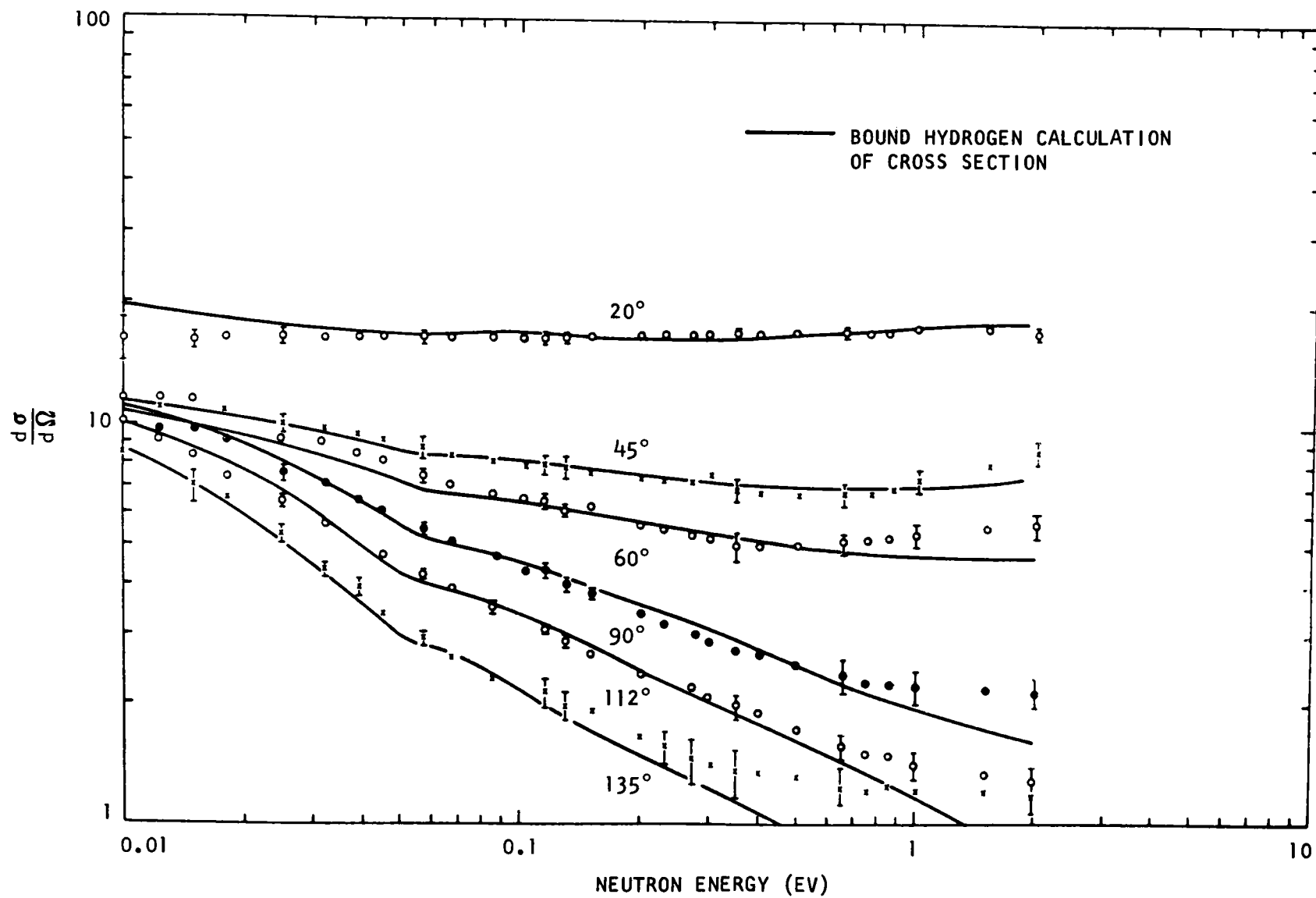


Fig. 10.17 -- Calculated and measured differential scattering cross sections for H<sub>2</sub>O

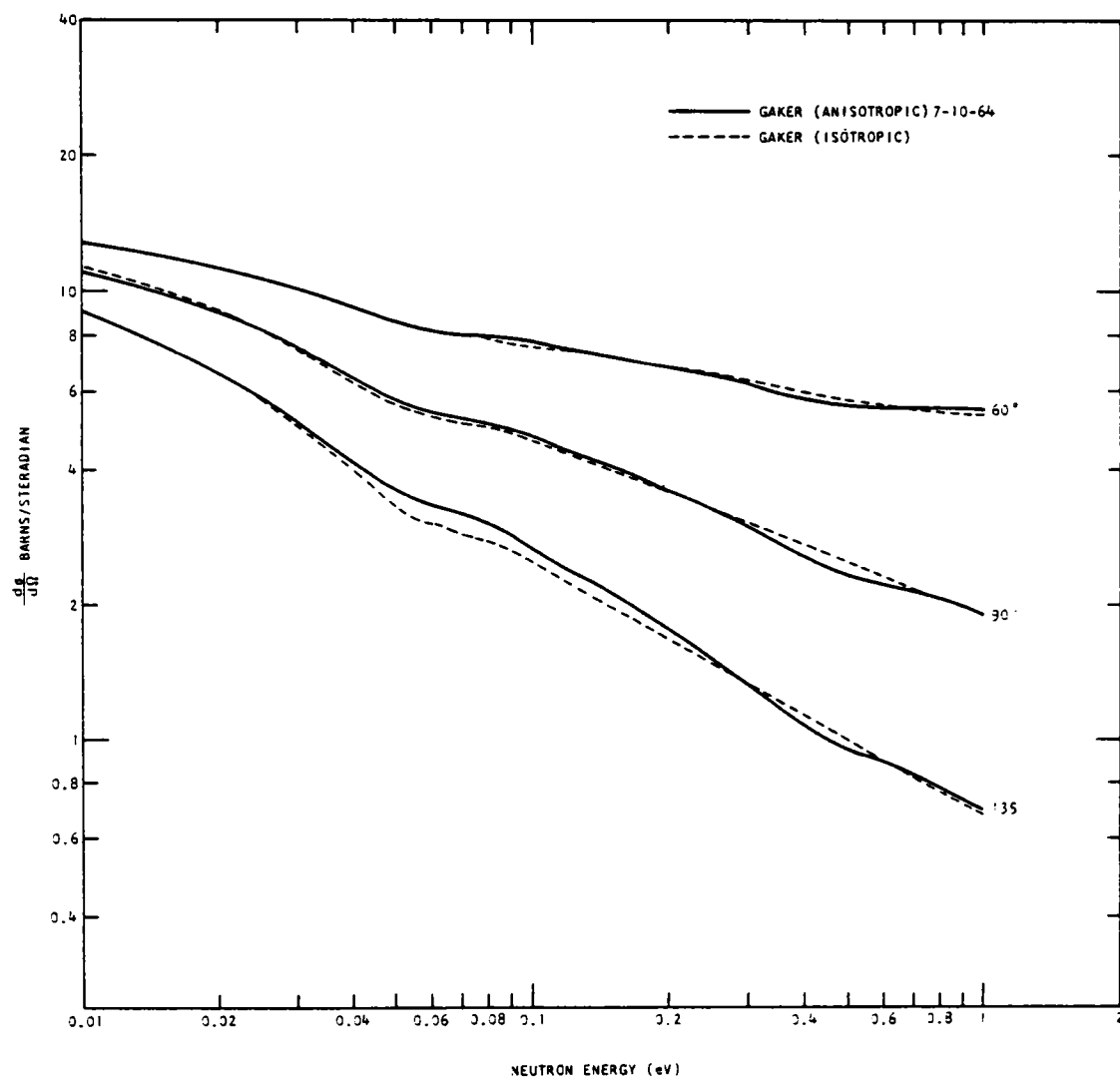


Fig. 10.18 -- Comparison of scattering cross sections calculated from the isotropic and anisotropic  $H_2O$  models

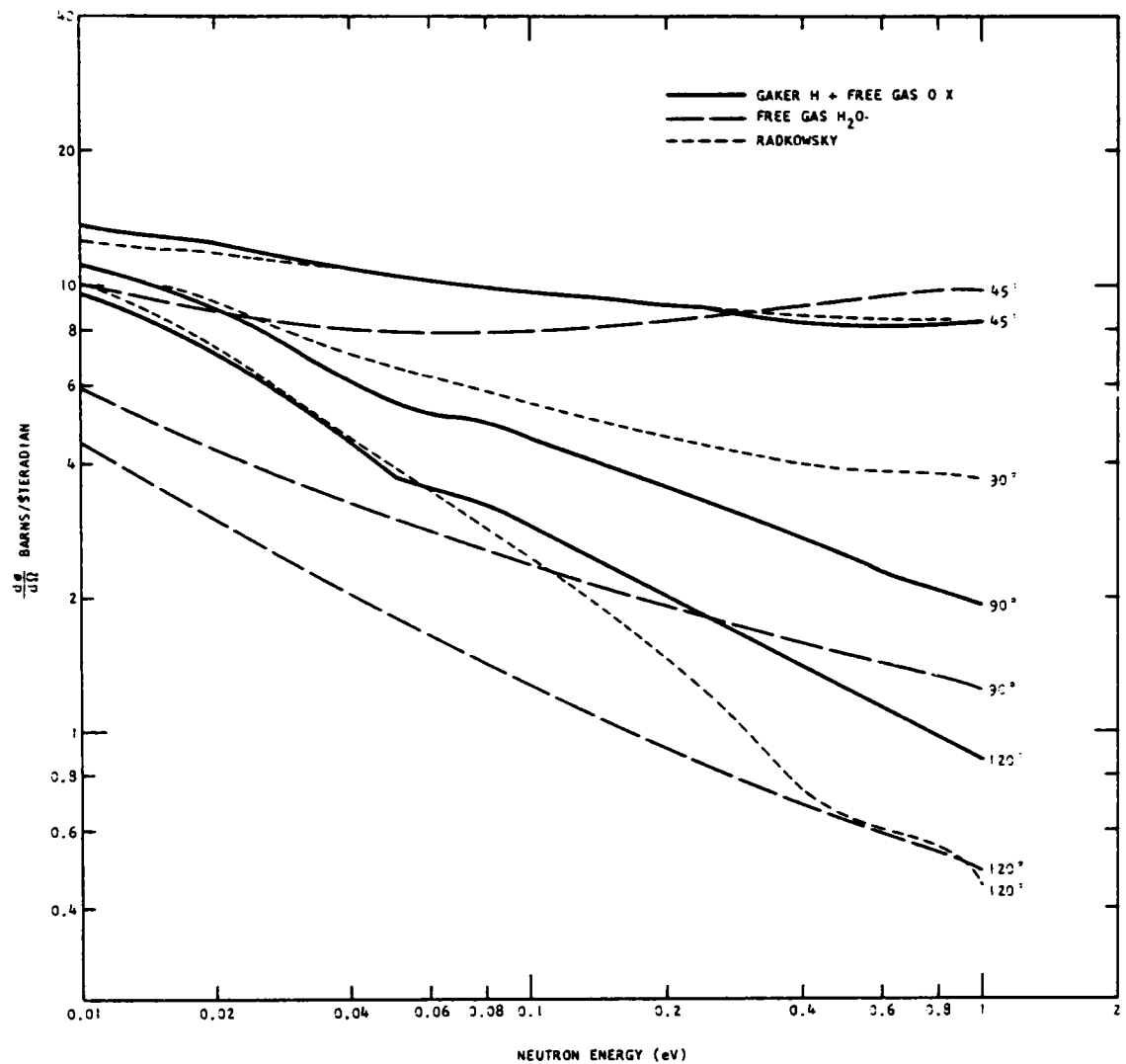


Fig. 10.19 -- Comparison of the scattering cross sections calculated from different models for H<sub>2</sub>O



where  $\sigma_f$  = free atom cross section,  
 $A$  = ratio of mass of scattering nucleus to neutron mass,  
 $k$  = Boltzmann's constant,  
 $E_0$  = initial energy of neutron,  
 $E$  = final energy of neutron,

$$\beta = \frac{E_0 - E}{kT} ,$$

$$\alpha = \frac{E_0 + E - 2\sqrt{E_0 E} \mu}{AkT}$$

$S(\alpha, \beta)$  = scattering law,  
 $\mu$  = cosine of angle of deflection of scattered neutron.

Integrating over all final energies we obtain

$$\frac{d\sigma}{d\Omega} = \frac{kT}{4\pi} \sigma_f \left( \frac{A+1}{A} \right)^2 \int_0^\infty e^{-\beta/2} \sqrt{\frac{E}{E_0}} S(\alpha, \beta) dE . \quad (10.5.5)$$

Changing the variable of integration from  $dE$  to  $d\beta$  and approximating the integrand by a numerical quadrature we obtain

$$\frac{d\sigma}{d\Omega}(E_0) = \frac{(kT)^2}{4\pi} \sigma_f \left( \frac{A+1}{A} \right)^2 \sum_{\ell} e^{-\beta_{\ell}/2} \sqrt{1 - \frac{\beta_{\ell} kT}{E_0}} S[\alpha(\beta_{\ell}, E_0, \mu), \beta_{\ell}] W_{\ell} , \quad (10.5.6)$$

where  $W_{\ell}$  is the weight function. If we now set

$$S[\alpha(\beta_{\ell}, E_0, \mu), \beta_{\ell}] = \sum_n A_{n, \ell, E_0, \mu} S(\alpha_n, \beta_{\ell}) , \quad (10.5.7)$$

where the  $\alpha_n$  are chosen independently and the  $A_{n, \ell, E_0, \mu}$  are interpolation coefficients, we obtain the set of linear equations

$$\frac{d\sigma}{d\Omega}(E_0) = \frac{(kT)^2}{2} \sigma_f \left( \frac{A+1}{A} \right)^2 \sum_{\ell} \sum_n e^{-\beta_{\ell}/2} \sqrt{1 - \left( \frac{\beta_{\ell} kT}{E_0} \right)} A_{n, \ell, E_0, \mu} S(\alpha_n, \beta_{\ell}) W_{\ell} \quad (10.5.8)$$

Thus we have a set of linear equations for the  $S(\alpha_n, \beta_\ell)$ . Preliminary tests of the procedure have been made with the free gas model and indications are that the experimental  $d\sigma/d\Omega$  data presently available are not exact enough to be subjected to this method of analysis. When final absolute cross sections are obtained for water we will proceed with a test of the procedure.

The single differential scattering experiment lends itself to further extensions and improvements in the future. Briefly these include studies of not so thin slabs where double and triple scattering is even more important. The transport solution of these clean geometry problems should not be ambiguous. One will lose sensitivity to the scattering kernel but the general problem should be akin to that encountered in a fuel-moderator array. Interposing various absorbers or energy selection devices between the scattering sample and black detectors introduces the possibility of biasing the sensitivity of the measurement either toward detection of elastic or inelastic scattering. In part Springer<sup>(67)</sup> has shown that by proper use of absorption one may determine energy moments of the scattering kernel. (The first two moments according to some<sup>(71)</sup> are all that is needed to describe the thermal spectrum). Another experiment of "fundamental" interest is the small angle scattering experiment which Forte<sup>(72)</sup> and Springer<sup>(67)</sup> have been carrying out to investigate clustering effects. A further experiment in this type of arrangement allows the possibility of performing crystal diffraction studies as shown by Buras.<sup>(73)</sup> Experiments with powdered samples permit one to set up at one angle only and study the diffraction pattern. Experiments with single crystals are also possible but in this case the scattering angle must be varied.



## XI. EXPERIMENTAL AND CALCULATIONAL TECHNIQUES

### 11.1 SENSITIVITY OF DETECTOR BANKS

The sensitivities of the detector banks at the 16-M and 50-M stations are checked regularly since they are extremely important in spectral measurements. These sensitivities enter directly into the calculation of flux per unit energy at each energy. The standard method for calibration of the 16-M detector bank is to compare its response to a given incident flux with the response of a standard detector to the same flux, the efficiency of the standard detector being obtained by calculations. The 50-M detector bank is checked by straight comparison to the 16-M detector bank since it is located in the same line of flight.

Two comparison detectors have been used, a bank of low pressure  $\text{BF}_3$  counters and a lithium glass scintillator. In the past<sup>(3)</sup> the 16-M sensitivities obtained with these comparison detectors have not been the same and considerable effort has been directed towards resolving the discrepancy. The details of these efforts for this year are given in references 52, 74 and 75, but the present position is summarized below. When the low pressure  $\text{BF}_3$  bank was used as the standard detector, the discrepancy in the 16-M  $S(E)$  was somewhat reduced by decreasing the post collimator diameter so that edge effects in the standard detector were eliminated. In addition, a more careful calculation of this standard detector's efficiency was made to determine accurately its departure from a  $1/v$  behavior. When the lithium glass scintillator was the comparison detector, the discrepancy in the 16-M  $S(E)$  was reduced by more careful monitoring and by greater attention to calculating the efficiency of that scintillator. There was good evidence to believe that the lithium content of the glass was somewhat less than the value of 7.2 wt% specified by the supplier. Finally a calculation was directly performed of the efficiency of the 16-M detector bank which was not a trivial problem due to its geometry; the bank consisted of 32  $\text{BF}_3$  counters stacked into seven rows. The sensitivity  $S(E)$  of the 16-M bank by these three methods is shown in Fig. 11.1. For comparison the  $S(E)$  obtained on 12-18-62 (our presently accepted sensitivity) is shown offset in the same figure. Though a small difference exists, we are not sufficiently confident of the later values of  $S(E)$  to change all of our spectral measurements. Instead we plan to repeat comparison measurements using a lithium glass detector where the  $\text{Li}^6$  content has been accurately determined by spectrographic means. Hopefully definitive values for the 16 M  $S(E)$  can then be obtained.

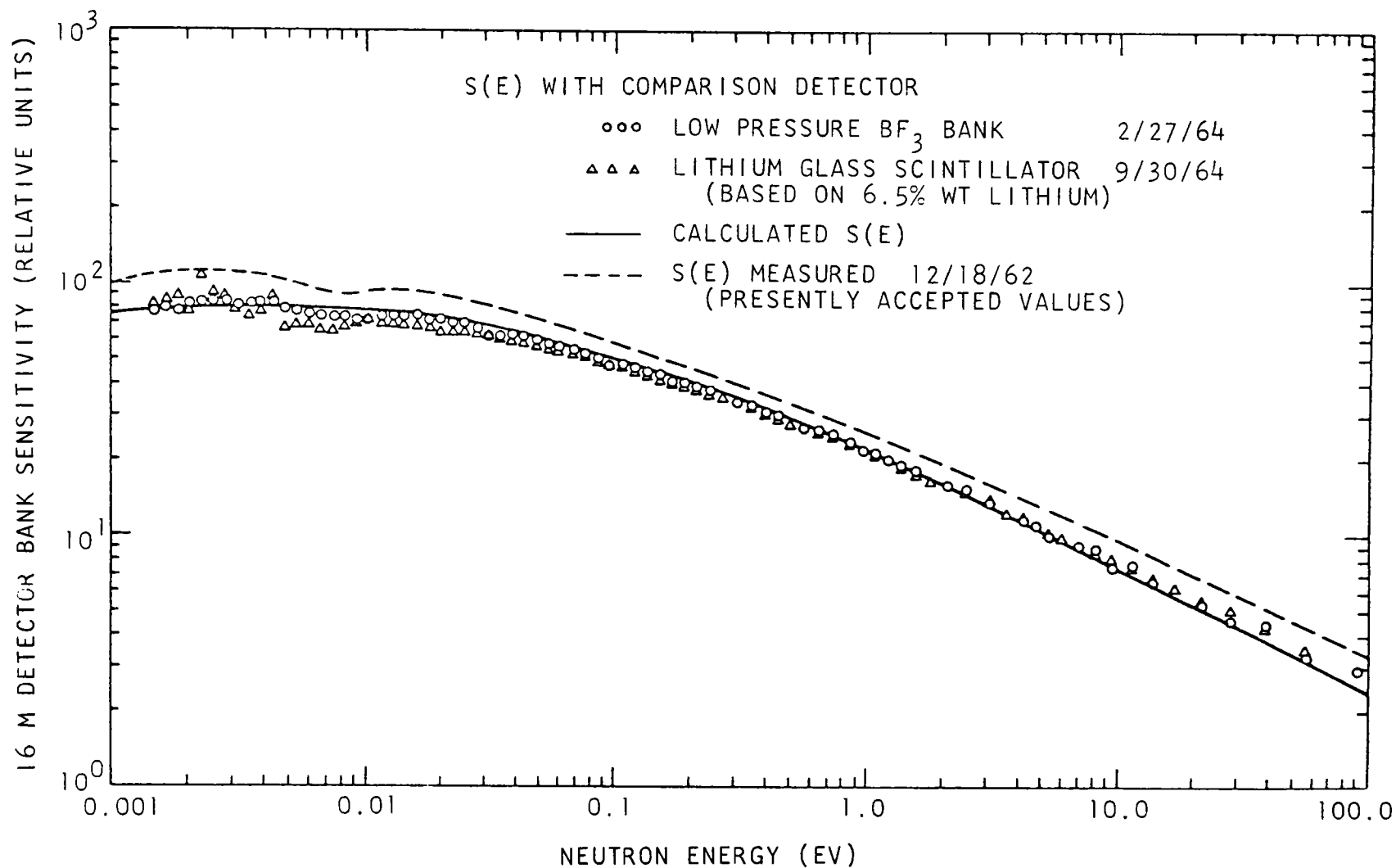


Fig. 11.1 -- Measured and calculated sensitivity of 16 M  $\text{BF}_3$  detector bank

The sensitivity of the 50-M detector bank was measured twice during this year, the second one being the most important since the old flight path of helium-filled gas bags was replaced by evacuated tubes. The resulting 50-M S(E) was essentially the same as in the first measurement in which a comparison with the 16-M detector bank was performed. Using the S(E) for the 16-M bank from 12-18-62, the values for the 50-M S(E) in Table 11.1 were obtained.

Table 11.1

## RELATIVE S(E) OF 50-METER DETECTOR BANK (11/22/63)

E(ev)	S(E)	E(ev)	S(E)	E(ev)	S(E)	E(ev)	S(E)
1,000,000	0.064	570	0.212	3	0.480	0.013	1.33
100,000	0.094	560	0.213	2	0.513	0.011	1.34
10,000	0.135	550	0.214	1.5	0.540	0.01	1.35
9,100	0.138	500	0.218	1	0.58	0.0095	1.35
8,000	0.140	400	0.225	0.9	0.59	0.009	1.35
7,300	0.142	300	0.235	0.8	0.60	0.008	1.35
6,300	0.146	245	0.242	0.7	0.615	0.007	1.35
6,100	0.147	230	0.246	0.6	0.63	0.006	1.35
5,700	0.148	220	0.247	0.5	0.65	0.005	1.35
5,500	0.149	200	0.250	0.4	0.675	0.004	1.35
5,000	0.150	150	0.262	0.3	0.71	0.0035	1.34
3,000	0.164	100	0.280	0.2	0.76	0.003	1.33
2,100	0.173	70	0.294	0.15	0.80	0.0025	1.32
1,500	0.182	50	0.309	0.1	0.86	0.002	1.30
1,000	0.194	30	0.330	0.09	0.875	0.0015	1.27
900	0.198	20	0.351	0.08	0.895	0.001	1.21
800	0.201	15	0.367	0.06	0.945	0.0005	1.06
700	0.206	10	0.390	0.05	0.99		
660	0.208	9	0.398	0.04	1.04		
640	0.209	8	0.405	0.03	1.12		
620	0.210	7	0.413	0.025	1.18		
600	0.210	6	0.426	0.02	1.24		
590	0.211	5	0.438	0.018	1.27		
580	0.212	4	0.455	0.015	1.32		

## 11.2 CALIBRATION OF ZIRCONIUM SCATTERER

Scalar flux measurements have been made in the past by using a zirconium scattering plug in a straight through hole instead of a re-entrant probe. In principle the scatterer performs the following integral:

$$\phi(E, Z) = \int_{-1}^{+1} \int_0^{\infty} \phi(E', Z, \mu) \sigma_s(E \rightarrow E', \mu) dE' d\mu \quad (11.2.1)$$

When the scatterer is heavy the energy change  $E \rightarrow E'$  becomes very small. If the scatterer is completely incoherent in its scattering, the approximation of the scattered flux to the scalar flux is an excellent one. At low energies, however, Bragg scattering (coherent elastic scattering) occurs in zirconium which distorts the scattered flux from the scalar value. An attempt has therefore been made to calibrate the particular zirconium plug used in its normal angular orientation by comparing the scattered flux at low energy with the  $90^\circ$  angular flux at the same location. In this calibration two assumptions are made:

- a. The  $90^\circ$  angular flux and the scalar flux are essentially the same.
- b. The angular ( $\mu$ ) dependence of  $\sigma_s$  is small. Consequently the results obtained for the calibration geometry are assumed to be independent of the flux gradient there and are taken as applicable to other geometries.

In this case an assembly of pure polyethylene was used in the flux comparison since it produces a very thermal spectrum. Figure 11.2 shows the ratio of the scattered flux to the  $90^\circ$  angular flux and indicates clearly the effects of Bragg scattering. This calibration function has been applied to measurements made in borated  $H_2O$  performed at various temperatures in a pressure vessel.<sup>(3)</sup> Figure 11.3 shows a spectrum measured at room temperature with and without the correction. The smoother appearance of the corrected curve gives confidence in the use of this calibration function for future measurements in the pressure vessel.

## 11.3 NEUTRON MONITOR STUDIES

During any measurement of neutron spectra, the intensity of the pulsed neutron source must be monitored to provide normalization of the spectra at various positions in the assembly under measurement and to allow for correct subtraction of the background. During this contract year studies of various monitoring devices were made in the integral neutron

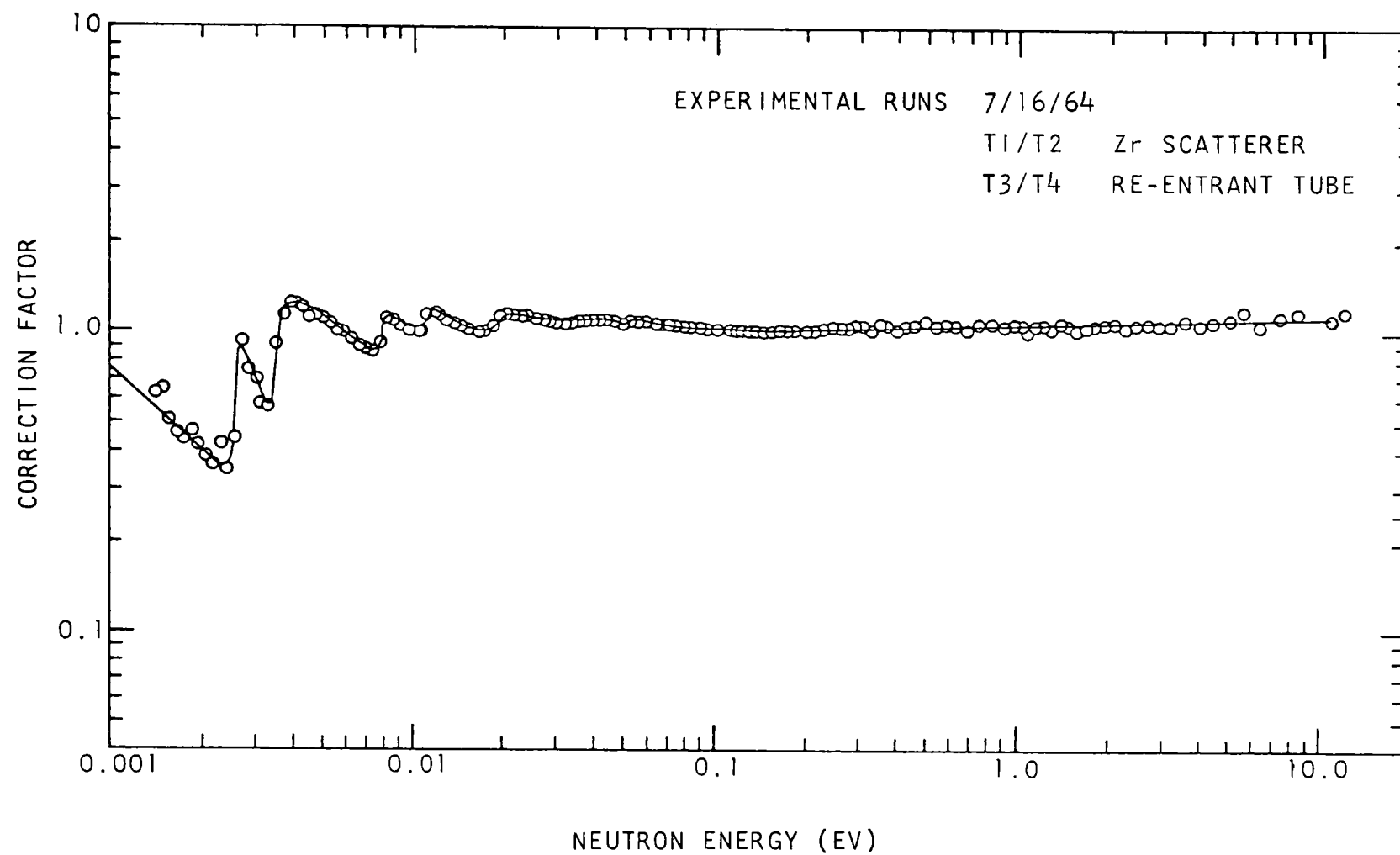


Fig. 11.2 -- Scalar Flux Correction factor for the zirconium scattering plug



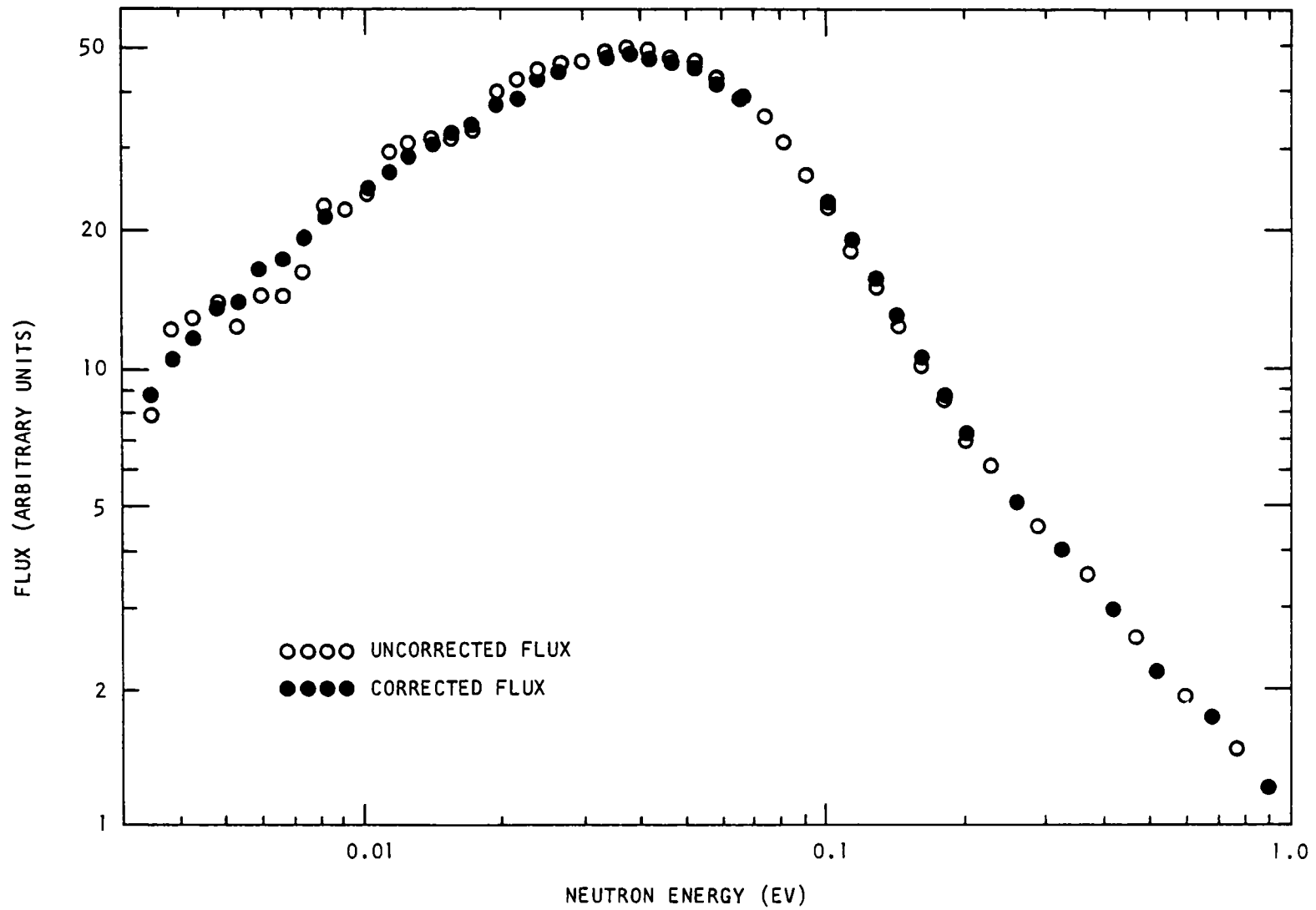


Fig. 11.3 -- Corrected and uncorrected scalar flux in borated water at 293°K

thermalization program which were reported in references 74 and 75. This section summarizes these studies and presents the general conclusions.

The detector types considered were a fission monitor and activation detectors. The principal advantage of activating foils for monitoring purposes was the ease with which they could be located on the experimental assembly so that were the assembly to be moved relative to the linac beam tube, they would detect any loss of beam on the target. The difficulty with the use of gold foils was that their activation was predominantly by the absorption of thermal neutrons, whereas it was desired to monitor the fast-neutron flux from the source. In using the gold foils, then, it was necessary to attach them to the measured assembly so that they were shielded from room return neutrons, and to position them uniformly about the source axis so as to reflect any shift in the position of the electron beam on the target with its consequent change of photoneutron yield. In practice it was not always possible to achieve these objectives.

Sulfur foils were tried but once, utilizing the  $S^{32}(n,p)P^{32}$  reaction, which has a threshold of about 1 MeV. The sulfur foils were used in groups of four, placed symmetrically about the source on an aluminum holder, but there was too much heat dissipated in that area, and the foils became flaky or pasty and proved unsatisfactory.

Finally, monitoring by aluminum utilizing the  $Al^{27}(n,\alpha)Na^{24}$  reaction, which has a threshold of some 6 MeV, was tried. The aluminum was machined into the shape of an end cap and slipped over the rear of the target. It was recognized that this kind of positioning would be satisfactory only when the source was at the front and not at the side of the assembly under measurement. Unlike the gold or the sulfur with their longer half lives, it was necessary to correct the activity of the aluminum for decay during the irradiation period.

Initially the fission monitor was attached rigidly to the source-assembly table by a long cadmium covered tube. At the tip of the tube was a six inch cylinder of polyethylene which was intended to thermalize neutrons for the fission counter to view. Furthermore in being attached to the assembly table, the fixed geometry was expected to allow correctly for any loss of beam on the target as the assembly was moved. Experience with the fission counter in this configuration showed that the predominant neutrons detected were fast neutrons from room return and not thermal neutrons from the polyethylene plug. In addition the long-term stability of the detector placed near to the target with its strong gamma flash was questionable. Since it was desirable to locate this counter, its preamplifier and power supply at some distance from the source in order to reduce the

effects of neutron or gamma radiation on the equipment, it was decided to detach the counter from the assembly table and locate it in a well shielded corner of the experimental room. In this arrangement, it was found that the counter stability was improved and that room return neutrons were a reasonably accurate measure of the target yield. Best results were achieved when the detector was gated on after a relatively long time (3 msec) after the neutron burst. The counter was also insensitive to small changes in the geometrical arrangement of the experimental assembly, a feature which at times was useful.

A complete survey was made of the monitor data obtained from these three independent monitors over the past few months. The fission counter, which gave the most immediate results, was usually the most reliable monitor. Comparisons between the normalized counts per neutron pulse for each monitor showed that our present method of monitoring was quite adequate for background subtraction. The signal-to-background ratio could normally be monitored to within a few percent, but even a 5% error in this ratio would only introduce an error of 1% in the measured spectra, if the background was 20%.

When the neutron monitor counts were used to normalize the measured spectra at various points, it became more important that the monitoring system produced reliable results, since the measured neutron flux,  $\phi(E)$ , was directly proportional to the number of monitor counts. It was found that the fission counter gave fairly consistent results, but the gold and aluminum monitors showed considerable differences between successive runs. This was particularly noticeable when the position of the assembly was changed with respect to the room and the target. This difficulty could conceivably be minimized if a cadmium covered gold foil were located inside the assembly near the neutron flux peak. Here the position of the gold would not be too critical and possible differences due to room return neutrons would be minimized. Also a more realistic representation of the neutron flux inside the medium would be obtained in this fashion. The reliability of the fission monitor, however, was not sufficiently good to dispense with backup monitors, for which we have presently standardized on gold foils.

#### 11.4 DATA REDUCTION METHODS

During this year some additional refinements were made in our procedure for reducing spectral data. These refinements are as follows:

1. The measured background is now corrected for count rate losses. This has significance only at energies above 50 eV, but it is part of the program to extend the range of the measurements.

2. A transmission function for the background plug has now been inserted. The measured spectrum  $\phi_m$  is related to the true spectrum  $\phi_t$  by

$$\phi_m(e) = \phi_t(E) \left[ 1 - T(E) \right]$$

where  $T(E)$  is the fractional transmission through the plug. For background plugs that are not completely "black" and at high energies, the formula above has been used successfully to correct  $\phi_m$ .

3. A preliminary method has been devised that correctly subtracts the background in a high energy spectral measurement using the TMC 201 time of flight logic unit. In addition, an automatic subtraction of the "afterglow" tail can be made. This correction has been applied to the fast neutron spectra through a thick graphite shield reported in Section 9.2.
4. A method has been obtained for subtracting off the background of delayed neutrons in spectral measurements on multiplying assemblies. The method is discussed in detail in Section 8.1.

#### 11.5. DESCRIPTION OF GAKER CODE

The GAKER code computes the double differential scattering cross section  $d^2\sigma/d\epsilon d\Omega$  as formulated by Nelkin<sup>(6)</sup> and integrates over angle to obtain the scattering kernel used in the local thermalization codes.

There have been several changes made in the code since it was received from H. Honeck.<sup>(12)</sup> Some of the changes were quite simple such as reading in a set of energies instead of velocities and velocity increments as Honeck had originally done. Other changes such as the addition of a third phonon term were more subtle. The more significant changes and new versions will be noted here along with a description of the original version of GAKER.

The standard version of the code is programmed to compute:

$$\frac{d^2\sigma}{d\epsilon d\Omega} = \frac{\sigma_b}{4\pi} \sum_{m=0}^2 \sum_{n=-10}^{10} \left( \frac{E}{E'} \right)^{1/2} e^{-\xi/A} f_{nm} \quad (11.5.1)$$

$$f_{nm} = \frac{1}{m!} \left( \frac{\xi}{\alpha} \right)^m e^{-n\omega/2T} I_n \left( \frac{\xi}{B} \right) \exp \left[ \frac{- \left( E - E' - n\omega + \frac{m\alpha}{\beta} + \lambda \xi \right)^2}{4E \lambda \xi} \right] \quad (11.5.2)$$

$$\xi = E' + E - 2\mu \sqrt{E'E} \quad , \quad (11.5.3)$$

$$\sigma_b = \sigma_f \left( \frac{A+1}{A} \right)^2 \quad , \quad (11.5.4)$$

$$\epsilon = E' - E \quad (11.5.5)$$

In general, for  $E_{cn} < E < E_{cn+1}$ ,  $E_{cn}$  an input number, each discrete oscillator has an energy  $\omega_n$  and a weight  $\lambda_n$  associated with an effective mass  $M_n$  ( $\lambda_n = 1/M_n$ ). The sum of all  $\lambda_n$  must equal the value  $1/M$  where  $M$  is the free particle mass. Oscillator  $n$  is treated exactly. Oscillator  $n+1$  is treated with a two term phonon expansion. Oscillators  $0, 1, 2, \dots, n-1$  are treated in the short collision approximation. Oscillators  $n+2, n+3, \dots$  are treated in the elastic limit. Then

$$\bar{E} = (\lambda_0 T + \lambda_1 \bar{E}_1 + \lambda_2 \bar{E}_2 \dots \lambda_{n-1} \bar{E}_{n-1})/\lambda \quad (11.5.6)$$

$$\bar{E}_n = \omega_n \left[ \frac{1}{e^{\omega_n/T} - 1} + \frac{1}{2} \right] \quad (11.5.7)$$

$$\lambda = \lambda_0 + \lambda_1 + \lambda_2 \dots \lambda_{n-1} \quad (11.5.8)$$

$$\frac{1}{A} = \frac{\lambda_n}{\omega_n \tanh \left( \frac{\omega_n}{2T} \right)} + \frac{\lambda_{n+1}}{\omega_{n+1}} + \frac{\lambda_{n+2}}{\omega_{n+2}} + \dots \quad (11.5.9)$$

$$B = M_n \omega_n \sinh \left( \frac{\omega_n}{2T} \right) \quad (11.5.10)$$

$$\beta = M_{n+1} \quad (11.5.11)$$

$$\frac{\alpha}{\beta} = \omega_{n+1} \quad . \quad (11.5.12)$$

In particular, for the case of hydrogen bound in water and incident energies  $E < E_{c1} = .32$  ev, the second vibrational mode is taken in the elastic limit, a phonon expansion is used for the first vibrational mode and the rotational and translational modes are both treated exactly. For  $E > E_{c1}$  the rotations are taken as free, a phonon expansion is used for the second vibrational mode and the first vibrational mode is treated exactly. The values used in the computation of the  $H(H_2O)$  kernel are:

$$\begin{array}{ll} M_T = 18 & \\ M_R = 2.32 & \omega_R = 0.06 \text{ ev} \\ M_{V1} = 5.84 & \omega_{V1} = 0.205 \text{ ev} \\ M_{V2} = 2.92 & \omega_{V2} = 0.48 \text{ ev} \end{array}$$

There are two changes in GAKER which can be or have been applied to all versions. First, the inclusion of an additional phonon term in (11.5.1) (i. e.,  $f_{n3}$ ). Secondly, the option of using incident energy or energy transfer as the criterion for determining which treatment to apply to the oscillators.

The current versions of GAKER and their functions are;

JAG, GAIN	Takes into account the anisotropy of the molecular vibrations.
GAD, GANG	Integrates the double differential scattering cross section over final energy.
DTOK	Consideration of molecular interference within a $D_2O$ molecule.
LHK <sup>(76)</sup>	Calculates a liquid hydrogen kernel

## JAG

The physics incorporated into the anisotropic version of GAKER has been reported.<sup>(77)</sup> Equation (11.5.1) for the anisotropic version becomes;

$$\frac{d\sigma}{d\epsilon d\Omega} = \frac{\sigma_b}{4\pi} \sum_{\ell=1}^{N_o} W_{\ell} \sum_{m=0}^2 \sum_{n=-10}^{10} \frac{E}{E'}^{1/2} e^{-\xi/A} f_{nm} \quad (11.5.13)$$

where  $N_o$  is an input number,  $f_{nm}$  remains of the same form and the parameters,  $A, B, \bar{E}, \alpha$ , and  $\beta$  are dependent on  $\ell$ . This dependence on  $\ell$ , for H as in  $H_2O$  is;

$\mu = \cos \theta_\ell$ ,  $\theta_\ell$  the orientation angle with weight  $W_\ell$

$$M_T = 18.0$$

$$M_R = \frac{1.5}{1-\mu^2}$$

$$\left\langle \frac{1}{\frac{1}{M_R}} \right\rangle = 2.25$$

$$M_{V1} = \frac{4.0}{1-\mu^2}$$

$$\left\langle \frac{1}{\frac{1}{M_{V1}}} \right\rangle = 6.0$$

$$M_{V2} = \frac{1}{\mu^2}$$

$$\left\langle \frac{1}{\frac{1}{M_{V2}}} \right\rangle = 3.0$$

### DTOK

This version is for computing a  $D_2O$  kernel. It is an extension of the work by Butler<sup>(17)</sup> and takes into account intramolecular interference scattering in addition to the self term considered in Honeck's<sup>(16)</sup> incoherent approximation. As is easily seen there can only be four different kinds of scattering terms. Their weights corresponding to all possible combinations within a  $D_2O$  molecule are as follows:

<u>Scattering Term</u>	<u>Weight</u>
$D_1 D_1$	2
$D_1 O$	4
$D_1 D_2$	2
$OO$	1

For this model and for  $E < E_c$ :

$$\frac{d^2 \sigma_{\nu\nu'}}{d\epsilon d\Omega} = \bar{a}_{\nu\nu'} \sqrt{\frac{E}{E'}} \left( \frac{2\bar{M}_1^{\nu\nu'}}{4\pi\bar{E}^{\nu\nu'}\kappa^2} \right)^{1/2} \exp \left[ -\frac{\kappa^2}{2A_1^{\nu\nu'}} \right] \sum_{k=0}^3 \sum_{n=-10}^{10} f_{kn}, \quad (11.5.14)$$

$$f_{kn} = \frac{1}{k!} \left( \frac{\kappa^2 Q_2^{\nu\nu'}}{2m\omega_2} \right)^k e^{-n\omega_1/2T} I_n \left( \frac{\kappa^2}{2B_1^{\nu\nu'}} \right) \exp \left[ - \frac{\left( E - E' - n\omega_1 + k\omega_2 + \frac{\kappa^2}{2\overline{M}_1^{\nu\nu'}} \right)^2}{2\overline{E}_1^{\nu\nu'} \kappa^2 / \overline{M}_1^{\nu\nu'}} \right] \quad (11.5.15)$$

where

$$\overline{a}_{\nu\nu'} = (A_\nu A_{\nu'} + \delta_{\nu\nu'} C_\nu^2) \frac{\sin b_{\nu\nu'} \kappa}{b_{\nu\nu'} \kappa} , \quad (11.5.16)$$

$$\frac{m}{A_1^{\nu\nu'}} = \sum_{i=1}^3 \frac{1}{\omega_i} \coth \frac{\omega_i}{2T} P_i^{\nu\nu'} \sim \frac{P_1^{\nu\nu'}}{\omega_1} \coth \frac{\omega_1}{2T} + \frac{P_2^{\nu\nu'}}{\omega_2} + \frac{P_3^{\nu\nu'}}{\omega_3} , \quad (11.5.17)$$

$$\frac{1}{m} B_1^{\nu\nu'} = \frac{\omega_1}{Q_1^{\nu\nu'}} \sinh \frac{\omega_1}{2T} , \quad (11.5.18)$$

$$\overline{M}_1^{\nu\nu'} = M = 20 , \quad m = 1$$

$$\overline{E}_1^{\nu\nu'} = T ,$$

$$\xi = \frac{\kappa^2}{2m} = E + E' - 2\mu \sqrt{EE'} . \quad (11.5.19)$$

For  $E > E_c$

$$\frac{d^2 \sigma^{\nu\nu'}}{d\epsilon d\Omega} = \overline{a}_{\nu\nu'} \sqrt{\frac{E}{E'}} \left( \frac{\overline{M}_2^{\nu\nu'}}{2\pi \overline{E}_2^{\nu\nu'} \kappa^2} \right)^{1/2} \exp \left[ - \frac{\kappa^2}{2A_2^{\nu\nu'}} \right] \sum_{k=0}^3 \sum_{h=-10}^{10} f_{kn} , \quad (11.5.20)$$

$$f_{kn} = \frac{1}{k!} \left( \frac{\kappa^2 Q_3^{\nu\nu'}}{2m\omega_3} \right)^k e^{-n\omega_2/2T} I_n \left( \frac{\kappa^2}{2B_2^{\nu\nu'}} \right) \exp \left[ - \frac{\left( E - E' - n\omega_2 + k\omega_3 + \frac{\kappa^2}{2\overline{M}_2^{\nu\nu'}} \right)^2}{2\overline{E}_2^{\nu\nu'} \kappa^2 / \overline{M}_2^{\nu\nu'}} \right] , \quad (11.5.21)$$



$$\frac{m}{A_2^{\nu\nu'}} \cong \frac{1}{\omega_1} \coth \frac{\omega_1}{2T} (P_1^{\nu\nu'} - Q_1^{\nu\nu'}) + \frac{P_2^{\nu\nu'}}{\omega_2} + \frac{P_3^{\nu\nu'}}{\omega_3} , \quad (11.5.22)$$

$$\frac{B_2^{\nu\nu'}}{m} = \frac{\omega_2}{Q_2^{\nu\nu'}} \sinh \frac{\omega_2}{2T} , \quad (11.5.23)$$

$$\overline{E}_2^{\nu\nu'} = \overline{M}_2^{\nu\nu'} \left[ \frac{T}{M} + Q_1^{\nu\nu'} \frac{\omega_1}{2} \coth \frac{\omega_1}{2T} \right] , \quad (11.5.24)$$

$$\frac{m}{\overline{M}_2^{\nu\nu'}} = Q_1^{\nu\nu'} + \frac{m}{M} . \quad (11.5.25)$$

The values used in computing the  $D_2O$  kernel are:

<u>Quantity</u>	$\mu = 1$	$\mu = 2$	$\mu = 3$
$P_\mu^{D_1 D_1} = P_\mu^{D_1 D_2}$	0.22800	0.074135	0.14787
$P_\mu^{OO}$	0.0055009	0.0022995	0.0046996
$P_\mu^{OD_1}$	0.11675	0.038217	0.076284
$Q_\mu^{D_1 D_2}$	-0.051968	-0.00055165	0.0025211
$Q_\mu^{OD_1}$	-0.022003	-0.0091980	-0.018798
$Q_\mu^{D_1 D_1} = Q_\mu^{D_2 D_2} = P_\mu^{D_1 D_1} = P_\mu^{D_2 D_2}$			
$Q_\mu^{OO} = P_\mu^{OO}$			

$$b^{D_1 D_1} = b^{DO} = 0$$

$$b^{OD} = 15.7 \text{ ev}^{-1/2} \quad \left( \frac{\kappa^2}{2m} \text{ in ev, where } m = 1 \right)$$

$$b^{D_1 D_2} = 2b^{OD} \sin \frac{105^\circ}{2}$$

$$4\pi (A_D^2 + C_D^2) = 7.6 \text{ barns}$$

$$4\pi (A_0^2 + C_0^2) = 4.24 \text{ barns}$$

$$4\pi A_D^2 = 5.4 \text{ barns}$$

$$4\pi A_0 A_D = 4.76 \text{ barns}$$

$$\omega_1 = 0.048 \text{ eV}$$

$$\omega_2 = 0.146 \text{ eV}$$

$$\omega_3 = 0.3385 \text{ eV}$$

The differences between DTOK and the standard version of GAKER are:

1. There are four independent calculations. The total kernel is the sum of all four partial kernels,  $D_1 D_1^2 (D_1 D_1) + 4(D_1 O) + 2(D_1 D_2) + (OO)$
2. The factor  $\frac{\sin b_{\nu\nu'} \kappa}{b_{\nu\nu'} \kappa}$  which is 1 for  $\nu = \nu'$
3. The definition of A, B,  $\overline{M}$ ,  $\overline{E}$ .

### GAD

GAKER computes the double differential scattering cross section and integrates over angle; it does not calculate  $d\sigma/d\mu$ . GAD is a modified version that does this. The essential differences between the two are:

1. GAD uses Simpson's rule for integrating over angles which are equally spaced for  $-1 \leq \mu \leq 1$  to obtain the total scattering cross section. GAKER uses Gaussian quadrature.
2. GAD does not compute the double differential at the point of singularity,  $\mu = 1$ , but extrapolates to it.

3. GAD computed the diagonal element incorrectly, the largest error in  $d\sigma/d\mu$  occurring for the lower energies. This error has been corrected.

### GANG

This version was originally made to check GAD which does not print out the double differential and therefore did not show the error mentioned in (3) above. As the version now exists it is somewhat limited in its applications since it was modified explicitly for light water. Its output for hydrogen is  $d^2\sigma/d\epsilon d\Omega$ ,  $\sigma$ , and  $\bar{E}'$  the average final energy for the angle  $\Omega$ . A constant value of  $d\sigma/d\Omega$  for oxygen is also used to give  $d\sigma/d\Omega$  for light water.

### GAIN

This is the anisotropic version of GANG.

## XII. UNIVERSAL SCATTERING CODE

### 12.1. INTRODUCTION AND SUMMARY

One of the most important tasks undertaken this year has been the development of a generalized scattering law code which it is hoped will be applicable to all the common moderators. The need for a code of this type has become imperative as the theoretical scattering description of each moderator has been improved. The difficulty now is that the present computer codes used like GAKER<sup>(12)</sup> and SUMMIT<sup>(26)</sup> will handle only one or at most two types of atomic motion. In addition these two codes are extremely difficult to run because the selection of some of the phonon expansion parameters and change-over frequencies is somewhat arbitrary and at times intuitive. The new code is designed to handle all types of atomic motion including free translations, isolated frequencies (delta-functions), distributed frequencies and diffusive motions, and will be able to convolve them in any desired combination. The code will be made as simple to operate as possible so that its use will require no great expertise. In this way the code will be useful to the reactor designer, and can be expected to spur research into the various moderators which is presently inhibited by the lack of computational ability. In Ref. 3 the "Annual Summary Report for 1963," the formulation for determining the scattering law was given. During this year that formulation has been programmed into the code GASKET. Eventually point and group scattering kernels will be obtained from the scattering law calculations of GASKET by means of the code FLANGE. In the following sections, the mathematical basis for these two codes and their associated subroutines is detailed, and a report is given as to their current status.

### 12.2. SCATTERING LAW

#### 12.2.1. GASKET Code

The GASKET program computes the thermal neutron scattering law

$$S\left(\frac{p^2}{2}, \epsilon\right) = e^{\epsilon/2T} \frac{1}{2\pi} \int_{-\infty}^{\infty} e^{i\epsilon t} X\left(\frac{p^2}{2}, t\right) dt \quad (12.2.1)$$

$$= \frac{1}{2\pi} \int_{-\infty}^{\infty} e^{i\epsilon t} X\left(\frac{p^2}{2}, t + i/2T\right) dt \quad (12.2.2)$$

$$= \frac{1}{\pi} \int_0^{\infty} X\left(\frac{p^2}{2}, t + i/2T\right) \cos \epsilon t dt, \quad (12.2.3)$$

where the third form (12.2.3) is valid because of property (12.2.8) below.  $S[(p^2/2), \epsilon]$  is therefore a real even function of  $\epsilon$ , and is related to the differential cross section by the well-known expression<sup>(54)</sup>

$$\frac{1}{\sigma_0} \sigma_s(E' \rightarrow E, \underline{\Omega}' \rightarrow \underline{\Omega}) = \left(\frac{E'}{E}\right)^{1/2} \left(\frac{M+1}{M}\right)^2 \frac{1}{4\pi} e^{-\epsilon/2T} S\left(\frac{p^2}{2}, \epsilon\right), \quad (12.2.4)$$

where

$$\epsilon = E - E' \quad (12.2.5)$$

is the energy transferred to the neutron, and

$$\frac{p^2}{2} = E + E' - 2\sqrt{EE'}\mu \quad (12.2.6)$$

is a measure of the momentum  $p$  transferred to the neutron;  $\mu$  is the cosine of the scattering angle;  $E'$  and  $E$  are the initial and final neutron energies, respectively;  $M$  is the ratio of the mass of the scattering particle to the mass of the neutron;  $T$  is the effective temperature; and  $\sigma_0$  is the free-atom scattering cross section.

The function  $X(p^2/2, t)$  satisfies the following "moment conditions" (listed originally by Placzek<sup>(78)</sup>):

$$X\left(\frac{p^2}{2}, t\right) \text{ is analytic in } t \text{ near } t = 0, \quad (12.2.7)$$

$$X\left(\frac{p^2}{2}, t + i/2T\right) \text{ is real for real } \frac{p^2}{2}, \text{ and real } t \quad (12.2.8)$$

(detailed balance condition),

$$\left. \frac{\partial}{\partial t} X\left(\frac{p^2}{2}, t\right) \right|_{t=0} = \frac{ip^2}{2M}, \quad (12.2.9)$$

$$\frac{\partial^2}{\partial t^2} X \left( \frac{p^2}{2}, t \right) \Big|_{t=0} = -\bar{T} \frac{p^2}{M} - \left( \frac{p^2}{2M} \right)^2 . \quad (12.2.10)$$

( $\bar{T} = 2/3$  of the mean energy of the scattering particles),

$$X \left( \frac{p^2}{2}, 0 \right) = 1 . \quad (12.2.11)$$

The fundamental simplifying assumptions to be made are (1) that  $X$  has the Gaussian form<sup>(79)</sup>

$$X \left( \frac{p^2}{2}, t \right) = \exp \left[ \frac{p^2}{2} G(t) \right] \quad (12.2.12)$$

or a direct generalization of this form (see Eq. (12.2.40)), and (2) that the motions of the scatterer which contribute to the self-scattering may be represented in terms of  $N$  independent mechanical modes:

$$G(t) = \sum_{n=1}^N G_n(t) . \quad (12.2.13)$$

It follows that

$$X \left( \frac{p^2}{2}, t \right) = \prod_{n=1}^N X_n \left( \frac{p^2}{2}, t \right) = \prod_{n=1}^N \exp \left[ \frac{p^2}{2} G_n(t) \right] . \quad (12.2.14)$$

The functions  $G_n(t)$  must, from Eq. (12.2.11), vanish for  $t = 0$ . They may therefore be expressed in the form

$$G_n(t) = \frac{w_n}{M} [\gamma_n(t) - \gamma_n(0)] \quad (12.2.15)$$

or

$$G_n(t + i/2T_n) = \frac{w_n}{M} [\gamma_n(t + i/2T_n) - \gamma_n(0)] . \quad (12.2.16)$$

Form (12.2.16) involves real functions only and is therefore easier to work with.  $T_n$  is the temperature appropriate to the  $n^{\text{th}}$  mode; it will normally be the same for all modes but some provision for exceptional cases is desirable. The quantities  $w_n$  are relative weights for the  $N$  modes, such that

$$0 \leq w_n \leq 1 \quad \text{and} \quad \sum_{n=1}^N w_n = 1. \quad (12.2.17)$$

Provision is made in the current GASKET program for the following modes:

1. Translational (free gas).
2. Brownian (diffusive) motion.
3. Vibrational (isotropic, with distributed phonon frequency spectrum).
4. Vibrational (anisotropic, with orientation parallel to primary lattice plane, with distributed spectrum).
5. Vibrational (anisotropic, with orientation transverse to primary lattice plane, distributed spectrum).
6. Vibrational (isotropic, with discrete frequency spectrum).

Other modes may be added to this list.

#### 12.2.2. Translation Mode

The free-gas scattering law is obtained from

$$G_1(t) = \frac{w_1}{M} (it - Tt^2) \quad (12.2.18)$$

or

$$G_1(t + i/2T) = -\frac{w_1}{M} \left( \frac{1}{4T} + Tt^2 \right). \quad (12.2.19)$$

The resulting contribution to the scattering law is easily evaluated as

$$S_1 \left( \frac{p^2}{2}, \epsilon \right) = (2\pi p^2 w_1 T_1 / M)^{-1/2} \exp \left\{ -\frac{M}{2p^2 T_1 w_1} \left[ \epsilon^2 + \left( \frac{p^2 w_1}{2M} \right)^2 \right] \right\}. \quad (12.2.20)$$

However, if other modes are present ( $w_1 < 1$ ), form (12.2.20) is not convenient. The reason is that form (12.2.20) must be combined by convolution with corresponding expressions for the other modes (see Eq. (12.2.37)), while form (12.2.19) may be combined with corresponding expressions by the simpler process of addition.

### 12.2.3. Brownian Motion

The following expression is obtained by R. J. Glauber<sup>(80)</sup> from the classical Langevin theory of Brownian motion:

$$\frac{1}{w_2} G_2(t) = - \frac{2T_2}{M\eta^2} (\eta|t| - 1 + e^{-\eta|t|}) , \quad (12.2.21)$$

where the viscosity  $\eta$  is in turn defined by

$$\eta = \frac{T_2}{DM} , \quad (12.2.22)$$

with  $D$  being a dimensionless diffusion coefficient. This expression, being strictly classical, is inconsistent with condition (12.2.9), which is a quantum-theory result. However if  $|t|$  is taken as the modulus of the complex variable  $t$ , the result is

$$G_2(t + i/2T) = - \frac{2T_2 w_2}{M\eta^2} [\eta \sqrt{t^2 + (2T)^{-2}} - 1 + \exp[-\eta \sqrt{t^2 + (2T)^{-2}}]] , \quad (12.2.23)$$

which is consistent with (12.2.9). To show this, it is sufficient to replace  $t$  with  $t - i/2T$  in (12.2.23) and expand the exponentials,

$$\begin{aligned} \frac{1}{w_2} G_2(t) &= - \frac{2T_2}{M\eta^2} [\eta \sqrt{t^2 - it/T_2} - 1 + \exp(-\eta \sqrt{t^2 - it/T_2})] \\ &\cong - \frac{2T_2}{M\eta^2} \left[ \frac{1}{2} \eta^2 \left( t^2 - \frac{it}{T_2} \right) + O(t^{3/2}) \right] , \end{aligned} \quad (12.2.24)$$

so that  $(1/w_2) G'_2(0) = i/M$  as required by (12.2.9).

### 12.2.4. Vibrational Modes

The vibrational modes are specified in terms of phonon frequency spectra  $f(\omega)$  as follows:

$$\gamma(t) = \int_{-\infty}^{\infty} \frac{f(|\omega|) \exp(\omega/2T)}{2\omega \sinh(\omega/2T)} e^{i\omega t} d\omega$$



$$= \int_0^{\infty} \frac{f(\omega)}{\omega} \left( \coth \frac{\omega}{2T} \cos \omega t + i \sin \omega t \right) d\omega , \quad (12.2.25)$$

$$\gamma(0) = \int_0^{\infty} \frac{f(\omega)}{\omega} \coth \frac{\omega}{2T} d\omega , \quad (12.2.26)$$

$$\begin{aligned} \gamma(t + i/2T) &= \int_{-\infty}^{\infty} \frac{f(|\omega|)}{2\omega \sinh(\omega/2T)} e^{i\omega t} d\omega \\ &= \int_0^{\infty} \frac{f(\omega)}{\omega} \operatorname{csch} \frac{\omega}{2T} \cos \omega t d\omega . \end{aligned} \quad (12.2.27)$$

It can be shown using (12.2.12), (12.2.15), and (12.2.17) that (12.2.25) is consistent with (12.2.9) provided that

$$\int_0^{\infty} f(\omega) d\omega = 1 . \quad (12.2.28)$$

Furthermore,  $f(\omega)$  must vanish at the origin at least as strongly as  $\omega^2$  in order that the integrals (12.2.25) through (12.2.27) should exist. This restriction is not an essential one, however, since in the expression (12.2.16) for  $G_n(t + i/2T)$ , singularities associated with zero frequency will cancel.

The upper limit of the integrals (12.2.25) through (12.2.28) is in reality a cutoff frequency  $\omega_{\max}$  rather than infinity. The physical significance of this cutoff is, of course, that a medium composed of discrete molecules cannot support vibrational modes with wavelengths much smaller than the mean spacing of the molecules. In a dilute gas this spacing approaches infinity, the cutoff frequency tends to zero, and the spectrum approaches

$$f(\omega) = \delta(\omega) , \quad (12.2.29)$$

a delta-function at zero frequency. The gas-law formulae (12.2.18) and (12.2.19) are easily derived from (12.2.16), (12.2.25) through (12.2.27), and (12.2.29). This result offers one approach to any difficulties associated with zero frequency as described in the preceding paragraph; however, still simpler methods are also available for that problem.

The quantity  $G_1(t)$  for the translational mode behaves as  $-t^2$  for large  $t$ , while  $G_2(t)$  for the Brownian motion behaves as  $-t$ . The corresponding  $X$  functions therefore vanish strongly for large  $t$ . In contrast, the integral (12.2.27) will at best behave as  $t^{-1}$ , so that  $G_n(t)$  and  $X_n(t)$  approach non-zero constants. Specifically, in this case,

$$\lim_{t \rightarrow \infty} X_n(t + i/2T) = \exp \left[ -\frac{p^2 w_n}{2M} \gamma_n(0) \right] \quad (12.2.30)$$

is the contribution to the Debye-Waller factor. If the total  $X$  function for the problem contains no contributions from translational or diffusive motion modes, the Fourier transform (12.2.3) will diverge. A similar situation arises if  $X(t)$  is oscillatory as  $t \rightarrow \infty$ . The program must therefore separate the divergent contributions to (12.2.3) from the other terms, and represent these by the appropriate delta functions.

The oscillatory behavior of  $X(t)$  arises for mode 6, the discrete vibrational spectrum, for which the spectrum is specified in the form

$$f_6(\omega) = \sum_k a_k \delta(\omega - \omega_k) , \quad (12.2.31)$$

where

$$\sum_k a_k = 1 , \quad (12.2.32)$$

in order to conform to (12.2.28). One obtains at once

$$X_6 \left( \frac{p^2}{2}, t + i/2T_6 \right) = \prod_k \exp \left[ -\frac{p^2 w_6 a_k}{2M\omega_k} \coth \frac{\omega_k}{2T_6} \right] \cdot \exp \left[ \frac{p^2 w_6 a_k}{2M\omega_k} \operatorname{csch} \frac{\omega_k}{2T_6} \cos \omega_k t \right] . \quad (12.2.33)$$

Since

$$e^{z \cos \theta} = \sum_{n=-\infty}^{\infty} I_n(z) e^{-in\theta} = I_0(z) + 2 \sum_{n=1}^{\infty} I_n(z) \cos n\theta , \quad (12.2.34)$$

each term in (12.2.31) generates a phonon series

$$X_{6,k} \left( \frac{p^2}{2}, t + i/2T_6 \right) = \exp \left[ - \frac{p^2 w_6 a_k}{2M\omega_k} \coth \frac{\omega_k}{2T_6} \right] \cdot \left[ I_0 \left( \frac{p^2 w_6 a_k}{2M\omega_k} \operatorname{csch} \frac{\omega_k}{2T_6} \right) + 2 \sum_{n=1}^{\infty} I_n \left( \frac{p^2 w_6 a_k}{2M\omega_k} \operatorname{csch} \frac{\omega_k}{2T_6} \right) \cos(n\omega_k t) \right] \quad (12.2.35)$$

The Fourier transform (12.2.2) or (12.2.3) of this quantity is

$$S_{6,k} \left( \frac{p^2}{2}, \epsilon \right) = \exp \left[ - \frac{p^2 w_6 a_k}{2M\omega_k} \coth \frac{\omega_k}{2T_6} \right] \cdot \left\{ I_0 \left( \frac{p^2 w_6 a_k}{2M\omega_k} \operatorname{csch} \frac{\omega_k}{2T_6} \right) \delta(\epsilon) + \sum_{n=1}^{\infty} I_n \left( \frac{p^2 w_6 a_k}{2M\omega_k} \operatorname{csch} \frac{\omega_k}{2T_6} \right) [\delta(\epsilon - n\omega_k) + \delta(\epsilon + n\omega_k)] \right\} \quad (12.2.36)$$

It is appropriate to account for such contributions after the S-function for other modes, if any, has been computed. Let  $S^{(K-1)}(p^2/2, \epsilon)$  be the scattering law computed for the other modes; or if there are none,  $\delta(\epsilon)$  may be used. The incorporation of (12.2.36) is accomplished by means of Fourier convolution:

$$S^{(K)} \left( \frac{p^2}{2}, \epsilon \right) = \int_{-\infty}^{\infty} S^{(K-1)} \left( \frac{p^2}{2}, \epsilon - \epsilon' \right) S_K \left( \frac{p^2}{2}, \epsilon' \right) d\epsilon' \quad (12.2.37)$$

For  $S_K$  of form (12.2.36), this convolution involves no numerical integration. The result of incorporating the first term in (12.2.31) is therefore

$$S^{(K)} \left( \frac{p^2}{2}, \epsilon \right) = \left[ \exp \left( - \frac{p^2 w_6 a_1}{2M\omega_1} \coth \frac{\omega_1}{2T_6} \right) \right] \cdot \sum_{n=-\infty}^{\infty} I_n \left( \frac{p^2 w_6 a_1}{2M\omega_1} \operatorname{csch} \frac{\omega_1}{2T_6} \right) S^{(K-1)} \left( \frac{p^2}{2}, \epsilon - n\omega_1 \right) \quad (12.2.38)$$

If  $S^{(K-1)}$  is continuous in  $\epsilon$ , the evaluation of (12.2.38) only requires interpolation. If  $S^{(K-1)}$  is, on the other hand, itself a delta-function distribution, then each term  $\delta(\epsilon - \epsilon_k)$  will generate a series of the form

$$\sum_n A_n \delta(\epsilon - \epsilon_k - n\omega_1) , \quad (12.2.39)$$

with coefficients defined by (12.2.38).

This process is then repeated for the remaining terms in (12.2.31).

Anisotropic vibrational modes (4) and (5) require special treatment also. Given the frequency spectra  $f_4$  (or  $f_{||}$ ) and  $f_5$  (or  $f_{\perp}$ ), the quantities  $G_4(t + i/2T)$  and  $G_5(t + i/2T)$  are formed in the usual way using (12.2.26), (12.2.27), and (12.2.16). The composite X-function is then defined as<sup>(6,26,81)</sup>

$$\begin{aligned} X_{4,5} \left( \frac{p^2}{2}, t + i/2T \right) &= \int_0^1 d\ell \exp \left[ \frac{p^2}{2} \ell^2 G_5(t + i/2T) \right. \\ &\quad \left. + \frac{p^2}{2} (1 - \ell^2) G_4(t + i/2T) \right] \\ &= e^{(p^2/2) G_4(t + i/2T)} \int_0^1 d\ell \exp \left[ - \frac{p^2}{2} (G_4 - G_5) \ell^2 \right] . \end{aligned} \quad (12.2.40)$$

The integral in (12.2.40) yields functions which are well-known<sup>(82)</sup>:

$$\begin{aligned} \int_0^1 d\ell e^{-x\ell^2} &= \frac{1}{\sqrt{x}} \int_0^{\sqrt{x}} e^{-\mu^2} d\mu = \frac{1}{\sqrt{x}} \text{Erf}(\sqrt{x}), \quad x > 0 \\ &= \Phi \left( \frac{1}{2}, \frac{3}{2}, -x \right) = \frac{1}{\sqrt{-x}} \text{Erfi}(\sqrt{-x}), \quad x < 0 , \end{aligned} \quad (12.2.41)$$

where  $\Phi$  denotes a confluent hypergeometric function. The discrete vibrational modes may also be anisotropic. These may be provisionally treated as distributed spectra, with the delta functions replaced by high, narrow peaks, and with the low-frequency portion of the spectrum

$(0 \leq \omega \leq \omega_1)$  replaced by a translational mode in order to avoid numerical difficulties at large  $t$  values.

#### 12.2.5. Problem Input

The six mode designations are listed following Eq. (12.2.17). The input contains 20 records, or blocks, as follows:

##### Block 1

NTP	Number of previously used values of $t$ (0 if none)
NT	Number of new values of $t$ required (0 if none)
NP	Number of values of $p^2/2$ (non-zero)
NE	Number of values of $\epsilon$ (non-zero)

##### Block 2

RWT (I), $I = 1 \dots 6$	Relative weight of mode I, unnormalized (ignored for mode 5)
--------------------------	--

##### Block 3

TMP (I), $I = 1 \dots 6$	Temperature for mode I, degrees K.
--------------------------	------------------------------------

##### Block 4

JS(I), $I = 1 \dots 4$	Number of frequencies and spectrum values, modes 3-6
------------------------	--

##### Blocks 5, 7, 9, 11

X(J), $J = JS(I), I = 1 \dots 4$	(present for each mode with $JS \neq 0$ ) Frequencies in $10^{-12} \text{ sec}^{-1}$
----------------------------------	---

##### Blocks 6, 8, 10, 12

Q(J), $J = JS(I), I = 1 \dots 4$	(present for each mode with $JS \neq 0$ ) Spectrum values, unnormalized
----------------------------------	--

##### Block 13

T(I), $I = 1 \dots NT$	(present for $NT \neq 0$ ) New values of $t$ , $\text{ev}^{-1}$
------------------------	--

##### Block 14

TP(N), $N = 1 \dots NTP$	(present for $NTP \neq 0$ ) Previously used values of $t$ , $\text{ev}^{-1}$
--------------------------	---

Block 15

GP3(N), N = 1 ... NTP (present for RWT(3)  $\neq$  0)  
Previously computed values of G,  
mode 3

Block 16

GP4(N), N = 1 ... NTP (present for RWT(4)  $\neq$  0)  
Previously computed values of G,  
mode 4

Block 17

GP5(N), N = 1 ... NTP (present for RWT(4)  $\neq$  0)  
Previously computed values of G,  
mode 5

Block 18

D Dimensionless diffusion coefficient  
for mode 2

M Mass of scattering nucleus, unified  
amu

Block 19

PP(I), I = 1 ... NP Values of  $p^2/2$  required, ev

Block 20

EE(I), I = 1 ... NE Values of  $\epsilon$  required, ev

12.2.6. Main Program

The main program reads the input, checks for input errors, and converts units as follows:

1. Temperatures in  $^{\circ}\text{K}$  are converted to ev by dividing by 11,604.9.
2. Frequencies in  $10^{-12} \text{ sec}^{-1}$  are converted to ev by dividing by 1519.30.
3. Mass in unified amu is converted to neutron mass units by dividing by 1.0086654.
4. Relative weights are normalized to unit sum (Eq. 12.2.17).

The main program then calls the subroutines which compute the values of  $G_n(t + i/2T)$  and  $X(t + i/2T)$  as required, merge these with any previously computed values, and generate the scattering law for the required arguments. The printed and punched output data are then written.

### 12.2.7. Subroutines

Most of the formulae are evaluated by subroutines, all of which utilize parameters placed in a common storage block. The subroutines are described below.

INTG and CØINT. These are trapezoidal integration routines in which the independent variable is specified as an arbitrary nondecreasing sequence. INTG computes the integral

$$\text{INT} = \int_{x_1}^{x_{\text{NS}}} Q(x) dx, \quad \text{NS} \geq 2, \quad (12.2.42)$$

where  $Q(x)$  is assumed to be piecewise linear within each of the  $\text{NS}-1$  intervals. The contribution of the interval  $(x_{s-1}, x_s)$  is then

$$\frac{1}{2} (x_s - x_{s-1}) (Q_s + Q_{s-1}), \quad x_s \geq x_{s-1}.$$

CØINT computes the integrals

$$P(y_r) = \int_{x_1}^{x_{\text{NS}}} Q(x) \cos(xy_r) dx, \quad \text{NS} \geq 2, \quad x_s \geq x_{s-1}, \quad \text{NR} \geq 1, \quad y_r \neq 0, \quad (12.2.43)$$

$$r = 1 \dots \text{NR},$$

where  $Q(x)$  is again assumed to be piecewise linear within each of the  $\text{NS}-1$  intervals. The contribution of the interval  $(x_{s-1}, x_s)$  is

$$\begin{aligned} P_s = \frac{Q_s}{y} & \left[ \left( 1 - \frac{\sin \theta_s}{\theta_s} \right) \sin x_s y + \frac{1 - \cos \theta_s}{\theta_s} \cos x_s y \right] + \\ & + \frac{Q_{s-1}}{y} \left[ \left( 1 - \frac{\sin \theta_s}{\theta_s} \right) \sin x_{s-1} y + \frac{1 - \cos \theta_s}{\theta_s} \cos x_{s-1} y \right], \end{aligned} \quad (12.2.44)$$

where  $\theta_s = (x_s - x_{s-1}) y$ . CØINT is used in the evaluation of formulae (12.2.3) and (12.2.27).

GAS. This routine evaluates formula (12.2.19) for  $G_1(t + i/2T)$ .

BRØWN. This routine evaluates (12.2.23) for  $G_2(t + i/2T)$ .

GTF. This routine evaluates formula (12.2.16) for  $G_n(t + i/2T)$ ,  $n = 3, 4$ , or  $5$ , using formulae (12.2.26) and (12.2.27), and normalizing input data with (12.2.28). The first step is the evaluation of the normalizing factor  $R$ , where

$$\frac{1}{R} = \int_0^{\omega_{NS}} f(\omega) d\omega = \frac{1}{3} f_1 \omega_1 + \frac{1}{2} \sum_{s=2}^{NS} (\omega_s - \omega_{s-1}) (f_s + f_{s-1}) . \quad (12.2.45)$$

Here,  $f(\omega)$  is assumed to be proportional to  $\omega^2$  in the interval  $0 \leq \omega \leq \omega_1$ . It is assumed that all of the  $\omega_s$ ,  $s = 1 \dots NS$ , and the  $t_r$ ,  $r = 2 \dots NR$  are non-zero. However,  $\omega_0 = 0$  is understood and  $t_1$  may be zero or non-zero. GTF computes, in turn, the quantities

$$\beta = \frac{1}{2T} , \quad (12.2.46)$$

$$g_0 = \frac{f_1}{\beta \omega_1^2} , \quad (12.2.47)$$

$$g_s = \frac{f_s}{\omega_s} \operatorname{csch}(\beta \omega_s), \quad s = 1 \dots NS , \quad (12.2.48)$$

$$\gamma_n(t_r + i\beta) = \int_0^{\omega_{NS}} g(\omega) \cos(\omega t_r) d\omega, \quad r = 1 \dots NR , \quad (12.2.49)$$

$$h_s = g_s \cosh(\beta \omega_s), \quad s = 0 \dots NS , \quad (12.2.50)$$

$$\gamma_n(0) = \int_0^{\omega_{NS}} h(\omega) d\omega , \quad (12.2.51)$$

$$G(t_r + i\beta) = \frac{w_n}{M} [\gamma_n(t_r + i\beta) - \gamma_n(0)], \quad r = 1 \dots NR . \quad (12.2.52)$$



XTG. This routine evaluates the function  $X(p^2/2, t_r + i/2T)$  according to formula (12.2.12), using a G-function containing contributions from modes 1, 2, and 3 at most.

XTGA. This routine evaluates formula (12.2.40) for the X-function containing the contributions of modes 4 and 5.

EERF. This routine evaluates the confluent hypergeometric function (formula (12.2.41) used in the XTGA routine.

The available formulae are:

$$\text{Eerf}(x) = \int_0^1 e^{-xu^2} du = \sum_{n=0}^{\infty} \frac{(-x)^n}{n! (2n+1)} \quad (12.2.53)$$

$$= e^{-x} \sum_{n=0}^{\infty} x^n / \left( \frac{3}{2} \right)_n, \quad (12.2.54)$$

where

$$\left( \frac{3}{2} \right)_n = \frac{3}{2} \cdot \frac{5}{2} \cdots \left( n + \frac{1}{2} \right) = \Gamma \left( \frac{3}{2} - n \right) / \Gamma \left( \frac{3}{2} \right),$$

$$\text{Eerf}(x) = \frac{1}{2} \left( \frac{\pi}{x} \right)^{1/2} - \frac{\frac{1}{2} e^{-x}}{x + \frac{1}{\frac{2}{2} + \frac{2}{x + \frac{3}{\frac{2}{2} + \frac{4}{x + \frac{5}{\frac{2}{2} + \dots}}}}} \quad (x > 0) \quad (12.2.55)$$

$$\cong \frac{1}{2} \left( \frac{\pi}{x} \right)^{1/2} - \frac{1}{2x} e^{-x} \left\{ \sum_{m=0}^{M-1} \left( \frac{1}{2} \right)_m (-x)^{-m} + O(|x|^{-m}) \right\} \quad (12.2.56)$$

The power series (12.2.53) and (12.2.54) are useful for  $|x| \ll 1$ , and the continued fractions expansion (12.2.55) for  $x \gg 1$ .<sup>(83)</sup> The asymptotic series (12.2.56) may be used for  $|x| \gg 1$  only; for negative  $x$  the first term is ignored. For  $x \sim 1$ , a Hastings approximation may be used:<sup>(84)</sup>

$$\text{Eerf}(x) \cong \frac{1}{2} \left( \frac{\pi}{x} \right)^{1/2} - (a_1 \eta + a_2 \eta^2 + a_3 \eta^3 + a_4 \eta^4 + a_5 \eta^5) \frac{e^{-x}}{\sqrt{x}}, \quad x > 0, \quad (12.2.57)$$

$$\eta = \frac{1}{1 + p\sqrt{x}},$$

$$p = 0.3275911,$$

$$a_1 = 0.225836846,$$

$$a_2 = -0.252128668,$$

$$a_3 = 1.259695130,$$

$$a_4 = -1.287822453,$$

$$a_5 = 0.940646070.$$

For negative  $x$  there appears to be no convenient recipe for the region  $x \sim -1$ . A related function has, however, been tabulated, (85)

$$I(x) = \int_0^x e^{(t^2 - x^2)} dt, \quad (12.2.58)$$

so that for  $x < 0$

$$\text{Eerf}(x) = \frac{1}{\sqrt{-x}} e^{-x} I(\sqrt{-x}) = \frac{1}{|x|^{1/2}} e^{|x|} I(\sqrt{|x|}). \quad (12.2.59)$$

(Since the utility of these alternative methods has not been fully evaluated, provision is made in the initial version of the program for all of them.)

MERGE. This routine merges two lists, both of which are in non-decreasing order. It is used to combine previously calculated and new values of  $G(t + i/2T)$ .

INX. This routine computes the Bessel functions  $I_n(x)$  from the backward recurrence relation

$$I_n(x) = \frac{2(n+1)}{x} I_{n+1}(x) + I_{n+2}(x). \quad (12.2.60)$$

### 12.2.8 Flange Code

This program utilizes the scattering law data generated by the GASKET code, and generates from these data both point kernels and group kernels.

Point kernels are calculated from the formula

$$\frac{\sigma_s^\ell(E' \rightarrow E)}{\sigma_o} = \frac{4\pi[\ell + (1/2)]}{\sigma_o} \int_{-1}^1 \sigma_s(E' \rightarrow E, \underline{\Omega}' \rightarrow \underline{\Omega}) P_\ell(\mu) d\mu, \quad (12.2.61)$$

where  $\mu = \underline{\Omega}' \cdot \underline{\Omega}$  and

$$\frac{1}{\sigma_o} \sigma_s(E' \rightarrow E, \underline{\Omega}' \rightarrow \underline{\Omega}) = \left(\frac{E}{E'}\right)^{1/2} \left(\frac{M+1}{M}\right)^2 \frac{1}{4\pi} e^{-\epsilon/2T} S\left(\frac{p^2}{2}, \epsilon\right), \quad (12.2.62)$$

Legendre moments of orders  $\ell = 0, 1, 2, 3$  may be generated. For the given values of  $E$  and  $E'$ , and the table of values of  $S(p^2/2, E)$  provided by GASKET, linear interpolation in  $\epsilon$  is used to define values of  $S$  corresponding to  $\epsilon = E' - E$ . The scattering angles corresponding to  $E$ ,  $E'$  and  $p^2/2$  are then computed from the relation

$$\mu = \frac{E + E' - p^2/2}{2\sqrt{EE'}} \quad (12.2.63)$$

These angles are not the ones needed for the integration over  $\mu$  in (12.2.61); these latter angles are specified in advance, and the appropriate values of  $S$  are obtained by interpolation.

Group kernels are calculated from the formula

$$G_{g' \rightarrow g}^\ell = \frac{\left(\ell + \frac{1}{2}\right) \left(\frac{M+1}{M}\right)^2}{\int_{E_{g'}}^{E_{g'+1}} \phi(E') dE'} \int_{E_{g'}}^{E_{g'+1}} dE' \frac{\phi(E')}{\sqrt{E'}} e^{E'/2T} \int_{E_g}^{E_{g+1}} dE \sqrt{E} e^{-E/2T} \int_{-1}^1 d\mu P_\ell(\mu) S\left(\frac{p^2}{2}, \epsilon\right), \quad (12.2.64)$$

where  $\phi(E)$  is taken to be identically 1 unless better information is available. Delta functions included in the specification of  $S(p^2/2, \epsilon)$  will in most cases be given special treatment, since they make possible the evaluation of (12.2.64) as a single quadrature.

The entire group kernel will be written on tape (or punched) in a form suitable for inclusion in the GGC-II data library.

Interpolation in the  $S(p^2/2, \epsilon)$  array is performed using an n-point Lagrangian interpolation routine. A special integration routine has been written and tested for calculation of the 0<sup>th</sup> through 3<sup>rd</sup> Legendre moments of the point and group cross sections. This routine integrates a vector function with up to four components, starting with an initial number ( $\geq 3$ , odd) of integration points and halving the integration intervals until either the integrals converge with decreasing interval or a maximum number of integration points ( $\geq 5$ , odd) is reached. A Richardson extrapolation<sup>(86)</sup> is then performed using the last two values of the integral.

### 12.3. STATUS OF THE CODES

About 75% of the coding for FLANGE has been completed and checked. Debugging will not be completed until the first version of GASKET is operational.

All coding for the first version of GASKET is completed. All sub-routines have been checked separately before inclusion in the complete program, which is now being checked. So far, the basic direct numerical integration of the X-function, Eq. (12.2.3), has been checked in the simplest case, free gas. The exact expression for S, Eq. (12.2.20), has been successfully checked against the calculation using the free gas G-function, Eq. (12.2.19), in the direct integration formula, Eq. (12.2.3). Tests of the distributed vibrational modes (corresponding to the SUMMIT<sup>(26)</sup> calculations) are now underway, using a Debye frequency spectrum as the test case. The basic integrals over frequency, Eqs. (12.2.26) and (12.2.27), have been verified, and experiments with the integration over t, Eq. (12.2.3), are now being made. So far, it has been found necessary to make several asymptotic expansions in the CØINT and GTF subroutines, corresponding to extreme values of t needed in the integration.

The diffusive motion and discrete vibrational spectrum modes have not yet been checked. These should give little trouble, the first being similar (in its use in the code) to the free gas mode, and the second using several already-tested routines borrowed from the local discrete vibrational codes. It is expected that the combination of distributed and discrete vibrational spectra will not lead to additional problems. The necessary convolutions are performed analytically, as indicated in Eqs. (12.2.37), (12.2.38), and (12.2.39).

H. C. Honeck of Brookhaven has proposed several extensions and modifications of the currently proposed FLANGE code. He points out the need for a code which is capable of interpolation in tables of experimental values of  $S(p^2/2, \epsilon)$ . By using an interpolation formula related to the form of the function, one should be able to fill in between fairly widely-spaced

experimental points. This approach would also provide a consistent method for combining calculated and experimental data. Honeck also pointed out that there are strongly singular regions at boundaries of the  $(p^2/2, \epsilon)$  plane at which something more sophisticated than straightforward extrapolation and interpolation may well be necessary. An analytical form for the S-function can always be found by the saddle-point integration scheme proposed by Egelstaff and Schofield;<sup>(54)</sup> the region of validity of the expression, of course, may be too small to be of use in many parts of the  $(p^2/2, \epsilon)$  plane.

### XIII. NEUTRON SPECTRUM BOOK

#### 13.1 INTRODUCTION AND SUMMARY

Much progress has been made in the compilation of data for the neutron spectrum book. This book gives measured and theoretical neutron spectra for a variety of poisons and moderators at different temperatures, and in several geometries. The book is designed to be a guide for reactor design groups in making comparative calculations to check the physics, mathematics, and numerical procedures which are used in their analyses. The format of the data presented in this book has been changed since its inception last year.<sup>(3)</sup> In fact, it may be changed later at the request of the EACRP (European-American Committee on Reactor Physics), which is interested in sponsoring the compilation. The principal changes made since last year are the addition of the ratio of theoretical to measured fluxes on the graph, the tabulation of the measured data, and the more complete reference system. An example of the present format is given in Fig. 13.1.

Twenty-nine spectra have now been completed and compiled by this laboratory, and additional cases which have been contributed by M. J. Poole from Harwell are now being evaluated. The Spectrum Book has been sent to a number of institutions and firms in this country for evaluation. The response has been very encouraging and some of the constructive criticisms received will be incorporated into future issues. It does appear that the book will find a useful place in reactor design literature.

#### 13.2 NORMALIZATION OF EXPERIMENT AND THEORY

A very important problem in the comparison of calculated and measured neutron spectra is their relative normalization. Since the theoretical spectrum is essentially exact at energies which are large compared to thermal and binding effects, it is tempting to do this normalization in the epithermal or  $1/E$  like region of the spectra. The joining of (infinite medium) thermal and epithermal spectrum is based on a neutron conservation equation of the type

$$\int_0^E \phi(E') \Sigma(E' \rightarrow E) dE' + S(E) = \phi(E) \left[ \int_0^\infty \Sigma(E \rightarrow E') dE' + \Sigma_a(E) \right], \quad (13.2.1)$$

## 90° ANGULAR NEUTRON SPECTRUM IN BORATED D<sub>2</sub>O

GA-D<sub>2</sub>O-2D

### CALCULATION PARAMETERS

SCATTERING KERNEL: GAKER (300°K, D(D<sub>2</sub>O), P<sub>0</sub> + P<sub>1</sub>)

TRANSPORT THEORY CODE: GAPLSN (ID 040364)

TEMPERATURE: 0.0255 ev

SOURCE: 1/E SLOWING DOWN

### ATOM DENSITIES

N = 2.608 X 10<sup>20</sup>

N = 5.672 X 10<sup>22</sup>

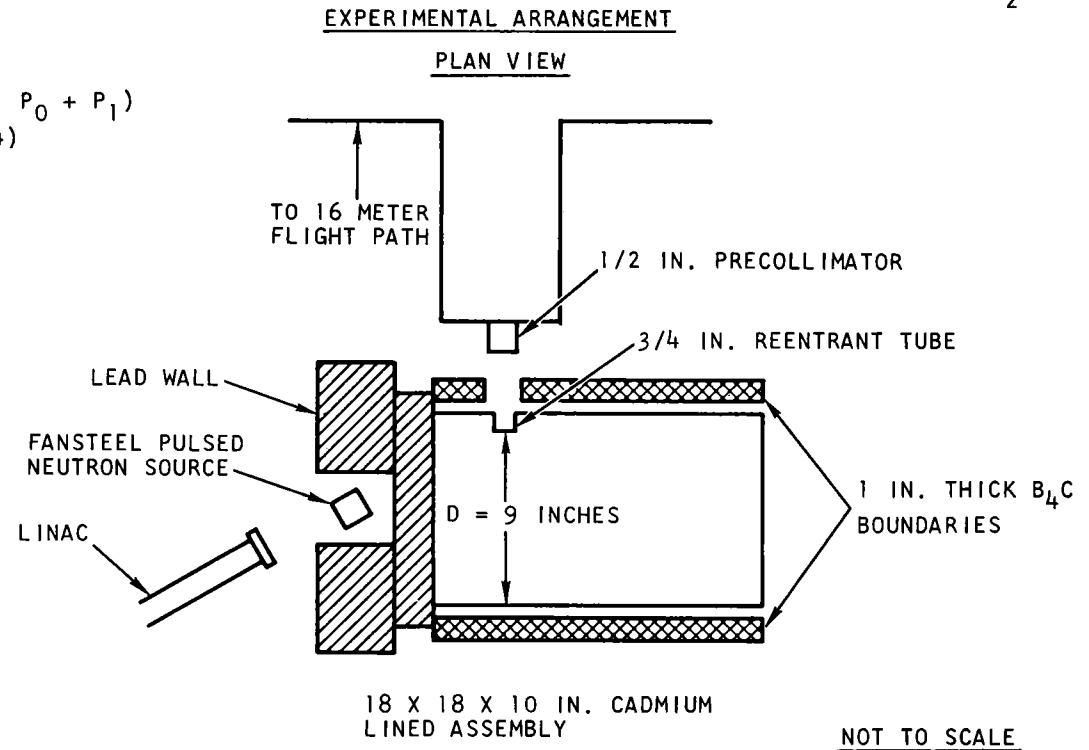
N = 1.430 X 10<sup>20</sup>

N = 2.849 X 10<sup>22</sup>

N = 9.150 X 10<sup>21</sup>

### LOCAL BUCKLING

B<sup>2</sup> TRANSVERSE = 0.00527



GENERAL ATOMIC LINAC-PULSED TIME-OF-FLIGHT  
TECHNIQUES 4/1/64 T7, T8

Fig. 13.1 -- Example of spectrum  
book format (Sheet 1 of 3)



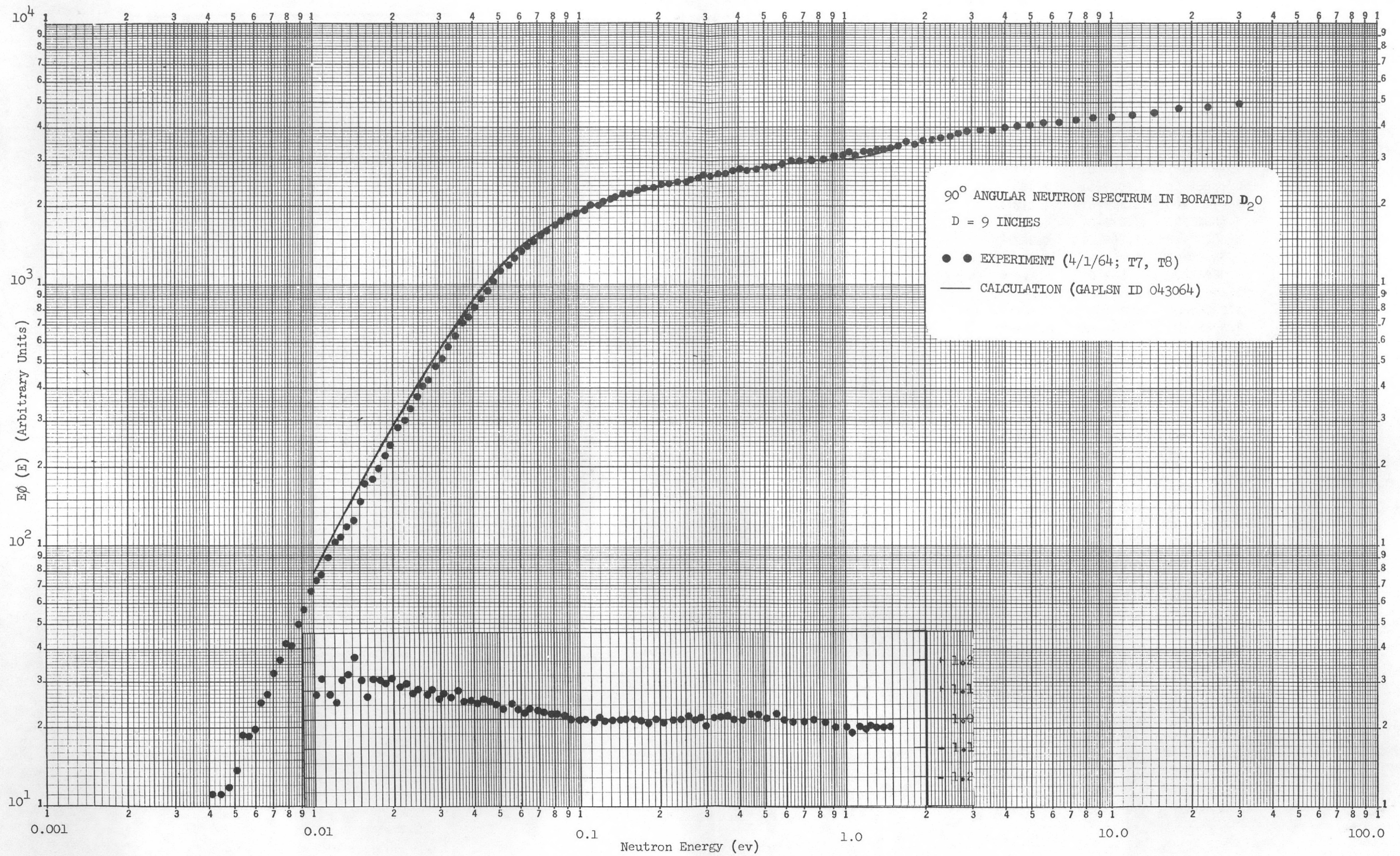


Fig. 13.1 -- Example of spectrum  
 book format (Sheet 2 of 3)



90° ANGULAR NEUTRON SPECTRUM IN BORATED D<sub>2</sub>O  
4-1-64 T7, T8

E(ev)	$\phi$ (E)	E $\phi$ (E)	E(ev)	$\phi$ (E)	E $\phi$ (E)	E(ev)	$\phi$ (E)	E $\phi$ (E)
3.01050+01	3.772-02	4.983+00	4.35045-01	1.438+00	2.744+00	3.67367-02	4.423+00	7.128-01
2.29377+01	4.761-02	4.791+00	4.06459-01	1.540+00	2.746+00	3.46069-02	4.127+00	6.266-01
1.80555+01	6.048-02	4.791+00	3.80601-01	1.629+00	2.720+00	3.26562-02	4.065+00	5.824-01
1.45811+01	7.192-02	4.601+00	3.57134-01	1.705+00	2.671+00	3.08651-02	3.872+00	5.243-01
1.20209+01	8.497-02	4.481+00	3.35772-01	1.803+00	2.656+00	2.92166-02	3.797+00	4.867-01
1.00803+01	1.007-01	4.454+00	3.16271-01	1.892+00	2.625+00	2.76959-02	3.573+00	4.341-01
8.57431+00	1.173-01	4.413+00	2.98420-01	2.016+00	2.639+00	2.62903-02	3.553+00	4.098-01
7.38222+00	1.335-01	4.325+00	2.82039-01	2.061+00	2.550+00	2.48855-02	3.384+00	3.695-01
6.42250+00	1.509-01	4.252+00	2.66970-01	2.164+00	2.534+00	2.34927-02	3.231+00	3.330-01
5.63845+00	1.675-01	4.144+00	2.53077-01	2.230+00	2.476+00	2.22128-02	3.046+00	2.969-01
4.98968+00	1.868-01	4.090+00	2.37233-01	2.368+00	2.464+00	2.10339-02	3.041+00	2.807-01
4.44677+00	2.058-01	4.015+00	2.20055-01	2.522+00	2.435+00	1.99456-02	2.730+00	2.389-01
3.98787+00	2.291-01	4.008+00	2.04676-01	2.698+00	2.423+00	1.88709-02	2.681+00	2.220-01
3.59651+00	2.474-01	3.904+00	1.90855-01	2.802+00	2.346+00	1.78104-02	2.539+00	1.984-01
3.26006+00	2.736-01	3.913+00	1.78387-01	2.989+00	2.339+00	1.68391-02	2.410+00	1.780-01
2.96870+00	2.972-01	3.870+00	1.67101-01	3.109+00	2.280+00	1.59480-02	2.460+00	1.721-01
2.71472+00	3.179-01	3.787+00	1.56853-01	3.257+00	2.242+00	1.51259-02	2.210+00	1.466-01
2.49200+00	3.409-01	3.727+00	1.47519-01	3.446+00	2.230+00	1.43207-02	1.977+00	1.242-01
2.29560+00	3.634-01	3.660+00	1.38994-01	3.578+00	2.182+00	1.35357-02	1.966+00	1.168-01
2.12154+00	3.890-01	3.621+00	1.31186-01	3.726+00	2.145+00	1.28135-02	1.885+00	1.060-01
1.96654+00	4.157-01	3.586+00	1.24017-01	3.856+00	2.098+00	1.21476-02	1.921+00	1.024-01
1.82794+00	4.326-01	3.469+00	1.17420-01	3.922+00	2.021+00	1.15000-02	1.782+00	8.991-02
1.70348+00	4.717-01	3.526+00	1.11335-01	4.130+00	2.017+00	1.08722-02	1.624+00	7.748-02
1.59132+00	4.892-01	3.416+00	1.04828-01	4.224+00	1.943+00	1.02945-02	1.616+00	7.299-02
1.48988+00	5.168-01	3.378+00	9.80517-02	4.408+00	1.896+00	9.76157-03	1.572+00	6.731-02
1.39784+00	5.341-01	3.276+00	9.19108-02	4.581+00	1.847+00	9.24569-03	1.416+00	5.742-02
1.31407+00	5.736-01	3.307+00	8.63285-02	4.613+00	1.747+00	8.74760-03	1.296+00	4.973-02
1.23301+00	5.987-01	3.238+00	8.12389-02	4.758+00	1.696+00	8.28870-03	1.128+00	4.102-02
1.16427+00	6.336-01	3.237+00	7.65858-02	4.835+00	1.625+00	7.86499-03	1.230+00	4.243-02
1.10113+00	6.589-01	3.183+00	7.23206-02	4.871+00	1.546+00	7.45606-03	1.109+00	3.629-02
1.04299+00	7.063-01	3.232+00	6.84013-02	4.906+00	1.472+00	7.06223-03	1.044+00	3.235-02
9.89333-01	7.278-01	3.159+00	6.47916-02	4.934+00	1.402+00	6.69880-03	9.112-01	2.678-02
9.16727-01	7.809-01	3.141+00	6.14596-02	5.000+00	1.348+00	6.34944-03	8.922-01	2.485-02
8.31207-01	8.397-01	3.062+00	5.80138-02	4.975+00	1.266+00	6.01415-03	7.498-01	1.979-02
7.57121-01	9.139-01	3.036+00	5.45081-02	4.912+00	1.175+00	5.70474-03	7.480-01	1.872-02
6.92518-01	9.836-01	2.988+00	5.13100-02	4.963+00	1.117+00	5.40817-03	7.874-01	1.868-02
6.35845-01	1.062+00	2.964+00	4.83845-02	4.800+00	1.019+00	5.11467-03	6.157-01	1.382-02
5.85855-01	1.147+00	2.947+00	4.57014-02	4.725+00	9.474-01	4.79175-03	5.682-01	1.195-02
5.41537-01	1.189+00	2.824+00	4.32348-02	4.596+00	8.718-01	4.44258-03	5.727-01	1.116-02
5.02064-01	1.284+00	2.827+00	4.09618-02	4.569+00	8.211-01	4.12279-03	6.172-01	1.116-02
4.66756-01	1.344+00	2.753+00	3.88628-02	4.423+00	7.541-01			

Fig. 13.1 -- Example of spectrum  
book format (Sheet 3 of 3)

where  $E_c$  is a convenient cut-off energy and where the source  $S(E)$  is given by

$$S(E) = \int_{E_c}^{\infty} \phi(E') \Sigma(E' \rightarrow E) dE' \quad (13.2.2)$$

and can be calculated once the high energy spectrum has been obtained. In practice this apparently simple procedure encounters several numerical difficulties, some of which are listed below:

1. The cutoff  $E_c$  should be at a fairly high energy for strongly bound systems. For instance, for H bound in  $H_2O$  it should not be smaller than 2 or 3 eV since the highest vibrational frequency of the  $H_2O$  molecule is 0.5 eV.
2. A high value of  $E_c$  makes the computation of the thermal kernel very expensive and it very often requires a larger number of phonons than originally provided by the kernel calculating codes. Sometimes, instead of increasing the number of phonons, it is better to make a new asymptotic approximation, since otherwise the kernel becomes too singular at higher energies.
3. In order to avoid the difficulties of a high value of  $E_c$ , it has become customary to use a 1 eV cut off and to tack on a free gas kernel with  $T=T_{eff}$ . ( $T_{eff}$  being the effective temperature of the bound system) for energies between 1 eV and the lowest energy of the slowing down calculation.

This procedure, however, has also proved to be unsatisfactory. The reason is that the discontinuity of the kernel produces a considerable jump of the scattering cross section which, in the example of Fig. 13.2 ( $H_2O$ ) actually falls below its free atom value. This should be compared with the cross section corresponding to a complete free gas kernel at  $T=T_{eff}$  which is also shown on the figure. The reason for the discrepancy is that in the first case the upscattering is calculated at all energies by detailed balance using room temperature  $T$ , whereas the correct upscattering should be determined by  $T_{eff}$ . In order to avoid this problem, one could think of using  $T$  for upscattering from below 1 eV and  $T_{eff}$  from above 1 eV. This, however, leads to an error of  $\Sigma_g$  below 1 eV of the same magnitude as the one just corrected for above 1 eV but of opposite sign.

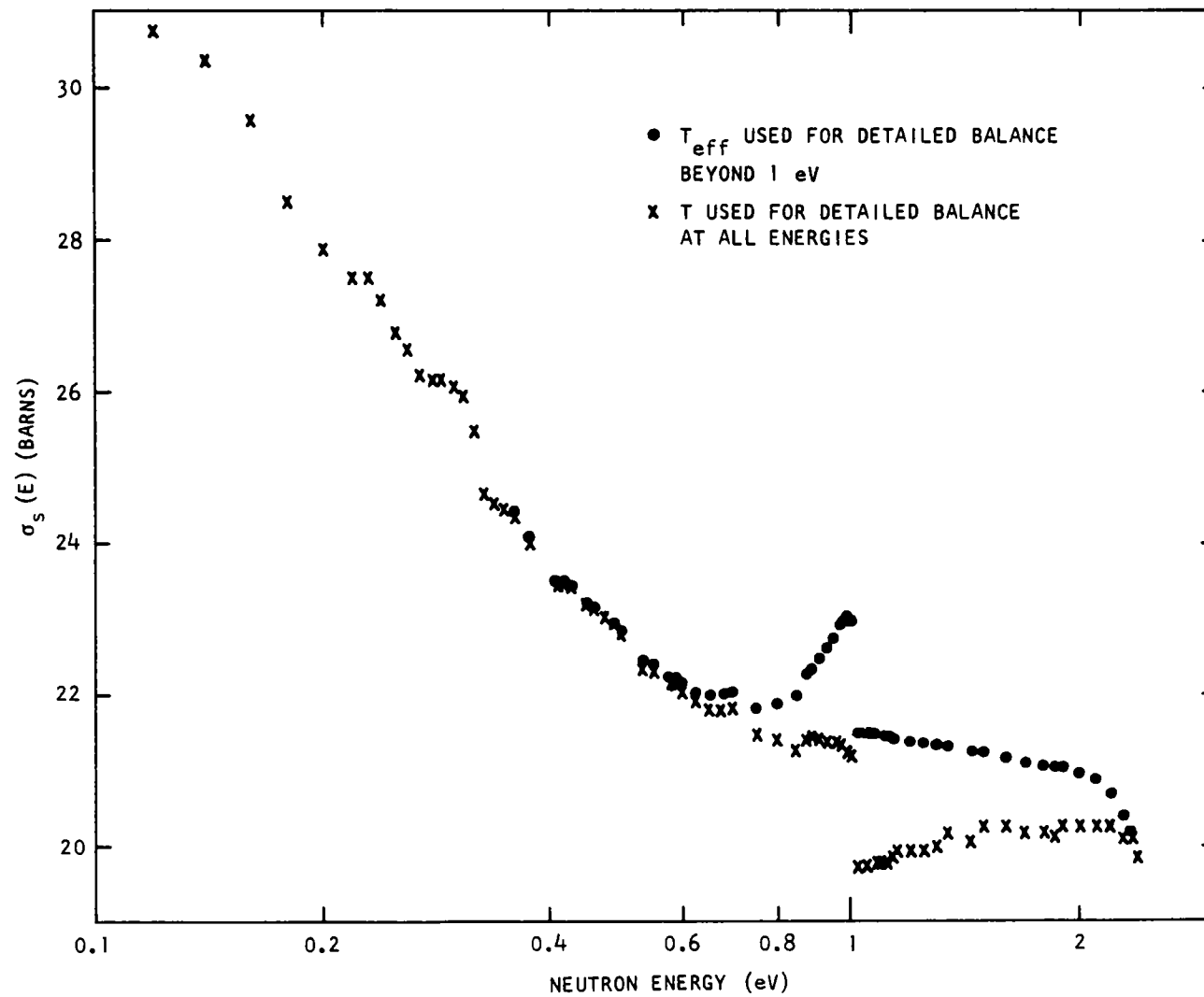


Fig. 13.2 -- Scattering cross section for  $\text{H}_2\text{O}$  in the thermal-epithermal joining region

In fact, no matter what temperature is used for the detailed balance above  $E_c$ , the discontinuity of  $\sigma_s$  at  $E_c$  is

$$\Delta\sigma = \int_0^{E_c} [\sigma_b(E_c \rightarrow E') - \sigma_{gT_{\text{eff}}}(E_c \rightarrow E')] dE' \quad (13.2.3)$$

where  $\sigma_b$  and  $\sigma_{gT_{\text{eff}}}$  refer to the two kernels joined at  $E_c$ , namely the bound kernel and the free gas kernel at  $T=T_{\text{eff}}$ .

The following example shows practically the mentioned difficulties. It is the case of a borated  $H_2O$  infinite medium with an  $H_3BO_3$  concentration of 43.7 g/l ( $\sim 2\%$ ) at 300°K. The spectrum calculation was done with the codes GAM II<sup>(87)</sup> (slowing down) and GATHER II<sup>(13)</sup> (thermal) using the standard energy mesh, which for the thermal range consists of 101 points between 0.001 and 2.38 eV. The bound H kernel was calculated with THERM-3, essentially the same code as GAKER.<sup>(12)</sup> (See section 11.5.) The source for the thermal spectrum is calculated by GAM and hence the thermal and epithermal parts of the spectrum should match at the cut-off energy  $E_c = 2.38$ .

However, as may be seen in Fig. 13.3, instead of a smooth joining, there is a jump of the order of 5%. It turns out, however, that about half of this can be explained by the fact that GAM uses the H scattering cross sections obtained from BNL-325, which really apply to  $H_2$  gas. At 2.38 eV, for instance, this is about 2.5% higher than the free atom cross section  $\Sigma_0 = 20.36$  barn. Since for H the slowing down source is

$$S(E) = \Sigma_{\text{tot}}(E_c) \phi(E_c) \quad (13.2.4)$$

it is clear that using  $\Sigma_0$  in GAM instead of the BNL-325 values, the jump should be considerably smaller. This change will be introduced in GAM in the near future. Figure 13.3 also shows the reduced jump obtained by multiplying the slowing down spectrum by  $\Sigma_{\text{tot}}(E_c)/\Sigma_0$ .

Rigorously speaking the source given by (13.2.1) should be multiplied by  $\text{erf} \sqrt{E/kT}$  but this factor has negligible influence on the flux at  $E = E_c$ .

For comparison the calculation has been repeated for a free H gas kernel as seen in Fig. 13.4 (where again the slowing down spectrum has been renormalized).

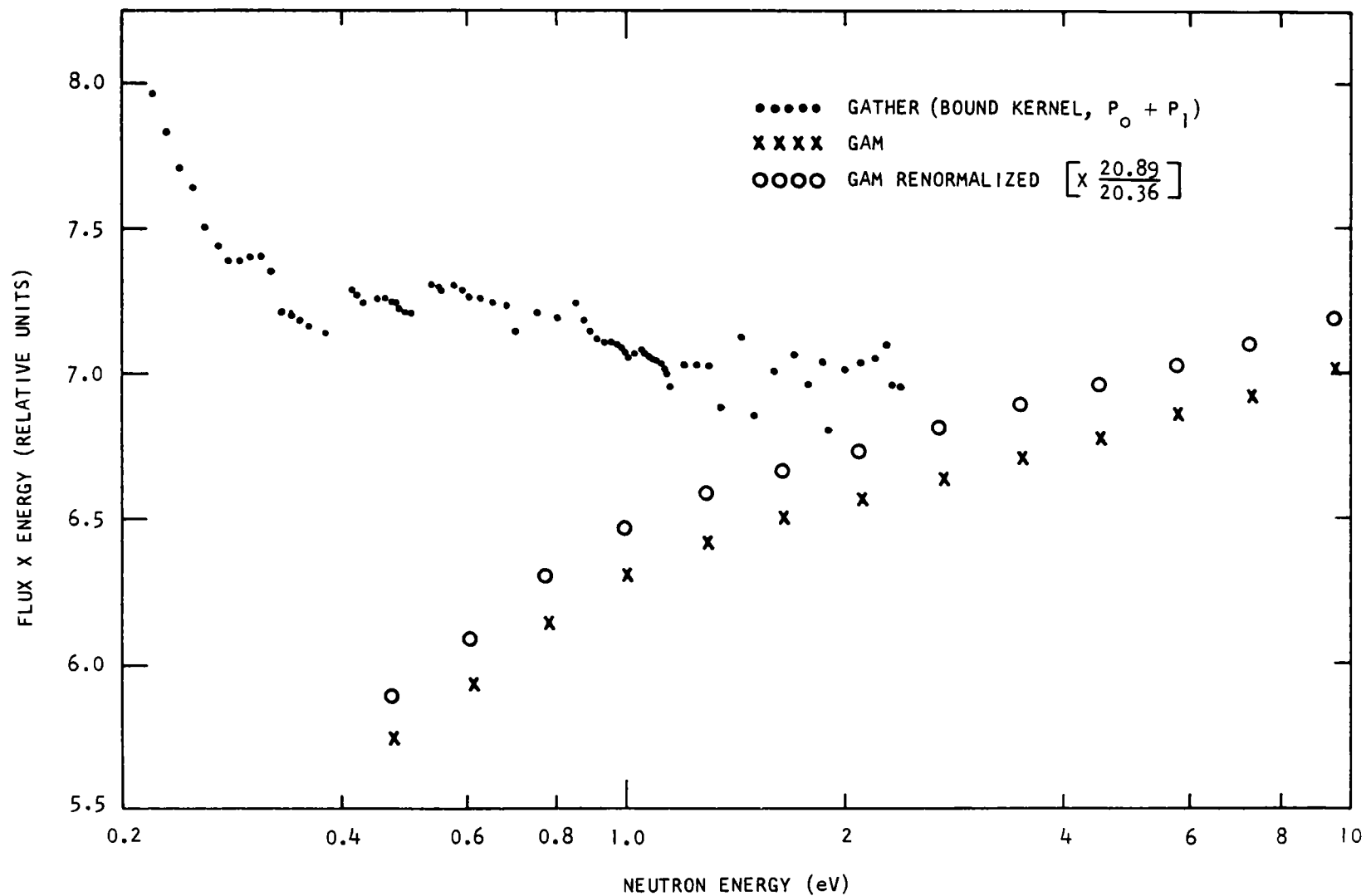


Fig. 13.3 -- Neutron flux in borated  $H_2O$  in the thermal-epithermal joining region based on the bound hydrogen model

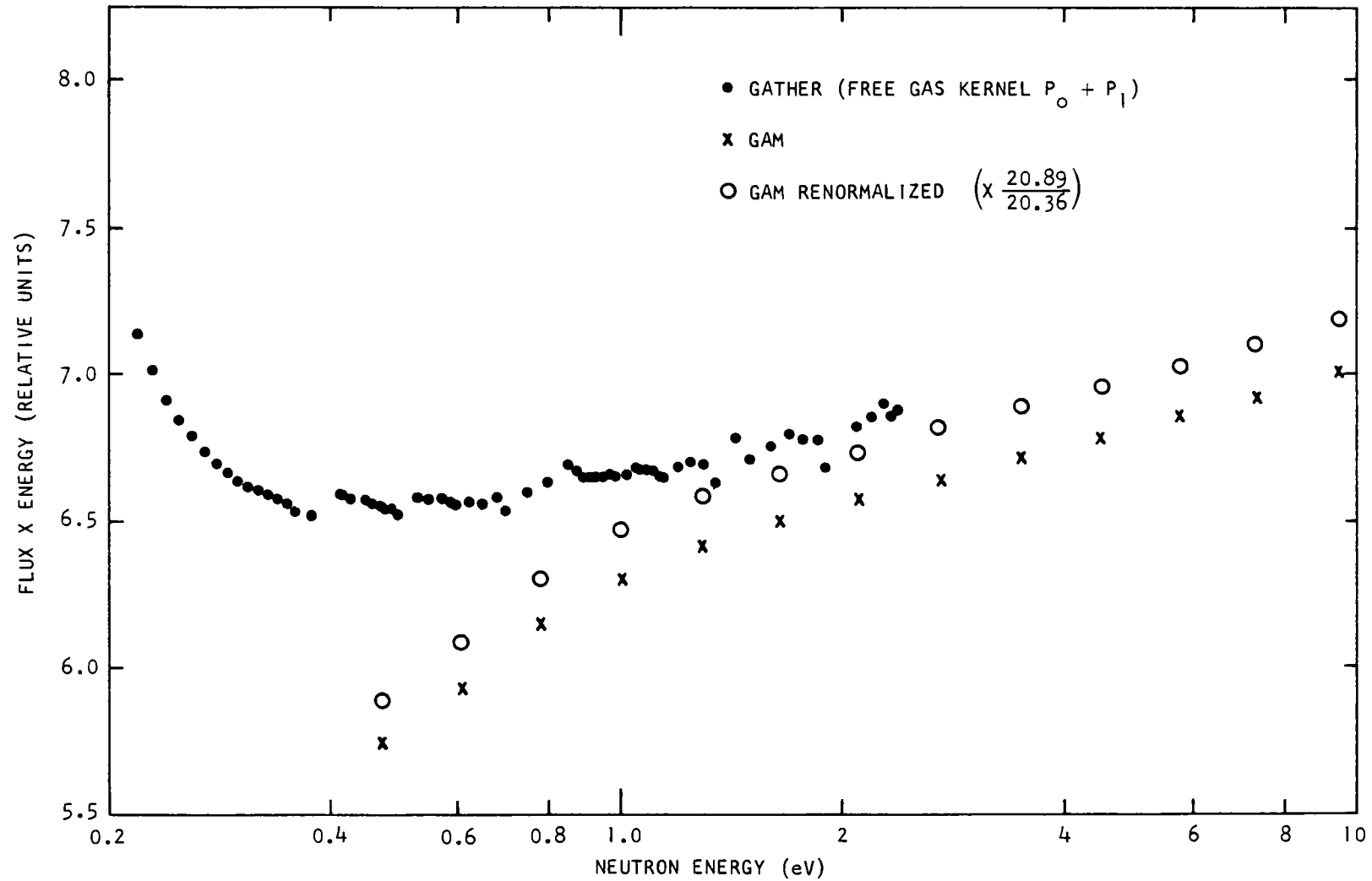


Fig. 13.4 -- Neutron flux in borated  $H_2O$  in the thermal epithermal joining region based on the free gas model

For the free gas, of course,  $E_c = 2.38$  eV is a much better cut off than for the bound kernel.

A further complication is due to the irregularity of the standard 101 point energy mesh which leads to considerable errors in the regions where the point density suddenly changes. This is particularly serious at 0.1 eV where the spacing suddenly jumps from 0.005 to 0.02 eV. How badly the cross section is affected by this factor can be seen in Fig. 13.5 which compares the results for the standard 101 point mesh with those for a 55 point mesh whose points are logarithmically spaced between 0.001 and 1.0 eV.

It appears that the simplest way out of the preceding numerical difficulties is to extend the range of the thermalization kernel to energies of several eV, either providing more phonons or making suitable asymptotic approximations.

An alternate approach would be to ignore the high energy normalization and simply normalize the thermal spectra only, to give the same absorption rate for theory and experiment. Of course, this criterion is only meaningful when absorption dominates over leakage.

For H in  $H_2O$ , or other hydrogenous compounds, another solution would be to use  $E_c \sim 1$  eV and tack on Parks' <sup>(88)</sup> asymptotic spectrum for  $E > E_c$ . The same can be said about single element moderators like graphite and Be, for which Corngold's <sup>(89)</sup> asymptotic expansion could be used (at least for  $1/v$  poisoned media). It is not clear, however, what to do with cases like  $D_2O$  or  $BeO$ .

Only infinite medium spectra were considered in what precedes (including finite media in which the leakage is represented by a  $DB^2$  term). In space dependent problems, the thermal and epithermal part of the spectrum should be determined simultaneously in one single GAPLSN calculation. The source to be used for this calculation could, perhaps, be derived from a measurement of the epithermal flux at the Au resonance. The group constants for this GAPLSN computation must be obtained from an infinite medium calculation (with appropriate  $DB^2$ ) according to the methods discussed previously. Since the normalization procedure has not been definitely decided, the measured spectra in the Spectrum Book are compared to theoretical values only up to 2.38 eV normalized by a simple fit in the  $1/E$  region.

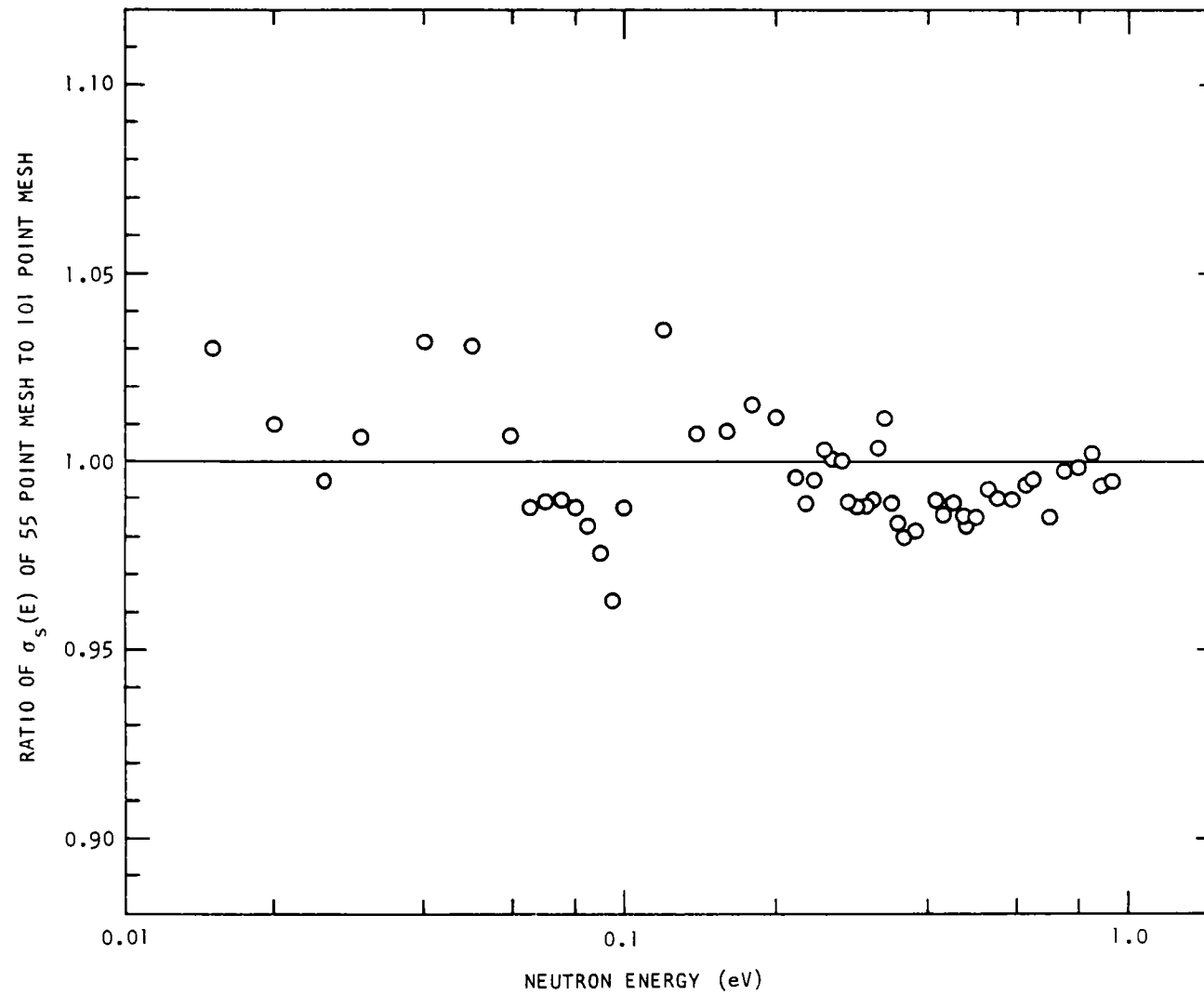


Fig. 13.5 -- Ratio of scattering cross section for  $H_2O$  using different GAKER energy mesh intervals





#### XI V. RESEARCH EQUIPMENT AT THE GENERAL ATOMIC LINAC FACILITY

The General Atomic Linac and its facility have been extensively modified during the last year to improve the accelerator installation as well as the flight-path-experimental space arrangement. Although these changes have been accomplished largely on private funds, certain integral parts of the setup, namely the evacuated neutron paths, have been built with AEC equipment funds.

A year and a half ago the linear accelerator consisted of three standard sections of L-band accelerator waveguide, each powered by a 10 megawatt klystron. The electron beam injection was accomplished with a standard ARCO electron gun and traveling-wave amplifier pulse. The arrangement of the facility at that time is shown in Figure 14.1.

We are presently rebuilding and upgrading the Linac in the manner shown in Figure 14.2. A 20 ampere injector is being designed and built for the improved machine and will be installed in the near future. Each of the three present waveguides will be powered by a 20 megawatt klystron; at present the conversion to 20 megawatt klystrons has been completed successfully on one of these sections. A fourth section of waveguide powered by a 20 megawatt klystron has been installed and will be tested with the new injector this fall. The present injector will be moved to the side, as shown in Figure 14.2, and has already been upgraded with a greatly improved grid pulser so that several amperes of beam current can be obtained from the Linac at short pulse widths.

The arrangement of the accelerating sections in the Linac cell will permit use of all four sections for neutron production; or three sections on some experiments, and the fourth can be used simultaneously for lower energy, high current experiments. The neutron yield will be increased by over a factor of two and as much as an order of magnitude for the shorter pulse work. With these changes, the General Atomic Linac will produce the highest neutron intensity of any known electron accelerator.

Good progress has also been made on partitioning the facility so that experiments can be set up while research goes on in other cells. The experimental room associated with the neutron flight paths is already completed as an independent cell area and is presently available over 40 hours a week for experimental setup even during machine operation. A new access way and shield door have been built to accommodate those using the room.

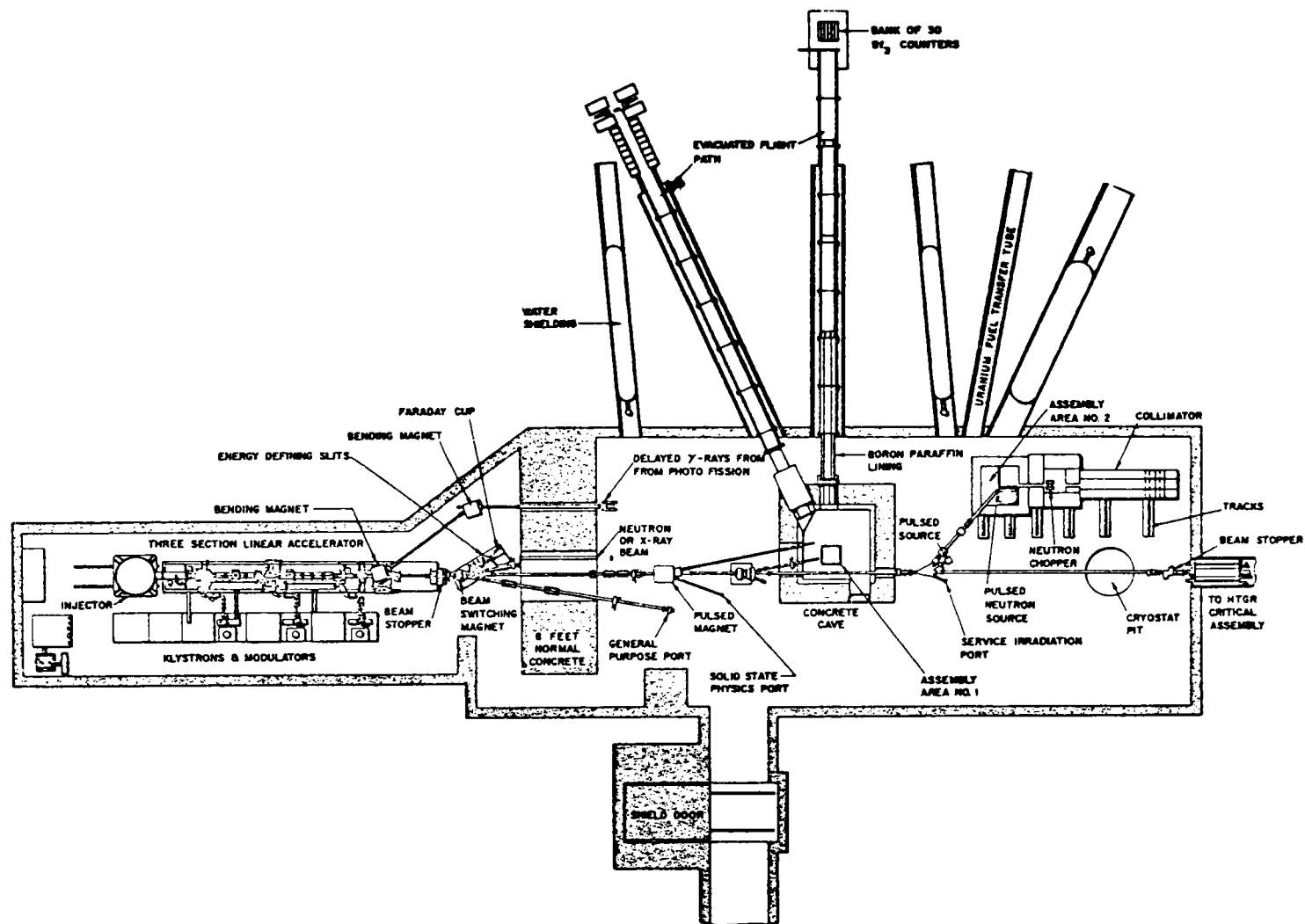


Fig. 14.1 -- Basic Linac facility 1963

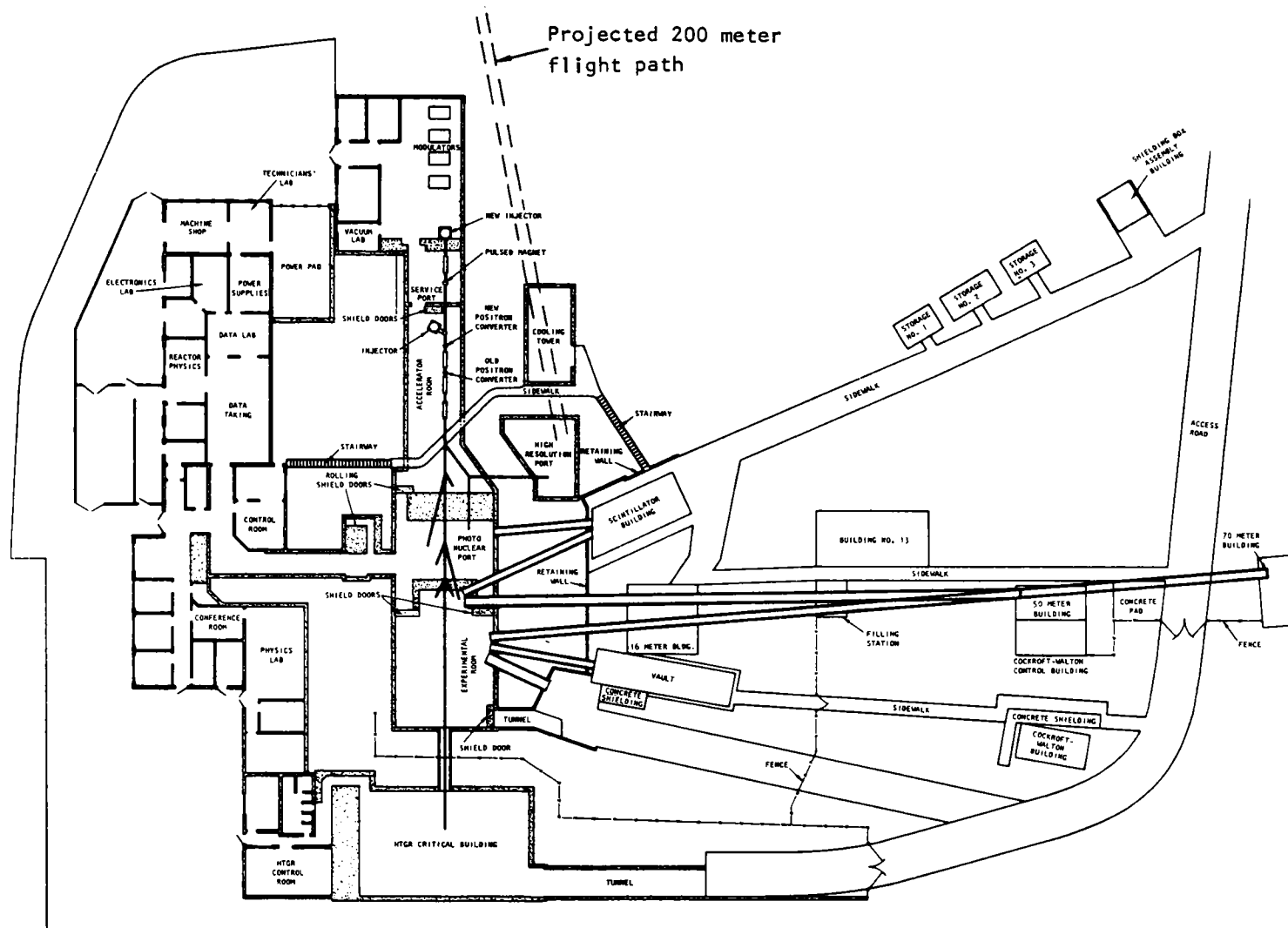


Fig. 14.2 -- Present and planned Linac facility

The flight path system has been extensively improved by replacing the helium gas-filled flight path with evacuated sections of steel pipe. Through an arrangement of pivots and rails the drift tubes can be rotated from one experiment to another while still evacuated. In this way the 50-meter flight path can be formed as an extension to the 16-meter flight path. This same extension is also used in forming the 70-meter flight path, which has been constructed recently, together with its associated terminal building. In addition, a third flight path (12 meter) has been set up specifically for the  $\frac{d\sigma}{d\Omega}$  experiments, with excellent shielding and beam definition properties.

The last change planned for this calendar year is the installation of the high-resolution-beam experimental room, which is planned mainly for use in monoenergetic gamma ray work. It is hoped that this same room may eventually be used as a high-intensity cell in our reactor physics program. This particular area is one of the few into which we could hope to bring a very long flight path (200 meters) for high-resolution neutron spectral work, particularly above the thermal energy region. Provision will be made so that such a path could be installed later, and discussions with the AEC are contemplated pointing out the desirability of such an installation at General Atomic to take advantage of the high neutron beam intensities available.

## REFERENCES

1. Beyster, J. R., et al., "Integral Neutron Thermalization, Annual Summary Report, October 1, 1960, through September 30, 1961," USAEC Report GA-2544, General Atomic Division, General Dynamics Corporation, 1961, 218p.
2. Beyster, J. R., et al., "Integral Neutron Thermalization, Annual Summary Report, October 1, 1961, through September 30, 1962," USAEC Report GA-3542, General Atomic Division, General Dynamics Corporation, 1962. 205p.
3. Beyster, J. R., et al., "Integral Neutron Thermalization, Annual Summary Report, October 1, 1962 through September 30, 1963," USAEC Report GA-4659, General Atomic Division, General Dynamics Corporation, 1963, 195 p.
4. Mostovoy, V., et al., Proc. 2nd Intern. Conf. Peaceful Uses Atomic Energy, Geneva, p/2152 (1958).
5. Honeck, H. C., and H. Takahashi, Nuc. Sci. Eng. 15, 115, February (1963).
6. Nelkin, M. S., "Scattering of Slow Neutrons by Water," Phys. Rev. 119, 741 (1960).
7. Koppel, J. U., and J. A. Young, Nuc. Sci. Eng., 19, 412 (1964).
8. Haywood, B. C. and L. M. Thorsen, USAEC Report BNL 719 (1962).
9. Poole, M. J., private communication.
10. Young, J. C., et al., "Neutron Spectra Measurements in  $H_2O$ ,  $CH_2$  and  $C_6H_6$ ," Nuc. Sci. and Eng. 18, 376 (1964).
11. Beyster, J. R., et al., "Measurements of Neutron Spectra in Water, Polyethylene and Zirconium Hydride," Nuc. Sci. and Eng., 9, 168 (1961).
12. Honeck, H. C., "THERMOS. A Thermalization Transport Theory Code for Reactor Lattice Calculations," Brookhaven National Laboratory, USAEC Report BNL-5826, 1961.

13. Joanou, G. D., C. V. Smith, and H. A. Vieweg, GATHER II, General Atomic Report GA-4132 (1963).
14. Alexander, J. H., G. W. Hinman, and J. R. Triplett, "GAPLSN: A Modified DSN Program for the Solution of the One-dimensional Anisotropic Transport Equation."
15. Beyster, J. R., et al., "Integral Neutron Thermalization, Quarterly Progress Report, October 1, 1962 through December 31, 1962," USAEC Report GA-3853, General Atomic Division, General Dynamics Corporation, 1963, 69p.
16. Honeck, H. C., "An Incoherent Thermal Scattering Model for Heavy Water," Trans. Amer. Nuc. Soc., Vol. 5, No. 1, 47 (1962).
17. Butler, D., Proc. Phys. Soc., 81, 276 (1963).
18. Zemach, A. C., and R. J. Glauber, Phys. Rev. 101, 118 (1956).
19. Ling, T. P., and J. L. Koenig, J. Molec. Spectra, 9, 228 (1962).
20. Goldman, D. T., and F. D. Federighi, Nucl. Sci. Eng., 16, 165 (1963).
21. Tasumi, M., and T. Shimahouchi, J. Molec. Spectra., 9, 261 (1962).
22. Wunderlich, B., J. Chem. Phys., 37, 1207 (1962).
23. Parks, D. E., unpublished.
24. Bach, D. R., et al., shown in the paper by D. J. Goldman and F. D. Federighi, Nucl. Sci. and Eng., 16, 165 (1963).
25. Young, J. C., J. A. Young, G. K. Houghton, G. D. Trimble, and J. R. Beyster, Nucl. Sci. and Eng., 19, 230 (1964).
26. Bell, Joan, SUMMIT, USAEC Report GA-2492 (1962).
27. Roberts, W. J., and J. Miller, "Neutron Thermalization in Zirconium Hydride," Nucl. Sci. and Eng. (in press).
28. Rosenbluth, N. N., and J. M. Nelkin, GA-471, 1958 - "Technical Foundations of TRIGA."
29. Whittemore, W. L., "Differential Neutron Thermalization Annual," October 1, 1962, USAEC Report GA-4434, "Neutron Interactions in Zirconium Hydride," USAEC Report GA-4490.

30. Whittemore, W. L., "Differential Neutron Thermalization, " unpublished and private communication.
31. Miller, J., R. L. Brehm, W. J. Roberts, USAEC Report NAA SR-7140 - December 3, 1962.
32. Bacon, G. E., "Neutron Diffraction," Oxford Press, 1955.
33. Stalinski, G., et al., J. Chem. Phys., 33, 933 (1960), discuss a typical case, the jumping of protons in  $\text{TiH}_{1.61-1.97}$ . NMR measurements show that the protons perform  $\sim 1000$  vibrations in a lattice site between jumps. We are grateful to Prof. W. E. Wallace of the University of Pittsburgh for this reference.
34. Nelkin, M. W., and G. B. West, "Calculations of the Prompt Temperature Coefficients for TRIGA, " unpublished data.
35. Miller, J., R. L. Brehm, and W. J. Roberts, Trans. Am. Nuc. Soc., 5, 49 (1962).
36. Dirac, P.A.M., "The Principles of Quantum Mechanics, " Oxford at the Clarendon Press, pp. 51-54 (1930).
37. Maradudin, A. A., and A. E. Fine, Phys. Rev. 128, 2589 (1962).
38. Sinclair, R. N., Proceedings of the "Symposium on Inelastic Scattering of Neutrons in Solids and Liquids, " Chalk River, Canada, 1962.
39. Schmunk, R. F., private communication.
40. Kothori, L. S., and K. S. Sirgini, Solid State Physics, Vol. 8 (Turnbull), Academic Press, N.Y. (1959).
41. Placzek, G., and L. Van Hove, Nuovo Cimento, 1, 233 (1955).
42. Young, J. A., and J. U. Koppel, Phys. Rev. 134, 1476 (1964).
43. Young, J. A., and J. U. Koppel, J. Chem. Phys. (to be published).
44. Egelstaff, P. A., in Proceedings of Symposium on Inelastic Scattering of Neutrons in Solids and Liquids, Vienna, 1960, International Atomic Energy Agency, 1961, p. 25.
45. Mihalczko, J. T. and V. I. Neeley, "The Infinite Neutron Multiplication Constant of Homogeneous Hydrogen Moderated 2.0 wt. % - U-235 Enriched Uranium, " Nuclear Sci. and Eng. 13, 6-11 (1962).



46. Young, J. C., et al., "Development of a Multiplying Assembly - Final Report," USAEC Report GA-2471 (1961).
47. Garelis, E., and J. L. Russell, Jr., Nuclear Sci. and Eng., 16, 263-270 (1963).
48. Garelis, E., "Theory of Pulsing Techniques," Trans. Am. Nucl. Soc., Vol. 6, No. 2 (1963).
49. Brown, J., et al., "Measurements of Subcritical Reactivity Using a Pulsed Neutron Source," Trans. Am. Nucl. Soc., Vol. 6, No. 2 (1963). Also USAEC Report GA-4838 (1964).
50. Sjöstrand, N. G., "Measurements on a Subcritical Reactor Using a Pulsed Neutron Source," Arkiv fur Fysik 11, 233, (1956).
51. Corngold, N., "On The Analysis of Pulsed, Multiplying Systems," USAEC Report GA-5404 (1964).
52. Integral Neutron Thermalization Quarterly Progress Report ending December 31, 1963, USAEC Report GA-4881.
53. Preiser, S., et al., "A Program for the Numerical Integration of the Boltzmann Transport Equation - NIOBE," Report ARL 60-314, December 1960. See also Argonne National Laboratory Report USAEC Report ANL-5800, 2d ed.
54. Nelkin, M., IAEA Symposium on Inelastic Scattering, Vienna, 1961.
55. Mostovoy, V. I., et al., A/CONF. 28/P/367. International Conference on the Peaceful Uses of Atomic Energy, Geneva, May 1964.
56. Young, J. A., and J. U. Koppel, Nuc. Sci. Eng. 19, 367 (1964).
57. Wikner, N. F., G. D. Joanou, and D. E. Parks, Nuc. Sci. Eng., 19, 108 (1964).
58. Whittemore, W. L., USAEC Report GA-4490 (Revised), Jan. 1964, 30p.
59. Reinsch, V. C., and T. Springer, "Messung des differentiellen streuquerschnittes und des mittleren Energieandering bei der Streuung langsamer Neutronen an Wasser und Eis," Z. Naturforschung, 16a, 112, (1960).

60. Beyster, J. R., and W. R. Mowry, USAEC Report GA-5373, June (1964), 16p.
61. Springer, T., et al., "On the Determination of the Diffusion Constants of  $H_2O$  and  $D_2O$  by Neutron Single-Scattering Experiments, " A/CONF.28/P/763. International Conference on the Peaceful Use of Atomic Energy, Geneva, May 1964.
62. Vinyard, G. H., "Multiple Scattering of Neutrons, " Phys. Rev. 96, 93 (1954).
63. Lemmel, H. D., "Messung des differentiellen Wirkungsquerschnittes bei Streuung von Thermalischen Neutronen an Flussigen Wasser bei Temperaturen bis zu  $200^{\circ}C$ . " Doctoral Thesis, Munich University, February 1964.
64. Lopez, W. M., J. R. Beyster, R. E. Nather, and J. L. Wood, USAEC Report GA-1584, 19 p.
65. Eisenhauer, C. M., and I. Pelah, Phys. Rev. 109, 1046 (1958).
66. Haas, R., W. Kley, K. H. Krebs, and R. H. Rubin, "Phonon Frequency Distribution of Vanadium, " Proceedings of the Symposium on Inelastic Scattering of Neutrons in Solids and Liquids, " Chalk River, Canada, 1962.
67. Springer, T., private communication (unpublished).
68. Poole, M. J., P. Schofield, and R. N. Sinclair, "Some Measurements of Thermal Neutron Spectra, " Proceedings of the Symposium on Exponential and Critical Experiments, IAEA, September 1963.
69. Beckurts, K. H., and K. Wirtz, Neutron Physics, Springer Verlag, Berlin (1964).
70. Radkowski, A., "Temperature Dependence of Thermal Transport Mean Free Path, " USAEC Report ANL-4476, July 1950, p.8
71. Cadilhac, M., J. L. Soule, and O. Tretiakoff, "Thermalization and Neutron Spectra, " A/CONF.28/P/73, International Conference on the Peaceful Uses of Atomic Energy, Geneva, May 1964.
72. Forte, M., W. Kley, and K. Krebs, "Interaction between Cold Neutrons and Condensed Matter, " EUR 1643.e, Ispra, March 1964.

73. Buras, B., J. Leciejewicz, W. Nite, I. Sosnowska, J. Sosnowski, and F. Shapiro, "Time of Flight Method for Crystal Structure Investigations and its Possibility in Connection with Very High Flux Reactors," A/CONF .28/P/488, International Conference on the Peaceful Uses of Atomic Energy, May 1964.
74. J. R. Beyster, et al., Integral Neutron Thermalization Quarterly Progress Report, January 1 through March 31, 1964, " USAEC Report GA-5176.
75. J. R. Beyster, et al., Integral Neutron Thermalization Quarterly Progress Report, April 1 through June 30, 1964, USAEC Report GA-5486.
76. Naliboff, Y.D., "LHK - An IBM 7044 to Calculate Cross Sections and Kernels for Liquid Para and Ortho Hydrogen" (unpublished).
77. Koppel, J. U., "Neutron Scattering by  $H_2O$  Taking into Account the Anisotropy of the Molecular Vibrations," Nuc. Sci. and Eng. 19, 412 (1964).
78. Placzek, G., Phys. Rev. 86, 377 (1952).
79. Sjölander, A., Arkiv Fysik 14, 315 (1958).
80. Glauber, R. J., in Lectures in Theoretical Physics, Vol. IV (Boulder, Colo.), ed. W. E. Brittin et al., Interscience, p. 571 (1962).
81. Parks, D. E., "The Calculation of Thermal Neutron Scattering Kernels in Graphite, USAEC Report GA-2438, (1961).
82. Erdelyi, A., et al., "Higher Transcendental Functions," Vol. 2, p. 147, (Bateman Manuscript Project).
83. Wall, H. S., "Continued Fractions," van Nostrand, 357 (1948).
84. Hastings, C., "Approximations for Digital Computers," Princeton, 169 (1955).
85. Lash Miller, W. and A. R. Gordon, J. Phys. Chem. 35, 2878 (1931).
86. Hildebrand, F. B., "Introduction to Numerical Analysis," McGraw-Hill Brook Company (1956).
87. Joanou, G. D., and J. S. Dudek, "GAM II - A  $B_3$  Code for the Calculation of Fast Neutron Spectra and Associated Multigroup Constants," General Atomic Report GA-4265, 89p., September 1963.

88. Parks, D. E., "The Effects of Atomic Motions on the Moderation of Neutrons," (unpublished data).
89. Corngold, N., Ann. Phys. 6, 368 (1959).



## APPENDIX A

### NEUTRON THERMALIZATION AND REACTOR APPLICATIONS



## NEUTRON THERMALIZATION AND REACTOR APPLICATIONS

John R. Beyster, General Atomic  
Noel Corngold, Brookhaven National Laboratory  
Henry C. Honeck, Brookhaven National Laboratory  
George D. Joanou, General Atomic  
Donald E. Parks, General Atomic

### 1. Introduction

The design of thermal reactors has often been based on approximate treatment of the nuclear physics and on extensive experimental tests of critical and exponential assemblies to determine or adjust reactor parameters. Recently, however, it has become important to improve our understanding of the physical phenomena occurring in reactors in order to develop reliable computational procedures for optimizing reactor design. These procedures require detailed knowledge of all relevant neutron cross sections, and reliable methods of predicting thermal reactor neutron spectra. The demand for cross sections of sufficient accuracy for reactor analysis is being answered by careful measurement.<sup>(1)</sup> However, the problem of predicting thermal reactor spectra under all spatial and temperature conditions likely to be encountered in a physical system requires in addition an understanding of thermal neutron scattering. A great deal of progress has been made in the last few years in developing this understanding. It is the primary purpose of this paper to describe these advances and their significance from the standpoint of reactor technology.

Underlying the earliest descriptions of thermal neutron scattering and spectra was the fact that the first reactors were very well thermalized ( $\xi\Sigma_s/\Sigma_a \gg 1$ ). As a consequence, it was useful and expedient to consider a Maxwellian distribution of thermal neutrons at a temperature  $T_n$  differing only slightly from the actual temperature of the moderator;<sup>(2)</sup>

$$T_n = T \left[ 1 + A \frac{\Sigma_a(kT)}{\xi \Sigma_s} \right] \quad (1)$$



One could presumably determine the value of the dimensionless coefficient  $A$  by measuring the activation of  $1/v$ -foils by neutrons belonging to the spectrum under investigation. This description of the spectrum is of little use for  $\Sigma_a(kT)/\xi\Sigma_s \gtrsim 0.1$ , or when the spectrum is appreciably influenced by resonance absorbers. Also, there is the difficulty caused by the absence of a well defined transition energy above which slowing down theory is valid and below which the spectrum is Maxwellian.<sup>(3)</sup> This latter difficulty is overcome in the Wilkins<sup>(4)</sup> and Wigner-Wilkins<sup>(5)</sup> theories of thermal neutron scattering in which the moderator is considered to be an ideal gas consisting of heavy nuclei or protons respectively. However, detailed theoretical and experimental studies of neutron thermalization have shown that these simple models are not usually adequate for reactor design calculations, and scattering cross sections which embody the characteristic crystalline and molecular properties of the moderator are necessary. Subsequent sections of this paper discuss theoretical procedures for calculating these scattering cross sections, the experimental tests performed to assess the adequacy of the procedures, and the sensitivity of typical reactor calculations to the scattering description.

## 2. Theory

The general theory of neutron thermalization by chemically bound systems, is based on the Fermi pseudo-potential approximation.<sup>(6,7,8,9)</sup> For thermalization studies, the fundamental cross section of interest is the differential cross section  $\sigma(E_0, E, \theta)$  for energy transfer from an initial energy  $E_0$  to a final energy  $E$  through an angle  $\theta$  in the laboratory system. For an isotropic moderator at temperature  $T$  consisting of a single atomic species of atomic mass  $M$ , this cross section can be expressed in the form<sup>(10)</sup>

$$\sigma(E_0, E, \theta) = \frac{1}{4\pi T} \sqrt{\frac{E}{E_0}} e^{-\frac{\beta}{2}} \alpha_b S(\alpha, \beta) = \frac{1}{4\pi T} \sqrt{\frac{E}{E_0}} e^{-\frac{\beta}{2}} \left[ \alpha_b S_s(\alpha, \beta) + \sigma_c S_d(\alpha, \beta) \right] \quad (2)$$

where  $\alpha_b$  is the bound atom cross section,  $\sigma_c$  is the bound coherent cross section,  $\alpha = (E_0 + E - 2\sqrt{E_0 E} \cos\theta)/MT$ ,  $\beta = (E_0 - E)/T$ , ( $\hbar = k = \text{neutron mass} = 1$ ).  $S(\alpha, \beta)$ , the scattering law, is a function of only the two variables  $\alpha$  and  $\beta$ . The self part  $S_s(\alpha, \beta)$  represents the scattering of a neutron by a single atom in the interatomic force field of all its neighbors while the distinct part  $S_d(\alpha, \beta)$  represents the effects of interference between neutron waves scattered from different atoms. Several physical and mathematical approximations are generally introduced to reduce the problem of calculating  $\sigma(E_0, E, \theta)$  to a tractable form. The first

approximation considered is that of neglecting interference effects in the inelastic scattering of neutrons. Marshall and Stuart<sup>(11)</sup> and Butler<sup>(12)</sup> have made calculations which show that interference effects are generally a small part of the inelastic scattering. Thus, it is expected that interference phenomena in inelastic scattering will have a small effect on most neutron spectra. For elastic scattering the interference effects are dominant except for hydrogenous moderators. These considerations result in the incoherent approximation for inelastic scattering in which for solids  $S_d(\alpha, \beta)$  is replaced by its elastic part,  $S_d^{el}(\alpha, \beta)$ , which is easily calculated.  $S_d^{el}$  in the latter case gives rise to the well known Bragg peaks in the scattering cross section. The Bragg effects are unimportant for most reactor spectral calculations but must be considered in the interpretation of the decay of a thermalized pulse in a finite medium.

$S_g(\alpha, \beta)$  which depends rather sensitively on moderator atomic motion, has a significant effect on thermal reactor spectra. Fortunately, this effect is not so pronounced as to require a completely detailed description of moderator atomic motions. Most calculations of  $S_g(\alpha, \beta)$  for moderators have as their basis:<sup>(10)</sup>

$$S_g(\alpha, \beta) = \frac{1}{2\pi} \int_{-\infty}^{+\infty} I(\alpha, \tau) e^{i\beta\tau} d\tau \quad (3)$$

with  $I(\alpha, \tau)$  given by the Gaussian Approximation

$$I(\alpha, \tau) = \exp \left\{ -\alpha \int_{-\infty}^{+\infty} \frac{\rho(\beta)}{\beta \sinh \beta/2} \left[ \cosh(\beta/2) - \cos \beta\tau \right] d\beta \right\} \quad (4)$$

The entire dependence of the neutron scattering on the motion of moderator atoms is contained in  $\rho(\beta)$  or equivalently  $\rho(\omega)$ , where  $\omega = T\beta/\hbar$ . In the case of a harmonically vibrating solid,  $\rho(\omega)$  is identical with the frequency distribution or density of modes of lattice vibrations. For other systems such as liquids, the interpretation of  $\rho(\omega)$  as a density of modes is not a rigorous interpretation. The form (4) of the Gaussian approximation is verified by many of the exactly soluble physical models: (1) the ideal gas (as a limiting case), (2) a system of isotropic Einstein oscillators, (3) a simple cubic crystal with one atom per unit cell, and (4) the diffusing atom model of a monatomic liquid.

In a real physical system, there are always effects which cannot be rigorously accounted for within the framework of the Gaussian approximation. Among these effects are the anharmonic vibrations in solids and molecules, the free or hindered rotations of a semi-rigid molecule, and the anisotropic but harmonic vibrations of atoms in a polycrystalline material. Although the corrections to

the Gaussian approximation are expected to have a rather small effect on neutron spectra, detailed calculations of the magnitude of these effects exist only for the cases of anisotropic motion of the atoms in  $C^{(13)}$  and  $H_2O^{(14)}$

The results given below show that with a physically realistic  $\rho(\omega)$ , the  $S_g(\alpha, \beta)$  calculated on the basis of the Gaussian approximation leads to agreement between many theoretical and experimental reactor design quantities. The same agreement cannot generally be obtained by rigorous application of the free gas or heavy gas models. Many of the codes that have been developed for calculating scattering law or scattering kernels are listed in Table I.

### 3. Experimental Comparisons

The frequency distribution  $\rho(\omega)$  for many of the common moderators has been obtained as a result of studies of double differential neutron scattering, lattice dynamics, Raman and infra-red spectroscopy, and specific heat, (see Section 3.1 below). Other experiments of a more integral nature help establish the adequacy for reactor design of these frequency spectra and the scattering cross sections derived therefrom (see Section 3.2).

#### 3.1 Determination of $\rho(\omega)$

Here we discuss some of the techniques for measuring the frequency distribution  $\rho(\omega)$ . Although the complete determination of  $\rho(\omega)$  usually depends on theoretical considerations using data from more than one type of experiment, this discussion is limited to techniques of neutron spectroscopy. One method of determining  $\rho(\omega)$  is to measure the one phonon incoherent scattering<sup>(15)</sup> cross section which is directly proportional to the frequency spectrum for crystals having simple cubic symmetry. This procedure is not generally useful since only vanadium, hydrogen, and certain special alloys scatter almost completely incoherently. A more efficacious technique is to measure the dispersion relations<sup>(16)</sup>  $\omega(\vec{k})$  vs  $\vec{k}$ , where  $\vec{k}$  is the phonon wave vector, by observing the one phonon coherent scattering of monoenergetic neutrons in a crystal symmetry direction. From this the force constants in a particular model for the atomic binding in the lattice can be calculated to determine  $\rho(\omega)$ .<sup>(17)</sup> The frequency spectrum of beryllium<sup>(18)</sup> determined by this procedure is shown in Fig. 1. A frequently used method of determining  $\rho(\omega)$  utilizes the scattering law  $S(\alpha, \beta)$ <sup>(10)</sup> measurements. The limit  $\alpha \rightarrow 0$  of  $S_g(\alpha, \beta)$  is proportional to  $\rho(\beta)$  and this serves as a basis for determining  $\rho(\beta)$  by extrapolating measured values of  $S(\alpha, \beta)/\alpha$  toward  $\alpha = 0$  for fixed  $\beta$ . A significant difficulty sometimes arises however, since  $S(\alpha, \beta) \approx S_g(\alpha, \beta)$  only for large

values of  $\alpha$ , whereas the extrapolation often must proceed from small values where interference effects are at a maximum. In addition, measurements of  $S(\alpha, \beta)$  often do not have sufficient accuracy. In Fig. 1 the frequency distribution derived from the extrapolation technique<sup>(19)</sup> is compared with  $\rho(u)$  determined from accurately measured dispersion relations. In Fig. 2 two frequency distributions for graphite which are currently used in reactor analysis are shown, (1) an approximate theoretical calculation of  $\rho(u)$  of Yoshimori and Kitano,<sup>(20,13)</sup> and (2)  $\rho(u)$  derived from the scattering law.<sup>(19)</sup> It would appear that significant discrepancies exist between various determinations of frequency distributions. Proposed frequency spectra exist for most of the other common moderators including  $H_2O$ ,<sup>(22)</sup>  $D_2O$ ,<sup>(12)</sup>  $BeO$ ,<sup>(19)</sup>  $CH_2$ ,<sup>(19)</sup>  $ZrH$ ,<sup>(21)</sup> and many other materials.<sup>(23)</sup> Although some of the frequency spectra are not accurately determined, they are known well enough for many reactor design calculations. For example, typical reactor spectra<sup>(18)</sup> calculated by using the two different frequency spectra proposed for the beryllium lattice in Fig. 1 differ in shape by about 10 percent.

### 3.2 Integral Data Comparisons

From the standpoint of reactor design it appears that only certain important properties of a moderator need to be predicted reasonably accurately. These include, for example, the total neutron cross section, the transport cross section or differential scattering cross sections, infinite medium or scalar neutron flux spectra, and/or  $M_2$  (the second energy moment). These quantities mainly depend on the  $P_0$  and  $P_1$  scattering matrices. Calculations at several laboratories have indicated that higher order scattering has little effect on the thermal neutron spectra and transport.

#### 3.2.1 Spectral and Cross Section Comparisons

The total cross section experiment for some of the common moderators has been performed with sufficient accuracy over the required energy range to provide a meaningful test of the scattering description. In Fig. 3, a recently measured total cross section of water<sup>(14)</sup> can be seen to agree quite well with the predictions of the bound hydrogen atom model for water. Similar results are available for other common moderators.

An integral experiment which is usually quite sensitive to the  $P_0$  energy transfer cross sections is the quasi-infinite medium neutron spectrum measurement. Experimental results are compared with calculations using the neutron diffusion equation,

$$(\Sigma(E) + DB^2)\phi(E) = \int_0^{E_m} \phi(E') \Sigma_s(E' \rightarrow E) dE' + S(E)$$

where  $D$  is the diffusion constant;  $B^2$  is the local buckling and is purposely made as small as possible;  $S(E)$  the epithermal source contribution; and  $E_m$  an upper energy limit in the slowing down energy region. Results from a typical series of temperature dependent spectral experiments<sup>(14)</sup> in  $H_2O$  are compared with calculations in Fig. 4. Similar comparisons included those made for water with various resonance absorbers,<sup>(24,25)</sup> graphite poisoned with  $1/v$  and resonance absorbers,<sup>(26,32)</sup> and  $D_2O$ ,<sup>(14,26)</sup>  $CH_2$ ,<sup>(24,28)</sup>  $BeO$ ,  $C_6H_6$ , and  $ZrH$ ,<sup>(14)</sup> all poisoned with  $1/v$  absorber. The effect of resonance absorption in the energy region 0.07 ev to 0.5 ev on neutron spectra affords a most stringent test of the scattering model. It is apparent from the studies of infinite medium spectra that scattering kernels based on the current state of our knowledge of  $\rho(w)$  can be utilized to make predictions with reasonable accuracy.

Several techniques have been used to test the transport properties of scattering kernels including measurements of angular flux  $\phi(E, x, \mu)$  in a finite one-dimensional medium, of differential scattering cross sections, and of spectra in reactor lattices. Fig. 5 shows a well defined experimental geometry and the angular flux spectral results for this thin  $1/v$  poisoned water slab. These spectra were calculated<sup>(14)</sup> using the  $S_n$  method of solving the neutron transport equation (GAPLSN). The  $P_0$  and  $P_1$  scattering matrices and epithermal source terms were necessary for the solution of the problem and the bound hydrogen kernel for water was used. Completely satisfactory agreement has not been attained as yet on this one dimensional problem possibly because of the difficulty of creating a perfect one-dimensional configuration. In addition Fig. 6 shows results for a one-dimensional graphite interface problem.<sup>(29)</sup> Measurements were not made in the direction of the flux gradient as in the previous case. It appears from the space dependent experiments conducted to date that angular flux spectra measured in the direction of large flux gradients are the most difficult to predict, and these cases are often of great concern to the reactor designer.

Another method of testing the angular portion of the scattering kernel is to measure  $\sigma(E, \mu)$ ,<sup>(30)</sup> the scattering angular distribution. Recent results for water<sup>(14)</sup> are compared with theory based on the bound hydrogen model in Fig. 7. The experimental results, from which multigroup diffusion constants can be derived for reactor analysis, agree well with theory except at forward angles above a few tenths ev neutron energy.

Thermal neutron spectrum experiments in reactor lattices<sup>(31,32,33,34)</sup> yield results which are generally quite sensitive to the neutron transport.

This experiment, however, is difficult to perform under clean experimental conditions because beam extraction can perturb the flux in the lattice. Interpretation is difficult since a highly directional flux is obtained which is not simply related to the scalar flux.<sup>(35)</sup> Recent work in large D<sub>2</sub>O lattices<sup>(34)</sup> has overcome some of these difficulties by using a scatterer to extract a beam. The experimental problem still remains in small H<sub>2</sub>O lattices.

### 3.2.2 Transient Phenomena

Typical reactor spectra may be characterized by their "slowing-down" and "thermal" components, while the spectra obtained in most pulsed and exponential experiments lack the slowing-down component. These experiments are nevertheless useful in testing models for scattering kernels, and in providing averaged diffusion parameters for use in few group theories. The analysis of the pulsed neutron source experiment<sup>(36)</sup> in a subcritical medium is based upon the representation:

$$N(\underline{r}, \underline{v}, \underline{t}) \sim \sum_k N_k(\underline{r}, \underline{v}) e^{w_k t} \quad (4)$$

which, for a system that is not too small, gives a scalar flux:

$$\lim_{t \rightarrow \infty} \int d\hat{n} N(\underline{r}, \underline{v}, \underline{t}) \sim U_0(\underline{r}) \sum_k N_k(v^2) e^{-\lambda_k t} \rightarrow U_0(\underline{r}) N_0(v^2) e^{-\lambda_0 t} \quad (5)$$

With  $1/v$  absorption, measurements of the variation of  $\lambda_0$  with buckling ( $B^2$ ) give the Maxwellian average of  $v\lambda_{tr}(v)$  and the cooling coefficient,  $C$  (which is related to the inelastic part of the scattering kernel). Discrepancies between theory and experiment are most apparent at large  $B^2$  (small samples). In H<sub>2</sub>O, measurements of  $C$  range from 2900 to 4800 cm<sup>4</sup>/sec, in graphite from 12 to 41 x 10<sup>5</sup> cm<sup>4</sup>/sec, and in beryllium 1 to 4 x 10<sup>5</sup> cm<sup>4</sup>/sec. There are two difficulties which have to be overcome. First, in the case of the coherent, crystalline, and relatively heavy moderators, it is not clear that the experimenter has been observing the asymptotic mode.<sup>(36)</sup> Second, the smallest samples considered have bucklings such that  $B < \lambda_{tr}$  lies in the range 0.1-1.0. Thus, the data that are most important in determining  $C$  are subject to large (and, at present, undetermined) transport corrections. Indeed, one finds curves of  $\lambda_0$  vs  $B^2$  which are different for water samples having different shapes ("square" and "flat"), yet are characterized by the same bucklings.<sup>(24,37,38)</sup> This difficulty will be aggravated in the case of coherent moderator materials where  $\lambda_{tr}$  increases as the sample size decreases.

Recent theoretical analysis of the pulsed source experiment has indicated additional difficulties.<sup>(39,40,41)</sup> The  $\lambda_k$  are eigenvalues of the unbounded scattering operator,

$$S N_k(v^2) = \int dv' \left[ v' \Sigma_s(v', v) - v \Sigma_s(v, v') \right] N_k(v'^2) \quad (6)$$

whose spectrum appears to consist of a set of discrete points, and a continuous set bounded from below by  $(v\Sigma_s)_{\min}$ . When the space-distribution is proportional to  $\exp(i \mathbf{B} \cdot \mathbf{r})$  one sees<sup>(42)</sup> that  $\lambda_0$  must be less than  $v(\Sigma_s + \Sigma_a)_{\min}$ , and that for sufficiently large  $B^2$  no fundamental mode exists. Nevertheless several experiments performed on crystalline materials give results which violate this limit. While it is possible that a rigorous transport treatment of the Boltzmann equation will undo this contradiction, it is apparent that the experiments should be repeated and verified.

Some measurements and calculations of  $\lambda_1$  for  $H_2O$  have been reported.<sup>(36)</sup> Though data are few, calculations have been refined considerably<sup>(41,42)</sup> and show that simple  $M_2$  expressions for  $\lambda$  and  $C$ <sup>(36)</sup> can be in error by as much as an order of magnitude. It is also likely that a discrete  $\lambda_1$  will not be observed in the common crystalline moderators.<sup>(43)</sup>

The analysis of the thermal neutron diffusion-length experiment gives similar results. Here,

$$N(\underline{r}, \underline{v}) = \sum_j e^{-\kappa_j \cdot \underline{r}} F_j(\underline{v}), \quad (7)$$

where the  $F_j$  are eigenfunctions of an operator closely related to equation (6). Again the spectrum of eigenvalues contains a discrete and a continuous portion, the latter setting in at  $\kappa = (\Sigma_s + \Sigma_a)_{\min}$ .<sup>(42,44)</sup> In a  $1/v$  system, the expansion of  $\kappa_0$  in powers of  $v\Sigma_a$  again yields  $\langle v\lambda_{tr} \rangle$  and  $C$ . Since the experiments are always carried out in "large" geometry, the difficulties associated with transport boundary conditions are avoided. The most successful experiments, to date, have been those performed in  $H_2O$ .<sup>(45)</sup>

In another group of experiments,<sup>(46,47)</sup> transients are induced by spatial discontinuities - in temperature and composition. The distributions are far from asymptotic, and an analysis via equation 7 appears unwise. It is based instead upon an expansion in terms of non-orthogonal energy modes which have Maxwellian shape, but different characteristic temperatures. Among the results are "re-thermalization cross-sections", which characterize the spatial relaxation of the neutron spectrum.

There are unanswered questions connected with much that we have sketched here, and, these issues will be pursued in the future. There is also promise at

present of direct practical applications of pulsed neutron techniques in the analysis of multiplying assemblies. (14,48,49,50)

#### 4. Thermal Reactor Calculations

A variety of techniques (Table II) have been used to compute thermal neutron spectra in reactors. (51) These methods include diffusion theory combined with a heavy gas kernel, multigroup transport theory with crystal or bound atom kernels, (52,53) and Monte Carlo methods. (54) The diffusion theory methods are most applicable to large media with smoothly varying properties (an homogenized reactor), while the transport theory methods are needed for small highly absorbing regions with sharp material discontinuities (reactor cells), or when angular distributions are important (strong flux gradients).

The principal approach is the multigroup method in which the energy region below a cutoff (usually around 1-2 ev) is divided into groups. If many groups are used, and 30-50 is common, the spacing of the groups is not critical (except when resonance absorbers are present) and it is a good approximation to evaluate all quantities at the center of the group rather than averaging over the group. If few groups are used, it is generally necessary to first compute a many group spectrum and average the kernels and cross sections over the few groups. The resulting few group kernels are applicable only to the class of problems determined by the weighting spectra. Next the kernels  $\Sigma_g(E' \rightarrow E, \mu)$  must be evaluated for the selected energy mesh. Most applications require the Legendre components of the kernel  $\Sigma_{sn}(E' \rightarrow E)$ . A variety of computer codes have been written to compute the Legendre component scattering matrices. (51) Examples of typical reactor calculations which show the sensitivity of the results to scattering models are given in the next two sections.

##### 4.1 H<sub>2</sub>O, D<sub>2</sub>O, and CH<sub>2</sub> Lattice Calculations

Many of the same techniques have been used to compute thermal spectra in light and heavy water lattices and polyethylene lattices. The kernels most frequently used are the Nelkin kernel, (22,55,56) the free gas kernel, (51) and the Brown-St John kernel. (57) The methods used to solve the transport equation include Monte Carlo, (54,58)  $S_n$  (59), and integral transport methods. (36,51) We will consider the lattice parameter  $\xi$  (disadvantage factor),  $f$  (thermal utilization),  $\eta$  (neutrons produced per neutron absorbed in the fuel),  $L^2$  (thermal migration area), and reaction rates.

Let us characterize the scattering kernel by its transport cross section



and  $M_2$  (essentially the zeroth and second energy transfer moments of the kernel), and discuss the sensitivity of the lattice parameters to them for a typical lattice.<sup>(51)</sup> The lattice is composed of 1/8 in. uranium plates (1.25% enriched) in light water. Measurements and calculations of the disadvantage factors and average moderator velocity have been made as a function of water to uranium ratio  $W/U$  for this lattice. The slopes of the  $\xi$  curves are determined by the energy variation of the transport cross section; the level is determined by both the transport cross section and by  $M_2$ . In this example the  $\xi$  predicted by the hydrogen gas kernel is 5% lower at  $W/U=4$  than predicted by the Nelkin kernel resulting in an 0.7% overestimate of  $f$ . The value of  $\eta$  depends mainly on  $M_2$  and the  $W/U$  ratio. For these lattices, a 20% change in  $M_2$  results in a 0.25% change in  $\eta$  at  $W/U=1$ , and a 0.6% change at  $W/U=4$ . Thus, the parameters  $\eta$  and  $f$  tend to be insensitive to the scattering kernel since they are ratios of reaction rates and the absorption and fission cross sections are nearly proportional to  $1/v$ . If resonance absorbers (i.e., plutonium) are used, the sensitivity will be considerably greater. Reaction rates and  $L^2$  are more sensitive to the kernel than  $\eta$  and  $f$ . For the above example, a 20% change in  $M_2$  would result in a 5.6% change in a  $1/v$  reaction rate and  $L^2$  at  $W/U=1$ , and a 2.8% change at  $W/U=4$ . These changes are significant for operating reactors since plutonium build up and control worth are directly related to the above sensitivity to reaction rate and  $L^2$ .<sup>(60)</sup> From  $H_2O$ ,  $D_2O$ , and  $CH_2$  lattice physics investigations it appears that better agreement between experiment and theory is generally obtained using bound atom scattering cross sections.

#### 4.2 Crystalline Moderators

The Wilkins heavy gas model,<sup>(4)</sup> the free gas model,<sup>(5)</sup> and the Parks kernel<sup>(13)</sup> for polycrystalline graphite have been extensively used in the calculation of thermal neutron spectra and reaction rates in graphite reactors. The use of the heavy gas model or the free gas model can lead to large uncertainties in reaction rates, power distributions, temperature coefficients, etc. For example, the value of  $M_2$  predicted for a free gas of mass 12 is 2.809 as compared to an  $M_2$  of 0.9784 predicted by the crystalline model. Figure 8 shows the spectrum predictions based on two physical models for a graphite-plutonium composition similar to that produced in a Calder Hall reactor. Table III shows the significant variations that one can expect to find between calculated average cross sections using both realistic (crystal) and non-realistic (free or heavy gas) scattering models. Suich<sup>(61)</sup> has shown for the BNL graphite research reactor that the Parks graphite kernel was found to yield the same  $\eta$  as a free gas of mass 21.4, while in order to predict  $f$ , a mass of 28.8 was needed. In addition, in order to predict  $\frac{1}{\eta} \frac{d\eta}{dt}$ , a mass of 32.4

was needed compared to a mass of 46.1 for  $\frac{1}{f} \frac{df}{dt}$ . Thus, typical calculations for the graphite lattices reported here are more sensitive to the approximations underlying the scattering kernel than are results for many water, heavy water and polyethylene lattices. Much less analysis has been done for representative Be and BeO moderated reactors but it is clear that in most cases, these systems should be somewhat less sensitive than graphite to the degree of physical exactness incorporated into the scattering kernel.

#### REFERENCES

1. WASH 1044 and WASH 1047, AEC Nuclear Cross Sections Advisory Group Compilations.
2. COHEN, E.R., NAA-SR-1127 1955; COVEYOU, R.R., J. Nuclear Energy 2, (1956) 153.
3. CORNGOLD, N., Annals of Physics, 6 (1959) 368.
4. WILKINS, J.E., Report CP-2481 (1944).
5. WIGNER, E.P. and WILKINS, J.E. (1944) AECD-2275.
6. FERMI, E., Ricerca Scientifica, VII, 2 (1936) 13.
7. VAN HOVE, L., Phys. Rev. 95 (1954).
8. WICK, G.C., Phys. Rev. 94 (1954) 1228.
9. PLACZEK, G., Phys. Rev. 87 (1952) 371.
10. EGELSTAFF, P.A. and SCHOFIELD, P. Nucl. Sci. and Eng. 12 (1962) 260.
11. MARSHALL, W. and STUART, R., Proceedings of Symposium on Inelastic Scattering of Neutrons, IAEA, Vienna (1960).
12. BUTLER, D., Proc. Phy. Soc. 81 (1963) 276 and 294.
13. WIKNER, N.F., JOANOU, G.D. and PARKS, D.E., General Atomic Report GA-4169 (1963).
14. YOUNG, J.A., ET AL., General Atomic Report GA-4659 (1964).
15. VAN HOVE, L., Phys. Rev. 93 (1954) 1207.
16. BROCKHOUSE, B.N., IAEA Symposium on Inelastic Scattering, Vienna (1960).
17. SCHUNK, R.E., BEUGGER, R.M., RANDOLPH, P.D. and STRONG, K.A., Phys. Rev. 128 (1962) 562.
18. YOUNG, J.A., Trans. American Nuclear Society (1963) and General Atomic Report GA-4638 (1963).
19. Proceedings of the Symposium on Inelastic Scattering of Neutrons in Solids and Liquids, Chalk River, Canada (1962).
20. YOSHIMORI, A. and KITANO, Y., J. Phy. Soc. Japan 11 (1956) 352.
21. WOODS, A.D.B., BROCKHOUSE, B.N., SAKAMOTO, M. and SINCLAIR, R.N., IAEA Symposium on Inelastic Scattering, Vienna (1960).
22. NELKIN, M.S., Phys. Rev. 110 (1960) 741.
23. MARADUDIN, A.A., ET AL., Theory of Lattice Dynamics in the Harmonic Approximation (SEITZ, F., and TURNBULL, D.B.I., eds.) Academic Press Inc., New York (1963).
24. BEYSTER, J.R., ET AL., General Atomic Report GA-2544 (1961).
25. POOLE, M.J., Paper SM 42/18, IAEA Symposium on Critical and Experimental Experiments, Amsterdam (1963).

26. SINCLAIR, R.N. and GOODE, P.D., Nuclear Physics Division Research Report AERE, PR/NP-5.
27. PARKS, D.E., BEYSTER, J.R. and WIKNER, N.F., Nucl. Sci. and Eng. 13, #4 (1962)
28. BACH, D.R., BUNCH, S.I., ROESSNER, J.R. and SLOVACEK, R.E., Trans. Amer. Nucl. Soc. 3 (1960) 490.
29. BARDES, R.G., HOUGHTON, G.H., PARKS, D.E. and BEYSTER, J.R., General Atomic Report GA-4812 (1963).
30. REINSCH, V.L. and SPRINGER, T., Z. Naturforschg. 16a (1961) 112/116.
31. BARCLAY, F.R., COATES, M.S. ET AL., Proc. BNL Conference on Neutron Scattering 2 (1962) 359.
32. CAMPBELL, C., Proceedings 2nd International Conference Peaceful Use of Atomic Energy, AE 16, Geneva (1958) P/10.
33. MOSTOVOI, V.I., Proceedings BNL Conference 2 (1962) 411.
34. JOHANSSON, E., JONSSON, E., ET AL., AKTIEBOLAGET ATOMENERGI, AE-123 (1963).
35. HONECK, H.C. and TAKAHASHI, Nucl. Sci. and Eng. 15 (1963) 115.
36. Proc. BNL Thermalization Conference, BNL-719, Vol. 3 and 4 (1962).
37. HALL, R.S. ET AL., Proc. Phys. Soc. (London) 79 (1962) 257.
38. KUCHLE, M., Nukleonik, 2 (1960) 131.
39. CORNGOLD, N., MICHAEL, P. and WOLLMAN, W., Nucl. Sci. and Eng. 15 (1963) 13.
40. KOPPEL, J.U., Nucl. Sci. and Eng. 16 (1963) 101.
41. OHANIAN, M. and DAITCH, P., Nucl. Sci. and Eng. (to be published).
42. CORNGOLD, N. and MICHAEL, P., Nucl. Sci. and Eng. (to be published).
43. CORNGOLD, N. and SHAPIRO, C., unpublished manuscript.
44. MAIOROV, L., Proc. BNL Thermalization Conference, BNL-719 (1962) 1375.
45. KOPPEL, J.U., Proc. BNL Thermalization Conference, BNL-719 (1962) 1012.
46. BENNETT, R.A., Proc. BNL Thermalization Conference, BNL-719 (1962) 838.
47. FEINER, F., ET AL., Proc. BNL Thermalization Conference, BNL-719 (1962) 900.
48. BECKURTS, K.H., Nucl. Instr. and Meth. 11 (1961) 144.
49. GARELIS, E. and RUSSELL, J.L., Nucl. Sci. and Eng. 16 (1963) 263/270.
50. SLOVACEK, R., ET AL., Trans. Am. Nucl. Soc. 6 (1963) 298.
51. HONECK, H.C., BNL-821, "A Review of the Methods for Computing Thermal Neutron Spectra" (1963).
52. GELBARD, E., IAEA Symposium on Critical Experiments, Amsterdam (1963).
53. LESLIE, D.C., Proc. BNL Thermalization Conference, 2, 592 (1962).
54. BROWN, H.D., Journal of Nuclear Energy, 8 (1959) 177.
55. HONECK, H.C., Trans. Amer. Nucl. Soc. 5 (1962) 47.
56. GOLDMAN, D.T. and FEDERIGHI, Nucl. Sci. and Eng. 16 (1963) 165.
57. BROWN, H.D. and ST JOHN, D., DP-33 (1954).
58. PFEIFFER, R. and STONE, W., KAPL-M-RPG-1 (1962).
59. HINMAN, G.W., General Atomic Report GAMD-3425 (1962).
60. PETERSON, G.T., ALINE, P. and MC WHORTER, R.J. IAEA Symposium on Critical Experiments, Amsterdam (1963).
61. SUICH, J., Nucl. Sci. and Eng. (in press).

**TABLE I**  
**CHARACTERISTICS OF SOME SCATTERING KERNEL CODES**  
 Allowed form of  $\rho(\delta)$

Code Name	Installation	Computer	Continuous	Delta Function	Diffusive Motion	Anisotropy	Moderators
ROBESPIERRE	GA	7090	No	Yes	No	No	H <sub>2</sub> O, D <sub>2</sub> O, CH <sub>2</sub>
GAKEE	BNL-GA	7090	No	Yes	No	No	H <sub>2</sub> O, D <sub>2</sub> O, CH <sub>2</sub>
KERNEL PAM	KAPL	S-2000	No	Yes	No	No	H <sub>2</sub> O, D <sub>2</sub> O, CH <sub>2</sub>
SUMMIT	GA	7090	Yes	No	No	Yes	Graphite
SUMMIT II	GA	7090 7044	Yes	No	No	No	ZrH, CH <sub>2</sub> , C <sub>6</sub> H <sub>6</sub> C, Be, BeO
LEAP PIXIE	Winfrith	7090	Yes	Yes	Yes	No	C, D <sub>2</sub> O, BeO, Be, H <sub>2</sub> O
GASKET	GA	7090 7044	Yes	Yes	Yes	No	All Moderators

**TABLE II**  
**CHARACTERISTICS OF SOME THERMALIZATION CODES**

Code Name	Installation	Computer	Language	Angular Representation	Geometry	Energy Representation	Scattering Kernels	Anisotropic Scattering
MARC	BAPI.	S-2000	TAC	Monte Carlo	Slab, Hexagonal Lattice	Monte Carlo	Arbitrary	P <sub>1</sub>
TRAM	KAPL	S-2000	TAC	Monte Carlo	Arbitrary	Monte Carlo	Arbitrary	P <sub>3</sub>
CASINO	SRL	704	FORTRAN	Monte Carlo	Hexagonal Lattice	Monte Carlo	Brown-St. John	P <sub>∞</sub>
WDSN	Winfrith	7090	FORTRAN	DSN	Cylinder	Multigroup	Arbitrary	No
GAPISN	GA	7090	FLOCO	DSN	(Slab, Cylinder, Sphere)	Multigroup	Arbitrary	P <sub>∞</sub>
THERMOS	BNL	7090	FORTRAN	Int. Trans.	Slab, Cylinder	Multigroup	Arbitrary	No
TET	DTMB	7090	FORTRAN	Disc. Ords.	Slab	Multigroup	Arbitrary	P <sub>3</sub>
SLOP-1	BAPI.	704	SAP	P <sub>1</sub> , P <sub>3</sub> , DP <sub>1</sub>	Slab, Cylinder, Sphere	Multigroup	Arbitrary	P <sub>3</sub>
ULCER	AI	7090	FORTRAN	P <sub>1</sub>	Slab, Cylinder, Sphere	Multigroup	Arbitrary	P <sub>1</sub>
SWAKRUM	KAPL	704	FORTRAN, SAP	P <sub>1</sub> , P <sub>3</sub> , DP <sub>1</sub>	Slab	Few Modes	Arbitrary	P <sub>3</sub>
SPECTROX	Winfrith	Mercury		Amouyal's Method	Cylindrical Cell	Diff. Eq.	Generalized Heavy Gas	No
KATE-1	BAPI.	S-2000	TAC	Infinite Medium		Diff. Eq.	H Gas	No
TEMPEST-II	AI	7090	FORTRAN	Infinite Medium		Diff. Eq.	H Gas or Heavy Gas	No
GATHER-II	GA	7090	FORTRAN	Infinite Medium Fourier Transform		Multigroup	Arbitrary	P <sub>1</sub>
QUICKIE	AI	7090	FORTRAN	Infinite Medium		Multigroup	Arbitrary	P <sub>1</sub>
GAZE-II	GA	7090 7044	FORTRAN		Slab, Cylinder, Sphere	Multigroup	Arbitrary	No
GAMBLE	GA	7090 7044	FORTRAN		x, y r, z	Multigroup	Arbitrary	No
S-X	HAPO	7090	FLOCO	(P <sub>1</sub> )SN	Slab, Cylinder, Sphere	Multigroup	Arbitrary	P <sub>1</sub>

**TABLE III**  
**EFFECTS OF CRYSTALLINE BINDING AND NUCLIDE CONCENTRATION ON THERMAL\* CROSS SECTIONS**

Moderator Temperature, °K	← 300 →			← 1200 →			← 1200 →	
Carbon to U-235 ratio	← 4000 →			← 4000 →			← ∞ →	
Carbon to Pu ratio	← ∞ →			← ∞ →			← 2000 →	
Scattering Model	Crystal	Free Gas	Heavy Gas	Crystal	Free Gas	Heavy Gas	Crystal	Heavy Gas
	σ (barns)	% Diff.	% Diff.	σ (barns)	% Diff.	% Diff.	σ (barns)	% Diff.
U-235 Absorption	321	+14	+17	227	+1.0	+1.5	99.3	-8.7
Pu-239 Absorption	940	-1.0	+1.7	1340	-0.22	+0.22	489	-8.8
Pu-240 Absorption	1100	+11	+5	982	+0.11	+1.6	1940	+64
Xe-135 Absorption	1,540,000	+7.4	+11	800,000	+1.8	+2.0	187,000	-22
Sm-149 Absorption	41,800	-3.6	-1.1	25,300	+1.1	+0.75	6680	-22
(1/v)** Absorption	0.515	+11	+14	0.374	+0.86	+1.2	0.210	-6.4

\* The cross sections are averaged over a group from zero to 2.38 ev.

\*\* The (1/v) represents a nuclide whose 2200 m/s absorption cross section is unity and varies inversely with velocity.

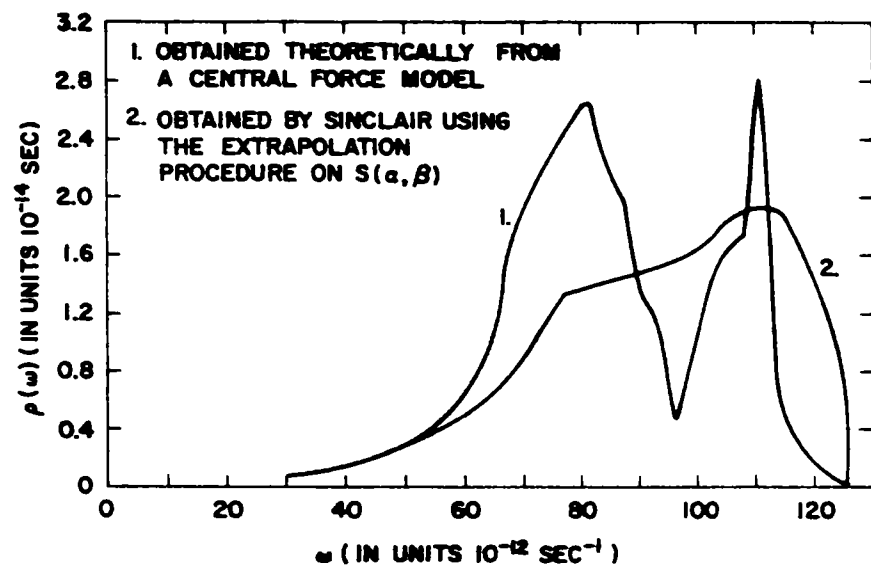


FIG. 1--FREQUENCY SPECTRUM OF BERYLLIUM

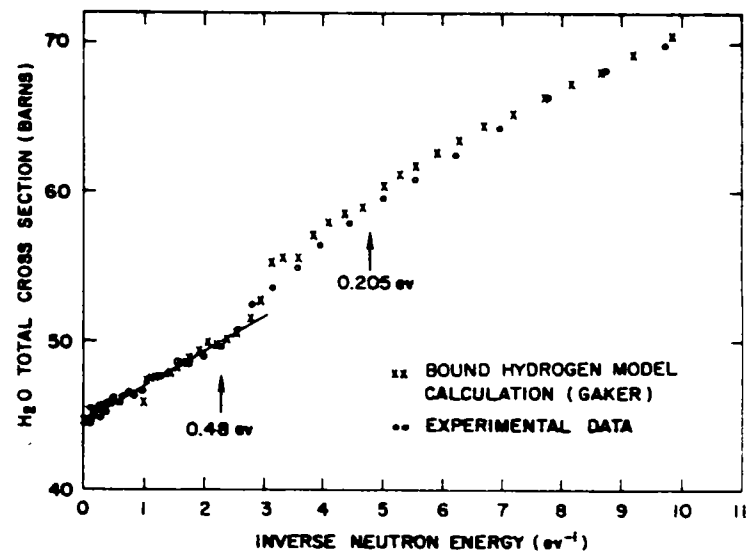
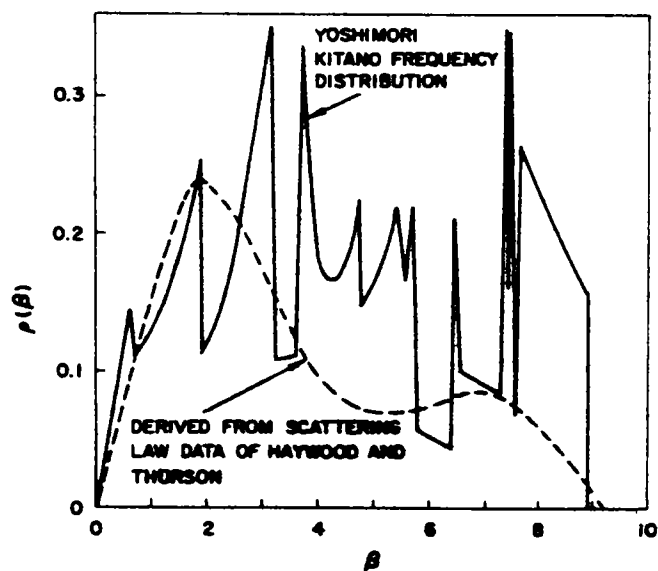
FIG. 3--VARIATION OF  $H_2O$  TOTAL CROSS SECTION WITH INVERSE NEUTRON ENERGY

FIG. 2--LATTICE FREQUENCY SPECTRA FOR GRAPHITE

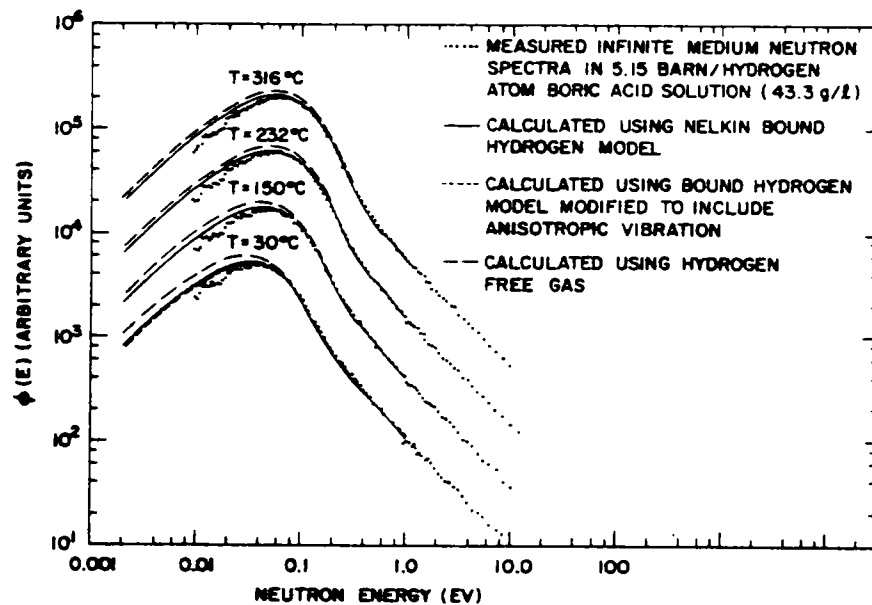


FIG. 4--INFINITE-MEDIUM NEUTRON SPECTRA IN BORATED WATER AS A FUNCTION OF MODERATOR TEMPERATURE

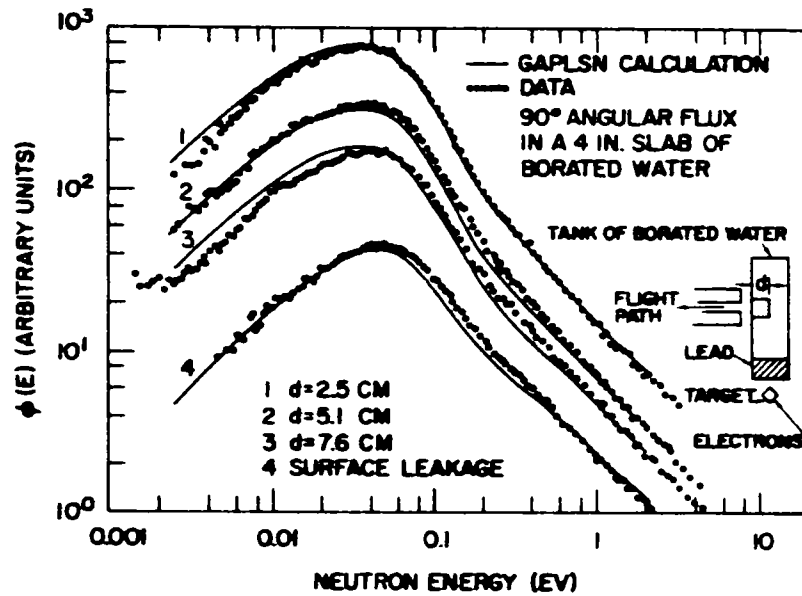


FIG. 5--90° ANGULAR FLUX IN A 4-IN. SLAB OF BORATED WATER

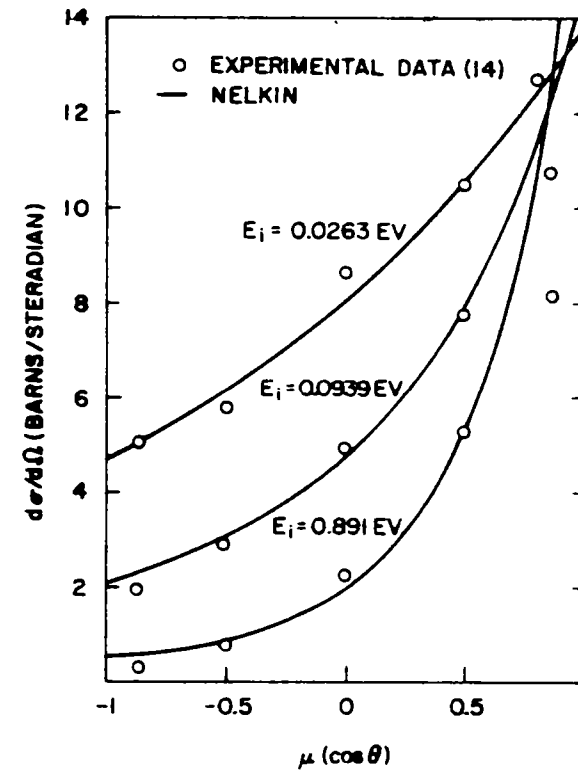


FIG. 7--MEASUREMENTS AND CALCULATIONS OF THE DIFFERENTIAL CROSS SECTION OF WATER

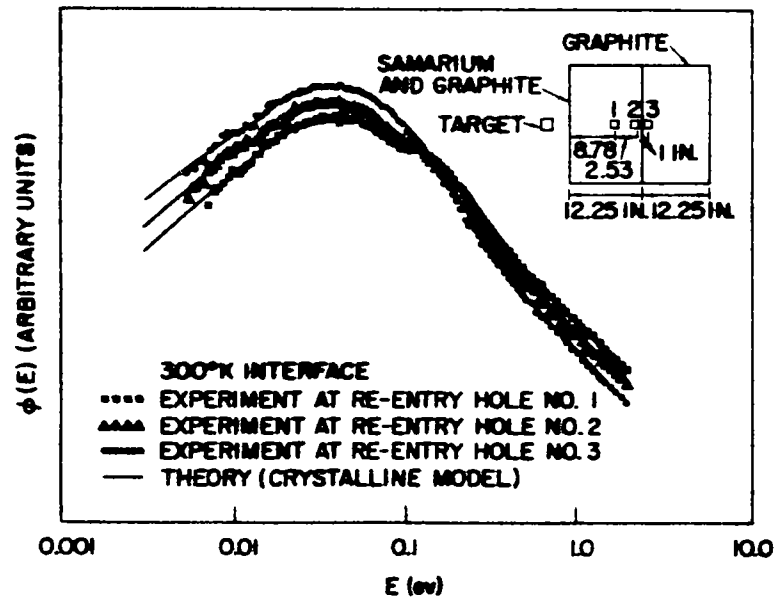


FIG. 6--THERMAL SPECTRA MEASURED IN INTERFACE ASSEMBLY

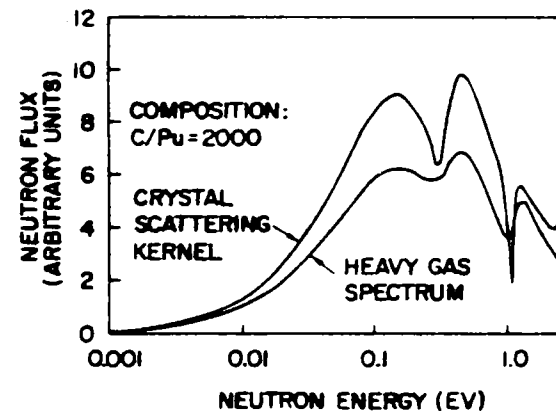


FIG. 8--THERMAL FLUX SPECTRA IN GRAPHITE AT 1200 K



## APPENDIX B

### LATTICE VIBRATIONAL SPECTRA OF BERYLLIUM, MAGNESIUM, AND ZINC





# Lattice Vibrational Spectra of Beryllium, Magnesium, and Zinc

JAMES A. YOUNG AND JUAN U. KOPPEL

General Atomic Division of General Dynamics, John Jay Hopkins Laboratory for  
Pure and Applied Science, San Diego, California

(Received 27 January 1964)

The lattice vibrational spectra of Be, Mg, and Zn have been obtained using the root sampling method. The force constants used in the calculations were those determined from measurements of the dispersion relations by slow neutron-scattering techniques. Calculations of the specific heat of each metal show good agreement with measured values.

## I. INTRODUCTION

IN recent years the scattering of slow neutrons in solids has proved valuable as a tool for investigating the dispersion relations of lattice waves in crystals. In particular, measurements have been made on beryllium, magnesium, and zinc, all having the hexagonal close-packed lattice structure. In the first case (Be), Schmunk *et al.*<sup>1</sup> have determined the force constants for a central force model with interactions out to fifth nearest neighbors. For Mg, Collins<sup>2</sup> determined the force constants for both a tensor force model and a central force model with interactions out to fourth nearest neighbors. A similar experiment by Borgonovi *et al.*<sup>3</sup> has given the force constants of zinc for the tensor force model used for Mg.<sup>2</sup> Using these experimentally determined force constants, we have computed the lattice

vibrational spectra and specific heat for each of the above metals.

## II. RESULTS

The vibrational spectrum of a crystal  $\rho(\omega)$  is defined such that  $\rho(\omega)d\omega$  is the fraction of frequencies  $\omega$  between  $\omega$  and  $\omega+d\omega$ . The method used here to approximate  $\rho(\omega)$  is to sample the frequencies  $\omega(\mathbf{k})$  for a large number of values of the wave vector  $\mathbf{k}$  in the first Brillouin zone of the crystal. The frequencies obtained must be weighted according to their degeneracy in the zone, and a histogram constructed of the number of frequencies falling in a given frequency interval.

In the Born-von Kármán<sup>4</sup> theory of lattice dynamics the frequencies  $\omega$  are determined by the following secular equation:

$$|D(\mathbf{k}) - M\omega^2 I| = 0, \quad (1)$$

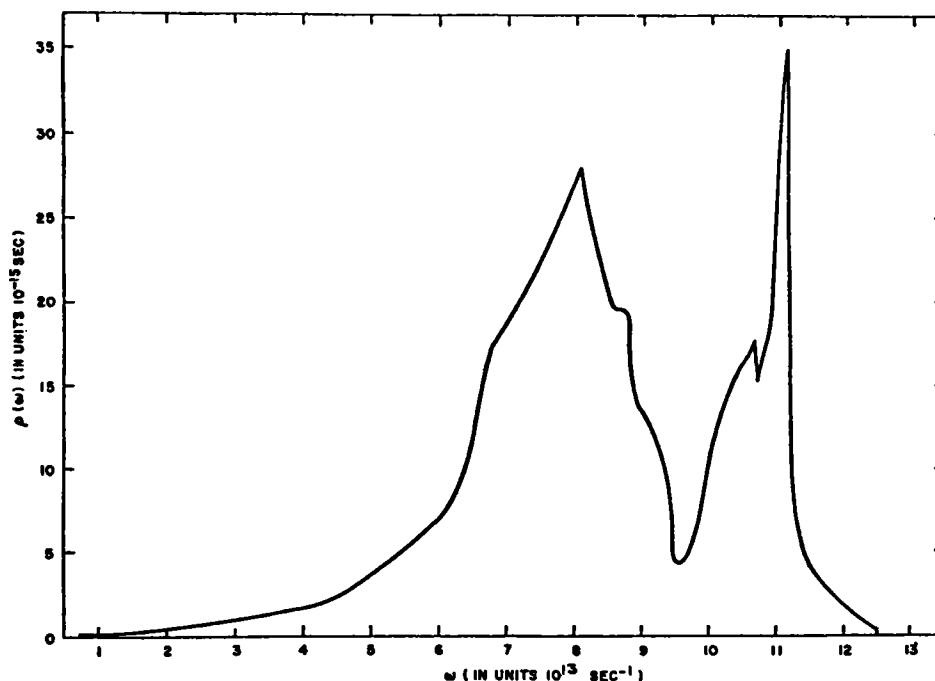


FIG. 1. Lattice vibrational spectrum of beryllium for a sampling of 10 261 points in the reduced Brillouin zone.

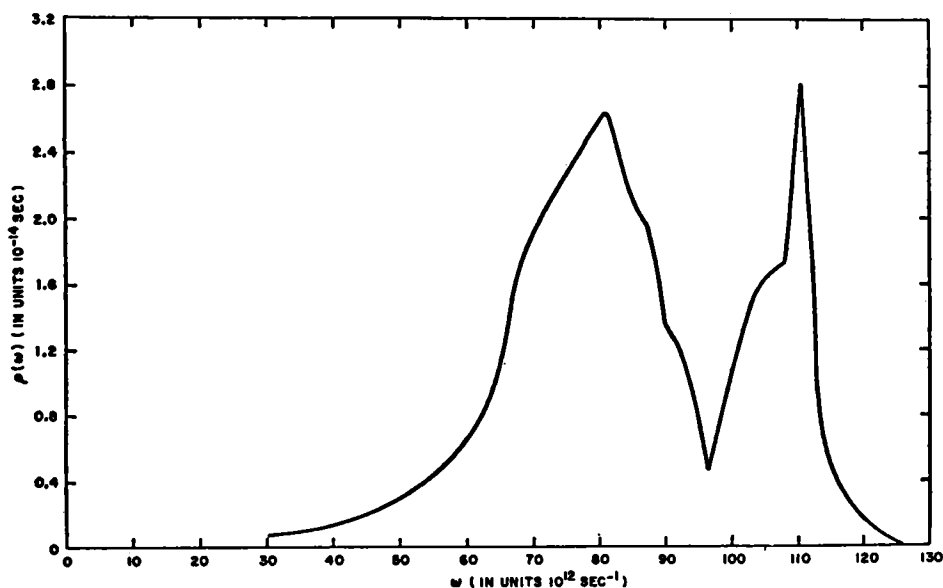
<sup>1</sup> R. E. Schmunk, R. M. Brugger, P. D. Randolph, and K. A. Strong, Phys. Rev. 128, 562 (1962).

<sup>2</sup> M. F. Collins, Proc. Phys. Soc. (London) 80, 362 (1962).

<sup>3</sup> G. Borgonovi, G. Caglioti, and J. J. Antal, Phys. Rev. 132, 683 (1963).

<sup>4</sup> M. Born and K. Huang, *Dynamical Theory of Crystal Lattices* (Oxford University Press, London, 1954).

FIG. 2. Lattice vibrational spectrum of beryllium for a sampling of 2413 points in the reduced Brillouin zone.



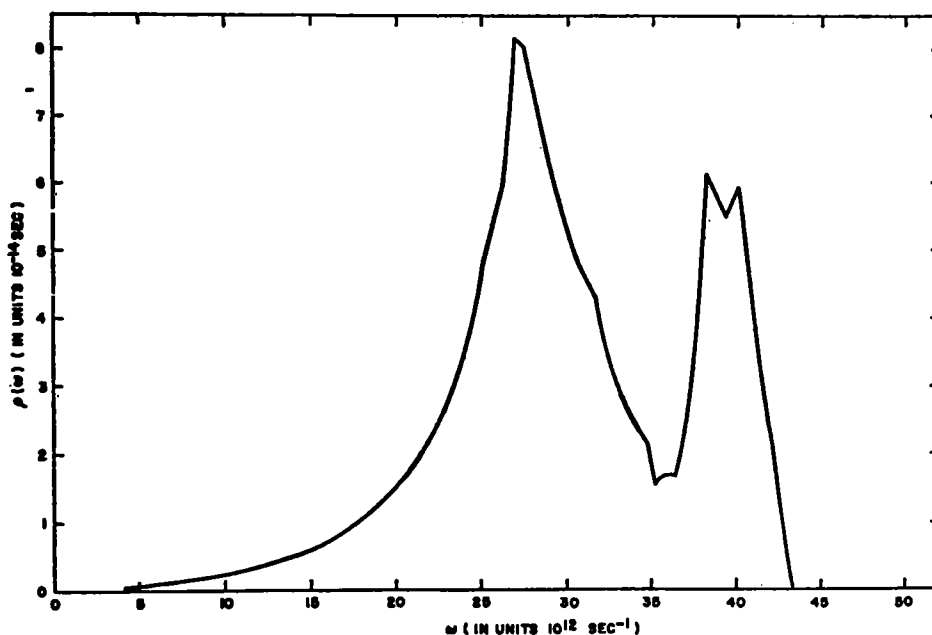
where  $M$  is the atomic mass and  $I$  the unit matrix. The matrix  $D(\mathbf{k})$  is  $6 \times 6$  for hexagonal close-packed crystals and depends upon the force constants of the lattice. Equation (1) has been solved for equally spaced points in that region which is one twenty-fourth of the first Brillouin zone, and irreducible under the symmetry operations that leave the roots of the secular equation invariant. The points are then weighted as to whether or not they are on the faces, edges, etc., of this reduced zone. For beryllium, the calculation was performed for 10 261 equally spaced points ( $\mathbf{k}$  values) in the reduced

zone, and the spectrum shown in Fig. 1. Figure 2 shows, for comparison, the same calculation for 2413 equally spaced points. We see that greatly increasing the number of points does not significantly change the vibrational spectrum.

In the case of magnesium, the calculation was performed for a sampling of 2413 equally spaced points in the reduced zone, for both the central and tensor force models. Figures 3 and 4 show the vibrational spectra for central and tensor forces, respectively.

The vibrational spectrum of zinc was also obtained

FIG. 3. Lattice vibrational spectrum of magnesium using the central force model.



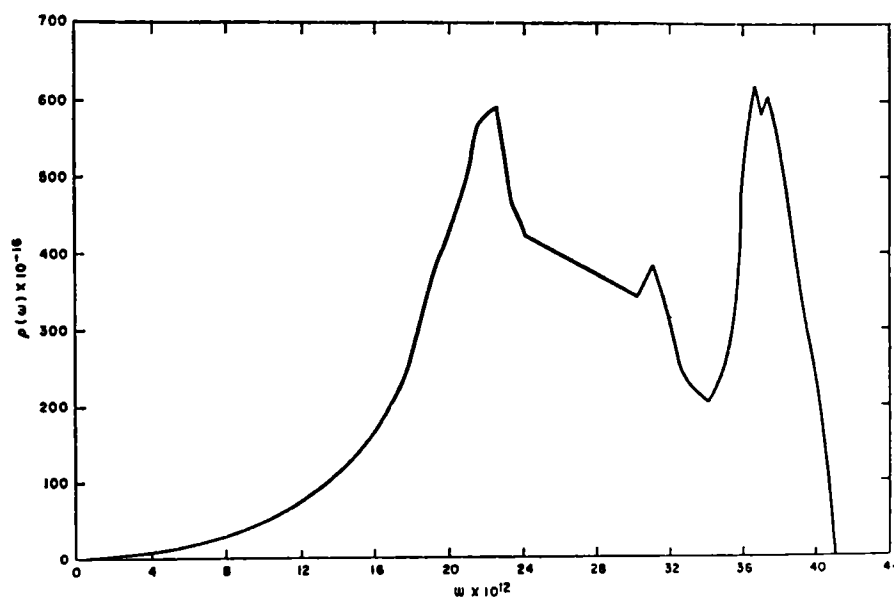


FIG. 4. Lattice vibrational spectrum for magnesium using the tensor force model.

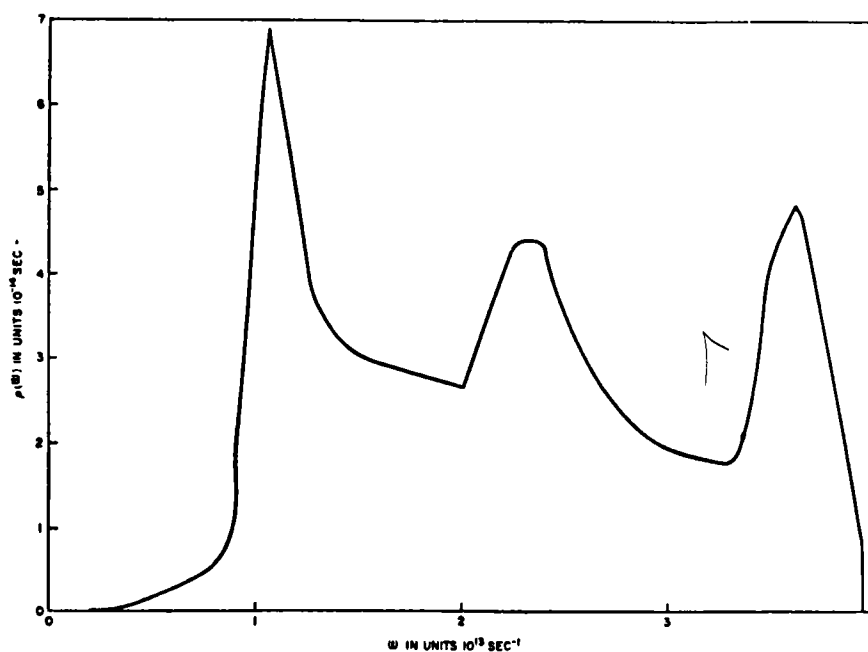


FIG. 5. Lattice vibrational spectrum of zinc using a tensor force model.

from a sampling of 2413 equally spaced points in the reduced zone with the tensor force model, and is shown in Fig. 5.

In order to make some comparison with experiment, the specific heat at constant volume  $C_V$ , which is given in terms of the frequency spectrum by

TABLE I.  $C_V$  for beryllium (cal/g).

$T$ (°K)	Computed value	Measured value
100	0.070	
150	0.195	
200	0.311	
293	0.455	0.466
400	0.535	

TABLE II.  $C_V$  for magnesium (cal/g).

$T$ (°K)	Computed value	Measured value
123	0.1839	0.1767
153	0.2023	0.2025
223	0.2236	0.2228
300	0.2329	

$$\frac{C_V}{3R} = \int_0^{\omega_{\max}} d\omega \left( \frac{\omega}{T} \right)^2 \frac{e^{\omega/T}}{(e^{\omega/T} - 1)^2} \rho(\omega), \quad (2)$$

where  $R$  is the gas constant,  $\omega_{\max}$  the maximum frequency of the crystal, and  $T$  the temperature measured

in energy units, has been computed for all three metals. Tables I-III compare the calculated specific heat with measured values,<sup>5</sup> for the vibrational spectra of Be, Mg, and Zn, respectively. The agreement is quite good in all cases, although specific heat comparisons do not provide a good test.

TABLE III.  $C_V$  for zinc (cal/g).

$T$ (°K)	Computed value	Measured value
72	0.0538	0.0573
173	0.0826	0.0814
300	0.0882	

#### ACKNOWLEDGMENTS

The authors would like to express their appreciation to D. Naliboff and D. Houston for their competent programming of the equations.

<sup>5</sup> *Handbook of Chemistry and Physics* (Chemical Rubber Publishing Company, Cleveland, Ohio, 1963).





